Topology Optimized Microgrippers for Nanomanipulation and Assembly

Ph.D. Thesis

Özlem Şardan Sukas

Supervisors

Peter Bøggild

Ole Sigmund

DTU Nanotech, Department of Micro- and Nanotechnology
at the Technical University of Denmark

October 15, 2009

To the only one I love:
my husband…

Abstract

This Ph.D. thesis deals with development of electrothermal microgrippers for nanomanipulation and assembly, within the scope of the EU funded NanoHand project. Topology optimization was used for the design of the polysilicon microgrippers. The topology optimized microgrippers have a size that is comparable with the conventional three-beam and rib-cage designs.

The performance of the post processed designs was verified through finite element simulations performed using COMSOL. The topology optimized actuators designed during this project are capable of supplying 1-2 orders of magnitude higher forces than the conventional three-beam and rib-cage electrothermal actuators with the same size. Hence, the topology optimized designs are suitable for miniaturization.

The stiffness values for the topology optimized designs with the highest and lowest performance are 234 N/m and 91 N/m, respectively. The end-effector temperatures of the topology optimized microgrippers are in the range 253-349 °C (at an operating temperature of 550 °C), being much lower than that of the three-beam design, which is 387 °C.

The designed topology optimized microgrippers were fabricated using conventional microfabrication processes at Danchip's National Cleanroom Facilities at DTU. The fabrication yield was increased from 30 % to 90-99 % through optimization of the critical process steps.

Efforts were made in order to solve the problems arising during packaging of the microgrippers. Although the quality of the interface was considerably improved, it was not possible to completely eliminate the out-of-plane movement of the microgripper end-effectors due to the thermal expansion of the printed circuit board (PCB) interface.

The dual beam focused ion-beam (FIB) system at the Center for Electron Nanoscopy (CEN) at DTU was used for repairing the defected devices and recovering the missing design features. FIB milling was also employed in functionalizing the microgripper end- effectors for achieving a smaller contact area with the manipulated sample and also realizing more advanced microgripper concepts, such as inverse and XY-microgrippers.

Mechanical and thermal performances of the fabricated microgrippers were characterized using various methods. Actuation curves of all microgripper designs were obtained with a nano-metric resolution using an optical manipulation setup. The results of the actuation experiments are in agreement with the finite element simulation results within 5-10 %.

Temperature profiles of the topology optimized designs were obtained through the temperature measurements using Raman spectroscopy. These experiments were performed at EMPA Materials Science and Technology, in Thun Switzerland. According to the results of the temperature measurements, the finite element model was improved to consider the heating of the carrier chip during the simulations. Hence, an agreement within 10-30 °C, which corresponds to 4-12 %, was achieved.

Nanomanipulation and assembly experiments inside SEMs were performed successfully using the topology optimized microgrippers, including the demonstrators of the EU funded NanoHand and the NanoRAC projects. These experiments were performed using various setups at DTU Nanotech, the Division of Microrobotics and Control Engineering (AMiR) at the University of Oldenburg, Germany and Klocke Nanotechnik, in Aachen, Germany.

During the nanomanipulation experiments performed with the topology optimized microgrippers, carbon nanotube (CNT) and NanoBIT (exchangeable tool tip)-enhanced AFM super-tips were assembled, CNTs and silicon nanowires (NWs) were manipulated onto Transmission Electron Microscope (TEM) grids for structural characterization and onto four-point probes (FPPs) for electrical characterization. All experiments were performed a number of times in a reliable manner.

AFM scans of 2.5 µm-deep and 500 nm-wide trenches etched in silicon were performed using both the CNT- and NanoBIT-enhanced super-tips. During these scans, the full-depth of the trenches was resolved, which is not possible with a standard pyramidal AFM tip.

The samples manipulated onto the grids were investigated using two different TEMs at DTU CEN (Center for Electron Nanoscopy). The high magnification TEM images reveal that the amorphous carbon layer covering the CNTs was locally damaged at locations held by the end-effectors. The reason for this damage can be the excess gripping force, the high end-effector temperature of the electrothermal microgrippers or a combination.

Resumé

Ph.D rapporten handler om udvikling af elektrotermiske mikropincetter til nanomanipulation, indenfor rammerne af et EU-projekt, NanoHand. Mikropincetter blev designet ved hjælp af topologi optimering, og fremstillet i 5 mikrometer tyk polysilicium for enden af en silicium chip.

Pincetternes egenskaber blev undersøgt med finite element simuleringer ved hjælp af programmet COMSOL. De topologioptimerede aktuatorer leverer op til 100 gange større gribe kræfter end konventionelle designs af omtrent samme størrelse, hvilket viser at topologioptimeringen er yderst effektiv til denne form for miniaturisering.

Fjederkonstanten af mikropincetterne lå mellem 91 N/m og 234 N/m. Under anvendelse af pincetten, er de maksimale temperaturer op til 550 °C, hvorimod temperaturen i gribepunktet kunne holdes i omegnen af 349 °C; dette er væsentligt bedre end de hidtidige design.

Pincetterne blev fremstillet med konventionelle silicium processering i DTU Danchip's rentrum. I løbet af projektet, lykkes det at forøge yield fra 30% til 90-99% gennem optimering af de kritiske proces trin. Et større arbejde angik forbedring af packacking; hvor kvaliteten af interfacet blev forbedret betydeligt, var det ikke muligt helt at eliminere ud-af-planet bevægelser af mikropincetterne, på grund af termisk udvidelse af chip holderen.

Et dual beam focused ion beam (FIB) system ved DTU CEN (Center for Elektron Nanoskopi) blev anvendt til at reparerere defekte grippere. FIB milling blev også anvendt til at modificere designet med sub-100 nm præcision, for at kontrollere kontaktområdet nøjagtigt; blandt andet blev særlige låsemekanismer fremstillet der gør det muligt for en pincet at blive fastholdt i lukkeposition uden termisk aktuation.

De mekaniske og termiske egenskaber af pincetterne blev karakteriseret ved forskellige metoder. Udbøjningskurver af alle designs blev målt med nanometer præcision ved hjælp af et optisk mikroskop, og var i overensstemmelse med finite elementer simulations resultater indenfor 5-10%.

Temperatur profiler af topologioptimerede design blev malt ved hjælp af Raman spektroskopi, ved EMPA Materials Science and Technology, in Thun, Schweiz. Disse resultater bidrog til at forbedre finite element modellen, indtil temperatur fordelingen nu kan forudsiges med 4-12 % nøjagtighed.

Nanomanipulation eksperimenter med en nanorobot indbygget I et elektronmikroskop blev udført både ved DTU Nanotech, Division of Microrobotics and Control Engineering (AMiR) ved Oldenburg Universitet, Tyskland og firmaet Klocke Nanotechnik, i Aachen, Germany.

I løbet af nanomanipulations eksperimenterne blev nanotråde, kulstof nanorør samt særlige, elektronstråle definerede ”NanoBITs” (Nano Bio Interchangeable Tips) manipuleret, og gennem en lang række eksperimenter anbragt på grids til TEM studier, på elektroder, samt monteret som high aspect ratio nåle for enden af AFM spidser.

De forbedrede AFM spidser førte til en langt mere præcis karakterisering af dybe strukturer, i sammenligning med konventionelle pyramideformede AFM spidser.

De manipulerede strukturer blev undersøgt I TEM, hvor det viste sig at kombinationen af høje temperaturer og mekanisk påvirkning, kan føre til beskadigelser af nanostrukturer.

Preface

I would like to express my thanks to the following great people…

Peter Bøggild, for being such a great supervisor! And for guiding and encouraging me not only for research but also for life…

Ole Sigmund, for introducing me to the world of topology optimization and his substantial guidance throughout the project…

The Nanointegration group, for being my family in Denmark…

> Especially, Dirch Hjorth Petersen and Kristian Mølhave, for being always open for fruitful discussions and brainstorming…
>
> And Karin Nordström Dyvelkov, for sharing her knowledge about the grippers and nanomanipulation with me. Also for teaching Danish to me… Mange tak!

The NanoHand partners for the great project…

> Especially, Volkmar Eichhorn for his precious help with almost half of my thesis! And all the joyful experiments we did together…

DTU Danchip Staff, for their precious help during the microfabrication of the microgrippers…

> Especially to Majken Becker, Conny Hougaard, Yvonne Grysting and Helle Vendelbo Jensen, for not only teaching me about the cleanroom and the processes but also being my friends, great friends! They were ready for help whenever needed…

Inger Ninna Hansen from Delta, for the perfect wire bonds of my devices and for welcoming me with a great smile, even if I have 25 chips to be bonded in two days…

DTU CEN Staff, for their help with the wonderful nanoscopy equipment!

> Especially, Andy Horsewell for welcoming our group to CEN in the first place…

DTU Nanotech administration, for their warm smile and help with the non-scientific matters…

> Especially to Peter B. Rasmussen for answering all of my questions and whenever I ask!

Ylva Eichhorn and Kasper Dyvelkov for bringing joy into the project with their little smiles…

Finally, to my family…

My mother, my father, my grandmother (mormor) and especially my brother, for their endless love and support… I missed them a lot!

And my husband, apart from everything he did to keep me going on, just for loving me and sharing my dreams…

This project was supported by the EU grants NANOHAND (IP 034274) and NANORAC (STREP 013680).

Table of Contents

ABSTRACT ..... **V**

RESUMÉ ..... **VII**

PREFACE ..... **IX**

TABLE OF CONTENTS ..... **XI**

CHAPTER 1 INTRODUCTION **1**

1.1 Introduction **1**

1.2 Background **2**

1.2.1 Nanomanipulation Systems 2
1.2.2 Micro/Nanogrippers 5
1.2.3 Topology Optimization 8
1.2.4 Focused Ion Beam (FIB) 12

1.3 Motivation **14**

1.4 Thesis Outline **16**

CHAPTER 2 DESIGN USING TOPOLOGY OPTIMIZATION **17**

2.1 Theory: Electrothermal Actuation **17**

2.1.1 Joule Heating 17
2.1.2 The Effect of Convection and Radiation 19

2.2 Theory: Topology Optimization **20**

2.2.1 Governing Equations 20
2.2.2 Finite Element Implementation 21
2.2.3 The Optimization Problem 21
2.2.4 Material Interpolation Scheme 24
2.2.5 Sensitivity Analysis 24

2.2.6 Numerical Implementation 24
2.2.7 The Topology Optimization Software 25

2.3 Material Selection 26

2.4 Design Procedure 27

2.4.1 Definition of the Design Domain 27
2.4.2 Topology Optimization 30

2.5 Design Results 31

2.6 Design Selection 33

2.7 Design Finalization 35

2.7.1 Post-processing of the Topology Optimized Design 35

2.8 End-effector Design 37

2.8.1 Electrostatic Forces 37
2.8.2 Van der Waals Forces 38
2.8.3 Capillary Forces 39
2.8.4 End-effectors with Less Stiction 40

2.9 Mask Design 42

2.10 Discussion 46

CHAPTER 3 FINITE ELEMENT ANALYSIS OF THE POST-PROCESSED DESIGN 47

3.1 Motivation 47

3.2 The Ideal Case 48

3.2.1 The Model 48
3.2.2 Results 52

3.3 The Non-Ideal Case 59

3.3.1 The Model 59
3.3.2 Results 62

3.4 Discussion 64

CHAPTER 4 FABRICATION 67

4.1 Introduction 67

4.2 The Conventional Process 67

4.2.1 The Process Sequence 67
4.2.2 Results 71

4.3 Modification of the Microgrippers using FIB 74

4.3.1 Applications for Microgrippers 75
4.3.2 FIB Experiments 77

4.4 Fabrication of Nanogrippers using FIB 81

4.4.1 The Procedure 81
4.4.2 Results 81
4.4.3 Challenges 82

4.5 Discussion 84

CHAPTER 5 PACKAGING 85

5.1 Introduction 85

5.2 Shadow Masking 85

5.3 Preparation of the Interface 88

5.3.1 Selection of the Metal Type 89
5.3.2 Selection of the Glue 90
5.3.3 Selection of the PCB Material 90

5.4 Discussion 93

CHAPTER 6 CHARACTERIZATION 95

6.1 Introduction 95

6.2 Actuation Characterization 95

6.2.1 The Setup 95
6.2.2 Results 99

6.3 Stiffness Characterization 100

6.3.1 Basic Theory and the Setup 100
6.3.2 Results 101

6.4 Temperature Characterization 102

6.4.1 Introduction to Raman Spectroscopy 102
6.4.2 Basic Theory 102
6.4.3 The Setup 104
6.4.4 Temperature Measurements using Raman Spectroscopy 105
6.4.5 Results 106

6.5 Discussion 110

CHAPTER 7 NANOMANIPULATION AND ASSEMBLY 113

7.1 Introduction 113

7.2 Nanomanipulation Setups 113

7.2.1 Setups at DTU 113
7.2.2 Setups at AMiR (University of Oldenburg, Germany) 115
7.2.3 Setup at Klocke Nanotechnik (Aachen, Germany) 116

7.3 The Procedure 117

7.4 Nanomanipulation and Assembly with Topology Optimized Microgrippers 123

7.4.1 Nanomanipulation and Assembly of CNTs 123
7.4.2 Nanomanipulation and Assembly of NanoBITs 127

7.5 Nanomanipulation with FIB Modified Microgrippers 130

7.6 Results of the TEM Experiments 131

7.7 Results of the AFM Experiments 133

7.8 Discussion 134

CHAPTER 8 CONCLUSIONS AND OUTLOOK 137

APPENDIX A TOPOLOGY OPTIMIZATION SOFTWARE 141

A.1 Tutorial: "How to use Topology Optimization Software "TopOpt" with a Case Study of 3-beam Electro-thermal Actuators 141

A.1.1 Abstract 141
A.1.2 Contents 141

A.2 Example Input Files for the Topology Optimization Software used for the Analysis Summarized in Section 2.3 169

A.2.1 "konst.dat" 169
A.2.2 "geom.dat" 170

APPENDIX B TOPOLOGY OPTIMIZATION RESULTS 173

B.1 Results for the Three-beam-based Designs 173

B.2 Results for the Gückel-based Designs 177

B.3 Results of the Analyses with Different Two-electrode Configurations 178

APPENDIX C MATERIAL PROPERTIES USED IN THE FINITE ELEMENT SIMULATIONS 179

C.1 Material Properties for Poly-Si 179

C.1.1 Constant Properties 179
C.1.2 Temperature Dependent Properties 179

C.2 Material Properties for SiO_2 180

C.3 Air Properties 180

APPENDIX D FINITE ELEMENT ANALYSIS RESULTS 181

D.1 Ideal Case Simulations 181

D.1.1 Temperature Distribution 181
D.1.2 Sensitivity to Design Variations 189

D.1.3 Sensitivity to Fabrication Variations 196
D.1.4 Elongation (x-Axis Displacement) 204

D.2 Non-ideal Case Simulations 207

APPENDIX E THE FABRICATION PROCESS 213

APPENDIX F NANOSTATION SOFTWARE 221

F.1 The User Interface 221

F.2 The Procedure for Actuation Measurements 224

APPENDIX G ACTUATION RESULTS 225

APPENDIX H RAMAN SPECTROSCOPY RESULTS 231

BIBLIOGRAPHY 243

PUBLICATIONS 251

***A.* Peer Reviewed Journals *(Attached in full-text to the end)* 251**

B. Conference Proceedings (Attached in full-text to the end) 251

C. Co-authored Publications 252

CHAPTER 1
Introduction

1.1 Introduction

With his famous talk in 1959, Richard Feynman opened the doors of a “very, very small world" [1]. He mentioned about many things, which people could hardly imagine at that time. For example, small “surgeon” robots: Once swallowed, they can move inside blood vessels, search for diseases and perform operations. Or “a billion little lathes”: With these tiny machines, which are 1/40,000 of the scale of a regular lathe, one can construct a miniature production line.

In addition to these, Feynman also mentioned about the challenges faced at the small-scale, such as the need for more powerful electron microscopes, miniaturization of tools or overcoming the increased stiction forces, i.e. Van der Waals attractions.

Since that time, the fields of micro- and nanotechnology have evolved with a drastically increasing pace. Today, some of the things Feynman talked about have already been achieved, while others are still being developed. These include manipulation of single atom [2], better electron microscopes [3] or miniaturization of computers [4]. However, other things, such as the tiny surgeon and the miniaturized production line, have not really been realized yet.

NanoHand is a European Union (EU) funded project, which aims to create the world’s first nanorobotic production system inside of a scanning electron microscope (SEM) [5]. NanoHand will construct a bridge between the macro- and the nanoworlds by providing integrated systems. This will enable a user to directly manipulate nanostructures and hence, assemble novel devices, ranging from carbon nanotube (CNT)-based nanoelectronic circuits to perhaps even the tiny surgeon mentioned above, which is not possible using existing methods.

The aim of this PhD project is to develop the nanomanipulation tools, i.e. the microgrippers, to be integrated in a nanorobotic production system, which is the subject of the NanoHand project. These microgrippers should be compatible with the other components of the full NanoHand system developed by the project partners, easy to view inside an SEM and capable of accurate adjustment of the gripping force. They should have high-precision, sub-micron end-effectors for accurate contact to the sample to be manipulated and end-effectors with a low-adhesion surface to enable safe and reliable release of the sample to be manipulated.

1.2 Background

1.2.1 Nanomanipulation Systems

Nanotechnology deals with development of materials and/or devices with sub-micron size. Being based on Feynman's vision of miniaturized machines, the word "nanotechnology" was first popularized by K. Eric Drexler in early 1980s [6, 7]. Advances in electron microscopy and invention of scanning tunneling microscope (STM) [8] and atomic force microscopy (AFM) [9] led to discovery of unique nanostructures, such as fullerenes, i.e. buckyballs [10], CNTs [11], nanoparticles/crystals [12] and semiconductor nanowires (NWs) [13]. Such nanostructures have a wide variety of applications in areas including health and medicine [14, 15], chemistry [16], energy [17], optics [18] and electronics [19, 20].

In most of these applications, nanoparticles/tubes are used in large numbers in a solution or in the form of a thin film layer. There are also some examples, where more advanced nanoelectromechanical systems (NEMS) are fabricated using individual nanostructures as building blocks. In these examples, nanostructures are either grown at predefined locations during the main fabrication process [21, 22], or manipulated to these locations afterwards taking advantage of external forces, including magnetic [23, 24], dielectrophoretic [25], microfluidic [26], optic [27] and acoustic [28] forces. However, these applications have not turned into widespread products since the methods used are incompatible with the conventional processes and they have rather low yield and reliability.

Nanorobotic manipulation is a promising approach to overcome the challenge of micro-nano integration, enabling reliable characterization of individual nanostructures and assembly of smart nanodevices. During the last decade, many groups have developed nanorobotic manipulation systems, which can be used inside an SEM or a transmission electron microscope (TEM) [29-36] (Figure 1.1).

In most nanorobotic manipulation systems, STM or AFM probes are used as the manipulation tool [30-35]. Although such tools are rather useful for characterization of various properties [37] and in-plane manipulation purposes, e.g. manipulation of nanoparticles, tubes or wires on a surface [2, 38, 39] (Figure 1.2 & Figure 1.3), they are not convenient for assembly of more complex NEMS devices.

One of the most common nanoassembly applications performed using such a probe system is assembly of nanotube/wire-enhanced super-tips, where the nanostructure is assembled on the probe itself [40, 41]. During these experiments, the nanotube/wire is attached to the probe tip by taking advantage of the Van der Waals forces and the adhesion is enhanced using different kinds of glues afterwards (Figure 1.4 & Figure 1.5).

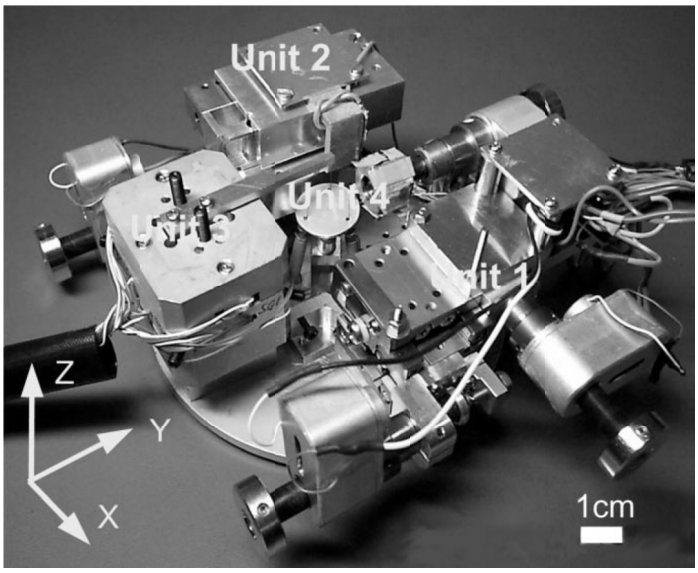

Figure 1.1 A 16-DOF nanorobotic manipulation system [31].

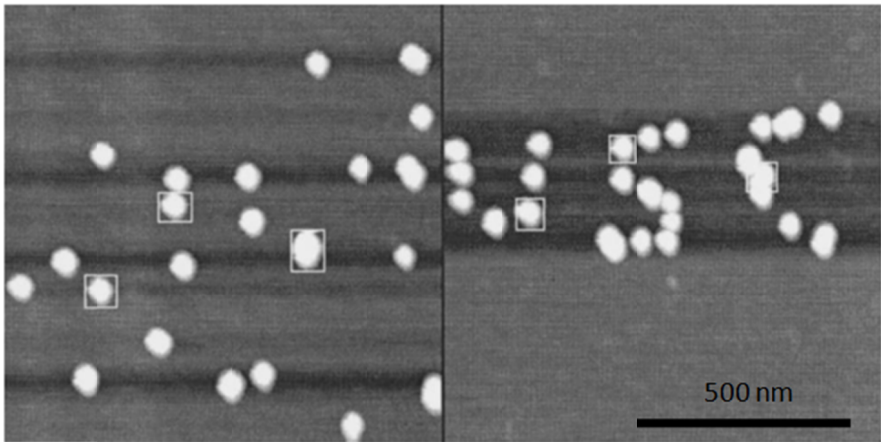

Figure 1.2 The random pattern of 15 nm Au balls [left] was converted into the ‘‘USC’’ pattern [right] by pushing with an AFM probe. White squares show the stationary balls [2].

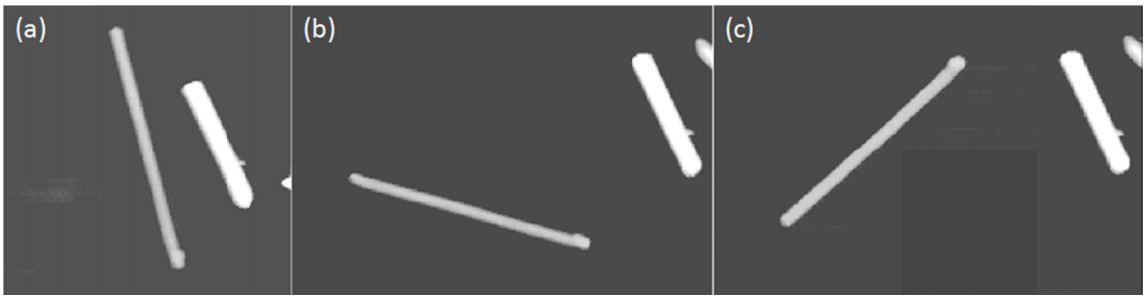

Figure 1.3 (a) In-plane rolling and sliding of the nanotube on the left with an AFM probe on a graphite substrate (no scale-bar provided) [38].

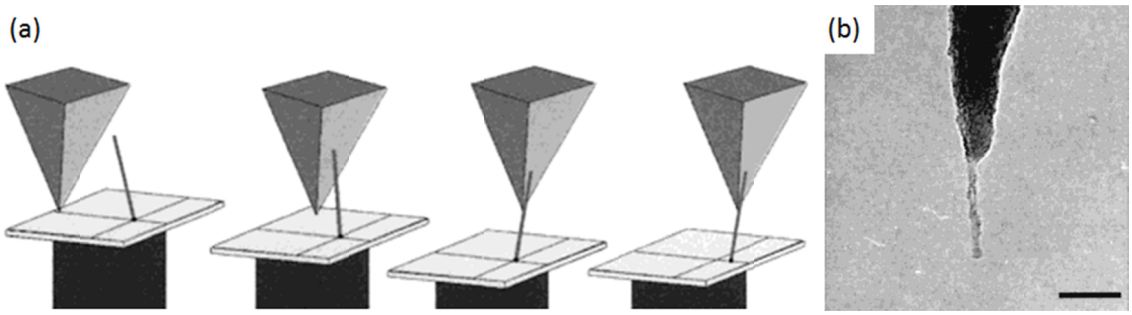

Figure 1.4 (a) Schematic representation of picking up a vertically aligned CNT using a microfabricated pyramidal tip and (b) TEM image of a glued nanotube tip, where the scale bar is 25 nm [40].

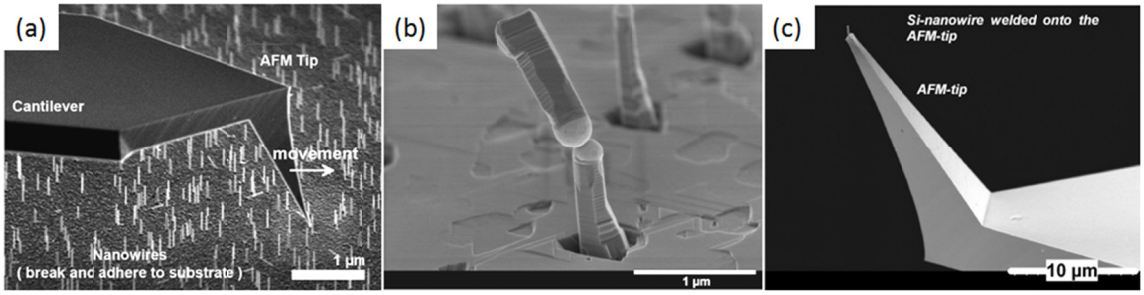

Figure 1.5 (a) Breaking NWs by mechanical force using a moving AFM tip. (b) Fractured NWs falling and adhering onto the substrate or other NWs. (c) A NW welded onto an AFM tip by electron beam deposition (EBiD) inside an SEM [41].

As an alternative to probes, active tools such as microgrippers can also be integrated with nanorobotic manipulation systems [36]. Microgrippers are more advantageous than probes since an additional mechanical force is provided by two (or more) opposing end-effectors. The following section is dedicated to a review of microgrippers and a comparison of different actuation principles for nanomanipulation.

1.2.2 Micro/Nanogrippers

Performance of the manipulation tool integrated in a nanorobotic system is of prime importance for successful and reliable nanomanipulation. Microgrippers are promising tools for automated nanomanipulation and assembly since they provide better control of the manipulated object. Starting from early 1990s, various groups have developed micro/nanogrippers of different materials and actuation principles [42-44]. There are also commercial suppliers, such as Nascatec [45] and Zyvex [46], which provide microgrippers. However, most of these are mainly suitable for micromanipulation purposes and only a few reproducible nanomanipulation experiments have been reported so far. This is due to the fact that the requirements on precision, reliability, strength and compactness of the manipulation tool are much stricter on the nano-scale. Most of the above mentioned devices are lacking at least one or more of these requirements.

The most common actuation mechanism used in microgrippers is electrostatic actuation. Electrostatic actuation principle is based on attractive forces, which are induced as a result of a potential difference applied between two electrodes separated by vacuum or a dielectric medium, e.g. air. Electrostatically actuated comb-drive microgrippers are also commercially available from Nascatec [45, 47]. The simplest form of an electrostatically actuated microgripper configuration is a set of parallel plate electrodes, where actuation is achieved by the electrostatic attraction of the movable electrode(s) towards the stationary electrode(s) [48, 49] (Figure 1.6 (left)). The electrostatic attraction forces can be increased by increasing the capacitance, i.e. increasing the plate area or decreasing the plate distance. By replacing the parallel plate electrode with a comb-drive structure, i.e. electrodes with arrays of matching comb fingers, many capacitors can be combined in parallel, and hence the effective overlap area can be increased [42, 47] (Figure 1.6 (right)).

Advantages of electrostatic actuators can be listed as precise actuation, low power requirement and short response time. Furthermore, the possibility of indirect actuation [49] by electrically grounding the movable electrodes and applying the operation voltage to the stationary one, prevents any possible current through the manipulated object, which leads to higher operation voltages to obtain reasonable actuation ranges. Major disadvantages of the electrostatic actuation method are low actuator forces and high operation voltages ranging from tens up to hundreds of volts.

Another actuation mechanism used in microgrippers is electrothermal actuation. Electrothermal actuation is based on thermal expansion of solids due to Joule heating. Thermally actuated microgrippers are commercially available from Zyvex [46]. Most common forms of an electrothermal actuators used in microgrippers are the Gückel, i.e. thin-thick beam [43, 50], and the Chevron [51, 52] actuators.

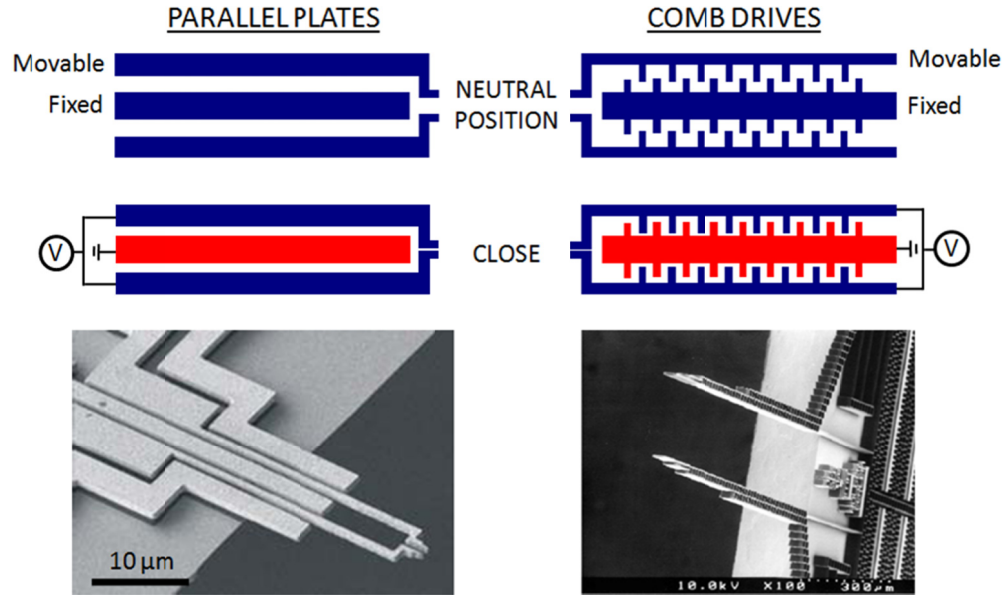

Figure 1.6 Principles and applications of electrostatic actuators to microgrippers: Parallel plate actuators [49] (left) and comb-drive actuators [47] (right).

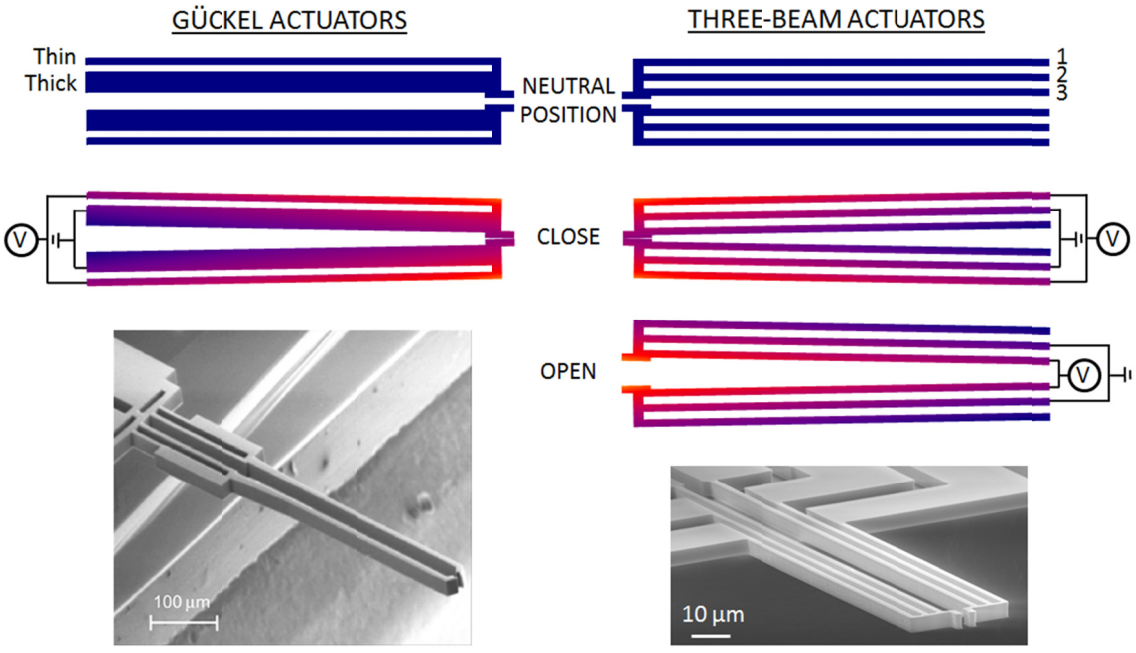

Figure 1.7 Principles and applications of electrothermal actuators to microgrippers: Parallel plate actuators [49] (left) and comb-drive actuators [47] (right).

The Gückel actuator is composed of two beams: A wide and a narrow beam (Figure 1.7 (left)), which are connected by a bar at the end to form a U-loop. When a current is passed through the structure, the narrow beam heats up and expands more than the wide beam. This causes bending of the structure, and hence, the displacement of the end-point towards

the thicker beam side. However, actuation is possible only in one direction. A variation of this design is the symmetric three-beam actuator [44], which is composed of three identical beams instead of two having different widths (Figure 1.8 (right)). Actuation is achieved via differential heating of the structure by passing the current only through the two neighboring beams, i.e. beams 1 and 2. Actuation in the opposite direction is also possible by passing the current through the other two neighbors, i.e. beams 2 and 3.

The Chevron actuator is composed of two beams connected at a small angle with respect to each other (Figure 1.8 (left)). A chevron actuator requires an absolute temperature change rather than a temperature difference to operate. A variation of the chevron actuator, i.e. the rib-cage actuator, can be constructed by connecting an number of chevron actuators in parallel [52, 53] (Figure 1.8 (center, right)), which provides more robustness.

Using Chevron actuators in microgrippers seems to be more preferable than using Gückel actuators since the heat generated during actuation can be far away from the end-effector locations. On the other hand, force and displacement are generated directly at the end-effector locations in Gückel actuators, where Chevron actuators require transmission of the generated force and displacement. This is rather challenging since the intermediate beams should be thick for better rigidity. However, thicker the beams, better the thermal conductance and hence, higher the temperature rise in the microgripper.

Compliant electrothermal microgrippers can be constructed in various forms, where the actuation principle is similar to the Gückel or the Chevron-based mechanisms. An example is the high-aspect-ratio polysilicon microgrippers, where the actuation is based on amplification of the relatively small displacement achieved by thermal expansion of the actuator beams [54, 55].

There are also bilayer electrothermal actuators, which can be constructed by depositing two different material layers on top of each other [56]. Here, the actuation relies on the mismatch between the coefficients of thermal expansion (CTEs) of the two materials.

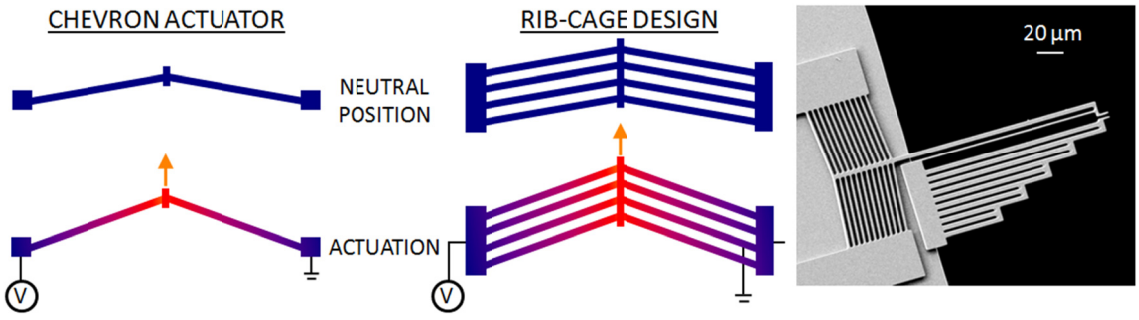

Figure 1.8 Principle of the chevron actuator (left) and its variation rib-cage design (center) together with its application to microgrippers [52] (right).

Advantages of electrothermal actuators can be listed as design flexibility, robustness and low operation voltages. However, the response times of electrothermal actuators is long compared to that of electrostatic actuators. Furthermore, high operation temperatures can be a disadvantage for micro/nanomanipulation purposes, limiting the range of possible applications. Despite these disadvantages, thermal actuators are still favorable for microgrippers since a high force can be generated even with a relatively small actuator. Finally, parallel-beam thermal actuators are capable of providing force feedback, which is an important requirement for advancements in the fields of micro- and nanomanipulation [44].

Although not being common, magnetic [57] and piezoelectric [58] actuation methods can also be used in designing microgrippers. However, both these methods are not well-suited for nanoscale applications, since they are not convenient for miniaturization.

A major requirement for nanomanipulation is miniaturization of the manipulation tool. Although the microgrippers referenced above are suitable for basic micromanipulation tasks, most them fail at nano-scale due to the relatively large size of the end-effectors with respect to the nanostructure to be manipulated. In order to meet the size requirement, there is an ongoing trend in designing smaller manipulation tools. These can be constructed from either microactuators with sub-micron actuators or nano-scale end-effectors.

Many groups fabricated nanogrippers by integrating nano-scale end-effectors to pre-fabricated micro-actuators using various methods [59-62]. In these examples, nanostructures are either grown at the actuator tips using a bottom-up approach, or assembled manually. Advances in lithographic techniques such as electron-beam lithography (EBL) [63] and nano-imprint lithography (NIL) [64] enable fabrication of sub-micron actuators. These methods are commonly used for fabricating simple nano-scale devices, such as beam resonators [65]. However, there are a few examples of nanogrippers fabricated using EBL or NIL [66].

The lack of nano-scale grippers is most probably due to the design challenge: One of the most important performance criteria for a manipulation tool is the gripping force. However, scaling-down a mechanical actuator results in a cubic decrease in its stiffness, and hence the gripping force. For this reason, conventional actuator designs are not suitable to be used in nanogrippers and design of novel actuators with optimum performance is essential. Topology optimization is a promising approach to overcome these problems [67]. In the following chapter, basics and applications of topology optimization will be introduced.

1.2.3 Topology Optimization

Topology optimization is a finite-element-based method, which relies on distribution of a certain amount of material within a well-defined design domain to perform a specific task [67, 68]. The optimum layout of the structure is found by using gradient-based deterministic optimization algorithms, which often has a vastly different topology and a superior performance than conventional designs.

Since the computer-based topology optimization method was first introduced in 1988 [68], it became more and more popular in both academia and industry. Due to the continuous developments in theory, computational methods and optimization algorithms, the application area of the method is extended to a wide variety of fields including aerospace [69], automotive [70], materials science [71] and microelectromechanical systems (MEMS) [72-74].

As an example, truss topology optimization is widely used in architecture and structural engineering, for designing bridges, cranes and electricity masts (Figure 1.9). The method relies on optimization of a mechanical truss structure, by defining potential nodes and bars within a design domain and determining the sizes (areas or volumes) of these bars.

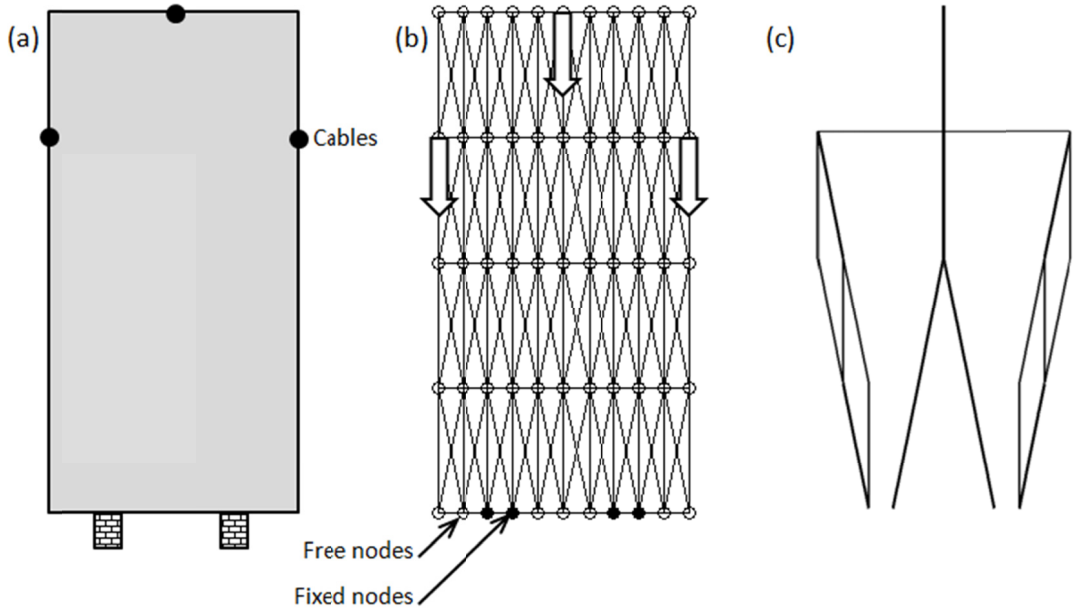

Figure 1.9 Design of an electricity mast using truss topology optimization: (a) Design domain showing the cable and the support locations. (b) Ground structure with load conditions and showing potential nodes and bars (c) The optimal design and topology (Design performed during the course *Introduction to Mathematics of Topology Optimization*).

Apart from the macro-scale, realization of elements such as hinges or bearings is either impossible or rather difficult at micro–scale. This is mainly due to the small size and process limitations. For this reason, MEMS devices are often composed of compliant mechanisms/actuators, where the actuation is due to elastic deformation. Therefore, topology optimization is a promising design approach in MEMS field (Figure 1.10). Instead of potential bars and nodes, the design domain for a compliant mechanism is composed of pixels and the method relies on determination of the intensity of these pixels, which represent the material density.

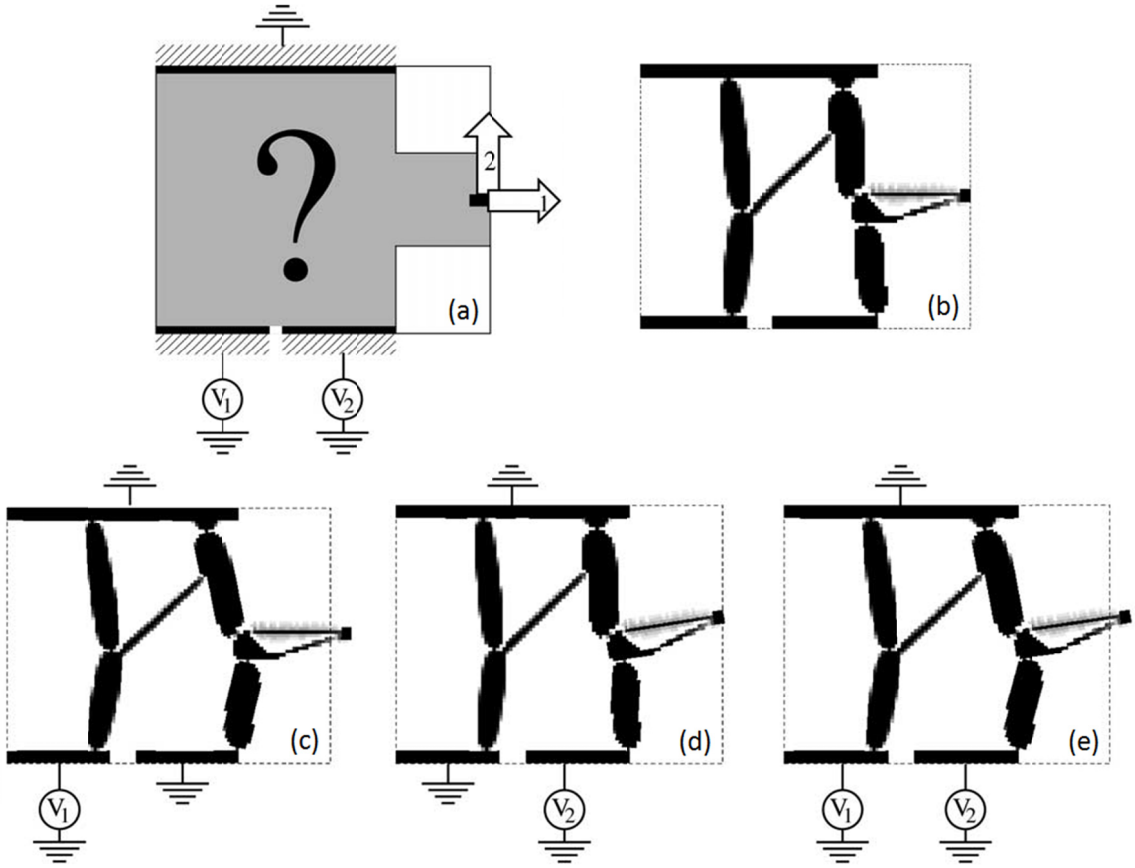

Figure 1.10 Design of an electrothermomechanical XY micro-scanner: (a) Design domain. (b) Topology optimization solution for linear analysis. (c) Horizontal, (d) vertical and (e) diagonal displacement modes of the actuator at 0.4 V input voltage [74].

However, realization of an optimum MEMS design is rather challenging, due to two reasons: (1) The grey-scale bitmap image resulting from topology optimization (Figure 1.11 (a)) should be converted to black-and-white (Figure 1.11 (b)) since it is impossible to fabricate a structure with a variable material density. This may result in errors on the order of ~10 % [74]. (2) Process variations during microfabrication (Figure 1.11 (c)), which is rather non-uniform, may result in loss of design features and/or changes in the dimensions of the optimum design. This adds on the error introduced in the conversion step. Hence, the performance of the actual structure turns out to be different from that of the original topology optimization output.

These variations can be minimized, and even be corrected, after fabrication using a focused-ion-beam (FIB) system. FIB is a powerful tool, which enables removal and/or deposition of material with a nano-metric precision. Furthermore, it can be used in realization of miniaturized structures, such as nanogrippers. Basics and applications of FIB will be introduced in the following section.

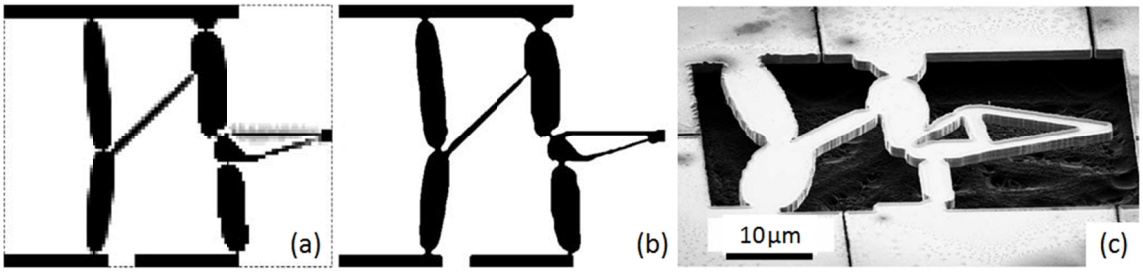

Figure 1.11 (a) Grey-scale output of the topology optimization program. (b) Black-and-white image with an increased resolution. (c) Electrothermomechanical actuator fabricated from electroplated nickel [74].

Recent advances in topology optimization enable consideration of fabrication variations during design and provide more robust designs [75]. The robust topology optimization approach relies on simultaneous solution of the optimization problems for the original structure, the eroded structure (one with decreased line-with) and the dilated structure (one with increased line-with).

1.2.4 Focused Ion Beam (FIB)

Focused-ion-beam (FIB) systems enable site-specific analysis, removal or deposition of materials with a high resolution. The method started to be developed in late 1970s, where the first commercial equipment was available in the late 1980s [76]. FIB has a wide variety of applications in semiconductor research and industry, including device modification, mask repair, process control, failure analysis and sample preparation [77]. However, the most promising approach is micromachining of MEMS devices [78, 79], enabling realization of more complex microstructures, which are impossible to realize with conventional microfabrication methods.

A typical FIB system resembles a SEM, where the focused beam of electrons is replaced by a focused beam of ions, most commonly gallium (Ga^+). Main components of an FIB system are the ion column, the work chamber, the vacuum system, the gas system and the user interface.

The schematic illustration of an FIB ion column can be seen in Figure 1.12 (a). The ion beam is generated from a liquid-metal ion source (LMIS), where application of a strong electric field causes the emission of positively charged ions from a liquid metal cone, which is formed at the tip of a tungsten needle. Then, the ion beam passes through the center of concentric electrodes, apertures and lenses, is deflected and accelerated by electric fields and focused to a fine spot on the sample.

The samples are placed inside a stainless-steel work chamber, which is equipped with a multiple-DOF motorized stage. The pressure level inside the chamber is maintained in the low vacuum range, i.e. ~10^{-7} mbar. The vacuum level inside the ion column and the work chamber is provided by a system of vacuum pumps. Most FIB systems are equipped with a gas handling system for delivering a number of gases onto the sample surface. These gases can be used for faster or more selective etching and also for deposition of various materials. All these sub-systems are controlled through a user interface, which generally runs on a workstation.

When high-energy ions hit the surface of a solid substrate, they lose energy to both the electrons and atoms of the solid. Incident ions have important physical and chemical effects on the substrate. Physical effects can be listed as: (1) Sputtering of the neutral and ionized solid atoms, which enables milling, (2) Displacement of the solid atoms, which results in damage, (3) Electron emission, which enables imaging and also causes charging of the sample and (4) Phonon emission, which results in heating. Imaging, milling and deposition processes are schematically illustrated in Figure 1.12 (b). Chemical effects are mainly dissociation of molecules through breaking of the chemical bonds, which enables deposition.

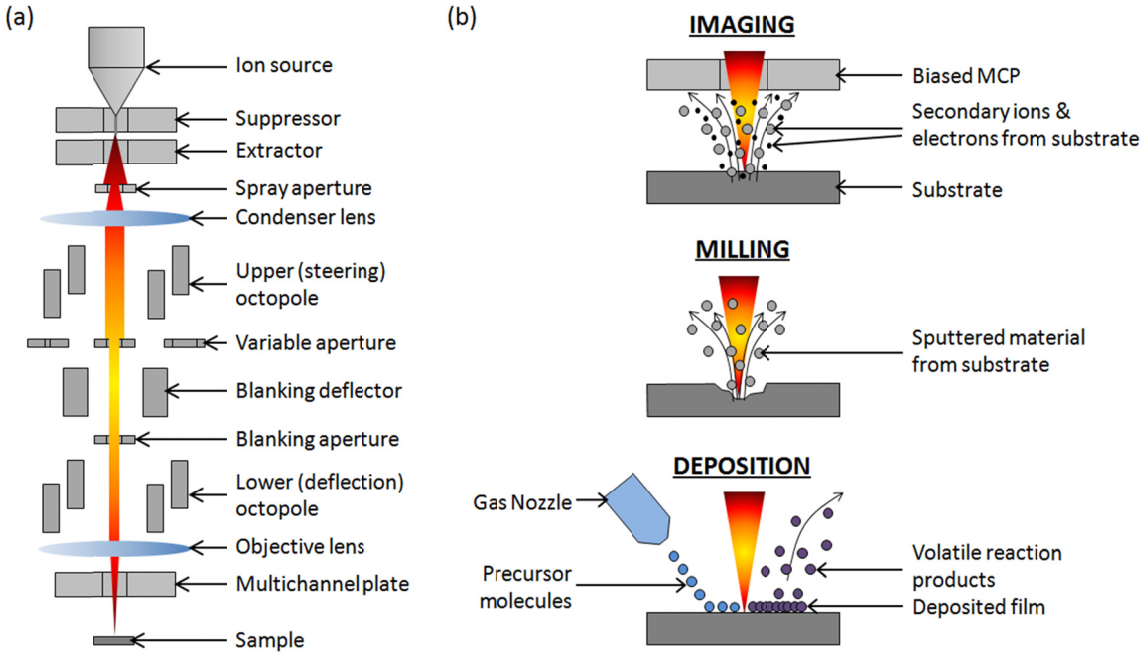

Figure 1.12 Schematic illustration of (a) an FIB ion column and (b) principles of FIB imaging, milling and deposition.

There are also dual-beam FIB systems, where an electron column, i.e. SEM, is incorporated with the ion column to provide enhanced capabilities. The electron beam can be used for imaging without damaging the sample surface. Furthermore, charging of the specimen can be reduced or eliminated by neutralizing with the electron gun, in order to enhance the FIB process.

1.3 Motivation

As mentioned in the Introduction, the aim of this PhD project is to develop the nanomanipulation tools, i.e. the microgrippers, to be integrated in a nanorobotic production system, which is the subject of the NanoHand project. The basic requirement for the microgrippers was the compatibility with the other components of the full NanoHand system developed by the project partners.

The main concern of the NanoHand project is manipulation and assembly of CNTs of different sizes: For manipulation of 20-30 nm diameter single walled CNTs from bundles inside microfabricated trenches, the nanomanipulation tool and its end-effectors are supposed to be relatively small. For manipulation of 300 nm diameter multi-walled CNTs from a vertically aligned array, the nanomanipulation tool is supposed to be capable of supplying the force necessary for detaching the CNTs from the sample substrate.

Furthermore, the microgrippers should be capable of accurate adjustment of the gripping force: Picking a nanostructure from a source substrate by applying a sufficiently large force (Figure 1.13) [52] and releasing it onto a target substrate in a controlled manner should both be possible. High gripping forces can be achieved with a good actuator design, where safe and reliable release of the manipulated sample requires end-effectors with a low-adhesion surface

As well as the microgripper itself, the end-effectors should also have a size that is comparable with the manipulated structures. This is since too large and bulky end-effectors may prevent access to small samples and they may block the electrons scattered from the sample, reducing the quality of the image during manipulation inside an SEM. For this reason, miniaturization of both the end-effectors and even the actuator itself is necessary.

Fabrication of smaller microgrippers with sub-micron end-effectors is not possible with the conventional microfabrication processes, where it requires utilization of more advanced techniques, such as EBL and FIB. These techniques enable realization of 5-40 times smaller grippers.

However, miniaturization of the conventional microgripper designs results in a decrease in the stiffness of the actuators, and hence in the available gripping force. As an example, a linear reduction of all dimensions of a three beam actuator (length L, height h and width w of the actuator beams) results in a linear decrease in the spring constant, $k_s = (11/4)Ehw^3/L^3$. Hence, the force available with the miniaturized versions of these conventional designs will not be sufficient for successful nanomanipulation of CNTs (Figure 1.13). In order to overcome this issue, the designed microgrippers should either be ~10 times stronger than the existing designs with the same size or as strong as them if smaller.

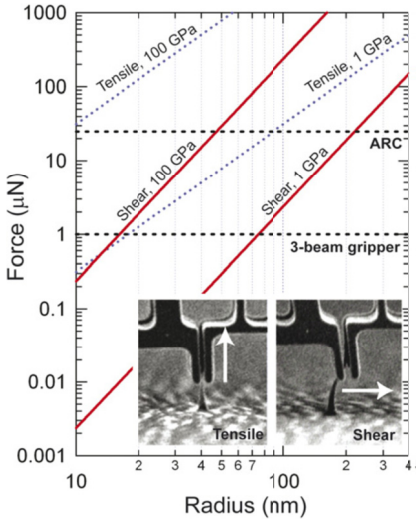

Figure 1.13 Detachment force estimates for tensile (vertical) and shear (lateral) pulling as a function of the CNT radius, where the dashed lines denote the available gripping force with the two conventional electrothermal microgripper: The three-beam and the asymmetric rib-cage microgrippers [52].

Due to the availability of high forces with a compact design, design flexibility and ease of actuation, electrothermal actuation principle was selected for the microgrippers. Apart from the mechanical performance of the electrothermal microgrippers, their thermal performance, e.g. the end-effector temperature during actuation, is of great importance for successful nanomanipulation: Too high temperatures may result in damage on the manipulated structure and even on the microgripper itself.

Topology optimization enables combination of high gripping forces, a large actuation range and low temperatures in a single device, which is suitable for miniaturization. EBL and FIB techniques enable realization of the topology optimized designs with a high-precision. Furthermore, using these methods, the end-effectors of the microgrippers can be shaped in order to reduce the contact area with the manipulated sample.

Characterization of the fabricated microgrippers is also rather important for reliable nanomanipulation and their future commercialization. The performance of the post-processed topology optimized designs can be estimated by finite element simulations using a proper finite element analysis software. Then, the validity of the finite element simulations can be cross-checked by a comparison of the results with actuation, force and temperature measurements.

Finally, the microgripper interface, i.e. the package, should be compatible with various nanomanipulation systems and it should be designed in order to maximize the performance of the microgrippers.

During this project, all of the above mentioned issues will be considered in order to realize high-performance electrothermal microgrippers for successive and reliable nanomanipulation purposes.

1.4 Thesis Outline

In CHAPTER 1, the backgrounds of nanomanipulation systems, micro/nanogrippers, topology optimization and FIB were introduced and the motivation of this Ph.D. thesis was established. The remaining chapters will be structured as follows:

In CHAPTER 2, the theories of electrothermal actuation and topology optimization will be explained. The steps followed in designing microgrippers will be described and results of topology optimization will be presented.

In CHAPTER 3, the finite element simulation procedure used in post-processing of the designed microgrippers will be explained. Model properties, mesh and boundary conditions will be listed. The results of the finite element analysis will be presented and compared with the results of topology optimization presented in CHAPTER 2.

In CHAPTER 4, the microfabrication procedure for the microgrippers will be explained, discussing the limitations and the challenges at each process step and proposing possible solutions and/or improvements. The microfabrication results will be presented. The principles of micro and nano-patterning using FIB will be described and the procedure used for modifying and functionalizing the microgrippers using FIB will be described. Then, a method or fabricating nanogrippers using FIB will be introduced and the results of both micro and nano-patterning experiment will be discussed.

In CHAPTER 5, the procedure for the packaging of the fabricated microgrippers will be explained, mentioning about the problems and suggesting solutions to these.

In CHAPTER 6, characterization of the microgrippers will be explained in detail. Procedures for actuation, stiffness and temperature measurements will be introduced. Characterization results and performance of the microgrippers will be discussed.

In CHAPTER 7, the nanomanipulation experiments performed using the microgrippers will be explained in detail. Setups used in these experiments will be described. Results of CNT, NW and NanoBIT, i.e. exchangeable tool-tips, manipulation experiments will be presented. Results will be discussed, mentioning about challenges and possible solutions and/or proposing potential improvements.

In CHAPTER 8, overall progress and achievements will be discussed, conclusions will be drawn according to these discussions and an outlook will be provided based on the future work and possible improvements.

Extensive appendices including tutorials, results and publications can be found at the end of the thesis.

CHAPTER 2
Design Using Topology Optimization

2.1 Theory: Electrothermal Actuation

The basics of electrothermal actuation and different electrothermal actuators were introduced in Section 1.2.2. In this section, the basic theory of electrothermal actuation will be explained in more detail.

2.1.1 Joule Heating

Joule heating is based on heating of a structure due to an electrical current passed through it. Considering a simple case, an infinitesimal volume element with length dx in a U-beam structure (Figure 2.1) and ignoring convective and irradiative heat transfers, the expression for the conservation of energy can be written as follows:

$$\frac{dQ_{in}}{dt} + \frac{dQ_{gen}}{dt} = \frac{dQ_{out}}{dt} \tag{2.1}$$

In the above expression, Q_{in} is the heat conducted to the element from a neighboring element, Q_{gen} is the resistive heat generated within the element and Q_{out} is the heat conducted away from the element to a neighboring element, where t is time.

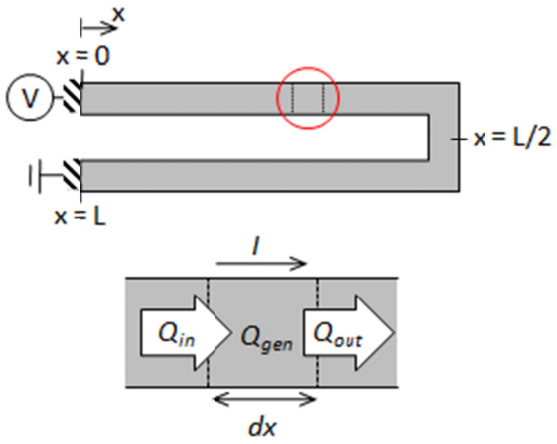

Figure 2.1 Schematic illustration of a U-beam structure (top) and an infinitesimal volume element within the structure (bottom).

The power generated within the element can be written according to:

$$\frac{dQ_{gen}}{dt} = I^2R \tag{2.2}$$

Where, I is the electrical current running through the element and R is the electrical resistance of the element. The above expression can be rewritten in terms of the current density J and the element's resistivity ρ, cross-sectional area A and length dx as follows:

$$\frac{dQ_{gen}}{dt} = (JA)^2\left(\rho\frac{dx}{A}\right) = \rho AJ^2dx \tag{2.3}$$

The rate of conductive heat transfer to and away from the element can be written as:

$$\frac{dQ_{cond}}{dt} = -\kappa A\frac{dT}{dx} \tag{2.4}$$

Where, κ is the thermal conductivity and (dT/dx) is the temperature gradient across the element.

Substituting Equations (2.3) and (2.4) into Equation (2.1) and rearranging:

$$-\kappa A\frac{dT_x}{dx} + \rho AJ^2dx = -\kappa A\frac{dT_{x+dx}}{dx} \tag{2.5}$$

$$\frac{dT_{x+dx} - dT_x}{dx^2} = -\frac{\rho}{\kappa}J^2 \tag{2.6}$$

As $x \to 0$:

$$\frac{d^2T}{dx^2} = -\frac{\rho}{\kappa}J^2 \tag{2.7}$$

Assuming perfect heat sinks with a temperature of T_0 at the ends of the U-beam structure and solving for the boundary conditions, the expression for temperature can be written as a function of x as follows:

$$T(x) = -\frac{\rho}{2\kappa}J^2(x^2 - Lx) + T_0 \tag{2.8}$$

The maximum temperature within the U-beam occurs at the midpoint, and can be calculated as follows:

$$T_{max} = T\left(\frac{L}{2}\right) = \frac{\rho}{8\kappa}J^2L^2 + T_0 \tag{2.9}$$

The total elongation of the U-beam can be calculated according to:

$$\Delta L = L\alpha\Delta T \tag{2.10}$$

Where, α is the coefficient of thermal expansion and ΔT is the difference between the initial and final temperatures, which can be calculated as follows:

$$\Delta T = T_{av,f} - T_{av,i} \tag{2.11}$$

The initial temperature of the beam is uniform and equal to the temperature of the heat sink (T_0). The final temperature of the beam is not uniform, where the average temperature can be calculated according to:

$$T_{av,f} = \frac{1}{L}\int_0^L T(x)dx = \frac{\rho}{12\kappa}J^2L^2 + T_0 \tag{2.12}$$

Substituting Equations (2.11) and (2.12) into Equation (2.10):

$$\Delta L = \frac{\rho}{12\kappa}J^2L^3 \tag{2.13}$$

Assuming the distance between the beams is negligible compared to the length of the U-beam, the midpoint displaces by an amount of $\Delta L/2$ along x-direction.

Derivation of the equations for a three-beam actuator, which is slightly more complicated, can be found in [44].

2.1.2 The Effect of Convection and Radiation

The effect of convection to the surroundings can be considered by inserting the below term to the right-hand side of Equation (2.1):

$$\frac{dQ_{conv}}{dt} = hP(T(x) - T_s)dx \tag{2.14}$$

Where, h is the convection coefficient, P is the perimeter if the cross-section area and T_s is the temperature of the surroundings.

The effect of irradiative heat transfer can be neglected since the operation temperatures of the electrothermal actuators generally do not exceed ~800 K.

2.2 Theory: Topology Optimization

The basics and previous applications of topology optimization were introduced in Section 1.2.3. Further information regarding topology optimization, including extensions and applications, can be found in [67]. In this section, design of electrothermomechanical actuators using topology optimization will be explained in detail according to the formulation given by Ole Sigmund in [53].

2.2.1 Governing Equations

As mentioned in the previous sections, the principle of electrothermomechanical actuators is based on Joule heating of a structure by passing a current through it. The generated heat results in a thermal strain, and hence structural deformation. Therefore, the electrothermomechanical design problem should be modeled in three domains: Electrical, thermal and mechanical.

MEMS structures are mostly planar due to fabrication limitations, for this reason the equations will be derived for the 2D domain. Furthermore, geometrical non-linearity, but linear material behavior will be assumed. Also, the system is weakly coupled, i.e. thermal equations are independent of mechanical displacements and electrical equations are independent of thermal field [53].

The general design domain for the electrothermomechanical design problem is referred to as Ω, which contains linear thermoelastic material (Figure 2.2). The boundaries are composed of the following six pair-wise disjoint regions as follows [53]:

$$\Gamma = \overline{\Gamma_{u_0} \cup \Gamma_{t_0}} = \overline{\Gamma_{u_1} \cup \Gamma_{t_1}} = \overline{\Gamma_{u_2} \cup \Gamma_{t_2}} \tag{2.15}$$

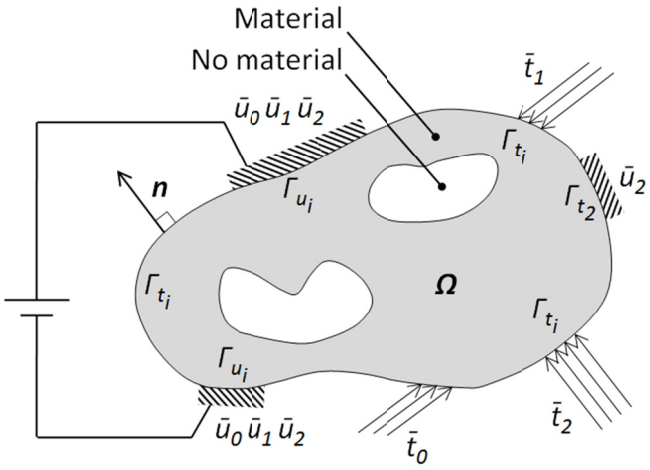

Figure 2.2 Loadings and boundary conditions for a general thermoelectromechanical load problem.

In the above expression, indices 0, 1 and 2 and subscripts u and t denote electrical, thermal, elastic, displacement and traction boundary conditions, respectively. Regions Γ_{u_i} can coincide, partly overlap or be fully disjoint. Same conditions apply to regions Γ_{t_i} .

Governing equations for the three fields can be written as follows [53], where variables and notations used are tabulated in Table 2.1:

For the electrical field:

$$\begin{aligned} \sigma_0 u_{0,ii} + b_0 = 0 \quad & \text{in } \Omega \\ u_0 = \bar{u}_0 \quad & \text{on } \Gamma_{u_0} \\ -\sigma_0 u_{0,n} = \bar{t}_0 \quad & \text{on } \Gamma_{t_0} \end{aligned} \tag{2.16}$$

For the thermal field:

$$\begin{aligned} \sigma_1 u_{1,ii} + b_1 = 0,\ b_1 = -\sigma_0 u_{0,i}^2 - h(\bar{u}_1 - u_1) \quad & \text{in } \Omega \\ u_1 = \bar{u}_1 \quad & \text{on } \Gamma_{u_1} \\ -\sigma_1 u_{1,n} = \bar{t}_1 \quad & \text{on } \Gamma_{t_1} \end{aligned} \tag{2.17}$$

For the elastic field:

$$\begin{aligned} s_{ij,j} + b_{2(i)} = 0 \quad & \text{in } \Omega \\ s_{ij} = E_{ijkl}(\eta_{kl} - \alpha_{kl} u_1) \quad & \text{in } \Omega \\ \eta_{ij} = \frac{1}{2}\left[u_{2(i,j)} + u_{2(j,i)} + u_{2(k,i)} u_{2(k,j)}\right] \quad & \text{in } \Omega \\ u_{2(i)} = \bar{u}_{2(i)} \quad & \text{on } \Gamma_{u_2} \\ s_{ij} n_j = \bar{t}_{2(i)} \quad & \text{on } \Gamma_{t_2} \end{aligned} \tag{2.18}$$

2.2.2 Finite Element Implementation

The governing equations derived above are implemented in the finite element notation. Some assumptions are made in order to simplify these equations [53]. First of all, body forces and the internal electric current source are assumed to be zero. Furthermore, the shape of the 2D design domain is assumed to be rectangular and rectangular finite elements are used for discretization, where the number of elements is N and the number of nodes is m. Finally, the structure is modeled using plane stress assumption.

The details of the finite element implementation can be found in [53].

2.2.3 The Optimization Problem

The design problem for an electrothermal actuator is based on distribution of a given amount of material in a planar design domain, such that the deformation, u_{out}, of a given stiffness, k_s, is maximized (Figure 2.3 (a)). The displacement component perpendicular to the output direction (cross-sensitivity), $\hat{u}_{out}$, can be constrained simultaneously. There can be solid (black) and void (white) areas, which are fixed throughout the optimization.

In order to eliminate short circuits, and therefore excessive temperatures, an upper bound constraint can be added on the electrical current.

Table 2.1 Conventions used in the governing equations.

u	State variables
u_0	Voltage
u_1	Temperature change
$u_{2(i)}$	Displacement component in direction i
$_{,i}$	Differentiation w. r. t. direction i
b_0	Prescribed internal current source per volume
h	Convection coefficient
b_1	Internal heat generation per volume & convection from the top surfaces (Function of u_0)
$b_{2(i)}$	Body force components
σ_0	Isotropic electrical conductivity
σ_1	Isotropic thermal conductivity
E_{ijkl}	Elastic stiffness tensor
$\bar{u}_0$	Prescribed voltage
$\bar{u}_1$	Prescribed temperature
$\bar{u}_{2(i)}$	Prescribed displacement components
$\bar{t}_0$	Prescribed current
$\bar{t}_1$	Prescribed heat flux
$\bar{t}_{2(i)}$	Traction force components
η_{ij}	Green-Lagrange strain tensors
s_{ij}	Piola Kirchoff stress tensors, (Function of u_1)
α_{ij}	Thermal expansion tensors
n_i	Components of the unit normal vector to the surface i

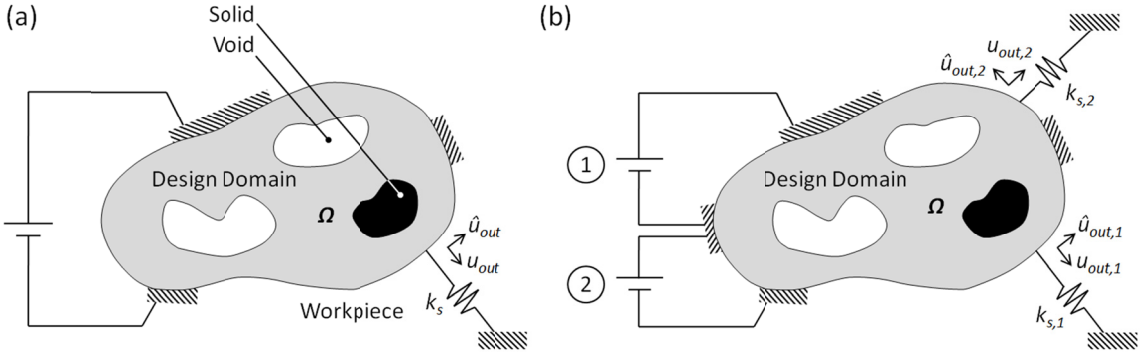

Figure 2.3 Design problem for electrothermomechanical actuators with (a) a single input and single output and (b) two inputs and two outputs.

Topology optimization relies on optimizing the material distribution by controlling material density of each finite element. For this reason, material properties are set to depend on the relative material density, ρ^e, in each element, e.

Hence, the optimization problem can be written accordingly, as follows [53]:

$$\underset{\rho}{\text{maximize}} \quad u_{out}(\rho) \qquad \text{such that} \quad \begin{aligned} &\sum_{e=1}^{N} \rho^e V^e \leq V^* \\ &I(\rho) \leq I^* \\ &\frac{\left(\hat{\mathrm{u}}_{out}(\rho)\right)^2}{\left(u_{out}(\rho)\right)^2} \leq \varepsilon^* \\ &0 < \rho_{min} \leq \rho \leq 1 \\ &\text{equilibrium equations} \end{aligned} \tag{2.19}$$

In Equation (2.19), V^e is the element volume, V^* is the constraint on the element volume, $I(\rho)$ is the electrical current, I^* is the upper bound on the electrical current, ρ_{min} is the lower bound on relative element densities ($\rho_{min} = 10^{-3}$) and ε^* is a small positive number (e.g. $\varepsilon^* = 10^{-2}$).

The objective function requires the output displacement, and hence the output force to be maximized. This entails the presence of the maximum amount of material within the actuator. For this reason, the volume constraint is always active in order to ensure convergence. Other advantages of the volume constraint can be listed as: Ensuring the production of narrow structures with thin members that can easily be under-etched, ensuring black & white designs, eliminating disconnected islands of material, and hence ensuring efficient use of the available material.

Solution of problems with multiple inputs and/or outputs is also possible by extending the optimization problem given in Equation (2.19). As an example, the optimization problem with two inputs and two outputs (Figure 2.3 (b)) can be written as follows [53]:

$$\underset{\rho}{\text{maximize}} \quad u_{out,1}(\rho) + u_{out,2}(\rho) \qquad \text{such that} \quad \begin{aligned} &\sum_{e=1}^{N} \rho^e V^e \leq V^* \\ &I_i(\rho) \leq I^*, \;\; i = 1,2 \\ &\frac{\left(\hat{\mathrm{u}}_{out,i}(\rho)\right)^2}{\left(u_{out,i}(\rho)\right)^2} \leq \varepsilon^*, \qquad i = 1,2 \\ &\frac{\left(u_{out,1}(\rho) - u_{out,2}(\rho)\right)^2}{\left(u_{out,1}(\rho) + u_{out,2}(\rho)\right)^2} \leq \varepsilon^* \\ &0 < \rho_{min} \leq \rho \leq 1 \\ &\text{equilibrium equations} \end{aligned} \tag{2.20}$$

In the above optimization problem, $u_{out,i}$ are the deflections of the output port i when the i^{th} electrical input is applied and $\hat{u}_{out,i}$ are the corresponding cross-sensitivities. Different than Equation (2.19), the 5th line of the optimization problem in Equation (2.20) ensures that the magnitude of the vertical deflections for workpieces 1 and 2 have values, which are close to each other.

2.2.4 Material Interpolation Scheme

Solution of topology optimization problems using mathematical programming algorithms require the design variables to be continuous [53]. Hence, material properties should be interpolated between solid ($\rho^e = 1$) and void ($\rho^e = 0$). For this purpose, a power-law, i.e. Solid Isotropic Material with Penalization (SIMP), approach is used, where the Young's modulus depends on a power of density and the Poisson's ratio is constant [80]. This approach enables interpolation of the material properties between solid and void using a smooth continuous function, which depends on only material density.

The power-law interpolation of the Young's modulus, E, can be written as [53]:

$$E(\rho^e) = (\rho^e)^p E^{(0)} \tag{2.21}$$

In the above expression, p is a penalization power, typically chosen larger than 3, and $E^{(0)}$ is the Young's modulus of the bulk material. As p increases, the stiffness of intermediate density elements decreases, and hence these elements become unfavorable. This results in black & white (0/1) designs, which are feasible for fabrication.

Note that, in the absence of a volume constraint, the penalization of intermediate densities will not have any influence.

2.2.5 Sensitivity Analysis

In order to solve the optimization problems given in Equations (2.19) and (2.20), the sensitivities of the linear output displacement of an actuator to the changes in the design variables must be calculated. For this purpose, $du_{out}/d\rho^e$ is computed using the adjoint sensitivity analysis method [81].

Furthermore, filtering of the sensitivities is essential in order to ensure mesh-independency of the design [67]. This is possible by modifying the design sensitivity of a specific element, based on the weighted average of the sensitivities of the neighboring elements [67].

Details of both sensitivity analysis and filtering of the sensitivities can be found in [53].

2.2.6 Numerical Implementation

The theory explained above is implemented into a custom-made executable program by Ole Sigmund [53]. The basics of this topology optimization software is explained in detail in the following section and details of the numerical implementation can be found in [53].

2.2.7 The Topology Optimization Software

The topology optimization software is written by Ole Sigmund in FORTRAN77 programming language and it runs on UNIX operating system [53]. The program can be used for solving both thermal and electrothermal problems including one or two different materials. Inputs to the program are two text files: “geom.dat” defining the design domain and “konst.dat” defining the optimization parameters. The main output is a grey-scale bitmap file of the structure, where the intensity of each pixel represents the relative material density. Other outputs include bitmap images of the deformed structure, the current distribution and the temperature distributions. Furthermore, as the program runs, parameters, such as displacement, force and stiffness, are printed on the terminal window at each step.

Instructions on how to use the topology optimization software and example input files can be found in APPENDIX A.

2.3 Material Selection

Apart from the topography and the dimensions, selection of the material for an electrothermal actuator is rather important, having a considerable influence on its performance. Electroplated metals [66, 82], polysilicon [50, 83] and shape memory alloys (SMAs), e.g. Ni-Ti, are the materials most commonly used for electrothermal actuators. Polymers are not preferred since they are mostly non-conducting. However, there are examples of polymer microgrippers with integrated metal heaters [43].

A comparison of different materials for electrothermal actuators is given in [82]. In this paper, it was concluded that nickel is the best choice, having 60 % better quality than polysilicon. However, considering especially microgrippers, polysilicon is preferable over any other metal due to its low surface adhesion (see Section 2.8).

Polysilicon is also compatible with conventional microfabrication, including high temperature processes. Furthermore, low-pressure chemical vapor deposited (LPCVD) polysilicon films have less internal stresses compared to metals. Hence, the suspended polysilicon beams exhibit less out-of-plane bending when released. Finally, polysilicon has a lower resistivity than metals, and therefore polysilicon actuators operate at lower voltages than metal actuators.

The minor disadvantages of polysilicon are the relatively low coefficient of thermal expansion, which results in more power dissipation for achieving a certain displacement, and variation of electrical and thermal properties due to deposition conditions.

Due to the many advantages listed above, polysilicon was selected as the device material for the electrothermal microgrippers.

2.4 Design Procedure

2.4.1 Definition of the Design Domain

The first step of the topology optimization is definition of the design domain. This includes definition of parameters such as domain size, material properties, stiffness and operating voltage, and setting up boundary conditions and constraints, such as the position of supports or the volume constraint.

For the purpose of designing electrothermal actuators, the design domain is defined being inspired by the three-beam and the Gückel actuators (Figure 1.7).

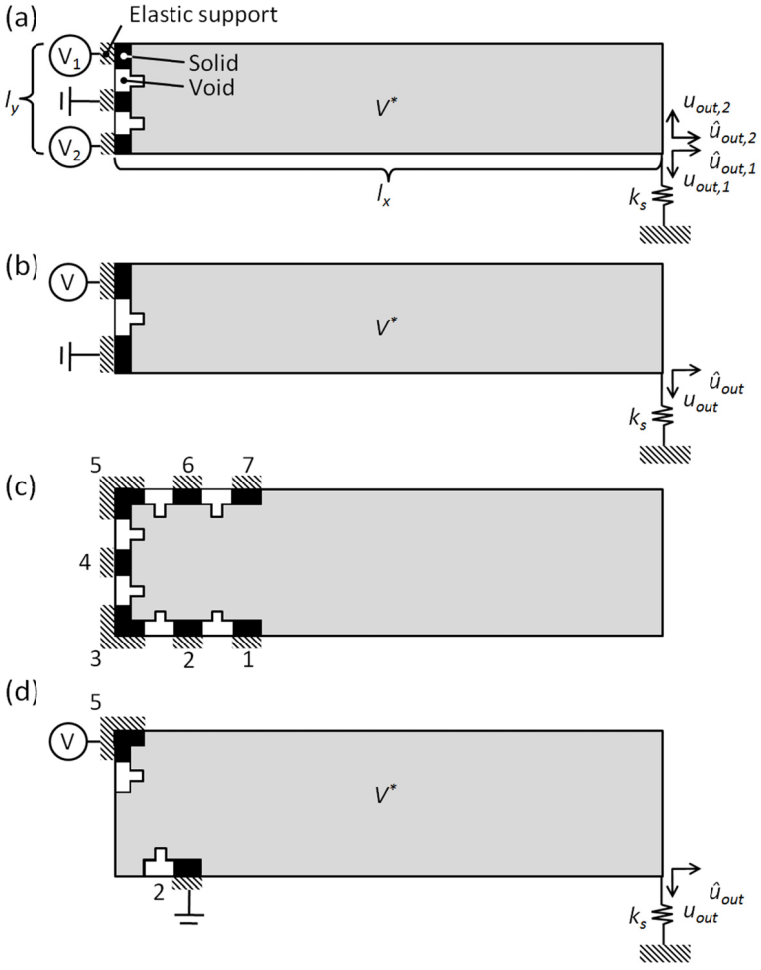

Figure 2.4 Design domains for topology optimization of (a) three-beam- and (b) Guckel-based actuators. (c) Pre-defined electrode locations for finding the optimum electrode locations and (d) an example design domain for the 2 & 5 configuration.

For the three-beam-based designs, which can both open and close, three different domain sizes are defined: 20 µm × 100 µm, 30 µm × 150 µm and 40 µm × 200 µm (Figure 2.4 (a)). Solid and void areas are defined in order to eliminate short-circuits between the electrical

supports. Furthermore, analyses are performed with different volume constraints, stiffness values and current constraints in order to find the best value for each of the three domains.

For the Gückel-based designs, which can only close, two different domain sizes are defined: 20 µm × 160 µm and 30 µm × 240 µm (Figure 2.4 (b)). Similar to the three-beam-based designs, solid and void areas are defined and analyses are performed with different stiffness values.

It is not possible to put a constraint on the maximum temperature in the topology optimization algorithm. In order to minimize the temperature, indirectly to some extent, a current constraint is applied in the very first analyses. However, application of a current constraint may result in structures with thinner beams, which sometimes have a higher maximum temperature (see Section 2.3 & APPENDIX B). For this reason, the usage of a current constraint is eliminated in the subsequent designs.

An additional set of analyses are performed in order to find the optimum location for the electrodes, i.e. elastic supports. For this purpose, a domain with 7 electrode locations is defined initially (Figure 2.4 (c)). Then, analyses with all possible two-electrode configurations are performed, e.g. 1 & 2, 1 & 3, 1 & 4, etc., where the input voltage is applied to one electrode and the other is set as ground (Figure 2.4 (c)).

Design parameters for all analyses and material properties used are tabulated in Table 2.2 to Table 2.5.

Table 2.2 Design parameters for the three-beam-based analyses (* See Section 2.3).

Domain length, l_x	100			150			200*			µm
Domain height, l_y	20			30			40*			µm
Device thickness, h	5			5			5*			µm
Volume constraint, V^*	30	45	60	20	30	40	15*	22.5	30	%
Stiffness, k_s	10	25	40	10	25	40	25*			N/m
Input voltages, V_1 & V_2	8			8			8*			V
Current constraint, I^*	-	5	10	-			-*			mA
No. elements in x-direction, $n_{el,x}$	100			100			100*			
No. elements in y-direction, $n_{el,y}$	20			20			20*			

Table 2.3 Design parameters for the Gückel-based analyses.

Domain length, l_x	160			240			µm
Domain height, l_y	20			30			µm
Device thickness, h	5			5			µm
Volume constraint, V^*	40			40			%
Stiffness, k_s	10	25	40	10	25	40	N/m
Input voltage, V_1	8			8			V
No. elements in x-direction, $n_{el,x}$	160			160			
No. elements in y-direction, $n_{el,y}$	20			20			

Table 2.4 Design parameters for analyses with different two-electrode configurations.

Domain length, l_x	160	µm
Domain height, l_y	60	µm
Device thickness, h	5	µm
Volume constraint, V^*	20	%
Stiffness, k_s	25	N/m
Input voltage, V_1	8	V
No. elements in x-direction, $n_{el,x}$	80	
No. elements in y-direction, $n_{el,y}$	30	

Table 2.5 Material parameters used during design.

Young's modulus, E	169	GPa
Poisson's ratio, ν	0.3	
Coefficient of thermal expansion, α	2.57×10^{-6}	K^{-1}
Electrical conductivity, σ	1.125 × 104	S/m
Thermal conductivity, k	148	W/(m·K)
Initial Temperature, T	26.85	°C

Note that, designs are performed using single crystalline silicon (SCS) material properties, initially. Furthermore, material properties can be defined only as constants in the topology optimization program and hence, it is not possible to consider the temperature dependency of (poly) silicon material properties during design. For this reason, material properties of SCS at an average working temperature of 500 °C are used in the topology optimization analyses [84]. However, temperature dependency of the material properties will considered during the finite element analysis of the post-processed design (see CHAPTER 3).

2.4.2 Topology Optimization

The number of discretization elements is selected considering the minimum line-width that can be obtained using conventional lithography. As an example, for the three-beam-based analyses, numbers of elements in x- and y-directions are 100 and 20, respectively. Hence, one pixel corresponds to 1 μm, 1.5 μm and 2 μm square elements, in 100 μm-, 150 μm- and 200 μm-long domains, respectively. Number of elements used for various designs can be found in Table 2.4.

The analyses are started with a filter radius (see Section 2.1.6) of 3 and gradually decreased to 2, 1.5 and 1.2, respectively, after every 250 iterations. If the convergence is not achieved after a total of 1000 iterations, additional 250 iterations with a filter radius of 1.2 are performed until the convergence is achieved.

Results of the topology optimization analyses will be presented in the following section.

2.5 Design Results

Results for the topology optimization analyses performed with different parameters are tabulated in APPENDIX B. In this section, the topology optimization results for a selected set of parameters will be presented.

The design parameters used for the analysis selected for further processing are marked with an asterisk (*) in Table 2.2. The outputs of the topology optimization algorithm after each 250-iteration steps can be seen in Figure 2.5. The basic structure remains almost the same, where the edges of the structure become sharper as the filter radius is decreased.

The performance criteria for the result are tabulated in Table 2.6. Note that, u_{out} and F_{out} are the output displacement and the output force at the given input voltage, and their ratio is equal to the pre-defined stiffness value, k_s. u_{free} and F_{blo} are the free displacement, which is the maximum displacement that can be achieved with zero output force, and the blocking force, which is the maximum force that can be achieved at zero displacement, respectively. T is the maximum temperature within the structure at the given input voltage. k is the overall stiffness of the structure, which is equal to the ratio of the blocking force to the free displacement. Finally, I is the current passing through the structure at the given input voltage.

In addition to the main output of the topology optimization algorithm, which is a grey-scale bitmap image, there are also some useful additional outputs including a grey-scale image of the displaced structure, current distribution within the structure and temperature distribution within the structure with two different color maps (Figure 2.6).

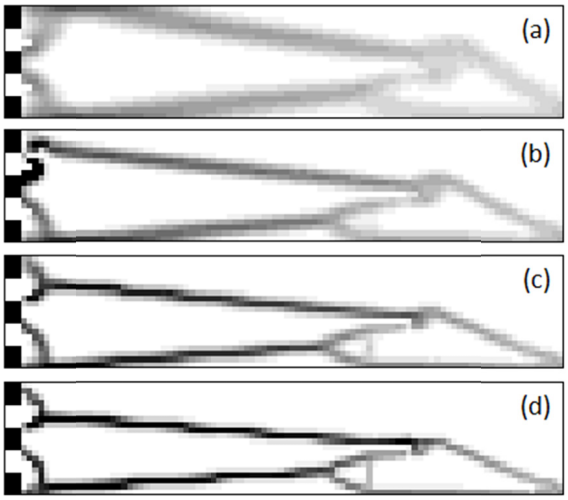

Figure 2.5 The output of the topology optimization algorithm after each 250 iteration with (a) r_{min} = 3, (b) r_{min} = 2, (c) r_{min} = 1.5 and (d) the final design with r_{min} = 1.2.

Table 2.6 Topology optimization results for the selected analysis: Performance criteria.

	Closing (Case 1)	Opening (Case 2)	
u_{out}	0.789	0.733	µm
F_{out}	19.72	18.33	µN
u_{free}	1.319	1.226	µm
F_{blo}	49.03	45.58	µN
T	648	633	°C
k	37.17	37.17	N/m
I	14	15	mA

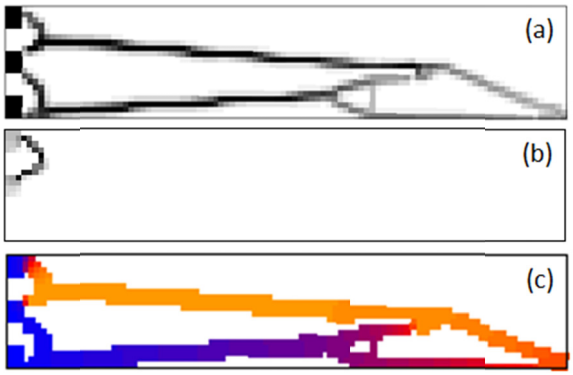

Figure 2.6 Additional outputs of the topology optimization algorithm: (a) Grey-scale image of the displaced structure, (b) current distribution within the structure, (c) temperature distribution within the structure, where blue and yellow represent the cold and the hot regions, respectively.

2.6 Design Selection

The last part of the design procedure is selecting the best design among the results of many outputs and finalizing the output image for fabrication.

The topology optimization algorithm may produce structures with rather complex features, such as small hinges, which are not possible to fabricate, and/or excess beams, which may restrict the working area when used as a microgripper (Figure 2.7 (a)). Furthermore, although the maximum temperature of the structure may be relatively low, the current may be running through the end-effector location, increasing the temperature of this region (Figure 2.7 (b)). Despite their good performance criteria, such designs should be eliminated.

The designs selected for fabrication, considering various aspects mentioned above, are presented in Figure 2.8 & Figure 2.9.

From this point on, these designs will be recalled with the names given in the captions of Figure 2.8 & Figure 2.9, e.g. Design A, Design B, etc. The results corresponding to the selected designs are highlighted with blue in all tables in APPENDIX B.

Figure 2.7 (a) Result of the analysis performed in a 100 µm × 20 µm domain with k_s = 10 N/m, V^* = 0.60 and I^* = 10 mA (see Table B.1). (b) Temperature distribution of the result of the analysis with a two-electrode configuration of 2-6 (see Table B.9).

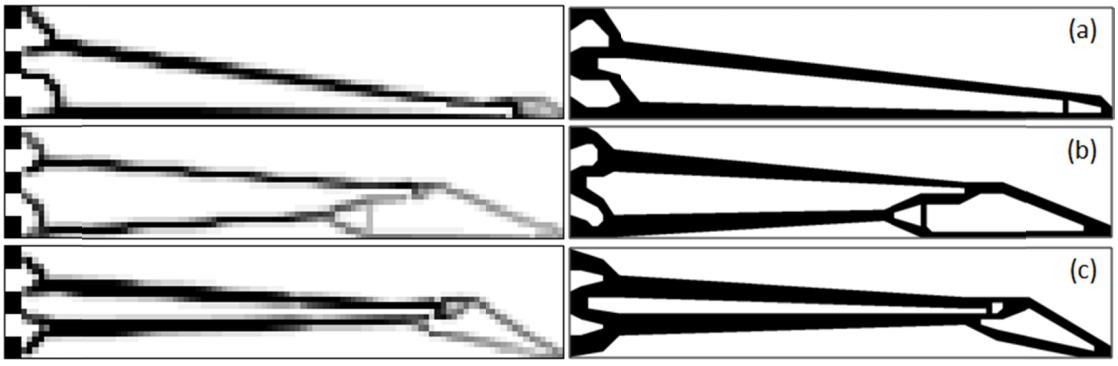

Figure 2.8 Original (left) and smoothed (right) versions of selected three-beam-based designs: (a) Design A: 150 µm × 20 µm domain, $V^* = 0.20$, $k_s = 40\ N/m$, (b) Design B: 200 µm × 40 µm domain, $V^* = 0.15$, $k_s = 25\ N/m$ and (c) Design C: 200 µm × 40 µm domain, $V^* = 0.225$, $k_s = 25\ N/m$.

The black & white versions (see Section 2.7) of all three-beam and Gückel-based microgrippers are fabricated as prototypes, initially (see Section 4.2.2). However, none of these designs were further improved since they have many fine features, which are not feasible for fabrication due to process limitations.

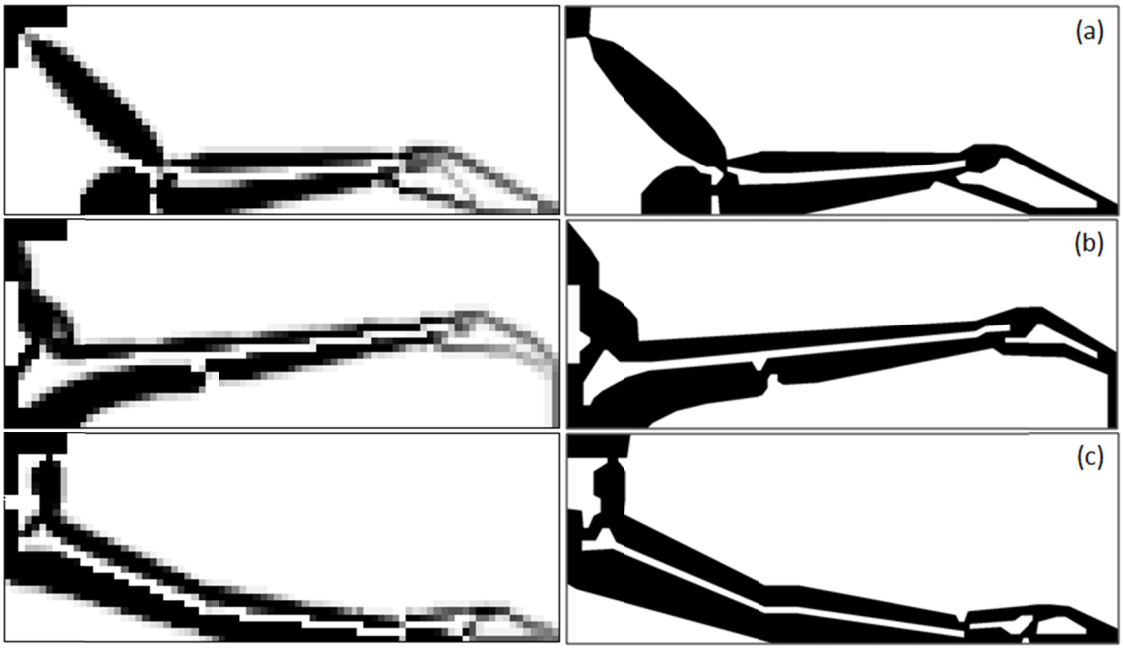

Figure 2.9 Selected designs with two-electrode configurations: (a) Design D: 2-5 configuration, (b) Design E: 3-5 configuration and (c) Design F: 4-5 configuration.

2.7 Design Finalization

2.7.1 Post-processing of the Topology Optimized Design

It is not possible to fabricate the grey-scale output of the topology optimization program, which has a non-uniform material density throughout its length. For this reason, the output image should be converted to black & white. Here, the threshold value used in conversion should be selected properly in order to eliminate missing design features and/or disconnected actuator beams. For the specific design in Figure 2.8 (b), results of black & white conversion with different threshold values are presented in Figure 2.10.

The black & white conversion performed with a threshold value of 0.2 was selected for further processing, where the missing pixel was manually corrected (Figure 2.10 (c)). However, the black & white design has a volume of 23 % instead of 15 %. Furthermore, the stiffness of the structure increased to 151 N/m from 37 N/m (Table 2.7). The reason behind these changes is that many pixels with intermediate densities become 1, and hence their Young's modulus considerably increases according to the power law (see Equation (2.21)). As an example, if a pixel with an intensity of 0.5 becomes 1, its Young's modulus increases by a factor of $(1/0.5)^3 = 8$.

Following black & white conversion, the edges of the beams should be smoothed and unfeasible design features should be eliminated, if necessary (Figure 2.11 (a)). In addition to this, the actual line of motion can be predicted through finite-element analysis (see Chapter 3) and any cross-displacement can be eliminated by proper tilting of the actuators while constructing the microgrippers. Hence, the displacement and the force in the gripping direction can be enhanced (Figure 2.11(b)). For this purpose, Designs A, B and C are tilted by 7.5°, 9.5° and 11°, respectively. The tilting step is an optional step and was not applied to all designs.

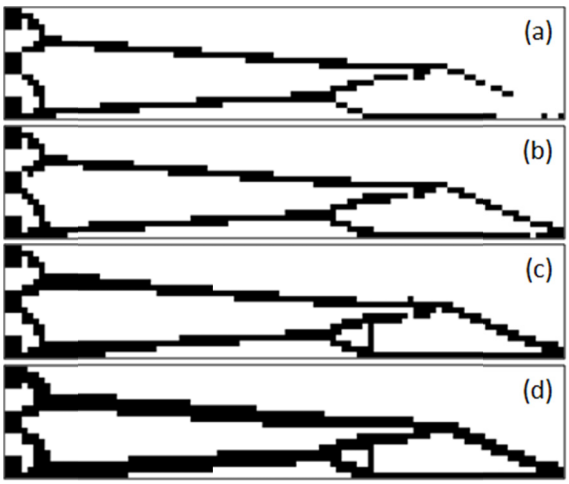

Figure 2.10 B & W conversion of the grey-scale output in Figure 2.8 (b) using threshold values: (a) 0.4, (b) 0.3, (c) 0.2 and (d) 0.1.

Table 2.7 Topology optimization results for Design B after black& white conversion (Figure 2.10 (c)): Performance criteria.

	Closing (Case 1)	Opening (Case 2)	
u_{out}	0.688	0.590	µm
F_{out}	17.20	14.75	µN
u_{free}	0.802	0.688	µm
F_{blo}	120.98	103.73	µN
T	619	617	°C
k	150.83	150.83	N/m
I	48	45	mA

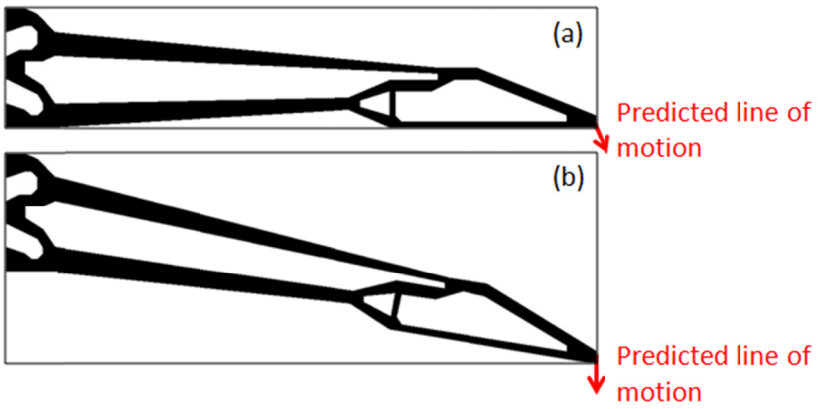

Figure 2.11 Finalization of the design in Figure 2.10 (c): (a) Smoothing the beams and (b) correcting the line of motion by tilting the actuator.

Cross-displacement can also be eliminated by setting up a constraint during topology optimization (see APPENDIX A). However, this adds to the non-linearity of the problem and the resulting structures may have more complex features, which are not possible to realize with conventional microfabrication techniques.

2.8 End-effector Design

One of the most important challenges of nanomanipulation is stiction, the unwanted adhesion of the manipulated nanostructure, mainly to the end-effectors. The main reason for stiction is the surface forces, which become more dominant at nano-scale due to the high surface-to-volume ratio. The mechanisms for the most dominant surface forces will be explained in the following sections.

2.8.1 Electrostatic Forces

Coulomb forces between two charged atoms or ions are the strongest of the physical forces that will be considered in Section 2.8. The expression for the free energy due to the Coulomb interaction between two charges, Q_1 and Q_2, can be written as follows [85]:

$$E(r) = \frac{Q_1 Q_2}{4\pi\varepsilon_0 \varepsilon r} \tag{2.22}$$

In the above expression, ε_0 is the permittivity of free space (= 8.854 $C^2J^{-1}m^{-1}$), ε is the relative permittivity of the medium and r is the distance between the charges.

The expression for the Coulomb force can be obtained from (2.23) as follows:

$$F(r) = -\frac{dE(r)}{dr} = \frac{Q_1 Q_2}{4\pi\varepsilon_0 \varepsilon r^2} \tag{2.23}$$

The Coulomb force is repulsive (+) for like charges, where it is attractive (-) for unlike charges.

For two charged parallel surfaces (Figure 2.12) the expressions for the Coulomb energy and the Coulomb force become [86]:

$$E(g) = \frac{CV^2}{2} = \frac{\varepsilon_0 \varepsilon V^2}{2g} \tag{2.24}$$

$$F(g) = \frac{dE(g)}{dg} = -\frac{\varepsilon_0 \varepsilon V^2}{2g^2} \tag{2.25}$$

In Equations (2.24) and (2.25), C is the capacitance and V is the potential difference between the surfaces.

Electrostatic forces may arise between the microgripper end-effectors and the manipulated sample since the microgrippers are actuated by applying a voltage difference. Furthermore, there is a considerable amount of charge transfer from the electron beam during manipulation inside an SEM. Charges may also build up due to the friction between the end-effectors and the manipulated sample, i.e. tribocharging [87].

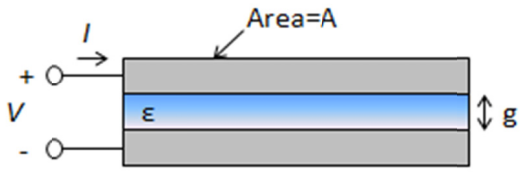

Figure 2.12 Schematic illustration of a parallel plate capacitor, i.e. two charged surfaces parallel to each other.

2.8.2 Van der Waals Forces

Van der Waals forces arise from instantaneous polarization of a non-polar or a polar molecule due to the fluctuations in the charge distribution of a neighboring non-polar or polar molecule (Figure 2.13) [87]. Although being not as strong as Coulomb attractions, they are always present and between all kinds of atoms and molecules.

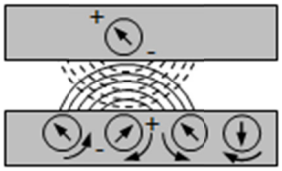

Figure 2.13 Schematic illustration of Van der Waals interaction, i.e. dipole-induced dipole interaction.

The interaction energy of the Van der Waals force between two atoms is given by:

$$E(D) = -\frac{C_{VdW}}{D^6} \tag{2.26}$$

Where, C_{VdW} is a constant, which depends on the dipole moments and the polarizabilities of the molecules, and D is the separation between them.

At large separations (> 10 nm), the London dispersion interactions become weaker due to the randomizing effect caused by the rapid fluctuations. This phenomenon is called retardation and it will result in a decay in the interaction energy as D^{-7} at large separations [88].

For two flat surfaces parallel to each other (Figure 2.14 (a)), the expressions for the Van der Waals interaction energy and the force per area can be written as follows [87]:

$$E(D) = -\frac{A_H}{12\pi D^2} \tag{2.27}$$

$$F(D) = -\frac{A_H}{6\pi D^3} \tag{2.28}$$

Similarly, for a cylinder with radius ,R, near a flat surface (Figure 2.14 (b)), the expressions for the Van der Waals interaction energy and the force per length can be written as follows [87]:

$$E(D) = -\frac{A_H\sqrt{R}}{12\sqrt{2}D^{3/2}} \tag{2.29}$$

$$F(D) = -\frac{A_H\sqrt{R}}{8\sqrt{2}D^{5/2}} \tag{2.30}$$

In the above expressions, A_H is the Hamaker coefficient, which depends on both the interacting materials and the interaction environment. The value of the Hamaker coefficient can be calculated according to Lifshitz theory as follows [85]:

$$A_H = \pi^2 C\rho_1\rho_2 \tag{2.31}$$

In the above expression, ρ_1 and ρ_2 are the numbers of atoms per unit volume in the two bodies and C is the coefficient in the atom-atom pair potential.

Typical values for the Hamaker constant for interactions between solids and liquids across vacuum or air are in the range from 10^{-20} to 10^{-19} J, where values for metals are higher [87].

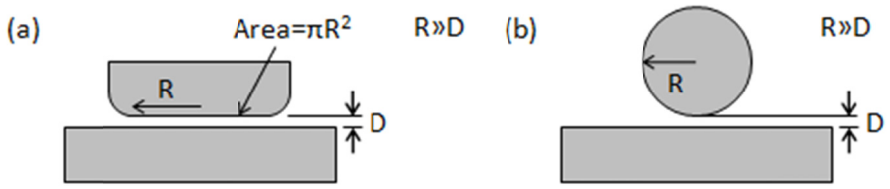

Figure 2.14 Schematic illustration of (a) two flat surfaces parallel to each other and (b) a cylinder with radius ,R, near a flat surface.

2.8.3 Capillary Forces

Even small amounts of water can act as an adhesive between two solid surfaces in contact due to capillary condensation around the contact sites. Considering two solid plates bridged by a drop of liquid (Figure 2.15 (a)), there exist a pressure difference at the liquid-air interface, which is given by the Laplace equation [89]:

$$\Delta P_{LA} = \frac{\gamma_{LA}}{r} \tag{2.32}$$

In the above expression, γ_{LA} is the surface tension of the liquid–air interface and r is the radius of curvature of the meniscus, which can be calculated from simple geometry as follows:

$$r = -\frac{g}{2\cos\theta_c} \tag{2.33}$$

Here, g is the distance between the two plates.

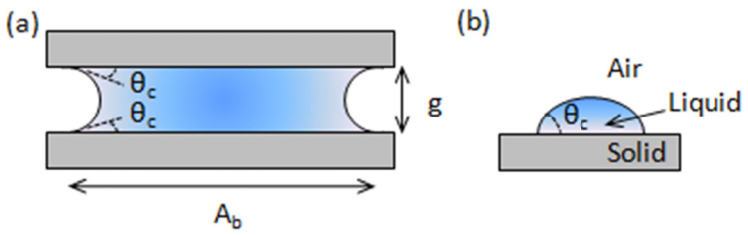

Figure 2.15 (a) A liquid droplet on a solid in air and (b) a non-spreading liquid bridging two solid surfaces.

At equilibrium, the expression for the force separating the plates can be written as follows:

$$F = -\Delta P_{LA} A_b = \frac{2A_b \gamma_{LA} \cos\theta_c}{g} \tag{2.34}$$

If the contact angle, θ_c (Figure 2.15 (b)), is smaller than 90°, the pressure inside the liquid drop is lower than the pressure outside and the resulting force will be attractive. Whereas, if θ_c is greater than 90°, the pressure inside the liquid drop is higher than the pressure outside and the resulting force will be repulsive.

Capillary forces may be seen between the microgripper end-effectors and the manipulated sample during manipulation in ambient air. Although being smaller than in ambient air, capillary forces may even be present in vacuum, e.g. inside the SEM chamber. However, high operation temperatures of the microgrippers may result in evaporation of any water film on the surface of the microgrippers and hence, elimination of the capillary forces.

2.8.4 End-effectors with Less Stiction

From the formulas for the surface forces given above, it can be concluded that the contact area, the Hamaker coefficient, the contact angle and the surface tension have an influence on the stiction force. As well as its mechanical, electrical and thermal properties, polysilicon was also preferred as the device material due to its low adhesion. Considering Van der Waals forces, the Hamaker coefficient of metals are rather high [87], which results in higher adhesion. Considering capillary forces, the contact angle of n-doped polysilicon is around 80° depending on the deposition and doping conditions [90], whereas it is 63° for electroplated nickel [91].

The adhesion forces at the end-effectors can be considerably reduced by coating them with an anti-stiction layer [92-94]. However, the melting temperature of these coatings should be higher than the end-effector temperature during operation. Furthermore, the coatings should be renewed as they become worn after a number of experiments.

As well as the properties mentioned above, the contact area has a significant effect on capillary and electrostatic forces. In order to reduce these forces, the contact area between the end-effectors and the manipulated sample should be as small as possible. This can be achieved by nanostructuring of the end-effector surfaces (Figure 2.16).

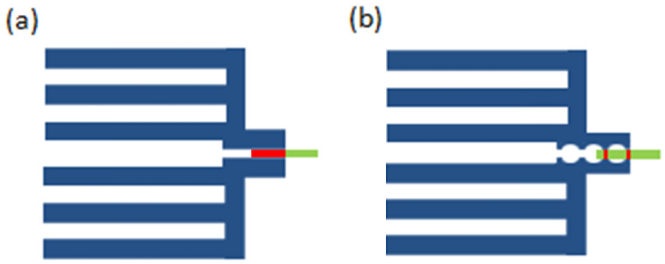

Figure 2.16.Schematic illustration of manipulation with (a) flat and (b) structured end-effectors, where the length of the sample contacted by the end-effectors is highlighted with red.

The side-walls of the microgrippers can be nanostructured during fabrication, using a Bosch advanced Silicon Etch (ASE). Bosch process is a switched process with alternating steps of octafluorocyclobutane (C_4F_8)-based passivation and sulfur hexafluoride (SF_6)-based etch steps. As well as realization of high-aspect-ratio (20-30:1) microstructures with smooth side-walls [95], the Bosch process can also be used for realization of side-walls scallops (Figure 2.17). The interval of the scallops can be controlled by tuning the etch parameters during the process.

As an alternative to plasma-based etching, electrochemical etching can also be used for nanostructuring of the end-effector surfaces [96, 97].

In this project, FIB milling was used for sub-micron structuring of the microgripper end-effectors in order to reduce the contact area with the manipulated sample. FIB milling has many advantages over the Bosch and the electrochemical etch methods: First of all, FIB milling enables better control on the shape and size of the micro/nanostructures, and hence realization of task specific end-effectors (see Section 4.3.2.1). Furthermore, the FIB milling process is easier and less time consuming than the above mentioned processes. Finally, the nanostructured end-effectors can immediately be tested and used after the FIB milling process. Further details on the end-effector design can be found in Section 4.3.2.1.

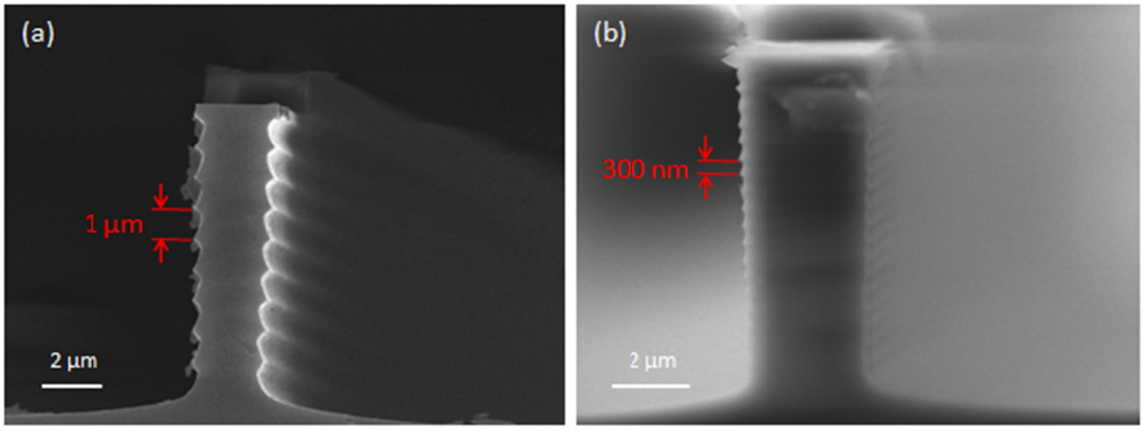

Figure 2.17.(a) Micro- and (b) nanostructured side-walls etched in silicon using Bosch process (Fabricated by RT Rajendra Kumar).

2.9 Mask Design

The mask layout was created using L-Edit 13 as the layout editor. The main design used is similar to the mask presented in [98]. However, the number of bonding pads and their dimensions were changed according to the requirements of each design (Figure 2.18). Furthermore, different lead shapes were designed in order to enhance the performance of the actuators.

The initial chip designs were composed of either one (Figure 2.18 (a)) or two (Figure 2.18 (b)) microgrippers with separated actuators. Here, all electrodes were connected to individual bonding pads and hence, the two actuators of the microgrippers can be operated independently. Additional three electrodes were placed at the bottom of these chips in order to enable flexibility and integration with various systems with electronics limitations.

Three different lead designs were used for these chips:

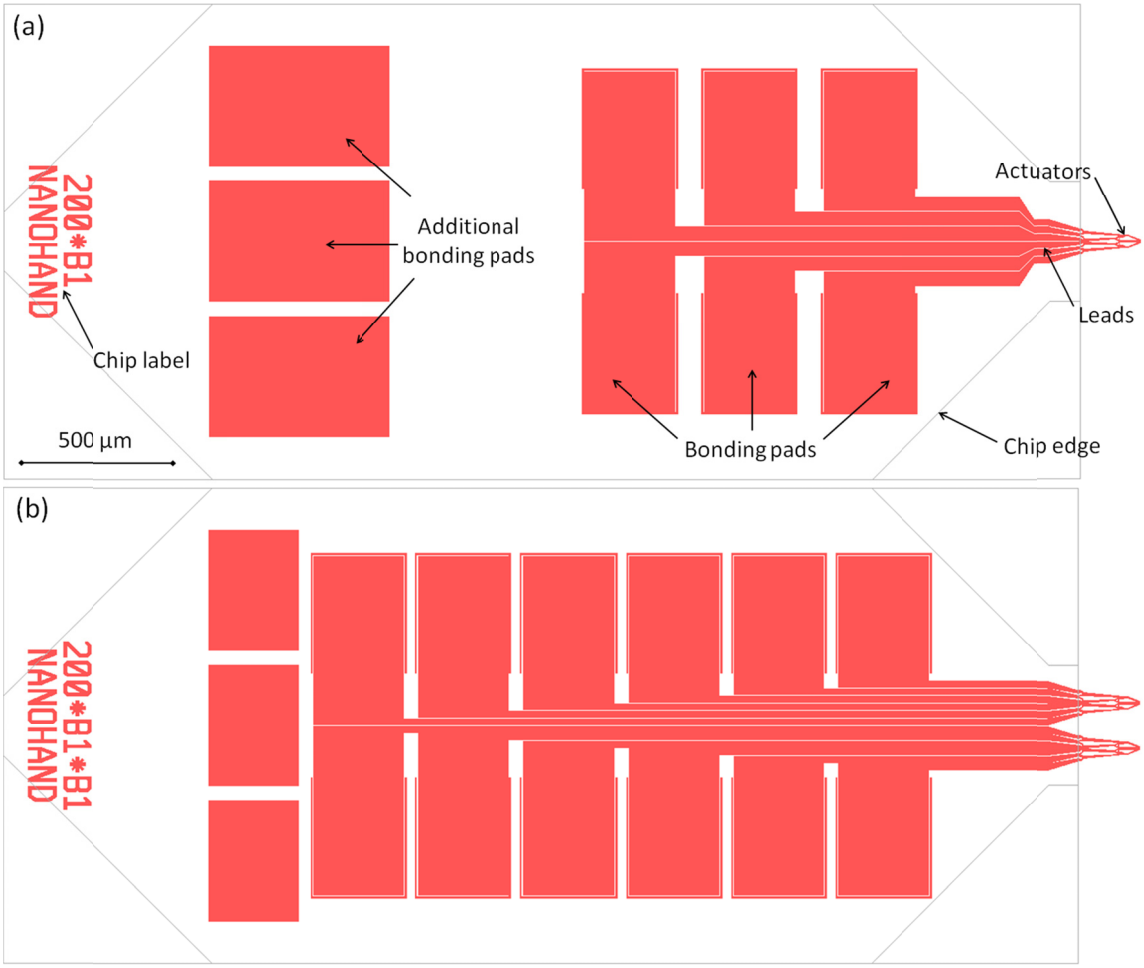

Figure 2.18 Initial chip layouts: (a) For one (6-pads) and (b) two (12-pads) microgrippers with separated actuators.

The basic lead design was composed of three leads for each actuator. All leads start with a trapezoidal section, continue with a 20 µm-wide rectangular path and connect to a separate bonding pad (Figure 2.19 (a)).

In order to enhance the actuation of the microgrippers at lower temperatures by reducing the heat transfer between the two heaters, a second lead design was created. Here, the outer- and the inner-most leads were the same as the regular design, where the initial ~100 µm-length of the middle lead was divided into two (Figure 2.19 (b)).

However, the effect was not as expected since the thinner leads with higher resistance resulted in excessive heating (see Section 6.4). Hence, the divided lead design is eliminated.

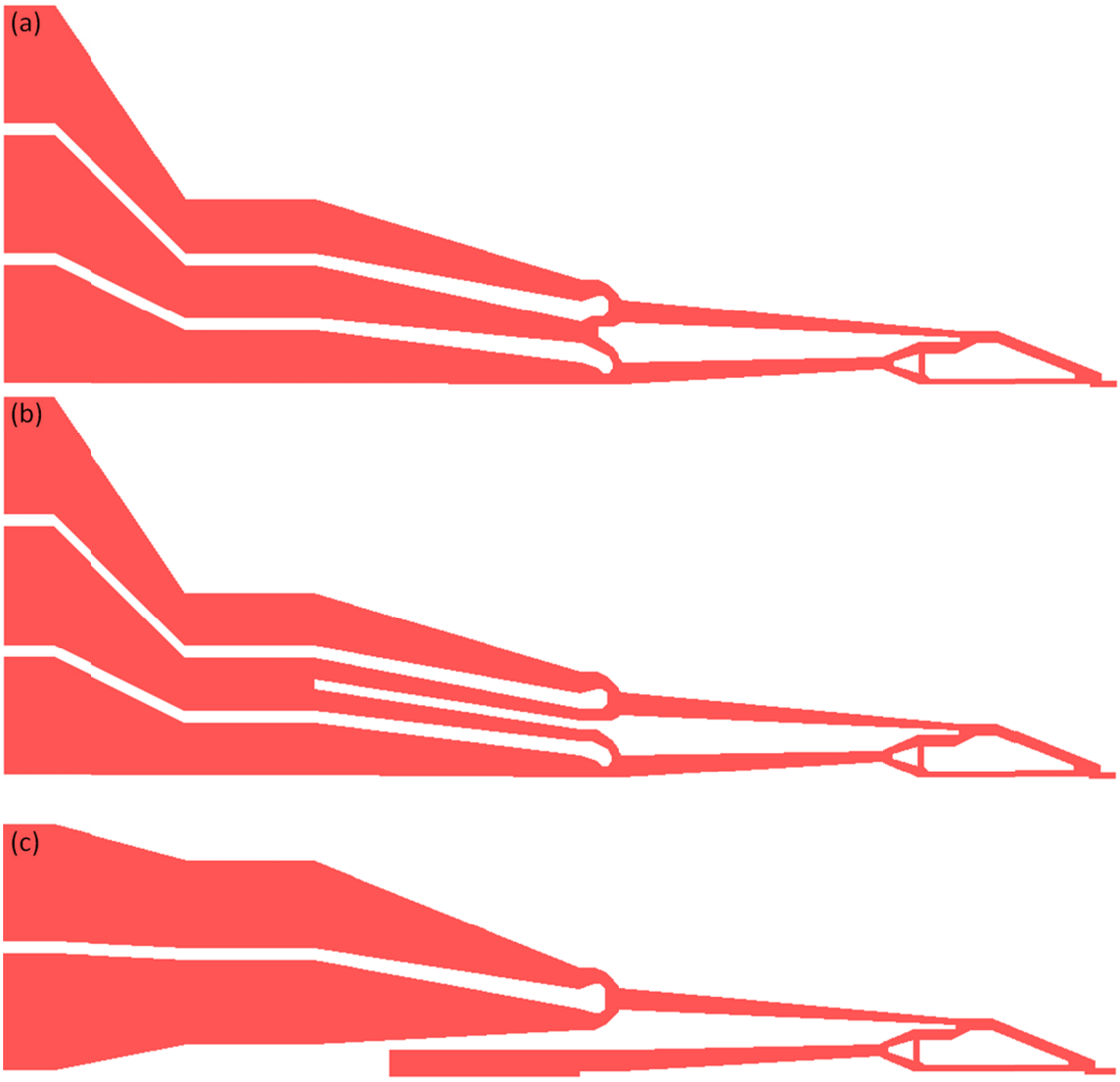

Figure 2.19 Different lead designs: (a) Basic, (b) divided and (c) two-electrode designs.

In order to obtain the effect desired with the divided electrode design mentioned above, the second electrode of the actuator was completely eliminated and the inner-most

electrode was replaced with an anchor (Figure 2.19 (c)). However, the microgrippers having this type of lead design become mono-directional and can only close.

In order to eliminate heating of the carrier chip and still maintain the bi-directional property, the chip layout was improved by widening the leads and connecting the matching electrodes of the two actuators to the same bonding pad (Figure 2.20 (a)). Hence, the initial trapezoidal regions were enlarged as large as possible (Figure 2.20 (b)) and the width of the connecting leads was increased to ~185 µm.

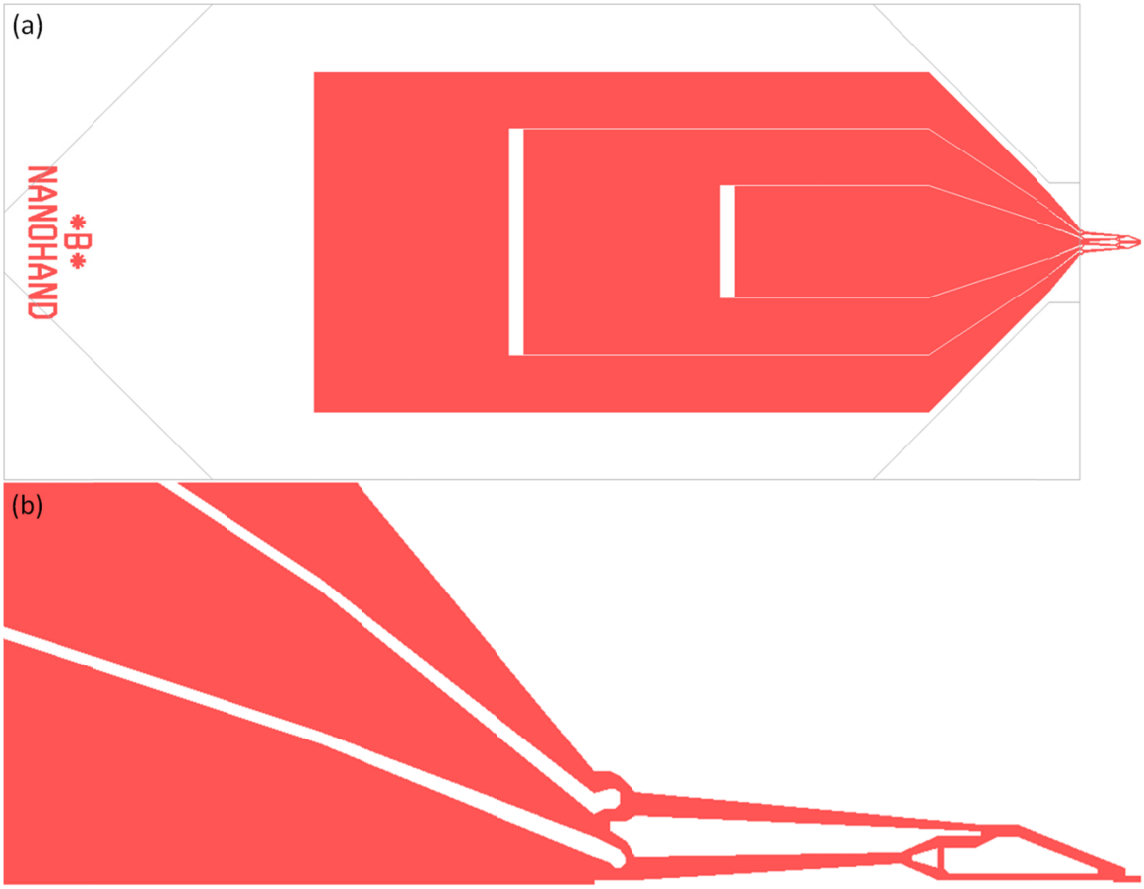

Figure 2.20 (a) The improved chip layout and (b) the corresponding lead design.

Summarizing, three masks were designed during the project:

Mask 13 – Topology Optimization I: Includes the pixelated versions of all topology optimized microgrippers. Each chip contains two-microgrippers: A topology optimized design on the left and a three-beam design having the same form-factor, i.e. volume, on the right. Hence, the 12-pad chip design (Figure 2.18 (b)) was used with the basic lead design (Figure 2.19 (a)) for all chips.

Mask 22 – Topology Optimization II: Includes the smoothed and tilted versions of designs A, B and C. Some chips contain a single device, and some contain two devices: either a topology optimized design and a three-beam design or two topology optimized designs. Hence, both 6-pad (Figure 2.18 (a)) and 12-pad (Figure 2.18 (b)) chip designs were used. With these, two different lead designs were used: The basic (Figure 2.19 (a)) and the divided (Figure 2.19 (b)) designs.

Mask 22 also contains Xylophone chips with 12 cantilever beams having different dimensions. These cantilevers were used during manipulation experiments (see Section 7.5). The devices with the two-electrode lead design (Figure 2.19 (c)) were fabricated later, by Mikkel B. Olesen during his M.Sc. project.

Mask 29 – Topology Optimization III: Includes the smoothed and tilted versions of designs A and B, and only smoothed versions of designs D, E and F. All chips contain a single device. The improved chip design (Figure 2.20) was used for all chips, having either 2 or 3 large bonding pads, according to the number of electrodes of the corresponding design.

Mask 29 also contains chips with a 300 µm × 200 µm rectangular beam, which has 12 leads. The aim was to use these chips for fabricating microgrippers using FIB (see Section 4.4). However, such experiments could not be realized due to time limitations.

2.10 Discussion

Topology optimization was used in the design of electrothermal microgrippers. Various topology optimization analyses were made with different design parameters and different boundary conditions. Among the resulting designs, only six were selected considering their performance and feasibility for microfabrication.

According to the results of the topology optimization algorithm, all of the selected designs are an order of magnitude stronger than the existing three-beam actuators.

Comparing the selected designs in Figure 2.8 and Figure 2.9, one may observe that the topology optimized actuators are mainly composed of localized heaters, which are horizontally away from the end-effector location, and connecting beams, which extrude from the heaters towards the end-effector location. This kind of structure resembles the rib-cage actuators in that, the heat is locally generated in heaters and conducted to the actuator beams. However, the actuation is more effective since the heaters are closer to the actuator beams.

Furthermore, most of these selected actuators have a front part, which is connected to the actuator beams with a hinge-like structure. In some designs, this front part is vertically away from the end-effector location, where it is the opposite way in some others. The reason may be that the volume constraint defined is higher than the requirement for the selected stiffness ratio in these designs. Hence, the topology optimization algorithm tends to move the front part away from the end-effector location, reducing the stiffness of the structure.

Variations of three of the selected designs were also created by tilting the actuators in order to enhance the actuation (y-axis displacement) and minimize the cross-displacement (x-axis displacement). This could also be done by putting a constraint on the cross-displacement during topology optimization (see APPENDIX A). However, the designs with a cross-displacement constraint, mostly, had a low actuation. This is since the topology optimization tends to minimize the displacement of the end-effector along x-direction, which is the main direction of thermal expansion. This also reduces the actuation along y-direction.

The mask layout for microfabrication was based on the design presented in [98]. Different lead designs were made in order to reduce the resistive heating of the leads, and hence the overall temperature of the carrier chip, which was observed during the temperature measurements (see CHAPTER 6).

CHAPTER 3
Finite Element Analysis of the Post-processed Design

3.1 Motivation

Finite element analysis of the actuators designed using topology optimization prior to fabrication is of crucial importance. The main reason for this is that the behavior of the finalized design may be different from the original output due to variations occurring during conversion to black & white and smoothing of the features. Furthermore, as stated in Section 2.2.1, material properties can be defined only as constants in the topology optimization program and hence, the effect of temperature dependency of the polysilicon (poly-Si) material properties should be considered through finite element analysis. Finally, the actual actuator will be connected to electrical contact leads, which lie on a silicon (Si) chip with a ~1 μm-thick silicon dioxide (SiO_2) layer underneath, rather than a perfect heat sink assumed during the topology optimization analyzes.

Finite element simulations of the topology-optimized actuators were performed using the MEMS Module of the COMSOL 3.4 & 3.5 simulation environments. Two different cases were investigated: *The ideal case*, where heating of the carrier chip was ignored, and *the non-ideal case*, where a portion of the chip was also included in the model to consider the chip heating. The ideal case simulations enable comparison of the performances of different actuator designs, regardless of the electrode design and the carrier chip dimensions. The non-ideal case simulations enable better prediction of the temperature profile of the actuators. Furthermore, the temperature of the carrier chip and the effect of the electrode design on the chip heating can be estimated using non-ideal case simulations.

In this chapter, the procedure used will be described in detail and the results will be presented for both simulation cases, being based on a selected design.

3.2 The Ideal Case

3.2.1 The Model

Finite element simulations for the ideal case were performed using a 3D model, which is composed of three application modes: *Conductive Media DC (emdc), Heat Transfer by Conduction (ht)* and *Solid, Stress-Strain (smsld)*. Although the actuators could also be modeled using a 2D model, a 3D model was preferred in order to better predict the conduction through the oxide layer underneath the leads and air convection.

Geometry, boundary, subdomain, mesh and solver settings for the ideal case will be explained in detail in the following sections.

3.2.1.1 Geometry Settings

The 3D model of a topology-optimized actuator was created by selecting the $z = 0$ work-plane in the *Draw Mode*, importing a 2D drawing of the actuator from a DXF file and extruding the imported geometry by 5 µm along the z-axis. In addition to the actuator itself, the first 100 µm-length of the electrical contact leads, which connect the actuator to the contact pads were also included in the model. Finally, the lead geometries were extruded by -1 µm along the z-axis, representing the SiO_2 layers underneath (Figure 3.1).

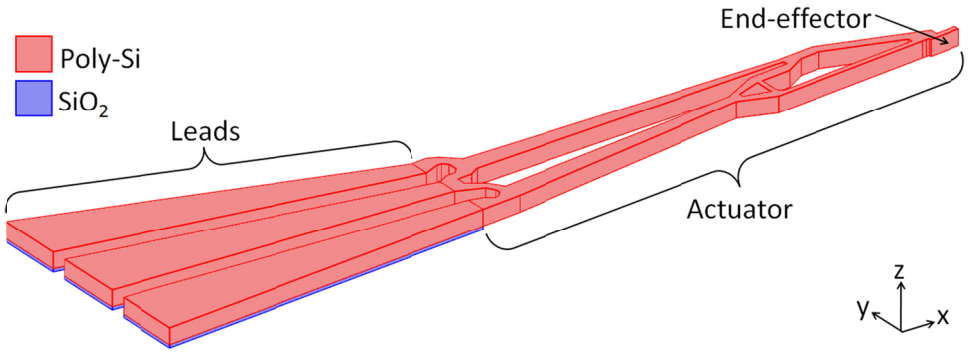

Figure 3.1 The ideal case 3D COMSOL model for the selected topology-optimized actuator design, i.e. Design B (see Section 2.3).

3.2.1.2 Subdomain Settings

Materials for the poly-Si and SiO_2 layers were selected from the materials library of COMSOL MEMS Module as "poly-Si" and "SiO2", respectively. However, the values of the temperature dependent material properties, such as electrical conductivity, were replaced with proper functions of temperature in the range from 0 K to 800 K [99]. Values out of this range were extrapolated. The material properties used in the simulations are tabulated in APPENDIX C.

In the *Heat Transfer by Conduction* application mode, a heat source was defined with the value "Q_dc" (or "Q_emdc", depending on the COMSOL version), which corresponds to the

resistive heating calculated during the electrical analysis. Also the initial temperature was set to 300 K for all subdomains in this application mode.

In the *Solid, Stress-Strain* application mode, and under the "Load" tab, the thermal expansion was included by defining the strain temperature as "T" and the strain reference temperature as 300 K. Here, "T" is the temperature calculated during the thermal analysis. Note that, this property is automatically included when COMSOL version 3.5 is used.

3.2.1.3 Boundary Settings

Boundary settings for the electro-thermo-mechanical simulation of the ideal case for the closing mode of the microgrippers are as follows:

In the *Conductive Media DC* application mode, electric potential boundary conditions were applied to the end surfaces of the poly-Si leads (Figure 3.2 (a)). For this mode, Lead 1 was set to an electric potential of "V0" and Leads 2 & 3 were defined as "Ground". All remaining boundaries were defined as "Electric Insulation".

In the *Heat Transfer by Conduction* application mode, temperature boundary conditions were applied to the bottom surfaces of the SiO_2 layers underneath the leads (Figure 3.2 (b)) by setting all to "300 K". The effect of air convection was included by defining a heat flux boundary condition to all boundaries, which are in contact with air. This heat flux can be defined as follows:

$$q = h_{air}(T_0 - T) \tag{3.1}$$

In the above expression, h_{air} is the heat transfer coefficient of air, which is defined as a function of temperature [99] (APPENDIX C), and $T_0 = 300K$ is the external temperature. Finally, all of the remaining boundaries were defined as "Thermal Insulation".

In the *Solid, Stress-Strain* application mode, the bottom surfaces of the SiO_2 layers underneath the leads were defined as "Fixed" (Figure 3.2 (b)), where the remaining boundaries were defined as "Free".

Boundary settings representing the ideal case of the opening mode of the microgrippers are the same as those for the closing mode, except the electrical boundary conditions for Leads 1 & 3 should be interchanged.

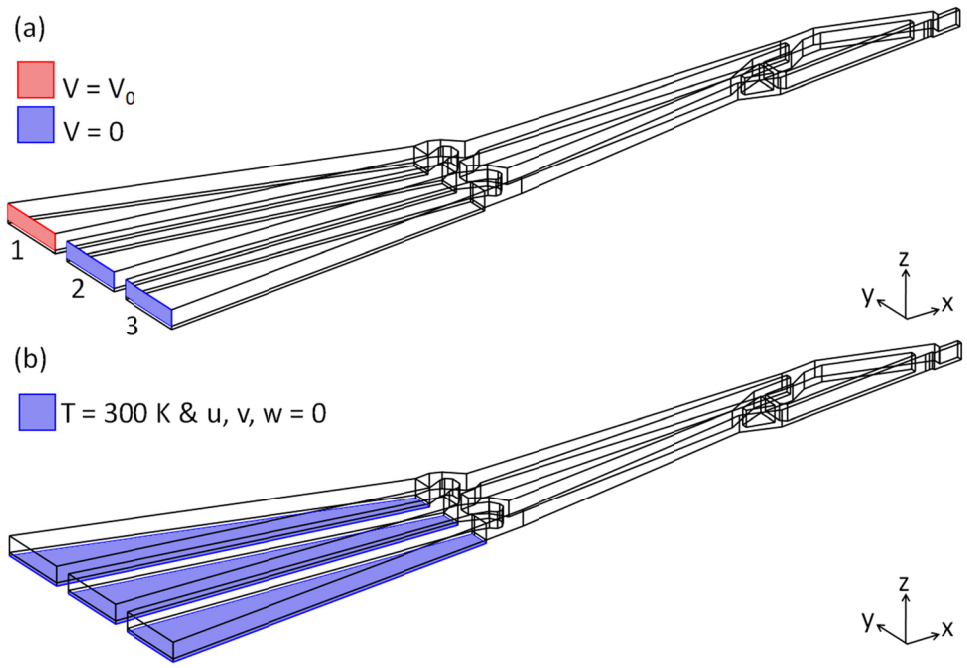

Figure 3.2 Boundary conditions representing the closing mode for the ideal case: (a) Voltage boundary conditions and (b) fixed temperature and fixed displacement boundary conditions.

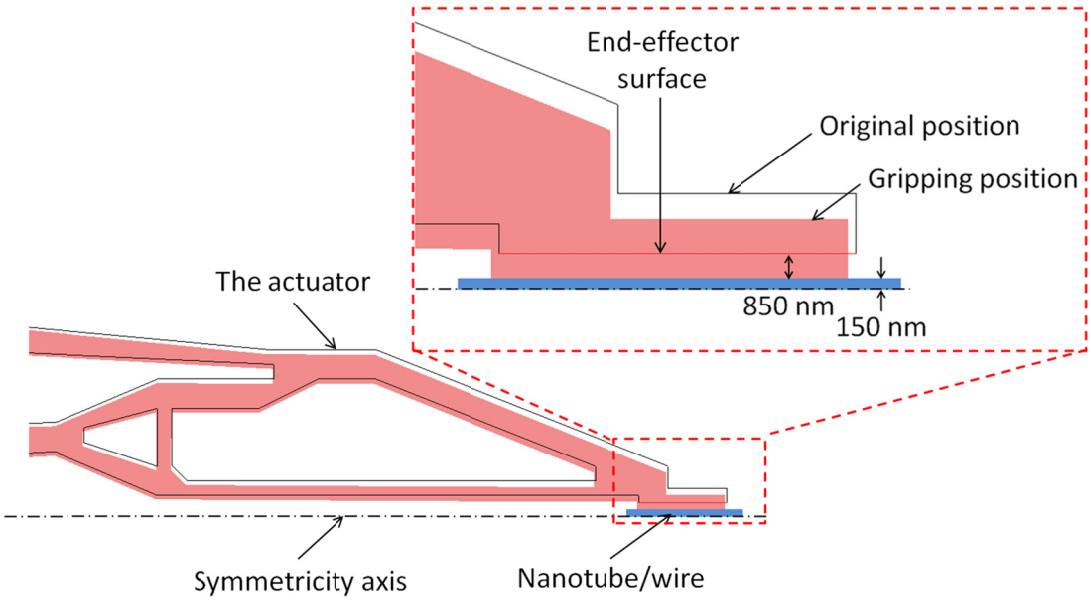

Figure 3.3 Illustration explaining the gripping of a nanotube/wire of 300 nm-diameter, with the details of the end-effector and the nanotube/wire in the inset.

Maximum gripping force that can be applied to a 300 nm-diameter sample (wire or tube) at a maximum operating temperature of 550 °C was determined by repeating the simulations, however with a prescribed displacement of 850 nm along -y-direction assigned at the end-effector boundary (Figure 3.3).

Finally, a stationary analysis was performed only in the mechanical domain with a prescribed displacement of 1 µm along y-direction assigned to the end-effector boundary. Hence, the structural stiffness of the actuator was estimated by integrating the force acting on the end-effector surface and dividing it by the displacement, i.e. 1 µm.

3.2.1.4 Mesh Settings

The actuators have a uniform cross-section, which makes it possible to create mesh layers along z-direction. This reduces the number of mesh elements and speeds up the finite element simulations. Also, it is of crucial importance to use a variable mesh size throughout the structure. This is since; the most critical regions of the topology-optimized actuators (e.g. the heater and the end-effector locations) should be finely meshed, where the remaining regions can be meshed with a coarser mesh.

The meshing procedure was as follows:

In the *Free Mesh Parameters* menu, the edges at the heater and the end-effector locations were meshed with a maximum element size of 1 µm (Figure 3.4 (a)). Then, top surfaces of the actuator and the leads were meshed with maximum element sizes of 2.5 µm and 5 µm, respectively (Figure 3.4 (b)). Finally, in the *Swept Mesh Parameters* menu, the mesh created on the top surfaces was swept along z-direction, using 2 and 1 element layers for poly-Si and SiO_2 subdomains, respectively (Figure 3.4 (c)). Quadratic second order mesh elements were used during all meshing steps.

3.2.1.5 Solver Settings

The electro-thermo-mechanical simulations of the topology-optimized actuators were performed using the parametric solver, where the parameter “V0” was swept from 0.5 to 6 V with 0.5 V steps.

The settings for simulations performed for finding the gripping force are the same as above.

Mechanical simulations of the actuators were performed using the stationary solver. The system solver was selected as “Direct (PARDISO)” for all cases.

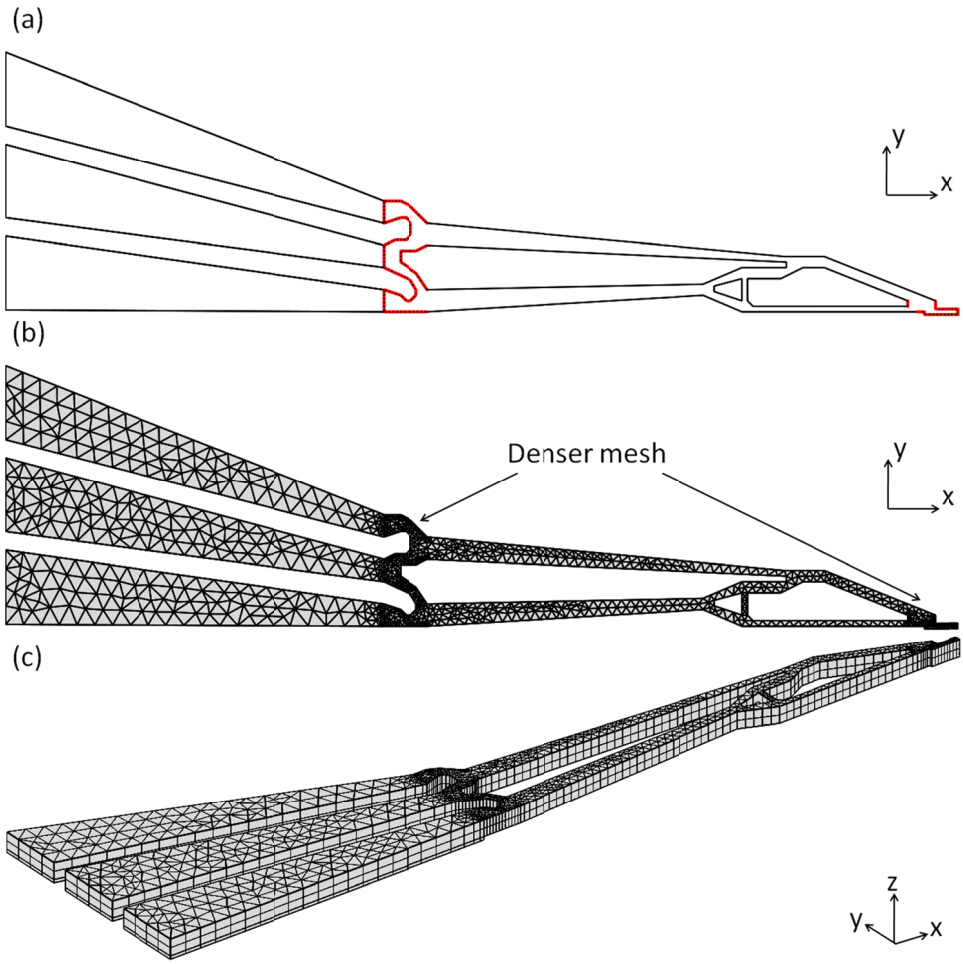

Figure 3.4 The meshing procedure for the ideal case: (a) Fine meshing of the critical edges, (b) meshing the top surfaces of the actuator and (c) sweeping the mesh throughout the structure.

3.2.2 Results

Temperature distribution plots, for both closing and opening modes of the smoothed version of Design B at 1 μm end-effector displacement, are given in Figure 3.5. For the closing case, the end-effector and the maximum temperature values are 265 °C and 495 °C, respectively. For the opening case, these values are 371 °C and 565 °C, respectively. Temperature values at the very end of the three leads are in the range 30-55 °C for both two cases.

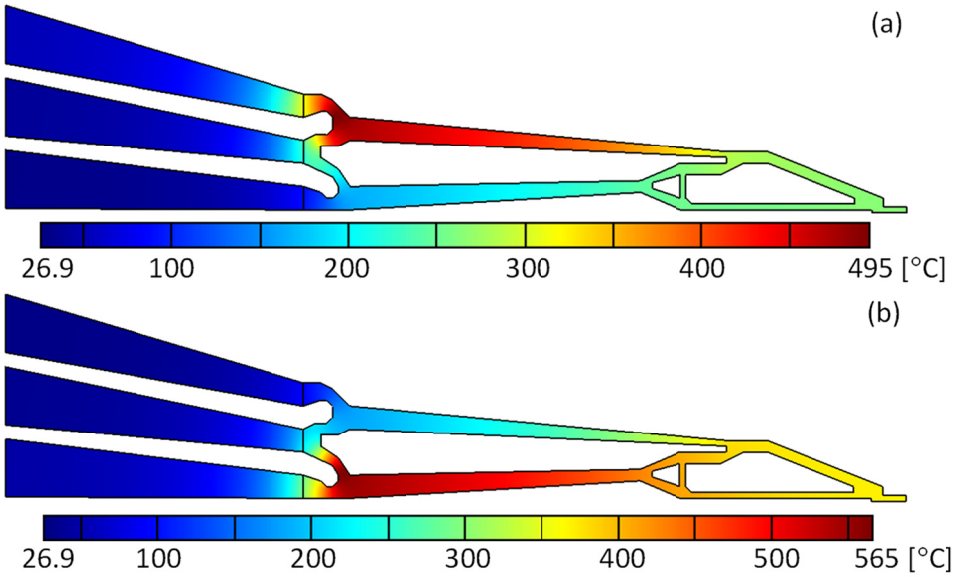

Figure 3.5 Simulation results for the ideal case, showing the temperature distribution within the topology optimized actuator at 1 µm displacement in (a) closing and (b) opening modes.

In order to investigate the effect of design variations, blocking force vs. free displacement curves for Design B at different design stages are plotted in Figure 3.6 and Figure 3.7. Here, the dashed lines represent the analyses performed using the topology optimization software, where the solid lines represent those performed using COMSOL. Furthermore, black curves represent the initial, grey-scale output of the topology optimization program, blue curves represent the original design after black & white conversion, the red curve represent the design with the smoothed beam and the green curve represent the tilted design.

In Figure 3.6 the color bar represents the maximum temperature within the actuators, where in Figure 3.7, it represents the end-effector temperature. The end-effector temperature comparison is not available for the analyses performed using the topology optimization software.

Results of the mechanical simulations performed using COMSOL (for finding the stiffness and the gripping force applied to a 300 nm-diameter nanotube/wire at a maximum temperature of 550 °C) are tabulated in Table 3.1 for Design B at different design phases. Here, the results for a three-beam actuator with 2 µm × 200 µm beams are also included for comparison.

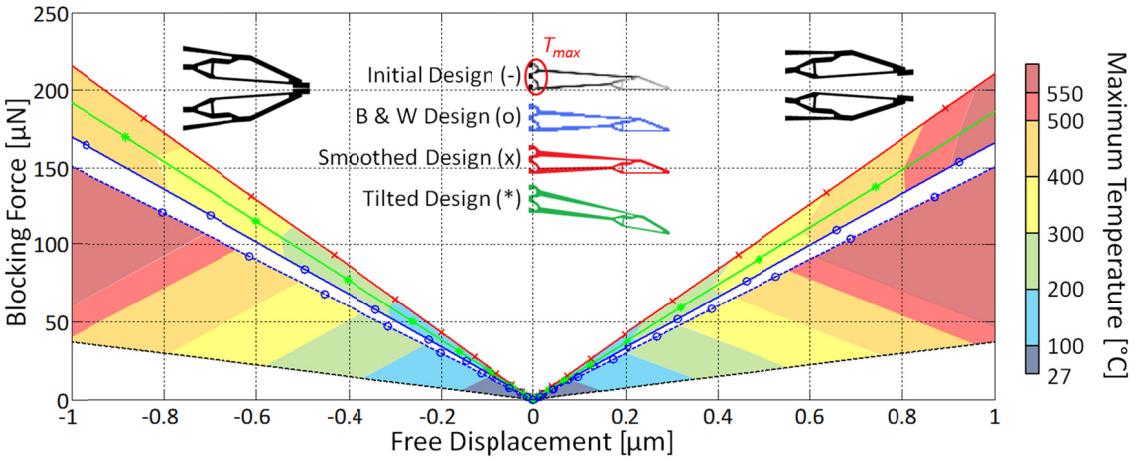

Figure 3.6 Finite element analysis showing the effect of design variations for Design B, with the color bar showing the maximum temperature: *Dashed lines.* Using the topology optimization software for the initial, grey-scale design (black) and the original, black & white design (blue). *Solid lines.* Ideal case analyses using COMSOL for the original, black & white design (blue), smoothed design (red) and tilted design (green).

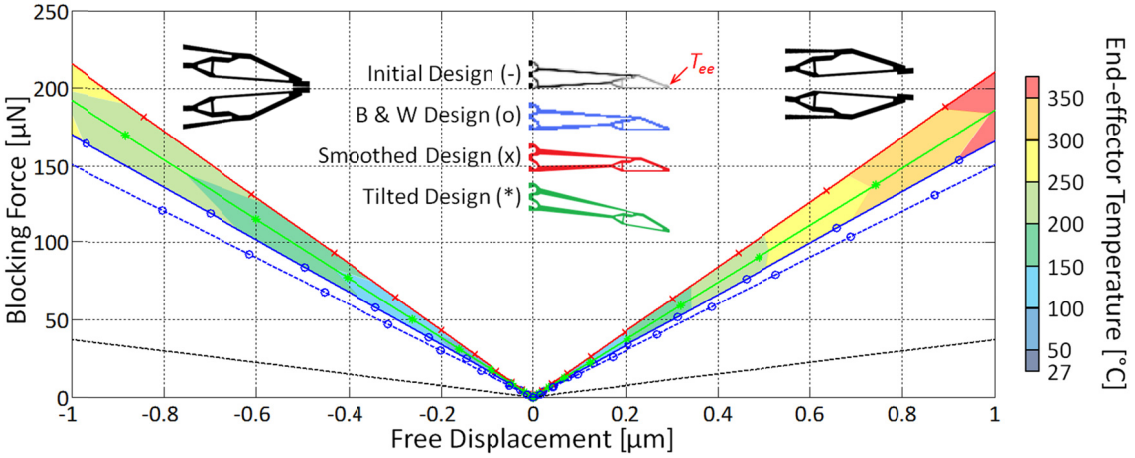

Figure 3.7 Finite element analysis showing the effect of design variations for Design B, with the color bar showing the end-effector temperature: *Dashed lines.* Using the topology optimization software for the initial, grey-scale design (black) and the original, black & white design (blue). *Solid lines.* Ideal case analyses using COMSOL for the original, black & white design (blue), smoothed design (red) and tilted design (green).

Table 3.1 Results for the mechanical simulations performed for determining the stiffness and the maximum gripping force applied to a 300 nm nanotube/wire at T_{max} = 550 °C for Design B at different design phases. Note that, the best (green) and the worst (red) performances at each column are highlighted.

	Stiffness [N/m]	Gripping Force, F_{grip} [µN] $T_{max} = 550\ °C$	End-effector Temperature, T_{ee} [°C]	
			@ contact, $(F_{grip} = 0)$	$T_{max} = 550\ °C$
Original, B & W Design	177	38.5	244	270
Smoothed Design	234	33.3	261	281
Tilted Design	219	55.3	226	255
Three-Beam Actuator (2 µmx200 µm)	2.2	10.2	294	387

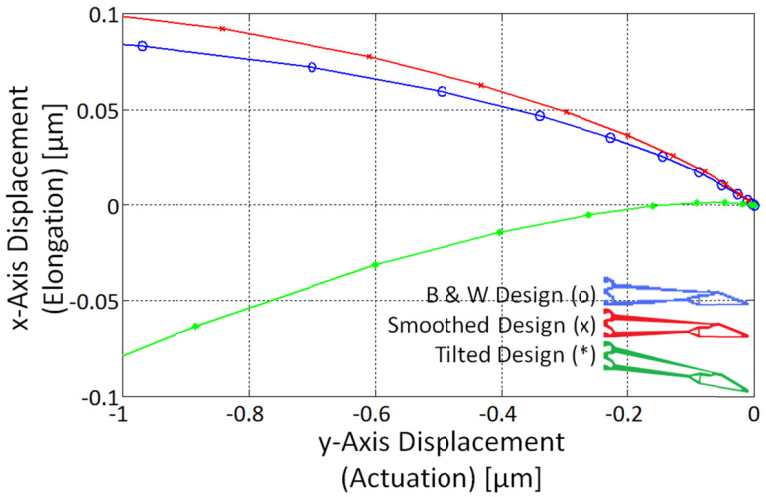

Figure 3.8 Elongation vs. actuation curves for different versions of Design B.

Elongation (x-axis displacement) vs. actuation (y-axis displacement) curves for different design variations are plotted in Figure 3.8. The out-of-plane displacement of the actuators is on the order of 100 nm to 200 nm, which is negligible.

Line-width of the actuators may vary during various steps of the microfabrication process, such as etching, photoresist exposure or development. In order to investigate this effect, the dimensions of the topology optimized actuator with the smoothed beams was uniformly increased and decreased with 500 nm steps and finite element analyses were performed on these variations. Blocking force vs. free displacement curves for smoothed Design B with various line-widths are plotted in Figure 3.9 & Figure 3.10.

In Figure 3.9, the color map represents the maximum temperature within the actuator, where in Figure 3.10, it represents the end-effector temperature. Only small variations were considered in these curves. If the variations are excessive, e.g. if the gaps are filled with material or if they are disconnected, the actuators will fail instantaneously and both the blocking force and the free displacement values will become zero.

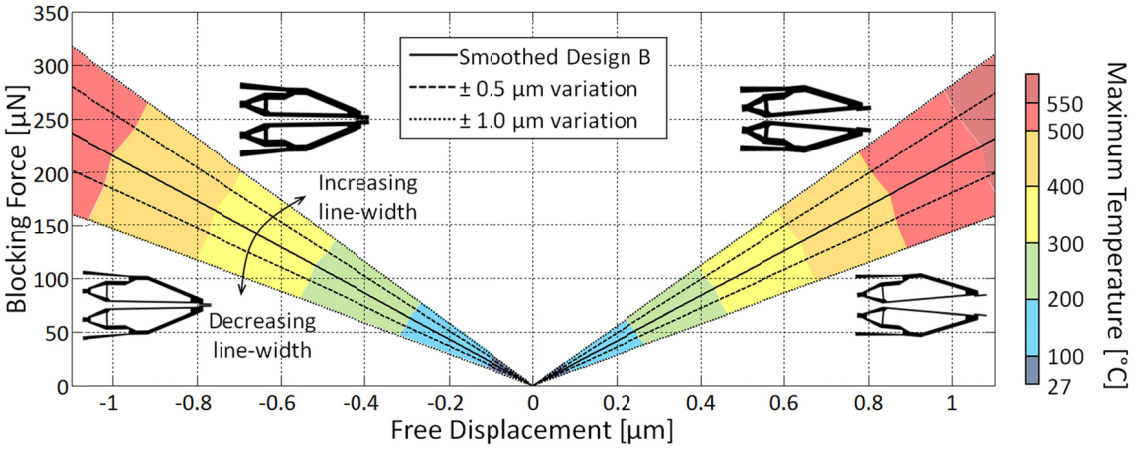

Figure 3.9 Finite element analysis using COMSOL, showing the effect of fabrication variations for Design B, with the color bar showing the maximum temperature: Ideal case analyses for the original, black & white design (blue), smoothed design (red) and tilted design (green).

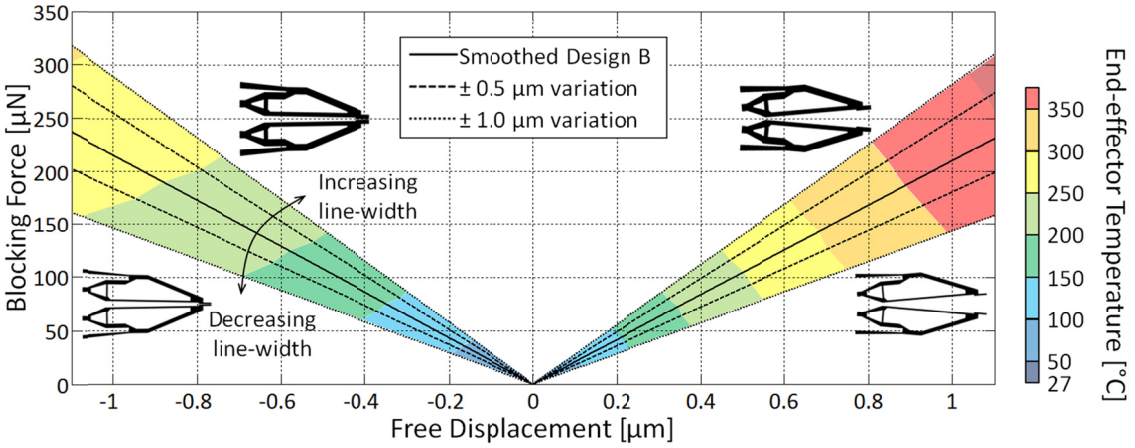

Figure 3.10 Finite element analysis using COMSOL, showing the effect of fabrication variations for Design B, with the color bar showing the end-effector temperature: Ideal case analyses for the original, black & white design (blue), smoothed design (red) and tilted design (green).

Table 3.2 Results for the mechanical simulations performed for determining the stiffness and the maximum gripping force applied to a 300 nm nanotube/wire at T_{max} = 550 °C for Design B with variable line-width.

	Stiffness [N/m]	Gripping Force, F_{grip} [μN] $T_{max} = 550$ ℃	End-effector Temperature, T_{ee} [°C]	
			@ contact ($F_{grip} = 0$)	$T_{max} = 550$ ℃
-1 μm variation	153	36.5	232	260
-0.5 μm variation	194	36.8	249	273
Smoothed Design	234	33.2	261	281
+0.5 μm variation	277	23.9	277	290
+1 μm variation	320	13.4	289	296

Results of the mechanical simulations performed are tabulated in Table 3.2 for Design B with variable line-width. Note that, gripping force value for the actuator with +1 μm variation is not available since the end-effector is not yet in contact with the nanotube/wire at a maximum temperature of 550 °C.

Similar plots and tables for all designs are given in APPENDIX D.

In order to compare the performance of different actuators, robustness of an actuator for a performance parameter, e.g. actuation or force, is defined as:

$$\mathcal{R}_X = \frac{X_o}{\left(\frac{dX}{dw}\right)} \tag{3.2}$$

In the above expression, $\mathcal{R}_X$ is the robustness of the actuator for a performance parameter X, X_o is the value of the performance parameter at a specific operating point and (dX/dw) is the variation of the performance parameter with the variation in the line-width. Note that, (dX/dw) can be determined from the slope of the X_o vs. w, plot, where w is the line-width.

All designs presented in CHAPTER 2 are compared for their robustness for force and actuation in Figure 3.11.

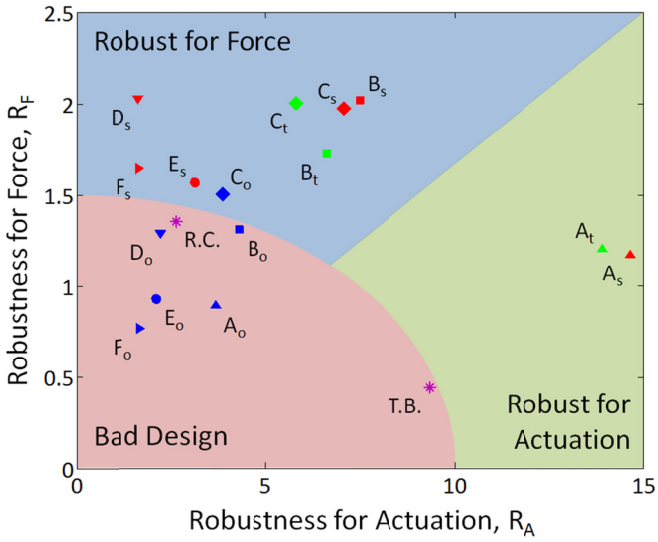

Figure 3.11 Robustness plot showing all designs (A, B, C, D, E and F), their variations (o: Original design, s: Smoothed design and t: Tilted design".) and the conventional three-beam (T.B.) and rib-cage (R.C.) designs. Note that, the convention for the subscripts is as follows: "o = Original", "s = Smoothed" and "t = Tilted".

3.3 The Non-Ideal Case

3.3.1 The Model

Finite element simulations for the non-ideal case were also performed using a similar 3D model as the ideal case. However, a large prism with a trapezoidal base was added to the initial geometry in order to model the carrier chip. Geometry, boundary, subdomain, mesh and solver settings for this case will be explained in detail in the following sections.

3.3.1.1 Geometry Settings

The 3D model of a topology-optimized actuator was extended to include a trapezoidal prism. This geometry was created by drawing a trapezoid, where top and bottom sides are equal to 100 µm and 217.5 µm, respectively. This shape was, then, extruded -100 µm along the z-axis with a -1 µm displacement (Figure 3.12). Since the prism represents only a fraction of the carrier chip, its dimensions are not equal to the actual dimensions of the carrier chip and the selected values are sufficient for the modeling purpose.

3.3.1.2 Subdomain Settings

Subdomain settings for the non-ideal case for the actuators, leads and the insulating layer underneath were the same as the ideal case.

Material for the carrier chip was selected as “Si(c)” from the materials library of COMSOL MEMS Module. However, the temperature dependency of the material properties of silicon was not considered since the temperature of the carrier chip does not rise as much as the electrothermal actuator. The silicon properties used in the simulations are also tabulated in APPENDIX C.

Remaining settings of the three application modes were the same as the ideal case.

3.3.1.3 Boundary Settings

Boundary settings for the electro-thermo-mechanical simulation of the non-ideal case were mainly the same as the ideal case for the actuator and the leads, except the boundary conditions at the bottom of the insulating SiO_2 layers (Figure 3.2 (b)): Since these boundaries are in contact with the carrier chip they were set as “Interior Boundaries” by default and the boundary conditions for all three application modes were considered to be continuum.

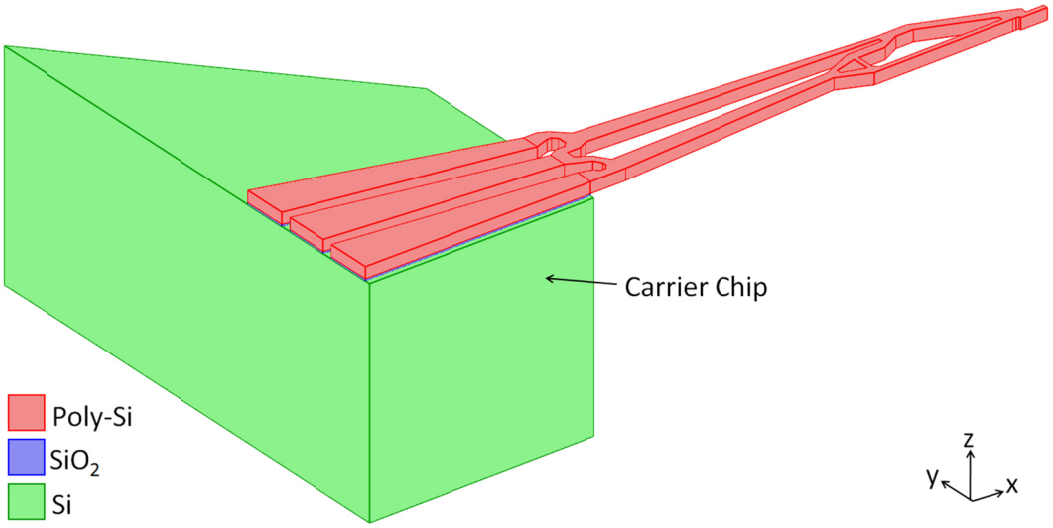

Figure 3.12 The non-ideal case 3D COMSOL model for Design B.

The boundary conditions for the carrier chip were set as follows:

In the *Conductive Media DC* application mode, all boundaries of the carrier chip were defined as "Electric Insulation".

In the *Heat Transfer by Conduction* application mode the inner boundaries of the carrier chip were defined as "Thermal Insulation" (Figure 3.13 (a)). A heat flux was applied to the bottom boundary of the carrier chip. This heat flux can be considered as the combination of (1) the convection heat transfer between the air and the printed circuit board (PCB), on which the chip is glued and the conduction heat transfers between (2) the print and the glue, (3) the glue and the carrier chip and (4) through the excluded portion of the chip itself (Figure 3.13 (b)). This heat flux is represented as:

$$q = c \cdot h_{air}(T_0 - T) \tag{3.3}$$

In the above expression, c is a constant, which can be determined using the results of the Raman temperature measurements (see Section 6.4). Finally, the heat transfer through the air is defined on the remaining boundaries of the carrier chip, i.e. those in contact with air, similar to the ideal case as defined in (3.1).

In the *Solid, Stress-Strain* application mode, the inner boundaries and the bottom boundary of the carrier chip were defined as "Fixed" (Figure 3.13), where the remaining boundaries were defined as "Free".

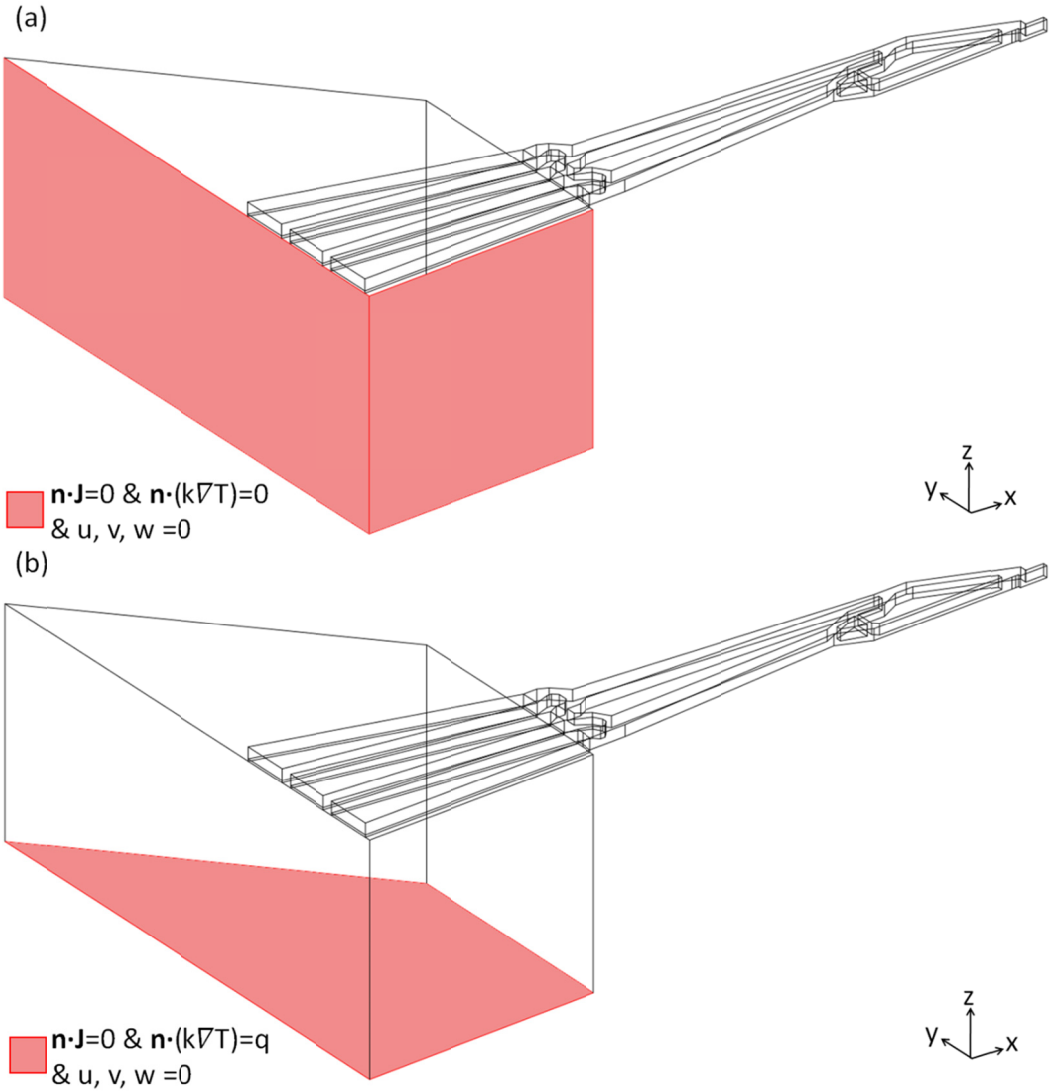

Figure 3.13 Boundary conditions representing the closing mode for the non-ideal case: (a) For the inner boundaries and (b) for the bottom boundary.

3.3.1.4 Mesh Settings

The actuators, the leads and the SiO_2 layers were meshed according to the same procedure as described in Section 3.2.1.4 (Figure 3.14). The carrier chip was meshed as follows:

In the *Free Mesh Parameters* menu, the upper boundaries of the carrier chip were meshed with a maximum element size of 25 µm. However, the created mesh was not swept through the structure along z-direction since it results in an excessive number of mesh elements. Instead, the carrier chip geometry was selected in the subdomain mode and meshed with tetrahedral elements, where the maximum element size was 25 µm.

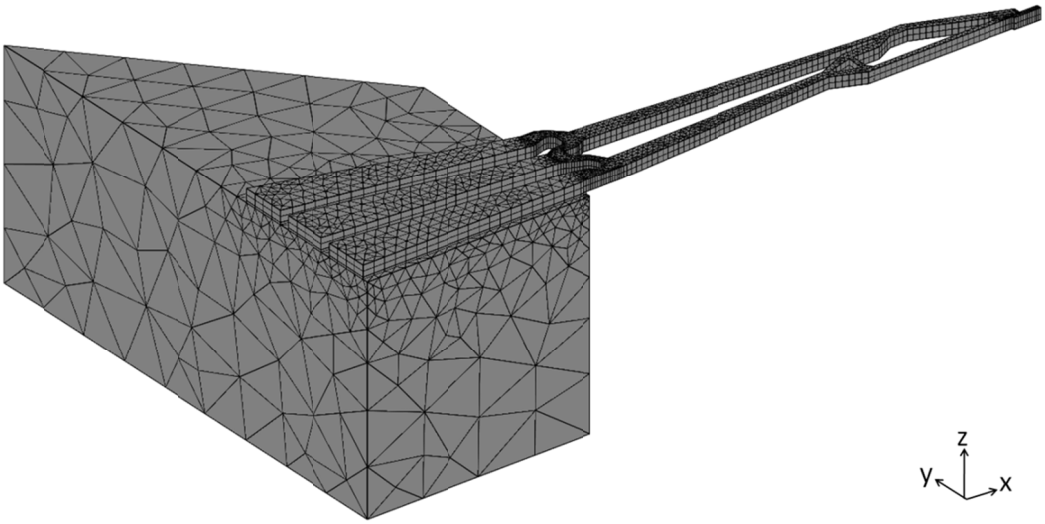

Figure 3.14 The mesh for the non-ideal case.

3.3.1.5 Solver Settings

The solver settings for the non-ideal case were exactly the same as the ideal case, which were described in Section 3.2.1.5.

3.3.2 Results

Temperature distribution plots, for both closing and opening modes of the smoothed version of Design B at 1 µm end-effector displacement, are given in Figure 3.15. For the closing case, the end-effector and the maximum temperature values are 331 °C and 626 °C, respectively. For the opening case, these values are 483 °C and 822 °C, respectively. Temperature values at the very end of the leads vary in the range from 186 °C to 216 °C for the two cases.

The mechanical simulation results for the non-ideal case are the same as those for the ideal case. However, there is a considerable difference between the thermal results of the non-ideal case and the ideal case due to the added effect of the carrier chip. This difference is in the range from 150 °C to 250 °C.

It is more rational to compare different actuators according to the results of the ideal case simulations since, the effects of the lead design and carrier chip dimensions on the performance of the actuators are minimized. For this reason, the results of the non-ideal case simulations will not be presented in detail as the ideal case simulations. However, a profound comparison of the non-ideal case simulations with the temperature measurement experiments will be presented in Section 6.4.

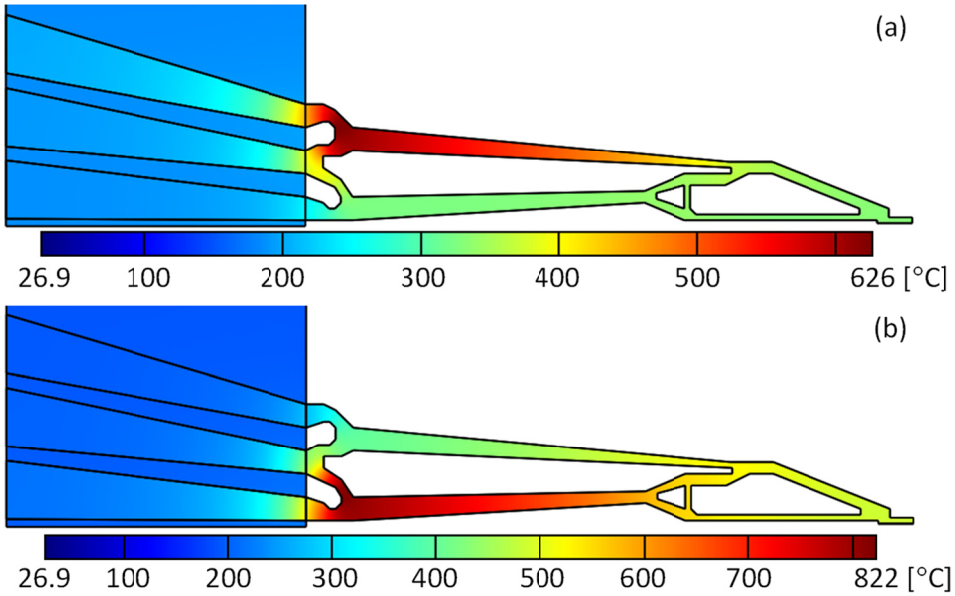

Figure 3.15 Simulation results for the ideal case, showing the temperature distribution within the topology optimized actuator at 1 µm displacement in (a) closing and (b) opening modes.

3.4 Discussion

Finite element simulations of the topology optimized microgrippers were performed using the MEMS Module of the COMSOL Multiphysics software. Two different cases were investigated: *The ideal case* ignoring the chip heating, and *the non-ideal case* considering the chip heating.

Mechanical simulations reveal that the topology optimized actuators are ~2 orders of magnitude stiffer than the conventional three-beam design. Furthermore, the gripping force applied by the topology optimized microgrippers at a presumptive operation temperature is 3 to 5 times larger than what is available by a three-beam microgripper. Also, the end-effector temperature of the topology optimized design is much smaller than that of the conventional design at the same operation temperature.

The mechanical results of the non-ideal case and the ideal case are the same. However, the thermal results of the non-ideal case are 150 °C to 250 °C higher than those of the ideal case due to the heating of the carrier chip. However, the main behavior of the actuators is the same for both cases in that; they reach the same amount of displacement at a higher temperature in the opening mode than in the closing mode.

The effect of design variations were investigated using the ideal case simulations (Figure 3.6 & Figure 3.7). According to the results, the performance of the original, black & white design is considerably different from that of the grey-scale output of the topology optimization algorithm. A reason for this is that, some grey pixels with intermediate densities become either black or white, resulting in a change in the stiffness of the structure. Furthermore, it was not possible to consider the temperature dependence of the poly-Si properties in the topology optimization analyses. However, material properties of poly-Si, such as the thermal conductivity, were defined as functions of temperature when doing the COMSOL simulations. Finally, different than the topology optimization analyses, the first 100 µm-length of the leads were also included in the COMSOL simulations, together with the insulating SiO_2 layers underneath them.

Smoothing the original design results in a further increase in the stiffness of the actuators since the effective width of a smoothed beam is larger than that of a pixelated beam. Tilting the actuator results in a decrease in the stiffness compared to the smoothed design. However, the gripping force available at the same operation temperature is higher for the tilted design than the smoothed design. The adverse effect of tilting is that, in the opening mode, the tilted design heats up more than the smoothed design for the same amount of actuation. This is since; tilting the actuator towards the closing direction results in a decrease in the y-component of the actuation in the opening mode and an increase in the x-component.

Smoothing the design results in more elongation, i.e. x-axis displacement of the end-effector, compared to the original design (Figure 3.8). On the contrary, tilting the smoothed design results in less elongation, and even displacement of the end-effector in the -x-direction, which enhances pulling.

The effect of fabrication variations were also investigated using the ideal case simulations (Figure 3.9 & Figure 3.10, Table 3.2). Obviously, the actuators become stiffer as the line-width increases. According to the results, ±1 μm variation in the line-width may result in ±7 % variation in the actuation and ±30 % variation in the actuator force at the same operation temperature. However, these values are specific for Design B and they may be different for different designs. In order to compare different designs, a figure of merit, "robustness" is defined according to (3.2). As can be deduced from Figure 3.11, robustness of a design increases with smoothing (compared to the original design), where it decreases with tilting (compared to the smoothed design). Design B is robust for both force and actuation, where Design A is more robust for actuation but less for force. In other words, the actuation of Design A varies less due to a line-width variation, where the actuator force available varies more. Oppositely, Design D is more robust for force but less for actuation.

As compared to the conventional electrothermal actuators, the three-beam and the rib-cage, smoothed and tilted versions of all topology optimized actuators show superior performance.

CHAPTER 4
Fabrication

4.1 Introduction

The designed topology optimized microgrippers were fabricated at Danchip's National Cleanroom Facilities. However, due to non-availability of the related equipment at the time necessary, low-stress Si-rich silicon nitride (Si_3N_4) deposition and bonding steps were performed in the Nanofabrication Laboratory at the Department of Microtechnology and Nanoscience at the Chalmers University of Technology in Sweden and Delta A/S, respectively.

In this chapter, the conventional fabrication process for the microgrippers and the procedure for preparing the interface will be explained in detail, initially. Then, modification of the microgrippers using focused ion beam (FIB) milling will be described and a method for fabricating "nanogrippers" using FIB will be proposed. Each section will be followed by presentation of the related results.

Note that, the details of the fabrication process can be found in APPENDIX E.

4.2 The Conventional Process

The process sequence used for the fabrication of the topology optimized microgrippers is mainly the same as the one presented in [98]. However, some steps were modified according to the design specific requirements.

In this section, the process sequence used for fabricating the topology optimized microgrippers will be explained in detail and the results from different batches will be presented.

4.2.1 The Process Sequence

The topology optimized electrothermal microgrippers can either be fabricated from single crystal silicon (SCS) or from polysilicon (poly-Si). If SCS is selected as the device material, silicon on insulator (SOI) wafers with a 5 µm device layer and a 1 µm insulating silicon dioxide (SiO_2) layer should be ordered from a supplier. If poly-Si is selected as the device material, the poly-Si on insulator (poly-SOI) wafers with the same specifications should be produced prior to the actual fabrication procedure.

In this thesis, poly-Si was selected as the device material (see Section 2.3) and the required poly-SOI wafers were produced as follows:

Initially, a 650 nm-thick SiO_2 layer was thermally grown on standard, 4-inch (100) Si wafers (Figure 4.1 (a)). This step was followed by deposition of a 5 µm-thick highly boron-doped polysilicon layer by low-pressure chemical vapor deposition (LPCVD) (Figure 4.1 (b)). The wafers were then annealed at 1000 °C for 1 h in order to reduce the internal stress in the deposited films.

Note that, both front- and back-sides of the wafers are coated during the thermal oxidation and LPCVD processes. Hence, before further processing, the poly-Si and SiO_2 layers at the back-side should be removed by a reactive-ion-etch (RIE) using a pure SF_6 plasma and a wet etch in buffered hydrofluoric acid (bHF), respectively (Figure 4.1 (c)).

The fabrication process starts with the definition of the poly-Si structures, i.e. actuators, leads and bonding pads. For this purpose, the front-side of the wafer should be patterned with the "Device Mask" through UV lithography. For this purpose, a 1.5 µm-thick AZ5214E PR layer was spun on the wafer (Figure 4.2 (a)) and a negative UV lithography process was performed with the following intermediate steps: First UV exposure for 3.3 s using the "Device Mask" (Figure 4.2 (b)), reversal bake at 120 °C for 120 s, flood UV exposure for 35 s and development for 65 s (Figure 4.2 (c)).

Note that, the alignment of the "Device Mask" parallel to the major flat of the (100) Si wafer is of critical importance. This is since the "Back-side Mask", which is aligned with respect to the "Device Mask", was designed considering the orientation of the crystallographic planes in the Si wafer and bad alignment results in deviation of the chip dimensions from the desired values.

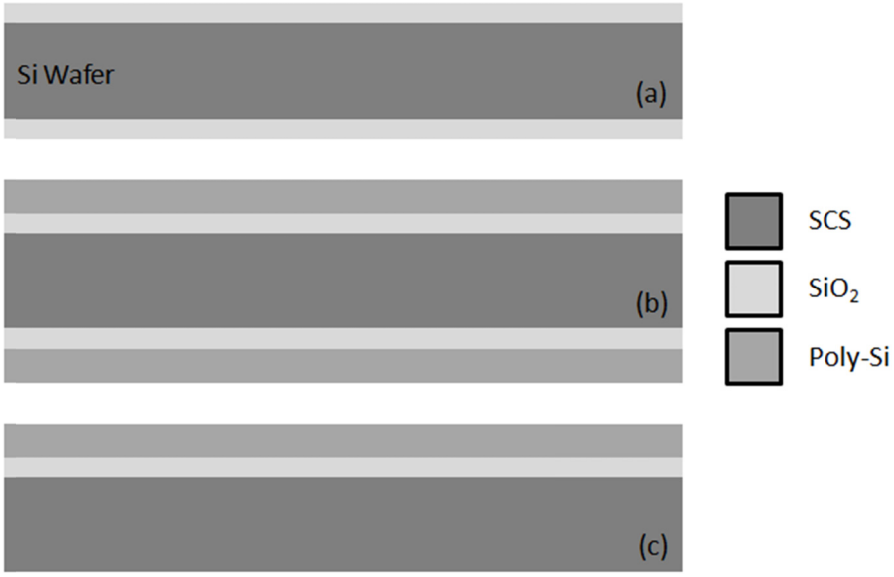

Figure 4.1 Production of poly-SOI wafers.

After masking the front side, the poly-Si device layer was etched anisotropically until the buried SiO_2 layer is reached using plasma-based silicon etch (Figure 4.2 (d)). This etch can be either a reactive ion etch (RIE), as presented in [98], or an advanced silicon etch (ASE) (see Section 4.2.2). Finally, the remaining PR is removed in oxygen plasma (Figure 4.2 (e)).

Next step of the fabrication process is the release of the individual chips using silicon nitride (Si_3N_4) as the etch mask. For this purpose, the wafer was coated with 350 nm-thick, low-stress, Si-rich Si_3N_4 on both sides by LPCVD (Figure 4.3 (a)). The wafer was cleaned with an RCA cleaning procedure prior to this process.

Then, the Si_3N_4 layer at the back was patterned with the "Back-side Mask" through UV lithography. This was done by spinning a 2.2 µm-thick PR layer on the back-side of the wafer and performing a positive UV lithography process with the following parameters: UV exposure for 9 s using the "Back-side Mask" and development for 70 s (Figure 4.3 (b)).

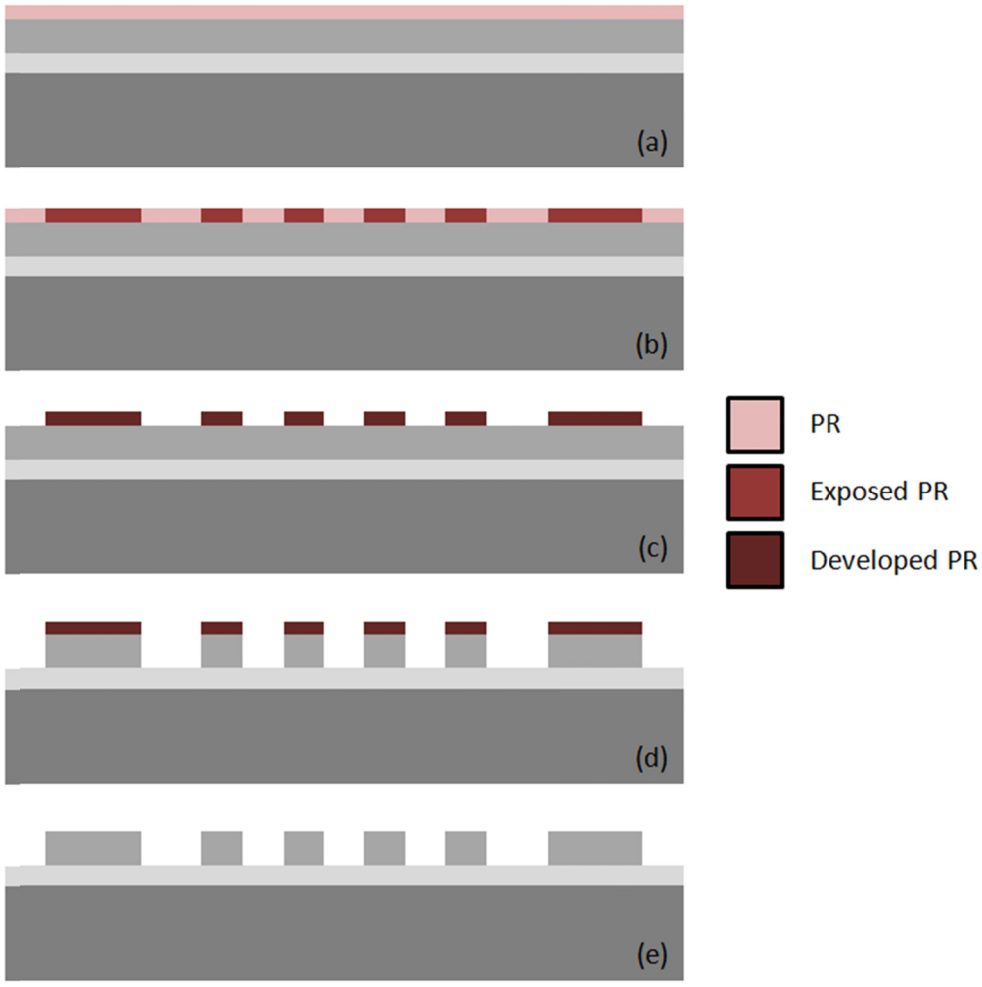

Figure 4.2 Front side lithography and etching of the high-aspect-ratio poly-Si structures.

In order not to damage the Si_3N_4 layer and the etched structures on the front, the use of special vacuumless chucks is of crucial importance during both the spinning of the PR and the UV exposure steps. Any damage on the Si_3N_4 layer on the front-side, such as nano-metric pinholes, may result in loss of devices during the potassium hydroxide (KOH) etch step (see below), and hence, decrease of the fabrication yield to less than 20 %.

The masked Si_3N_4 layer at the back-side was, then, etched using RIE (Figure 4.3 (c)). Following the removal of the remaining PR in an oxygen plasma, individual carrier chips were released by wet etching of the Si wafer all through its thickness in a KOH solution at 80 °C ((Figure 4.3 (d)). Finally, the Si_3N_4 layers on both sides of the wafer were removed by wet etching in a phosphoric acid (H_3PO_4) solution at 180 °C (Figure 4.3 (e)).

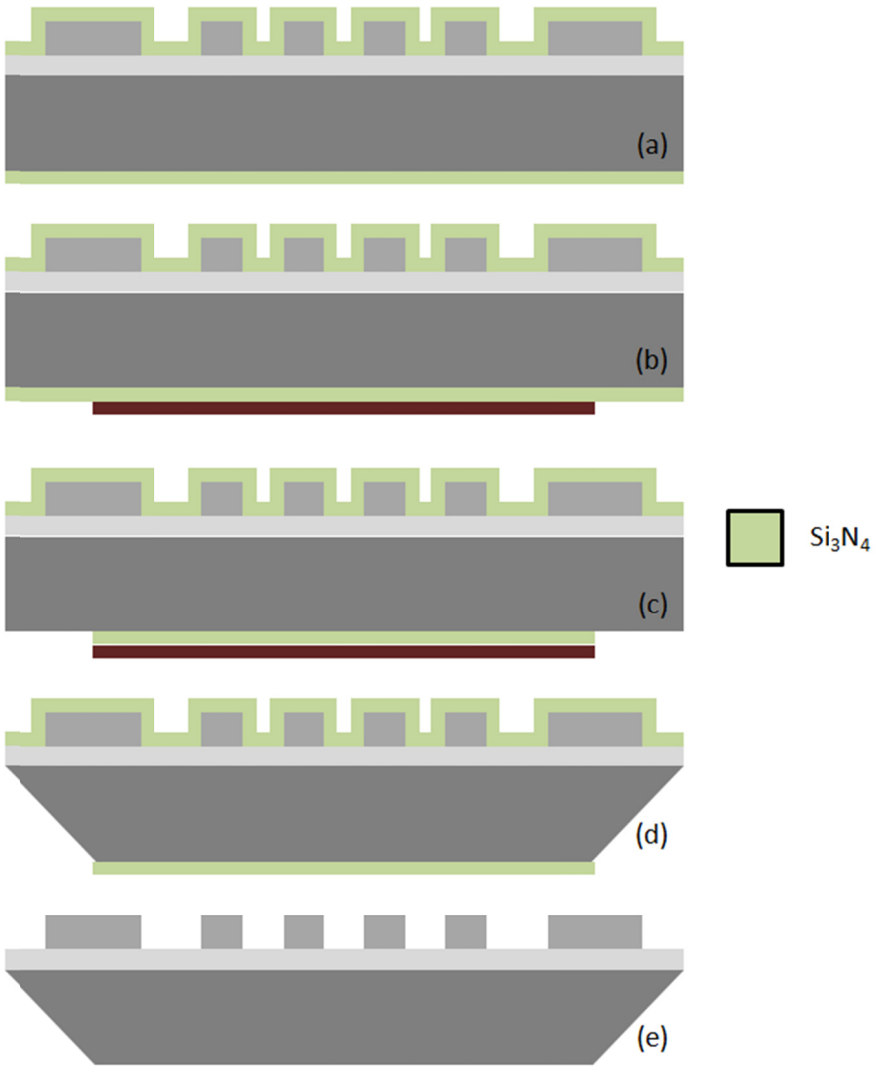

Figure 4.3 Releasing of the individual chips.

Following the release of the individual chips, the actuators, i.e. microgrippers, were released by under-etching the SiO_2 layer underneath in bHF (Figure 4.4 (a)). As the last step, a thin layer of metal (10/190 nm Ti/Pt) was evaporated on the bonding pads in order to enable wire bonding (Figure 4.4 (b)). The actuators are protected with a mechanical shadow mask to prevent unwanted metal deposition. Any short-circuit between the bonding pads were eliminated due to the undercut of the SiO_2 layer resulting from the isotropic bHF etching [98].

The shadow masking procedure is explained in detail in Section 5.2.

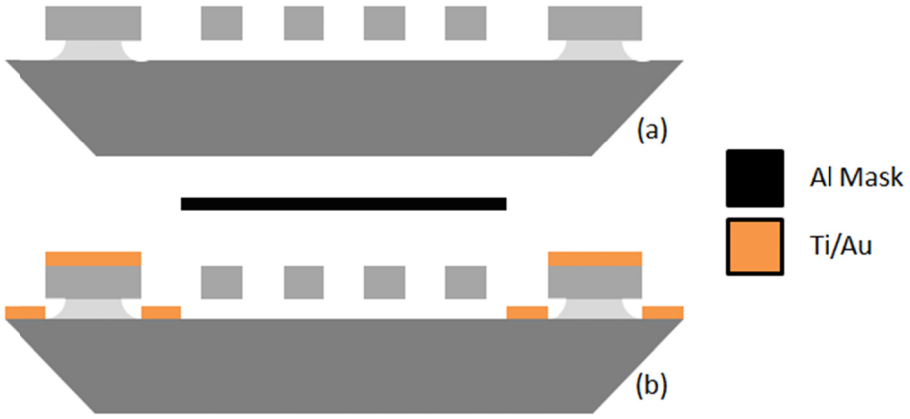

Figure 4.4 Releasing of the actuators and metal deposition.

4.2.2 Results

The first prototypes of the topology optimized microgrippers , i.e. Mask 15 (see Section 2.9), were fabricated using RIE as presented in [98], using RIE for etching the poly-Si device layer. This recipe was mainly optimized for three-beam microgrippers, which have a rather homogeneous geometry. However, the aspect-ratio dependent etching (ARDE) effect becomes more dominant for the topology optimized designs, which have a more complex geometry, including both small and large features close to each other. Due to the ARDE effect, smaller structures are etched slower than the larger structures. Hence, the resulting etch was rather non-uniform throughout the wafer and the small beams did not survive until the buried SiO_2 layer was reached (Figure 4.5).

Fabrication yield of the 1st fabrication batch was ~30 %. The main reason for this was the low quality of the Si_3N_4 layer and pinholes forming in this layer due to improper handling of the wafers during backside lithography. Hence, most of the chips were lost during release. This can be eliminated by using special, vacuumless holders during both resist spin and exposure steps.

Another reason for the low fabrication yield was the slight misalignment of the backside mask. Hence, the front edge of some chips was narrower than designed and the leads of the microgrippers on these chips were overhanging.

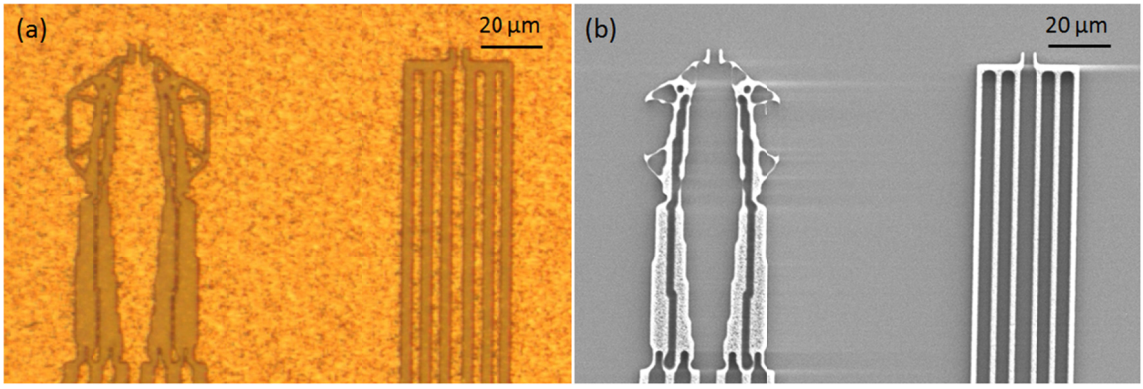

Figure 4.5 Comparison of topology optimized (left) and three-beam (right) microgrippers: (a) Optical image of the patterned PR layer on the poly-Si device layer and (b) SEM image of the devices on SiO_2 after RIE. Note that, the designed value of the minimum line-width is 1 µm for the topology optimized design.

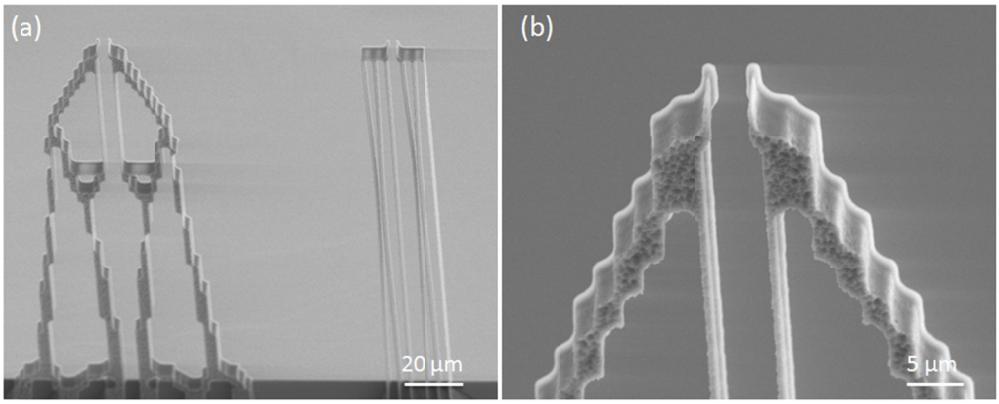

Figure 4.6 Comparison of topology optimized and three-beam microgrippers: (a) Tilted SEM image of the devices after complete release with (b) a more detailed view of the topology optimized actuator showing the non-uniformity of the side-walls. Note that, the designed value of the minimum line-width is 2 µm for the topology optimized design (Design B).

Dimensions of the resulting devices were ~1 µm smaller than those designed. Furthermore, the side-walls were non-uniform, where the beams had trapezoidal cross-section with the line-width being larger at the base (Figure 4.6).

In order to obtain a more uniform etch throughout the wafer and vertical side-walls, the RIE etch was replaced with an ASE etch. This recipe was a non-switched process, initially optimized for etching nano-scale structures. Although the vertical etch rate is rather low, it well-suitable for etching the high-aspect ratio microgrippers since the lateral etch rate is almost negligible. The resulting etch was rather uniform and all devices, either with small or large features, were successfully completed (Figure 4.7 (a)). There was almost no deviation of the dimensions from the original design and the beams had a vertical side-wall profile (Figure 4.7 (b)).

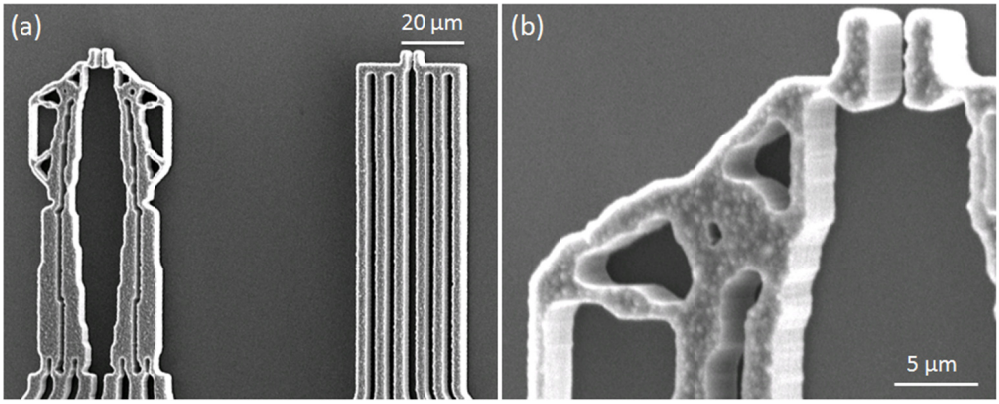

Figure 4.7 Comparison of topology optimized and three-beam microgrippers: (a) Tilted SEM image of the devices on SiO_2 after ASE with (b) a more detailed view of the topology optimized actuator showing the vertical side-walls. Note that, the designed value of the minimum line-width is 1 µm for the topology optimized design.

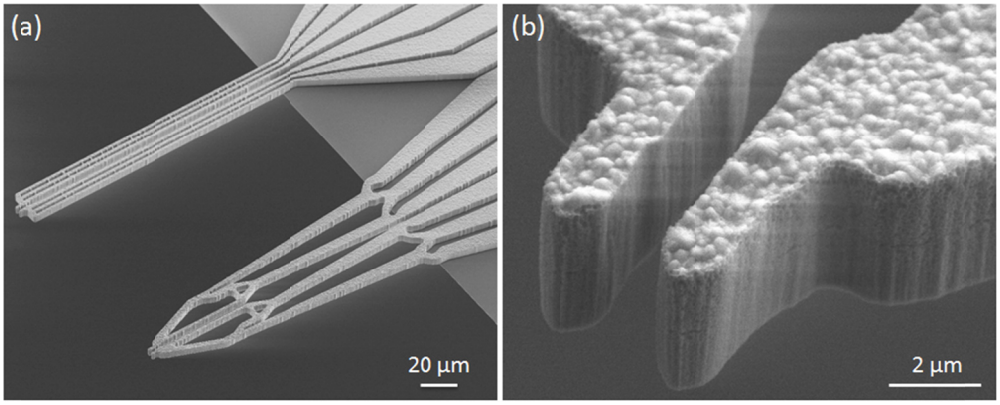

Figure 4.8 Devices fabricated during the second fabrication batch: (a) Tilted SEM image of Design B and a three-beam microgripper and (b) a more detailed view of Design B showing the vertical side-walls.

After fabrication and testing of the first prototypes, many designs were eliminated, according to feasibility of fabrication and performance, and only 6 designs were selected for further development (see Section 2.6). Two more fabrication batches were performed to fabricate these designs with the improved process, using ASE: Batch two with Mask 22 and batch three with Mask 29 (see Section 2.9).

Fabrication yields of the 2nd and the 3rd batches were ~90 % and ~99 %, respectively, where the wafers were uniformly etched and all devices have vertical side-walls (Figure 4.8 & Figure 4.9). The yield of the 2nd batch was less than that of the 3rd due to the imperfect front side lithography step, which yielded in devices with missing design features and rough or merged end-effectors (Figure 4.10). Such defects may yield to a change in the performance of the microgrippers to a great extent, preventing complete closing of the end-effectors and even hindering actuation. Defected devices can be repaired and functionalized by separating and reshaping the end-effectors using FIB (see Section 4.3.2.1).

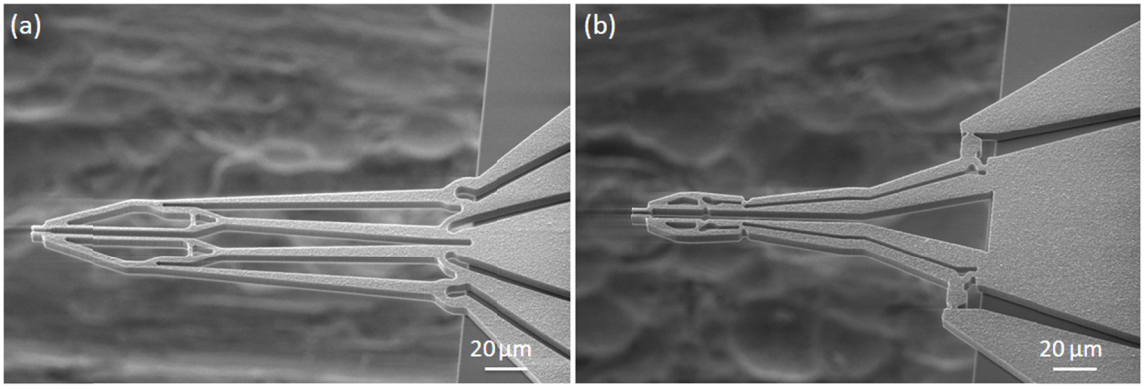

Figure 4.9 Devices fabricated during the third fabrication batch: Tilted SEM images of (a) Design B and (b) Design F.

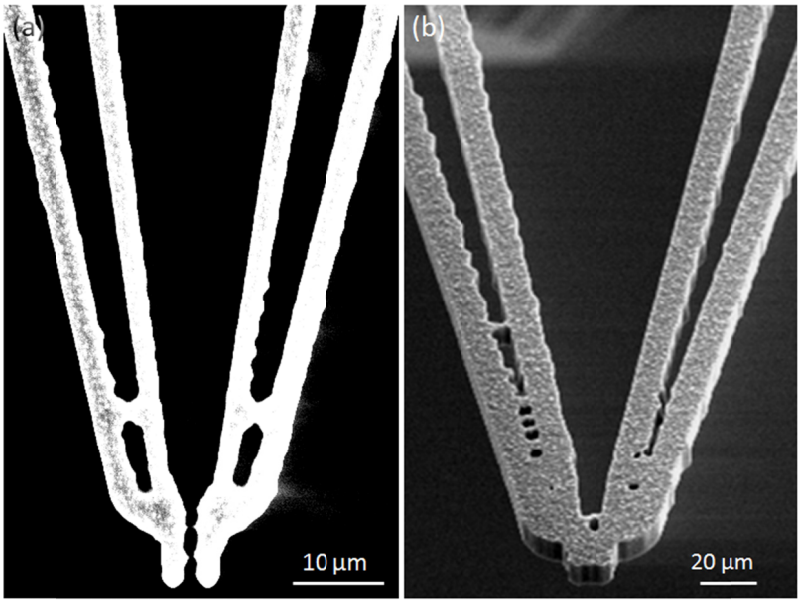

Figure 4.10 SEM images showing devices with defects: (a) Top view of the front part of Design A with rough end-effectors and (b) tilted view of the same design with merged end-effectors and missing design features.

4.3 Modification of the Microgrippers using FIB

Conversion of the designed features and dimensional accuracy during microfabrication is of vital importance for achieving the desired performance from the topology optimized actuators. However, this is rather difficult to achieve with conventional UV lithography and fabricated structures may contain many defects such as merged end-effectors, increased and/or reduced dimensions (Figure 4.10). Such defected structures can be turned into functional devices by proper modification via focused ion beam (FIB) milling [76, 77].

In this section, applications of FIB milling for microgrippers will be summarized, initially. Then, the procedure for the modification experiments will be explained and the results will be presented.

4.3.1 Applications for Microgrippers

FIB milling is a promising approach for functionalization and recovery of microgrippers. The basic application is separating the merged end-effectors, either for recovering a defected device (Table 4.1 (a) → (b)) or realizing a sub-micron gap and sharp end-effectors, which are not possible due to the limitations of the conventional fabrication processes (Table 4.1 (a) → (c)). Devices having a smaller gap distance close with less actuation, and hence, gripping is achieved at a lower temperature. Furthermore, sharper end-effectors enable easier access to nanostructures in obscured places, e.g. nanowires in trenches.

In addition to straight cuts, more complex end-effector shapes, which are rather difficult to fabricate, can also be realized using FIB. As an example, the contact area between the end-effectors and the nanostructure can be reduced by milling symmetrical teeth along the inner surfaces (Table 4.1 (a) → (d)). Smaller contact area reduces the attraction forces between the end-effectors and the nanostructure, and hence, release becomes easier (see Section 2.8).

By milling interdigitated teeth instead of symmetrical, a new microgripper concept can be realized: inverse microgrippers (Table 4.1 (a) → (e)). Such microgrippers are closed at the neutral position and open when actuated. Using inverse microgrippers, a gripped nanostructure can be indefinitely fixed between the end-effectors, transferred to another set-up, serve as an exchangeable tool-tip or stored in-between experiments.

Furthermore, XY microgrippers can be designed using topology optimization and self-locking end-effectors can be realized using FIB (Table 4.1 (f)). Here, one of the actuators is fixed and the other actuator moves along x-direction by applying the voltage to the first electrode, and along y-direction by applying the voltage to the second electrode. The sample is indefinitely clamped between the end-effectors when the voltages are released.

Table 4.1 Summary of different microgripper concepts and end-effector designs.

		Neutral Position	Gripping/Actuation	Inverse Gripping
Microfabricated	(a) Merged end-effectors		N/A	N/A
	(b) 2-µm gap distance		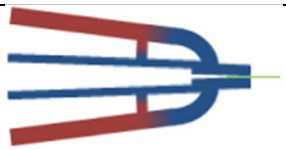	N/A
FIB-modified (from (a))	(c) Sharp end effectors/ Sub-micron gap			N/A
	(d) Sharp end effectors, sub-micron gap/ Symmetrical teeth			N/A
	(e) Sharp end effectors, sub-micron gap/ Inter-digitated teeth			
		Neutral Position	Two-step Actuation	Self-locking
	(f) Matching end-effectors/ Sub-micron gap		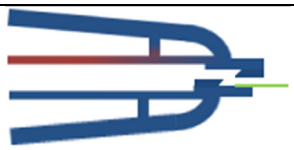 X 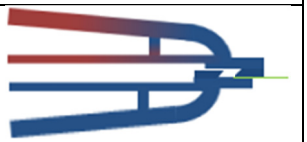 Y	

4.3.2 FIB Experiments

FIB milling experiments were performed at the Center for Electron Nanoscopy (CEN) at DTU. The Quanta 3D dual-beam SEM/FIB workstation was used for FIB milling of the microgrippers. The very first experiments were performed together with A. Nicole MacDonald.

The patterns to be milled were defined by either directly drawing geometrical shapes available in the user interface or importing in the form of different file formats. The available file types are bitmap files, where the areas to be milled are represented with blue and the remaining areas are represented with white, and stream files, which are ASCII text files addressing the coordinates to be milled, the milling order and the dwell time for each coordinate. Different milling currents should be used for different material types and geometries. Typical currents for imaging, metal deposition and high milling are 10 pA, 0.3 nA and 7 nA, respectively.

4.3.2.1 Functionalization of the End-effectors

Microgrippers with merged end-effectors were functionalized by FIB milling. Initially, the two-actuators were separated by defining a 0.3 µm × 6 µm rectangular pattern at the center of the filled area between the end-effectors (Figure 4.11 (a)). In order to decrease the contact area, three 2 µm-diameter circles were also defined at the same location. Note that, the circles were milled simultaneously as the rectangle in order to eliminate re-deposition of material in the rectangular area during milling of the circles. The current values used for milling the 5 µm-thick poly-Si microgrippers were in the range 0.5-1 nA: Higher currents were used when milling larger areas in order to reduce the milling time.

Then, the end-effectors were sharpened by defining ~35°-tilted, 2 µm × 5 µm rectangles over the bulky exterior of both end-effectors (Figure 4.11 (b)). Since these areas are relatively far away from the initially milled areas, no re-deposition occurs. Hence, the end-effectors were successfully functionalized with a sub-micron gap and matching teeth (Figure 4.11 (c)).

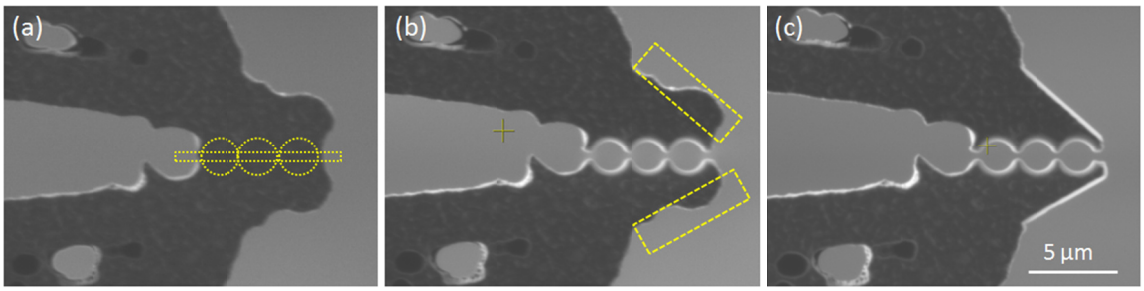

Figure 4.11 Separation, functionalization and refinement of end-effectors of a defected microgripper: (a) Merged end-effectors before FIB milling and the region to be removed for separation and functionalization. (b) Separated end-effectors after the first FIB milling and the regions to be removed for further refinement. (c) End-effectors with circular matching teeth after the second FIB milling.

Many end-effector designs, including those presented in Table 4.1 were realized by FIB milling (Figure 4.12), as well as the self-locking end-effectors of the topology optimized XY-microgrippers fabricated by Mikkel B. Olesen during his M.Sc. study (Figure 4.13). More information regarding topology optimized XY-microgrippers can be found in his report [100].

Nanomanipulation experiments performed with the microgrippers having FIB-modified end-effectors (Figure 4.12) will be presented in Section 7.5.

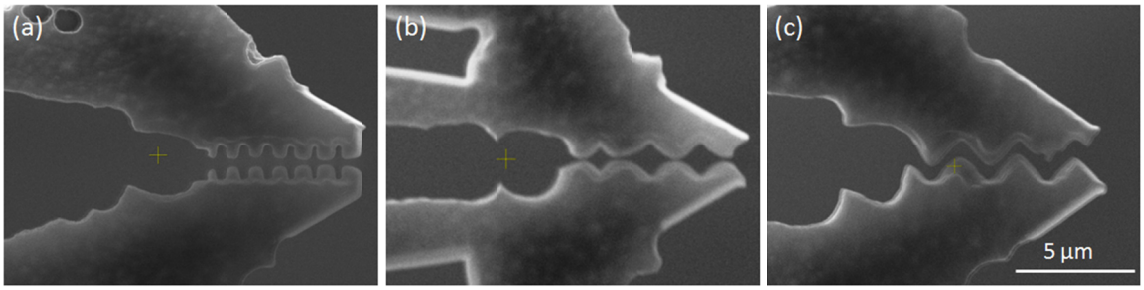

Figure 4.12 Microgrippers with FIB-modified end-effectors: (a) Rectangular matching teeth, (b) diagonal matching teeth and (c) interdigitated teeth (inverse gripping) designs.

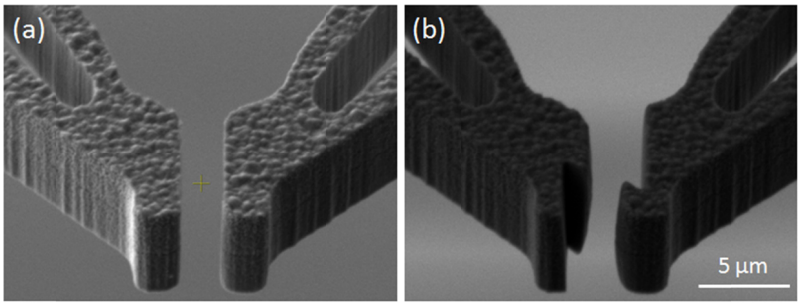

Figure 4.13 Topology optimized XY-microgrippers with FIB-modified, self-locking end-effectors: (a) Before and (b) after modification.

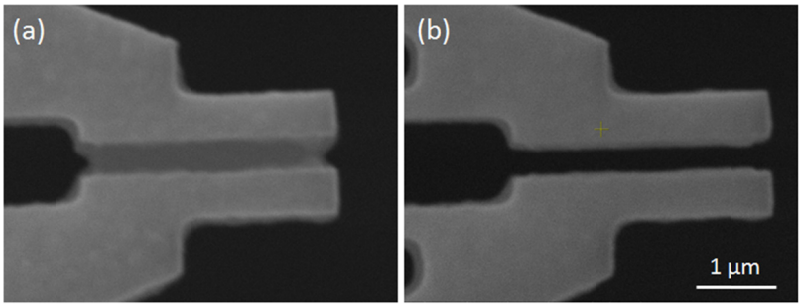

Figure 4.14 Separation of merged end-effectors of a sub-micron gripper with a 300 nm-gap: End-effectors (a) before and (b) after FIB milling.

In addition to the microgrippers, sub-micron grippers fabricated by Alberto Cagliani [101] were also modified using FIB, where merged end-effectors were separated by 300-500 nm-gaps (Figure 4.14). Nanomanipulation experiments performed with the sub-micron grippers are presented in [101]. Note that, the milling current used during these experiments was 0.5 nA.

4.3.2.2 Recovery of Design Features

In addition to the functionalization of the end-effectors, FIB milling can be used for recovering missing design features and removing structural or contamination defects.

As a first example, topology optimized Design A has a polygonal hole at the front side of the actuator (Figure 2.8 (a)). However, this feature may be missing due to microfabrication errors (Figure 4.10). This missing design hole was defined by drawing polygons at the front side of each actuator (Figure 4.15 (a)). Furthermore, another rectangle was defined in order to remove a small kink, at the inner side of the lower actuator. Then, all patterns were milled simultaneously and the defected microgrippers were corrected (Figure 4.15 (b)).

As a second example, heater beams of the XY-microgripper are connected to the anchor due to an error during the mask design (Figure 4.16 (a)). It is not possible to properly actuate such a device. However, this defect can be corrected by separating the heaters from the anchor by defining rectangles in-between (Figure 4.16 (b)) and FIB milling (Figure 4.16 (c)).

FIB can also be used for tungsten (W) and platinum (Pt) deposition. This feature can be used for recovery of broken microgrippers. As an example, 1 µm-thick W layer was deposited over the fracture area on a broken beam, both from the top and from the side (Figure 4.17). However, functionality of this device was not tested.

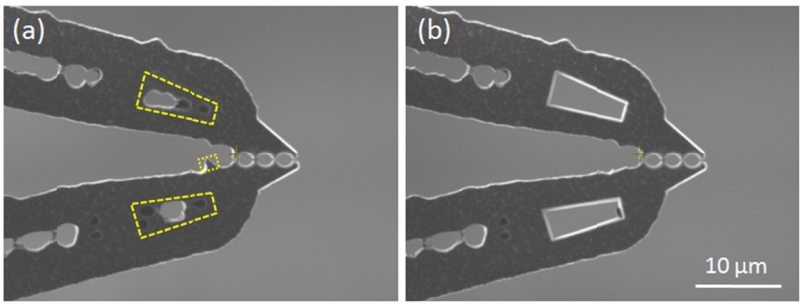

Figure 4.15 Example of recovery of design features of a defected microgripper using FIB milling: (a) Regions to be milled for recovery of design features and removal of defects. (b) The corrected microgripper after FIB milling.

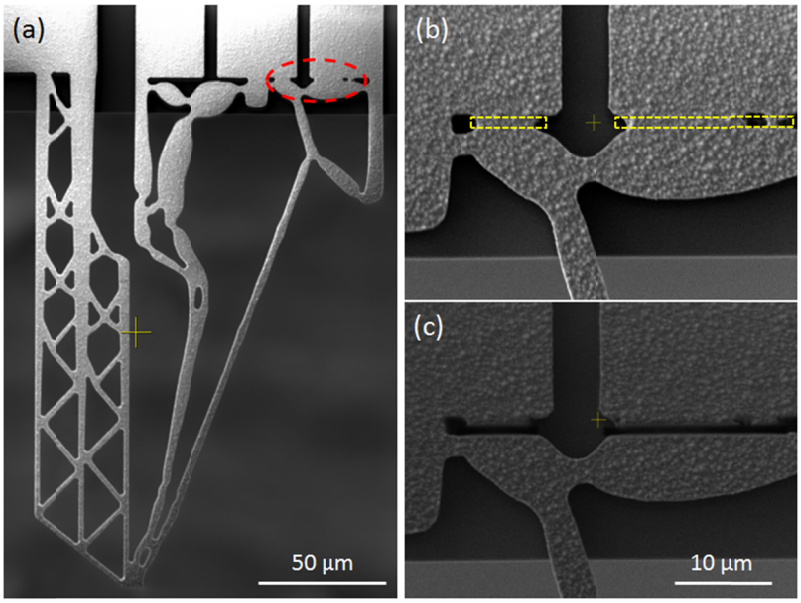

Figure 4.16 Correcting design errors using FIB milling: (a) Top view of the topology optimized XY-microgrippers, showing the merged heaters and contact leads. (b) Detailed view of the merged features and the rectangular regions to be milled. (c) The corrected heaters after FIB milling.

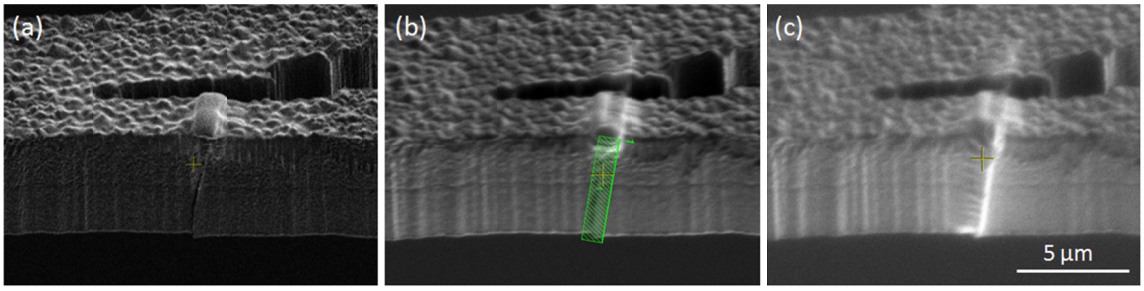

Figure 4.17 Recovery of a broken microgripper by FIB deposition: (a) Tilted side view of the broken beam with the previously deposited Pt on the top surface. (b) Area defined for Pt deposition from the side surface. (c) The beam after Pt deposition on both surfaces.

4.4 Fabrication of Nanogrippers using FIB

As well as modifying microfabricated grippers, FIB milling can also be used for top-down fabrication of a complete nanogripper from a microfabricated, rectangular cantilever template (membrane), developed by Dirch H. Petersen.

In this section, the procedure for fabricating nanogrippers using FIB milling will be introduced, initially. Then, challenges and advantages of the method will be stated. Finally, the results of the FIB experiments for fabricating nanogrippers prototypes will be presented.

4.4.1 The Procedure

Fabrication of nanogrippers using FIB requires fabrication of rectangular cantilevers with a number of leads connected to individual bonding pads (Figure 4.18). The process sequence for the rectangular cantilevers is similar to that of the poly-Si microgrippers, except that the material is single crystalline silicon (SCS) and thicknesses of the device and the oxide layers are 130 nm and 400 nm, respectively.

After the milling pattern for a nanostructure, e.g. grippers, probes or TEM membranes [102], is created, it is imported to the user interface of the FIB system. Then, the designed nanostructure is realized by FIB milling of this pattern on the rectangular cantilever.

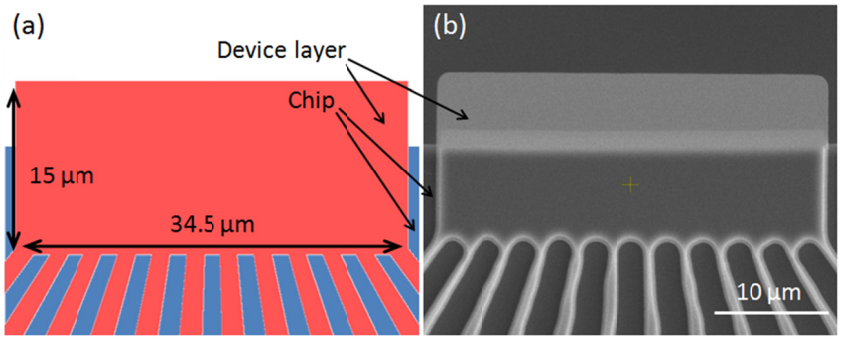

Figure 4.18 (a) Dimensions and (b) an SEM image of a microfabricated rectangular cantilever.

4.4.2 Results

FIB milling experiments were performed again at CEN at DTU, using the Quanta 3D dual-beam SEM/FIB workstation. The experiments were initiated together with Dirch H. Petersen and continued mainly by Anders Lei as a part of his M.Sc. study and partly together.

Initially, bitmap files were used for defining the milling pattern during the fabrication of the initial prototypes. However, getting more experienced, the main devices were fabricated using stream files: Text files, where the number of passes, the coordinates of the pixels to be milled and the dwell time for each pixel are defined.

Milling currents used for the 130 nm-thick nanogrippers were in the range from 10-30 pA, being much lower than those used for the 5 µm-thick microgrippers.

The minimum line-with that can be achieved by FIB milling and milling parameters were investigated through a set of experiments. These experiments, as well as the development of a fast prototyping FIB system, were mainly performed by Anders Lei during his M.Sc. study [102].

The sequence showing fabrication of nanogrippers using FIB milling can be seen in Figure 4.19. Two milling patterns were defined using two stream files: For the actuators with fine features and for the lead, which have a larger line-width. The actuators were aligned to be free-hanging from the chip edge, where the leads should be on the chip. These nanogrippers fabricated together with Anders Lei were not tested. However, characterization of similar nanodevices can be found in his report [102].

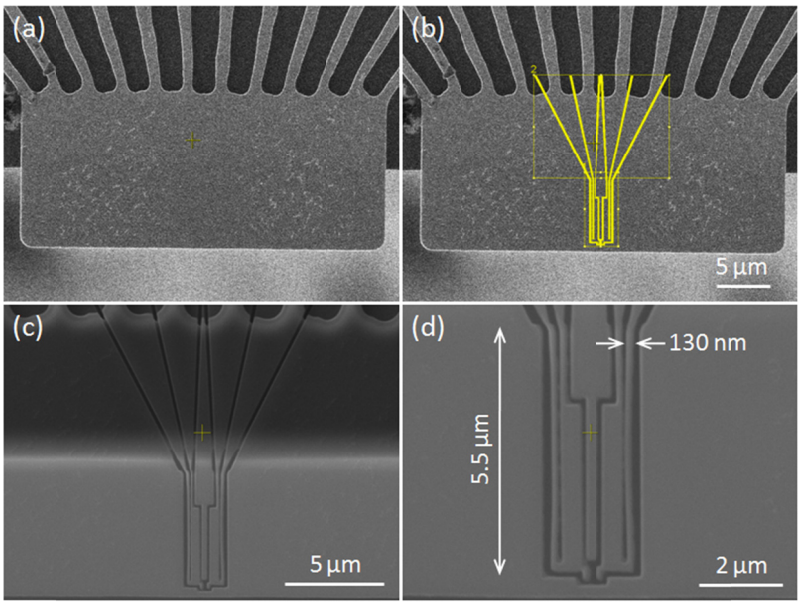

Figure 4.19 Fabrication of nanogrippers using FIB milling: (a) The microfabricated cantilever before milling. (b) Proper alignment of the milling pattern (stream file) with respect to the leads. (c), (d) Low and high magnification images of the nanogrippers showing the dimensions.

4.4.3 Challenges

The main challenge of the method presented above is the drift in the system, which becomes more and more important at nano-scale. Drift may be due to the stage of the microscope or due to the poor adhesion between the chip and the sample stub. Drift may cause misalignment of the milling patterns, unresolved structures and deviation of the resulting structure from the original design.

Furthermore, the FIB milling process is highly dependent on the system used. For this reason, milling parameters such as the dose, the number of passes and the milling current should be determined, initially, in order to achieve the minimum line-width available and to optimize the milling process. Another challenge is ion damage during both imaging and milling. The ion image should be well optimized in order to obtain a better resolution. Also,

the milling patterns should be aligned properly with respect to the cantilever and previously milled structures. These require imaging of the sample with the ion beam, which results in ion beam damage. In order to minimize the damage, optimization of the ion beam image should be performed at locations away from the cantilever and the leads, as an example at the chip edge. The damage during alignment can be eliminated by designing chips with alignment marks at specific locations and aligning the milling patterns with respect to these instead of the cantilever edges and the leads.

During milling, ions hit the side-walls of the milled structure, destroying the crystalline structure and creating an amorphous layer near the surface (Figure 4.20 (a)). The crystalline structure can be partly recovered by proper annealing of the NW (Figure 4.20 (b)). Current annealing can be used for this purpose. The method relies on passing a current through the FIB milled nanowires, where the current is gradually increased in loops (Figure 4.20). Such experiments were performed by Anders Lei and the details can be found in his report [102].

However, current annealing may lead to structures with a variable conductivity. The reason for this is that, the temperature distribution of a resistively heated structure is non-uniform. Hence, regions with higher temperature will have lower resistivity, where regions with lower temperature will have higher resistivity.

The non-uniformity mentioned above can be eliminated by annealing the FIB milled structures in a furnace, either gradually by increasing the temperature in loops, or instantaneously by continuously increasing the temperature.

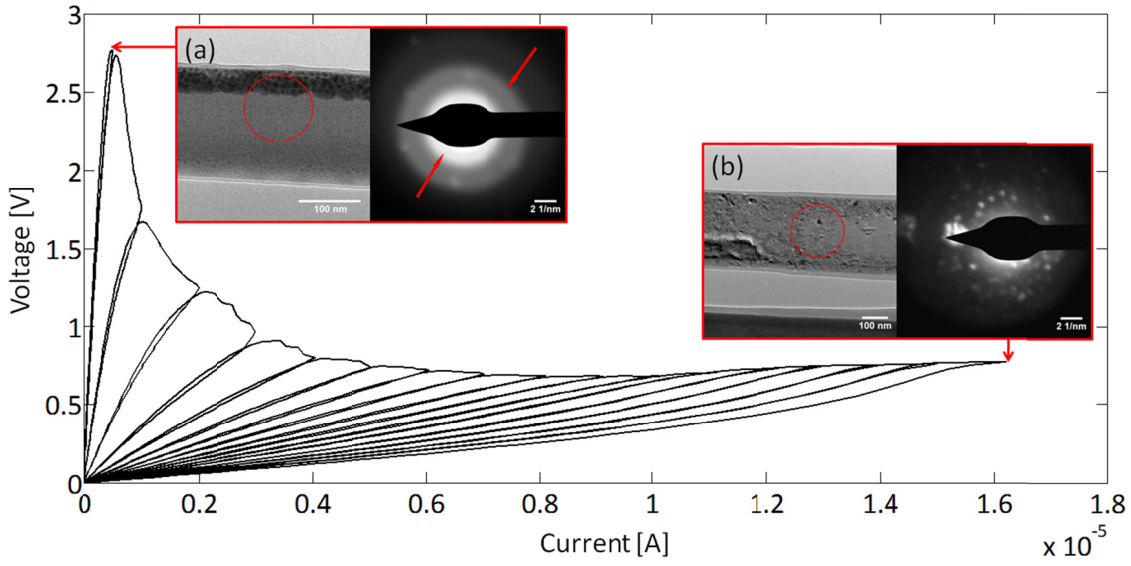

Figure 4.20 Current vs. voltage graph showing gradual annealing of FIB milled silicon NWs, with TEM images (left) and diffraction patterns (right) of an FIB milled Si NW (a) before and (b) after annealing [102].

4.5 Discussion

Topology optimized microgrippers were fabricated from n-doped polysilicon, through a conventional microfabrication process. The anisotropic etching of the poly-Si device layer was improved by replacing the RIE process with a non-switched ASE process. Although the process time was increased, the side-wall uniformity was improved and the ARDE effect was minimized. The reason for this is that, mixing the etch gas with fluorocarbons, e.g. sulfur hexafluoride (SF_6) with octafluorocyclobutane (C_4F_8), instead of oxygen (O_2) results in a more directional etching and improves the uniformity of the side-wall profile [103]. Together with this improvement and the usage of special holders during backside processing, the fabrication yield was considerably improved from 30 % to 99 %. The fabrication yield was further increased by functionalizing the devices with merged end-effectors and missing design features, by FIB milling.

FIB milling was also used for realization of novel microgripper concepts, such as XY- and inverse microgrippers, and fabrication of nanogrippers. Although there are still many issues to be resolved, including drift, re-deposition and ion damage, FIB milling is a powerful approach with many applications related to micro/nanogrippers.

The major advantage of the method is that, it shortens the design cycle. Designed structures can be fabricated and tested immediately, within a single working day. According to the results, the existing design can be modified and this improved design can be fabricated and tested, also within the same working day.

Furthermore, the method enables realization of devices with more complicated, non-repeating nanometric design features, which is not possible with the existing methods.

Finally, the material properties of the Si nanogrippers fabricated by FIB milling are different from the bulk Si material properties due to the amorphization issue mentioned in the previous section. This may be considered as a disadvantage since the FIB milled nanodevices should be annealed before using. However, it is actually an advantage since the resistivity of the material can be tuned according to the application, and devices with variable resistivity can be created by taking advantage of topology optimization.

CHAPTER 5
Packaging

5.1 Introduction

Microelectronics packaging concerns the establishment of a proper interface that enables integration of a fabricated MEMS device into a system. Main functions of a package can be listed as, providing mechanical support, providing electrical connections to the other components of the system, protecting the device from the environment and enabling easy handling.

The packaging procedure for the topology optimized microgrippers simply includes deposition of a metal layer on the carrier chip using a shadow mask, gluing of the carrier chip on a printed circuit board (PCB) and wire bonding. Selection of the metal type, the glue and the PCB material is of prime importance, influencing the performance of the microgrippers.

In this chapter, the shadow masking procedure will be described in detail, comparing two different approaches: the single-chip and the wafer-scale shadow mask approaches. Then, preparation of the interface will be explained, mentioning about the considerations taken into account during selection of the most important components.

5.2 Shadow Masking

The single-chip masking procedure was as follows:

An individual chip was removed from the wafer using special Teflon coated tweezers [98] and mounted on a carbon pad placed on a standard 4-inch Si wafer. Then, the actuators were masked by folding a small piece of copper (Cu) tape in a rectangular Ω–shape and placing it over the front side of the chip (Figure 5.1).

The single-chip masking procedure is rather time consuming since the procedure should be repeated for each and every individual chip. Furthermore, the accuracy of the relative position and orientation of the Cu tape (and therefore the metal boundary) with respect to the chip edge depends on the operator's skills (Figure 5.2). As a consequence, the closing voltage of two different devices and/or the two actuators of a microgripper may be different from each other.

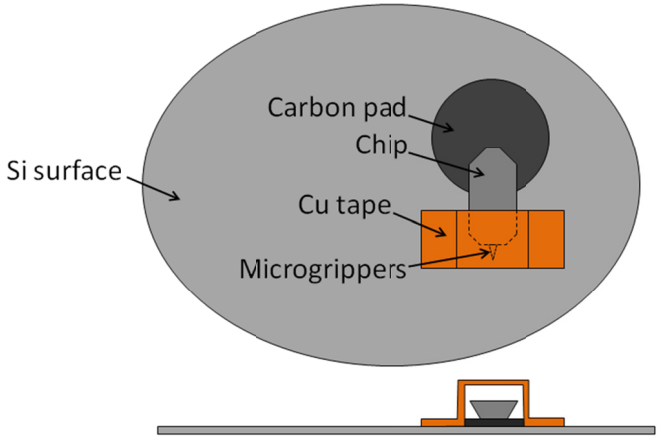

Figure 5.1 Schematic illustration of the single-chip masking procedure: Top (top) and front (bottom) views.

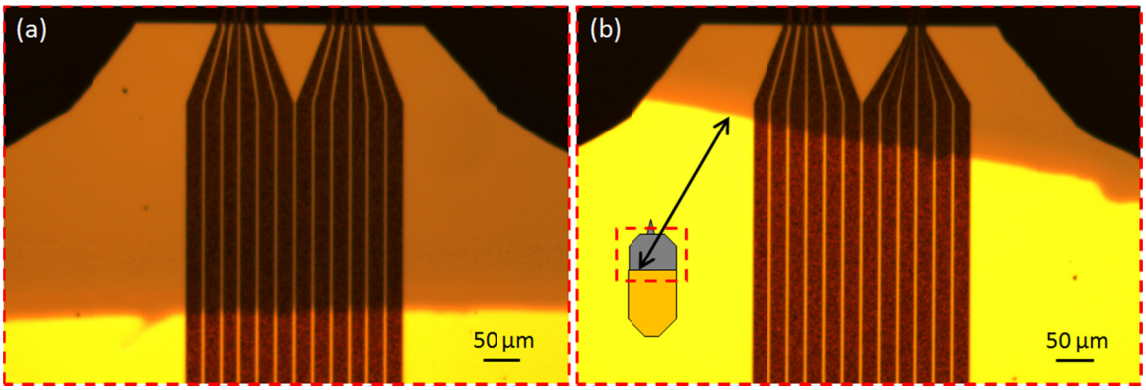

Figure 5.2 Optical microscope images showing metal boundaries on two different chips, masked using the single-chip approach: (a) A straight metal boundary, where performances of the two actuators are almost the same, and (b) a slanted metal boundary, where left actuators actuate more than right ones at the same voltage. Note that, the actuators in (a) actuate at a higher voltage than those in (b).

In order to overcome the issues mentioned above, a wafer-scale shadow mask was fabricated at Danchip's mechanical workshop (Figure 5.3 (a)). The shadow mask is 6-inch in diameter and it was fabricated from a 4 mm-thick aluminum (Al) plate. Hence, it is compatible with the 6-inch wafer holders of the metal evaporation chambers at Danchip's cleanroom. 2.5 mm × 3 mm elliptic holes were drilled through with horizontal and vertical pitches of 3 mm and 5 mm, respectively. These holes protect the microgrippers while exposing the bonding pads to the evaporated metal. The shadow mask has a stepped cross-section, where only the edge of a 4-inch wafer touches the mask surface (Figure 5.3 (b)).

The wafer-scale shadow mask enables deposition of metal on all of the chips on a 4-inch wafer at once. Furthermore, the variations in the position and shape of the metal boundary disappear to a great extend (Figure 5.4).

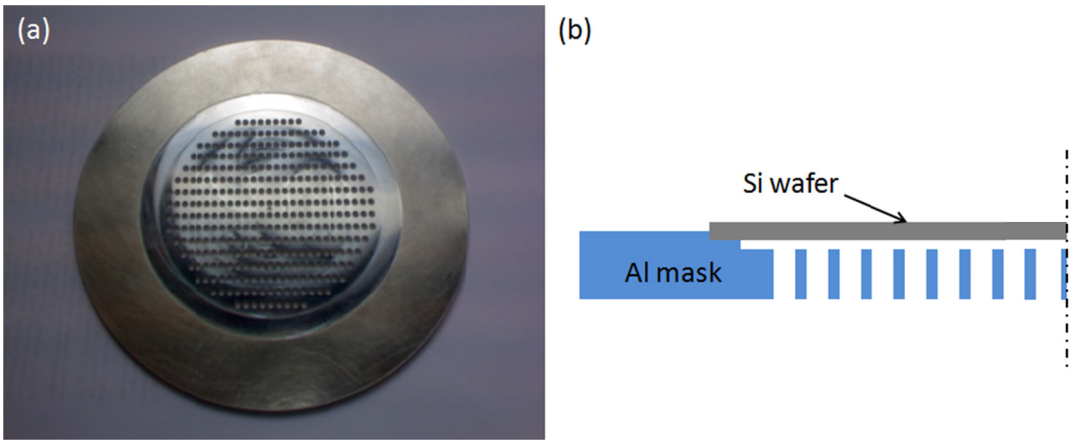

Figure 5.3 (a) The wafer-scale 6-inch Al shadow mask with (b) a schematic illustration of its cross-section and placement of a 4-inch wafer.

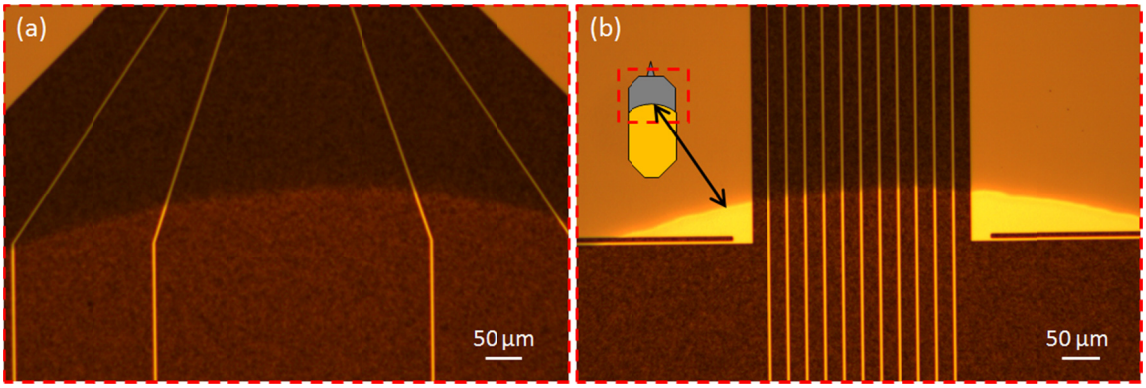

Figure 5.4 Optical microscope images showing metal boundaries on two different chips masked using the wafer-scale shadow mask: (a) One with 3-pad design, and (b) another with a 12-pad design, where the metal layers are rather uniform.

5.3 Preparation of the Interface

After the fabrication process is over, individual chips should be mounted on an interface to enable electrical connection with the actuators. This interface is a PCB, which can fit into a zero insertion force (ZIF) socket with 6 leads. Then, the bonding pads on the chip should be wire bonded to metal leads on the PCB to achieve electrical connection. The components of the interface are shown in Figure 5.5.

Selecting the interface elements properly is of prime importance, influencing the performance of the microgrippers. For this reason, the selection procedures for the three main components of the interface are explained in detail below, comparing different choices, mentioning about the observations made during experiments and describing the changes made.

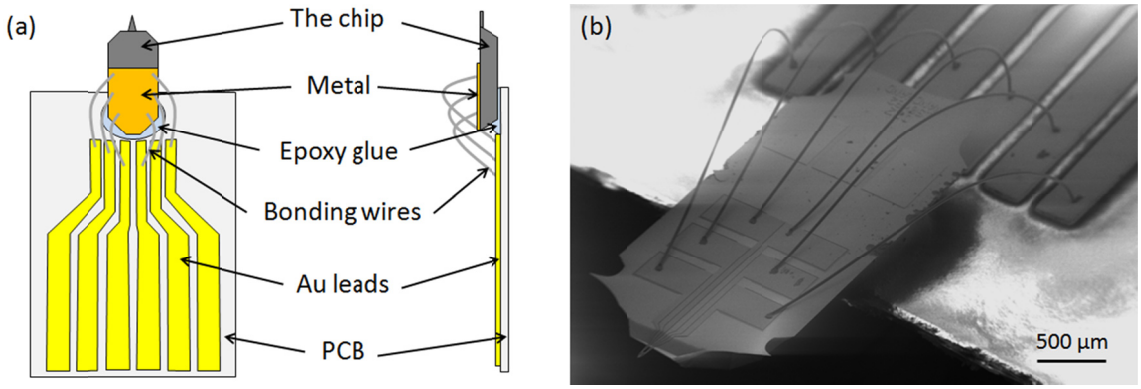

Figure 5.5 (a) Schematic illustration of the interface: Top (left) and side (right) views. (b) SEM image showing the tilted view of a finished chip and the interface.

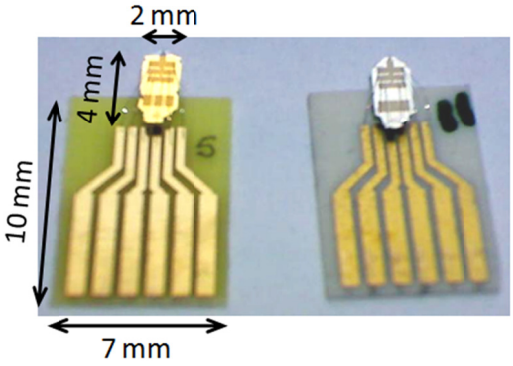

Figure 5.6 Two different interface assemblies: The initial assembly (Ti/Au metal layer, epoxy glue and FR-4 PCB) (left) and the final assembly (Ti/Pt metal layer, arctic alumina glue and RO4003C PCB) (right).

5.3.1 Selection of the Metal Type

The resistance of the metal layer deposited on the chip should be low in order to minimize the resistance and hence, the resistive heating of the chip. For this reason, the resistivity of the selected metal should be low and the deposited thickness should be as large as possible. However, the thickness of the metal layer should not exceed 1/3 of the SiO_2 layer underneath the device layer in order to prevent short circuits between the bonding pads. Finally, the melting temperature of the metal should be higher than that of the device material ($T_{m,poly\text{-}Si}$ = 1415 °C) in order to prevent evaporation of the metal layer prior to device failure.

Initially, gold (Au) was selected as the metal and 100 nm thick Au was deposited on the chips with a 10 nm titanium (Ti) seed layer (Figure 5.6 (left)). However, during actuation and manipulation experiments, it was observed that the Ti/Au layer on the chip was melting due to the high temperatures (Figure 5.7). The melted Au droplets were landing on the sample substrate and contaminating the CNTs/NWs during the nanomanipulation experiments.

In order to eliminate the melting of the metal layer, platinum (Pt) was used instead of Au (Figure 5.6 (right)) since it has a higher melting point ($T_{m,Pt}$ = 1768 °C > $T_{m,Au}$ = 1064 °C). However, the resistivity of Pt is higher than that of Au (ρ_{Pt} = 105 nΩ·m > ρ_{Au} = 22.14 nΩ·m). For this reason, the thickness of the deposited layer was increased to 190 nm, which is the ultimate limit for a SiO_2 thickness of 650 nm.

Hence, no disappearing of the metal layer was observed during the experiments performed with the chips having a 10 nm/190 nm Ti/Pt layer.

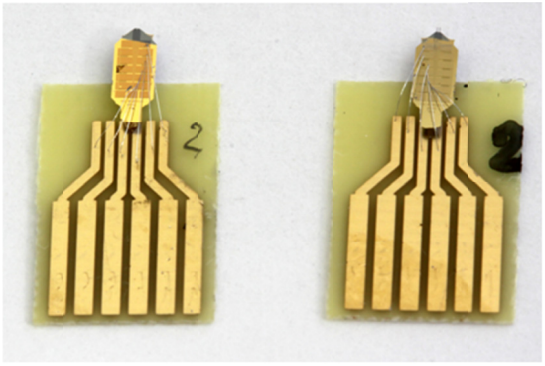

Figure 5.7 Comparison of two microgripper chips: One prior to actuation with a shiny Au layer (left) and one after operation at high temperatures, where the Au layer is melted, and hence faded (right). *Image by Jesper Scheel.*

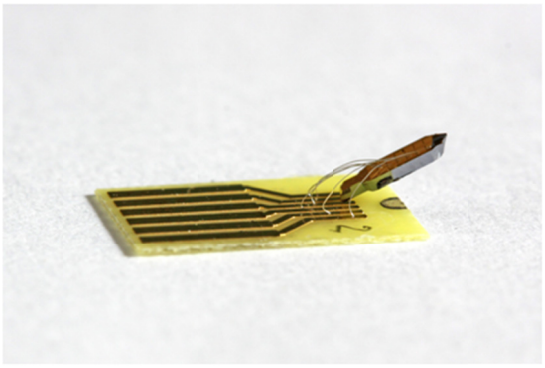

Figure 5.8 A chip detached from the PCB due to evaporation of the glue during actuation, where the bonding wires are still attached. *Image by Jesper Scheel.*

5.3.2 Selection of the Glue

The melting point of the glue used in mounting the chip on the PCB should be as high as possible in order to prevent evaporation and unpredicted motion of the chip during the experiments.

Initially, a two-component epoxy adhesive was used for gluing, where the curing was performed at 80 °C for 1 h. However, the maximum operation temperatures for two-component epoxy glues vary in the range from 60 °C to 140 °C. However, the temperature of the microgripper chips in some cases exceed this limit during actuation (see Section 6.4), which results in detachment of the chip from the PCB (Figure 5.8). This happens rarely during the experiments, however, mostly during handling.

For this reason, the two-component epoxy adhesive was replaced with a two-component arctic alumina thermal adhesive, which has a maximum operation temperature greater than ~200 °C. Another advantage of the arctic alumina is that, it cures at room temperature. Finally, it has a higher thermal conductivity than epoxy ($k_{Arctic\ Al.}$ = 18-30 W/(m·°C) > $k_{Epoxy.}$ = 0.167-0.418 W/(m·°C)), which enhances transfer of the generated heat away from the microgripper chip.

Although rather high operation temperatures were reached, evaporation of the glue and detachment of the microgripper chip was not observed with the arctic alumina thermal paste.

5.3.3 Selection of the PCB Material

The coefficient of thermal expansion (CTE), the maximum operation temperature and the thermal conductivity are of prime importance when selecting the PCB material. The CTE of the PCB material should be low in order to reduce elongation of the interface and hence, out of plane and/or forward motion of the microgrippers during actuation. The maximum temperature that the PCB material can withstand should be higher than the temperature of

the carrier chip during operation. And finally, the thermal conductivity of the PCB material should be high in order to enhance removal of the excess heat from the carrier chip.

Initially, Flame Retardant 4 (FR-4) was used as the material for the PCB (Figure 5.6 (left)). It is a standard, flexible PCB material, which is an epoxy-fiberglass composite. Properties of FR-4 are listed in Table 5.1. Note that, dimensions of the prints can be seen in Figure 5.6, where thicknesses of the PCB and the Au leads were 0.3 mm and 50 µm, respectively.

However, it was observed that the microgrippers were moving out-of-plane by an amount of 5-10 µm during actuation. Further investigating by looking at the ZIF socket/PCB interface, it was observed that this out-of-plane motion is due to the elongation and/or bending of the whole print. Furthermore, the PCB region underneath the carrier chip was changing color, i.e. burning, due high operation temperatures (Figure 5.9 (a)).

The PCB material was replaced with RO4003C from Rogers Corporation (Figure 5.6 (right)). It is an advanced PCB material, which is a hydrocarbon/ceramic-glass composite. Properties of RO4003C are listed in Table 5.1. Note that, dimensions of the RO4003C prints are the same as the FR-4 prints (Figure 5.6 (a)).

Although the burning problem was considerably reduced, the elongation problem was not completely solved with the RO4003C prints (Figure 5.9 (b)).

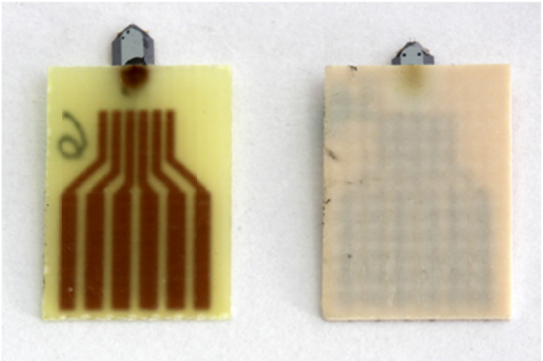

Figure 5.9 Comparison of two prints after excessive actuation (bottom views): A FR-4 PCB (left) and a RO4003C PCB (right). *Image by Jesper Scheel.*

99.6 % Alumina (Al_2O_3) substrates can be a solution to the elongation problem since all its properties are superior to those of FR-4 and RO4003C (Table 5.1).

Table 5.1 Comparison of the material properties of three different PCB materials.

	FR-4 [104]			RO4003C [105]			99.6 % Alumina [106]
Glass Transition Temperature, T_g [°C]	140			> 280			-
Melting Temperature, T_m [°C]	-			-			2072
Coefficient of Thermal Expansion, CTE [µm/(m·°C)]	x	y	z	x	y	z	7.7
	15	18	50-70	11	14	46	
Thermal conductivity, k [W/(m·°C)]	0.49			0.64			32

5.4 Discussion

In this chapter, the details of the shadow masking procedure were described. Initially, two different approaches were compared: The single-chip and the wafer-scale shadow mask approaches. The single-chip approach is rather time consuming and yields to variations in the performance of the microgrippers due to the variations in the position of the metal boundary.

The wafer-scale approach enables metal deposition on every chip on a wafer at the same time. Furthermore, the performance variation can be minimized by proper alignment of the mask with respect to the wafer. However, bending of the wafer due to the mechanical stresses, which arises during various process steps may prevent perfect alignment. For this reason, the position of the metal layer on the chips located near the wafer edge may be slightly misaligned.

The procedure for preparing the interface was explained, mentioning about the considerations taken into account during selection of the most important components: The metal type, the glue and the PCB material.

Initially, Ti/Au was used as the seed layer for wire bonding, a two-component epoxy glue was used for mounting the carrier chip on the PCB interface and FR-4 was selected as the PCB material. However, all these components were replaced in order to enhance the performance of the microgrippers.

First of all, the Ti/Au layer deposited on the chips was evaporating at high operation voltages since Au has a relatively low melting point (lower than poly-Si). For this reason, Au was replaced with Pt, which has a higher melting point (even higher than poly-Si), and the evaporation problem was eliminated.

However, resistivity of Pt is higher than that of Au, which may result in an increase in the resistive heating. In order to minimize this effect, the thickness of the metal layer was increased to 200 nm from 110 nm. However, it was not possible to investigate the effect of the increased metal layer thickness since temperature measurements (see Section 6.4) were performed only on chips with a thicker metal layer.

Secondly, two-component epoxy glue was also evaporating since the carrier chip heats up to temperatures beyond the glues maximum operation temperature. This was resulting in detachment of the carrier chip from the PCB interface during handling. For this reason, two-component arctic alumina adhesive was used instead and the detachment problem was completely eliminated.

Another advantage of arctic alumina is that, it enhances transfer of the excess heat away from the carrier chip since it has a higher thermal conductivity than epoxy.

Finally, the FR-4 PCB interface was elongating and bending, mostly downwards, during actuation. This was resulting in out-of-plane movement of the carrier chip, and hence the end-effectors of the microgrippers during operation.

Furthermore, the PCB region underneath the carrier chip was burning due to the high carrier chip temperature.

In order to overcome the above mentioned problems, the FR-4 PCBs were replaced with RO4003C PCBs, which have lower CTE values in all x- y- and z-directions and a considerably higher maximum operation temperature. Although burning of the PCB interface was eliminated to a great extent, the out-of-plane bending problem was not completely resolved.

99.6 % Alumina (Al_2O_3) substrates can be a solution to the elongation problem, since it has a much lower CTE, which is the same for all directions.

As an alternative, a fully mechanical packaging approach can be used, where the carrier chip is mechanically clamped by metal pins and springs. This will eliminate the gluing step, which is rather time consuming. Furthermore, the bonding pads can be designed accordingly, so that the electrical connection with the microgrippers can be achieved through the metal pins used for clamping. Hence, the wire bonding step will also be eliminated, which is again rather time consuming and the chips can be exchanged in-between the experiments. Finally, in order to remove excess heat from the carrier chip, it can be connected to a heat sink by means of a copper wire or a thermally conductive tape.

CHAPTER 6
Characterization

6.1 Introduction

Characterization of a MEMS device is of great importance for calibration of the finite element model and further improvement of the device for obtaining a reliable product out of it. This chapter is about characterization of topology optimized microgrippers, which includes actuation, stiffness and temperature characterizations.

6.2 Actuation Characterization

Characterization of the topology optimized microgrippers' actuation was performed using an optical nanomanipulation setup at the Nanointegration Lab (DTU Building 346-145). In the following sections, the setup will be introduced, the procedure for actuation characterization will be described in detail and the results will be presented, respectively.

6.2.1 The Setup

The optical manipulation system is composed of a high magnification Navitar optical lens system, a camera, a cold halogen light source, a motorized Newport XYZ stage with a motion controller, a Keithley sourcemeter, a computer and a holder, in which the PCB interface fits (Figure 5.1).

6.2.1.1 Mechanical Support

Some components of the setup, i.e. the objective, the camera and the stage together with the holder, are placed on a hydraulic table in order to eliminate vibrations. In order to minimize the interaction of these components with the surroundings and other components of the setup, such as the sourcemeter or the motion controller, the hydraulic table was mounted on the wall.

In order to enhance the stability and the flexibility of the setup, the table-like aluminum support was replaced with a more stable and flexible support, which was manufactured by Søren Petersen at Danchip's mechanical workshop (Figure 6.2). In this new support, the objective is held from both ends with two clamps (Figure 6.3). The collars are attached to the microscope pole, which can slide inside the U-shaped base pole. Hence, it is possible to investigate samples requiring a large holder or mount multiple manipulators under the objective. The base pole is supported by triangular bases. The material is aluminum for all parts, except the polycarbonate clamps.

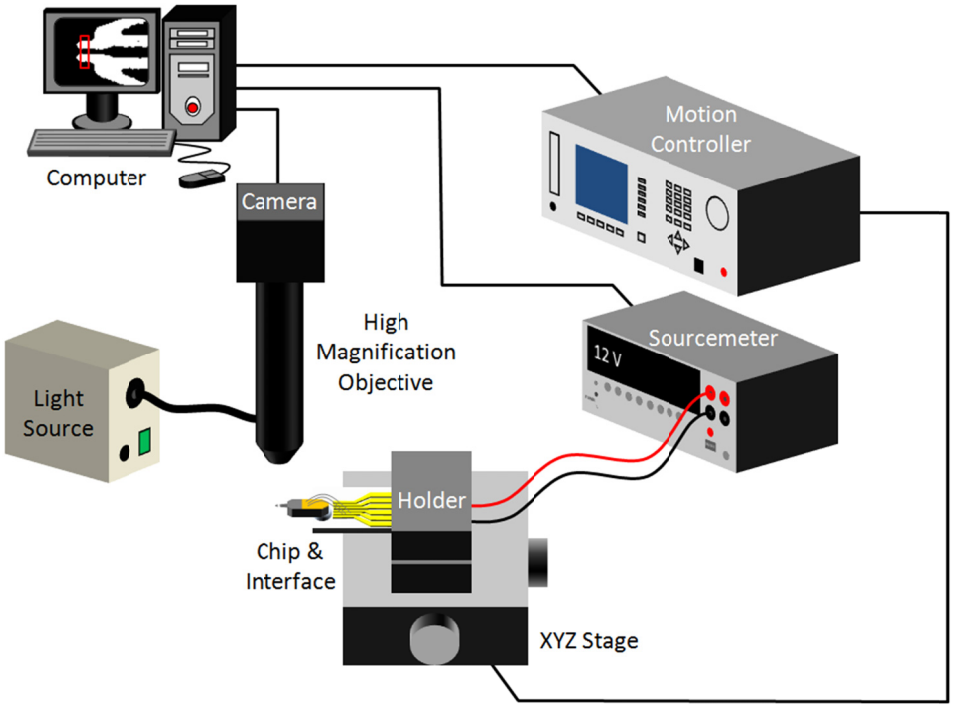

Figure 6.1 Schematic illustration of the actuation setup.

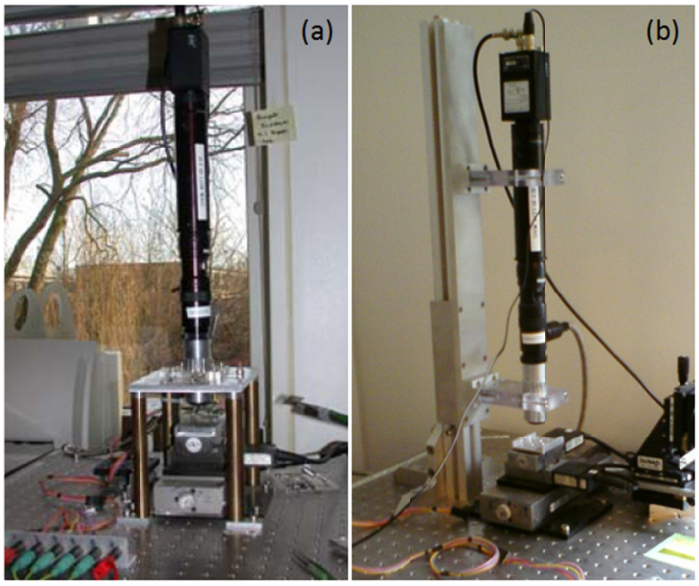

Figure 6.2 Mechanical supports for the optical manipulation setup: (a) The initial version (*image from intern Julie Kirkegaard's report, December 2005*) and (b) the improved, new version.

6.2.1.2 Components

Specifications of the most important components of the setup are as follows:

The high magnification optical lens system (Navitar Zoom 6000) has a 0.7 X to 4.5 X zoom range and a 2X lens adapter. A ½" monochrome CCD camera (JAI CV-M50) is attached to the objective and a halogen type light source (Moritex MHF-M1002) is used for illumination.

The XYZ stage has three components: Two linear stages for x- and y-axes (Newport MFA-CC), which have a travel range of 25 mm, a minimum step size of 0.1 µm and a maximum speed of 2.5 mm/s and a vertical stage for the z-axis (Newport UZS80CC), which has a travel range of 4.5 mm, a minimum step size of 0.2 um and a maximum speed of 4 mm/s.

The stages are connected to a multi-axis motion controller (Newport MM4005), which has four channels, i.e. can control up to four motors. The motion controller is connected to the computer via the GPIB port.

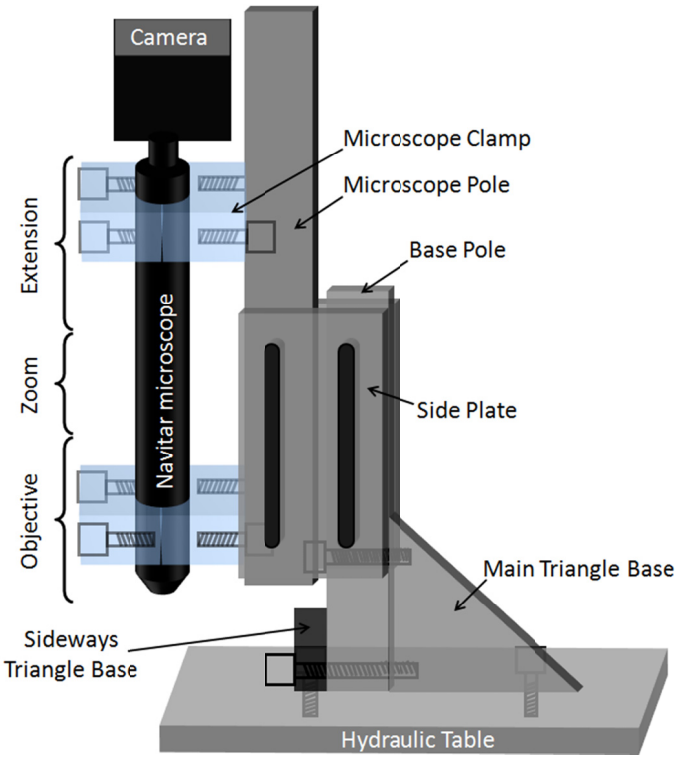

Figure 6.3 Schematic illustration showing the side view of the new mechanical support.

The sourcemeter (Keithley 2400) is also connected to the computer via the GPIB port. This instrument is capable of sourcing and measuring currents in the range from 10 pA to 10 A with 0.02 % accuracy and voltages in the range from 1 μV to 1100 V with 0.35 % accuracy. It also allows 4- and 6-point measurements in the range from 2 Ω to 200 MΩ, with 1 μΩ resolution.

Windows 98 operating system is installed on the computer since it is compatible with the drivers of most of the components. Both the XYZ stage and the sourcemeter can be controlled via a LabView program written by Kristian Mølhave and Peter Bøggild. This program enables real time measurement of the relative gap distance with a nanometric resolution using an image processing algorithm.

The basics of the LabView program and the procedure for performing actuation measurements using this program is described in detail in APPENDIX F.

6.2.1.3 The Holder

The initial holder for the microgripper interface was composed of an aluminum base, a FR-4 PCB with gold leads and a ZIF socket with 6 pins (Figure 6.4 (a)). The PBC was mounted on the aluminum base with two screws and two small springs. The ZIF socket was glued on the PBC, where its pins were soldered to individual gold leads. The electrical connection with the sourcemeter was achieved through six wires soldered to the gold leads one end and connected to a six-pin male ribbon connector.

In this holder arrangement, the microgripper interface, i.e. the PCB on which the microgripper chip is glued, is hanging freely from the ZIF socket. However, this arrangement is not stable since the interface bends downwards due to excess heating during actuation. This makes actuation measurements impossible since the end-effectors go out-of-focus by ~10 -20 μm.

In order to eliminate this problem, the PCB-based holder was replaced with an all-metal holder. The new holder was also manufactured by Søren Petersen at Danchip's mechanical workshop. In this new holder, the ZIF socket is clamped between two aluminum plates. Furthermore, the microgripper interface is supported from the bottom by an aluminum block and from sides with two screws. Hence, the mechanical stability of the microgripper interface and the heat transfer are improved.

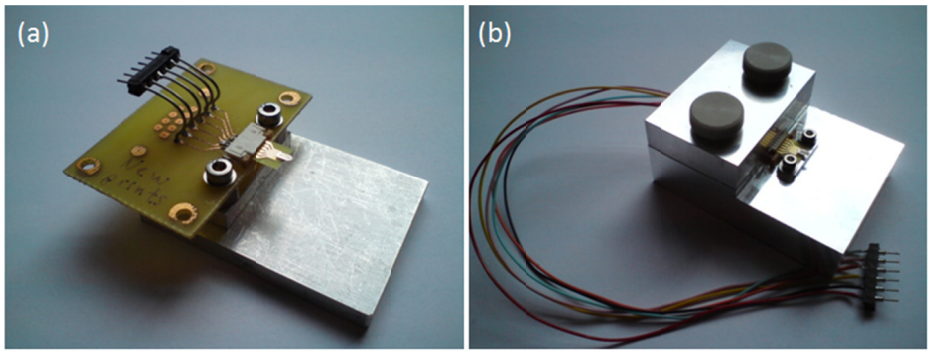

Figure 6.4 Holders for the optical manipulation setup: (a) The initial, PCB-based and (b) the new, all-metal holders.

6.2.2 Results

The above described procedure was repeated for different types of microgrippers. Then the serial resistance of each microgripper was subtracted from the measurements according to:

$$V = V_{exp}\left(1 - \frac{R_s}{R_{tot}}\right) \tag{6.1}$$

In the above equation, V_{exp} is the experimental voltage values and R_s and R_{tot} are the serial and total resistances respectively. Serial resistance should be calculated individually for each chip, according to the position of the metal layer.

Comparison of the experimental results and the finite element simulations for smoothed Design B can be seen in Figure 6.5. Similar plots for the original and the tilted versions of Design B and all other designs can be found in APPENDIX G.

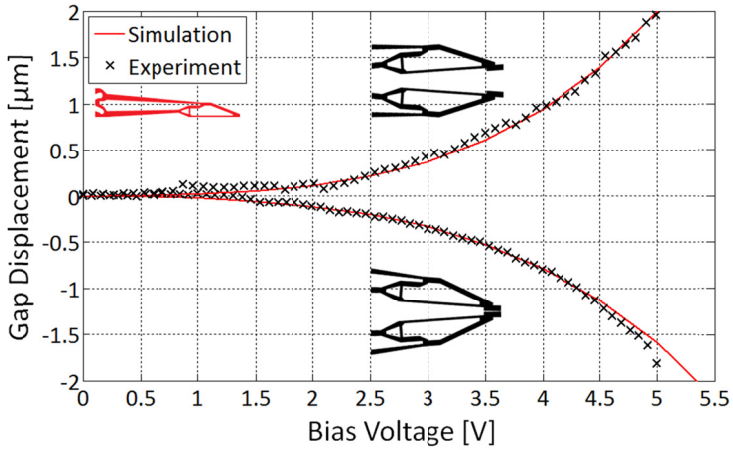

Figure 6.5 Comparison of the experimental results and the finite element simulations for smoothed Design B with large electrodes.

6.3 Stiffness Characterization

Stiffness values of the topology optimized actuators were determined through atomic force microscope (AFM) force measurements. In this section, the basic theory behind the measurements and the setup will be introduced, initially. Then, the results will be presented and compared with the topology optimization and the finite element simulation results.

6.3.1 Basic Theory and the Setup

Atomic force microscopy is generally used for investigating surfaces at an atomic scale[9, 107]. It also enables measurement of displacements down to 0.02 nm and hence measurement of forces down to 0.2 nN, using a typical cantilever with a spring constant of 10 N/m [87].

AFM can also be used for investigating mechanical properties of micro- and nanostructures. As an example, elasticity, strength and toughness of silicon carbide (SiC) nanorods and multi-walled CNTs (MWCNTs) can be determined through AFM force measurements [108].

The method presented in [108] was used for determining the stiffness of the topology optimized actuators together with Christian Kallesøe and Kristian Mølhave. However, the setup used is slightly different in that vertical forces were measured instead of lateral forces. This is since the measured nanostructures were pinned perpendicularly on a lateral surface in [108], where the measured actuators were mounted laterally here (Figure 6.6).

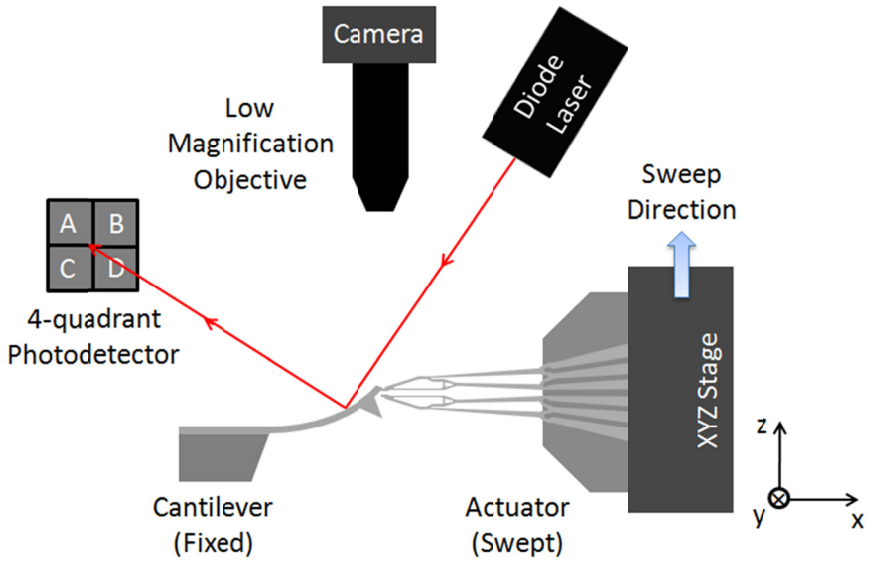

Figure 6.6 Schematic illustration of the force measurement setup.

Initially, the actuator to be measured was mounted on the AFM stage, i.e. the XYZ stage, and its end-effector was aligned 1-2 μm above the cantilever's end. Then, the actuator was swept upwards, i.e. z-direction, bending the cantilever. During this sweep, the z-position of the stage, z_{stage}, and the voltage difference created between the two quadrants of the photodiode , ΔV_{AB}, were recorded.

Finally, a reference measurement was performed in a similar manner, by sweeping a rigid surface upwards. Hence, the stiffness of the actuator, k_{act}, can be calculated according to [109]:

$$k_{act} = \frac{k_{cant}}{\left(\frac{\alpha_{ref}}{\alpha} - 1\right)} \tag{6.2}$$

Where, k_{cant} is the stiffness of the cantilever, α is the slope of the z_{stage} versus ΔV_{AB} curve recorded while sweeping the actuator upwards and α_{ref} is the slope of a similar curve recorded during the reference measurement.

Step by step derivation of Equation (6.2) is described in detail in [109].

6.3.2 Results

Stiffness measurements were performed only for Design B, including all its variations. Results of these measurements are tabulated below, together with the values calculated theoretically and through finite element simulations.

Table 6.1 Comparison of the results of the stiffness measurements with theory and finite element simulations.

	Spring Constant (Stiffness), k_s [N/m]		
	Theory	Finite Element Simulation	Experiment
Initial Design B	N/A	(TOPOPT) 37.2	N/A
Original Design B	N/A	(TOPOPT) 151 (COMSOL) 177	9.1
Smoothed Design B	N/A	(COMSOL) 234	10.7
Tilted Design B	N/A	(COMSOL) 219	11.9
Three-beam Design (2 μm × 200 μm beams)	2.2	(COMSOL) 2.2	1.1-3.4

6.4 Temperature Characterization

Temperature characterization of the topology optimized microgrippers was performed by measuring the temperature at various points along the actuators during actuation using Raman spectroscopy. In the following sections, Raman spectroscopy will be introduced, the principle of temperature measurements using Raman spectroscopy and the setup used for the temperature measurement experiments will be described. Finally, the results will be presented for a specific design, i.e. Design B (see CHAPTER 2 & CHAPTER 3).

6.4.1 Introduction to Raman Spectroscopy

Raman scattering is a fundamental form of molecular spectroscopy, which is used to obtain information about the structure and properties of molecules from their vibrational translations [110, 111]. It is well-suitable for temperature and mechanical stress measurement on MEMS devices, mainly devices made from silicon due to its high scattering cross-section [112, 113].

6.4.2 Basic Theory

When light interacts with matter, there are three possibilities: The photons may be absorbed, scattered or passed through the material without any interaction. If the energy of an incident photon corresponds to the energy difference between the ground state and an excited state, the photon may be absorbed and the molecule is promoted to the higher energy excited state. In absorption spectroscopy, this energy change is measured by detecting the energy loss of radiation from the light. If the photon scatters from the material, there is no need for it to have an energy that matches the energy gap. The scattered photons can be observed by collecting light at an angle to the incident light beam. Scattering is widely used in many applications, such as measuring the particle size and size distribution down to sub-µm sizes.

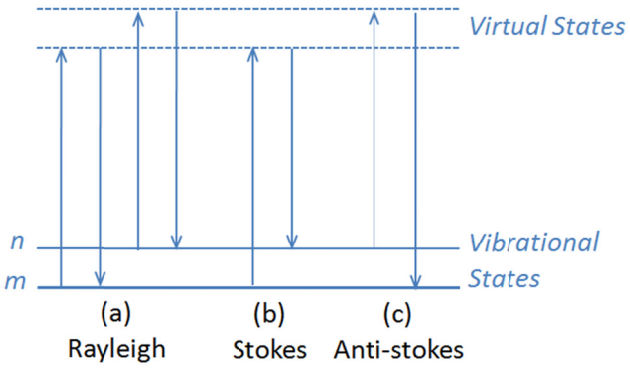

Figure 6.7 Energy diagrams of the Rayleigh and Raman scattering processes.

If only electron cloud distortion is involved in a scattering process, the phonons are scattered with very small frequency changes since the electrons are lighter. Such scattering is referred to be elastic and it is the dominant process. Elastic scattering for molecules is called Rayleigh scattering. It is the strongest process since most of the photons and most of the photons scatter according to this process. It does not involve any energy change and hence, the photon returns to the same energy state (Figure 6.7 (a)).

In cases, where nuclear motion is induced, energy is transferred either from the incident photon to molecule or from the molecule to the scattered photon. Hence, the energy of the scattered photon becomes different from that of the incident photon by one vibrational unit. Such scattering is referred to be inelastic and called as Raman scattering. It is a naturally weak process since only one in 10^6-10^8 scattered photons is Raman scattered. In Stokes scattering, a Raman scattering process from the ground vibrational state (*m*) leads to absorption of energy by the molecule and its promotion to a higher energy excited vibrational state (*n*) (Figure 6.7 (b)). Some molecules may be present in an excited state such as (*n*) as a result of thermal energy. Scattering from these states to the ground state (*m*) is called anti-Stokes scattering, which involves energy transfer to the scattered photon (Figure 6.7 (c)).

The relative intensities of the two Raman scattering processes depend on the various states of the molecule. The populations can be determined from the Boltzmann equation as follows:

$$\frac{N_n}{N_m} = \frac{g_n}{g_m} exp\left(-\frac{(E_n - N_m)}{kT}\right) \tag{6.3}$$

In the above equation, N_n and N_m are the number of molecules in excited (*n*) and ground (*m*) energy levels respectively, *g* is the degeneracy of levels *n* and *m*, $E_n - E_m$ is the difference between vibrational energy levels and *k* Boltzmann's constant ($1.3807 \times 10^{-23}\ \mathrm{J \cdot K^{-1}}$). At room temperature, the number of molecules expected to be in an excited vibrational state will be small compared to a low-energy state. Hence, anti-Stokes scattering will be weaker than Stokes scattering. Anti-Stokes scattering becomes even weaker as the vibrational frequency increases due to decreasing population of the excited states. Whereas, anti-Stokes scattering increases compared to Stokes scattering as the temperature rises.

Raman scattering is recorded only on the low-energy side to give Stokes scattering. However, anti-Stokes scattering can also be used in some applications. As an example, fluorescence interference occurs at a lower energy than the excitation frequency and using anti-Stokes scattering avoids interference. Also, temperature can be measured from the differences in the intensities of Raman bands in Stokes and anti-Stokes scattering.

6.4.3 The Setup

Temperature measurements are performed together with Jinquan Liu using the Dilor XY Modular Raman Spectrometer at EMPA Materials Science and Technology in Thun, Switzerland (Figure 6.8). The setup is composed of two main parts: The spectrograph and the fore monochromator (Figure 6.9). The laser from a coherent Innova 90 Ar^+ laser, with a 514.5 nm wavelength, is focused on the sample after passing through a beam splitter and a 50X/100X Olympus objective. The position of the sample can be adjusted by blanking the laser beam and switching to a camera, which is connected to a monitor.

The beam reflected by the sample is filtered by an optical system of mirrors, slits and gratings in the fore monochromator. Then, the filtered beam enters the spectrograph, where it is focused on a CCD camera with a 1024 × 256 resolution, again by passing through an optical system of parabolic mirrors, mirrors and gratings.

Data acquired by the CCD is transferred to a computer, instantaneously processed by the NGS LabSpec software and displayed on the computer screen.

The sample stage is automated in X and Y directions and can be controlled via the user interface. This enables mapping of a certain area by performing measurements at a number of predefined points.

The device to be measured is placed on the sample stage and connected to a power supply through an interface and can be actuated during the temperature measurements.

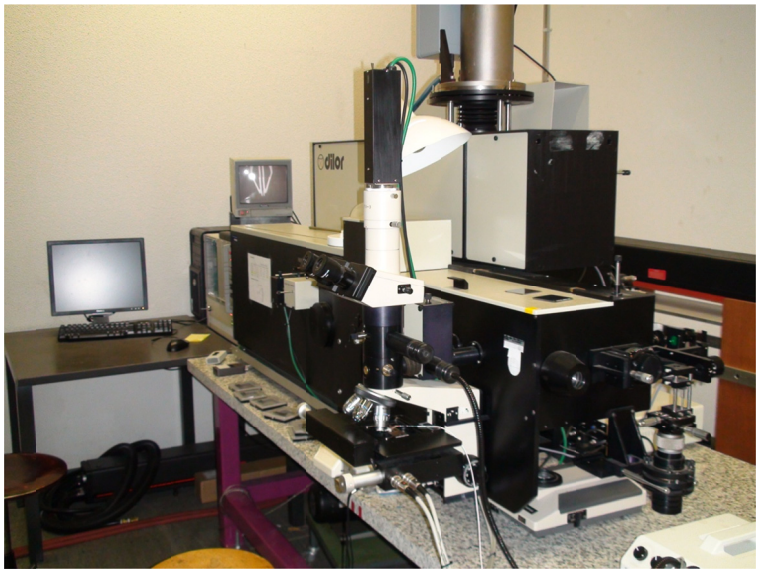

Figure 6.8 The Dilor XY Modular Laser Raman Spectrometer used in the experiments.

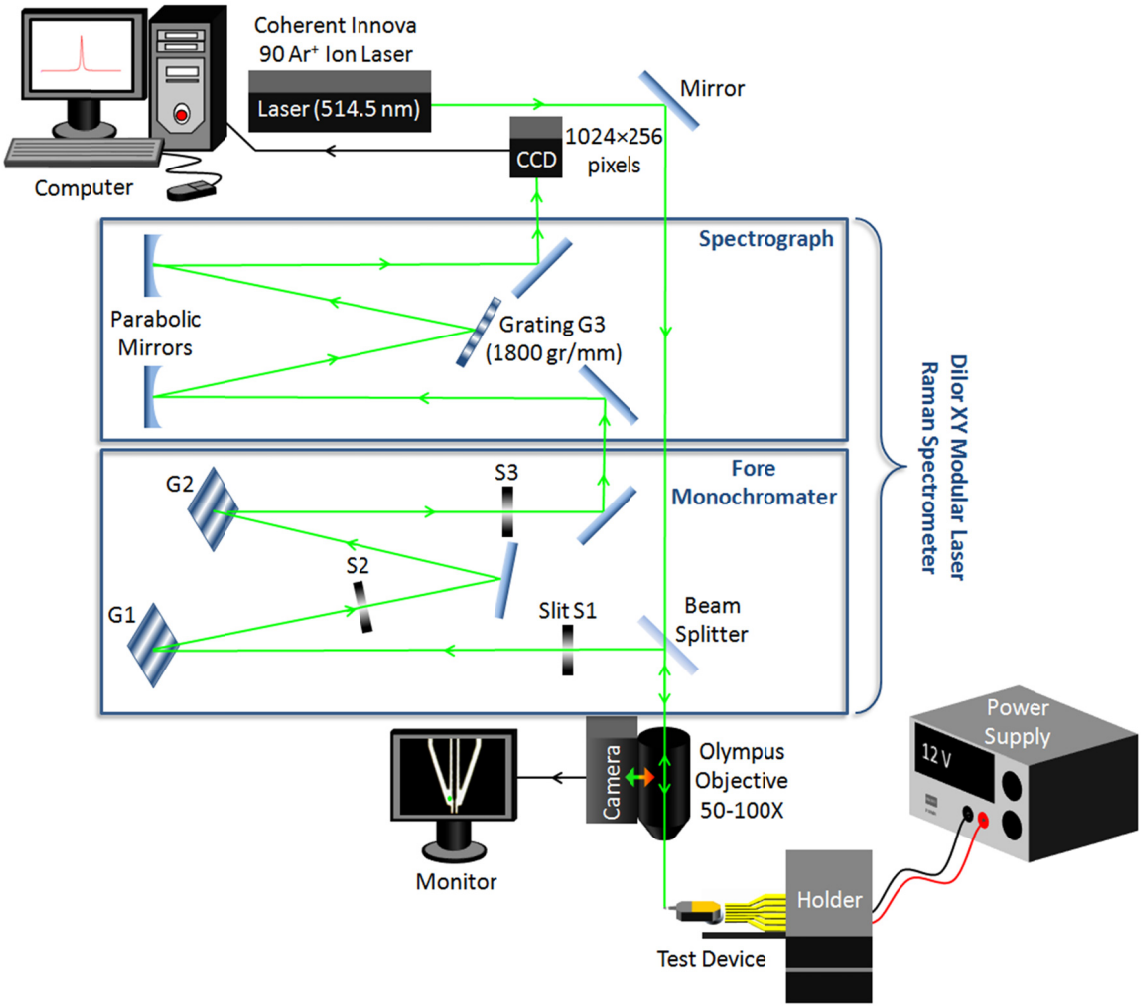

Figure 6.9 Schematic illustration of the details of the Dilor XY Modular Laser Raman Spectrometer.

6.4.4 Temperature Measurements using Raman Spectroscopy

Raman spectroscopy allows determination of high or low temperatures from the intensity ratios of the Stokes and anti-Stokes peaks (Figure 6.10), i.e. I_{Stokes} and $I_{anti-Stokes}$, according to [114]:

$$\frac{I_{Stokes}}{I_{anti-Stokes}} = \left(\frac{\nu_0 - \nu_m}{\nu_0 + \nu_m}\right)^4 exp\left(\frac{hc\nu_m}{kT}\right) \tag{6.4}$$

In the above equation, ν_0 is the wave number of the laser line, ν_m is the wave number of a band of the sample, h is Planck's constant, c is the velocity of light, k is Boltzmann's constant and T is the absolute temperature of the sample.

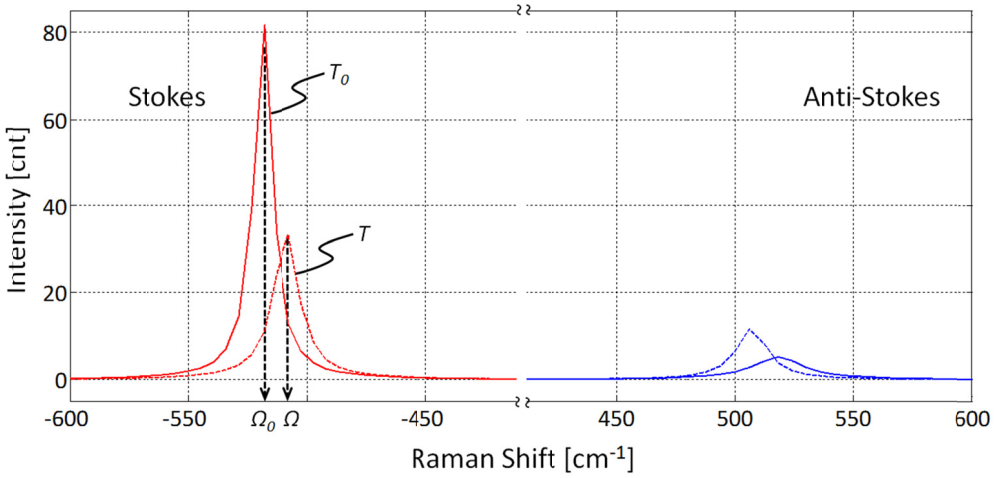

Figure 6.10 A typical Raman spectra: Stokes and anti-Stokes peak positions at the initial temperature, T_0, and at an elevated temperature, T.

Rearranging Equation (6.4), the expression for the absolute temperature of the sample becomes:

$$T = \frac{-\nu_m \times 1.43879}{ln\left(\frac{I_{Stokes}}{I_{anti-Stokes}}\right) + 4ln\left(\frac{\nu_0 - \nu_m}{\nu_0 + \nu_m}\right)} \tag{6.5}$$

However, this equation is not applicable when anti-Stokes peaks are weak. In such situations, the temperature can be obtained from the location of the Stokes peak and the linear coefficient of peak shift associated with temperature, $d\Omega/dT$,using [115]:

$$T = T_0 + \left(\frac{\Omega_0 - \Omega}{\left(\frac{d\Omega}{dT}\right)}\right) \tag{6.6}$$

In the above equation T_0, is the initial temperature, Ω_0 is the location of the Stokes peak at T_0 and Ω is the position of the Stokes peak at T (Figure 6.10).

6.4.5 Results

6.4.5.1 Point Measurements

Temperatures at different locations of the topology optimized actuators were measured and compared with the results of the finite element simulations performed using COMSOL Multiphysics. For this purpose, 9 or 10 points were defined on the actuators and along their leads (Figure 6.11).

The peak positions and linear coefficients of peak shift for poly-Si varies over a wide range [112, 115-117]. Furthermore, the mechanical stress within the sample has a great influence on its Raman spectra. Hence, the values of Ω_0 $d\Omega/dT$ should be determined by performing calibration measurements. The Stokes peak position at the initial temperature, $T_0 = 25\ °C$,

was determined for each actuator by performing reference measurements at the first, i.e. the end-effector, and the last, i.e. the inner lead, points without actuation. The linear coefficient of peak shift associated with temperature was also determined by performing calibration measurements using a hot-plate as $d\Omega/dT = 0.035\ cm^{-1}{}^{\circ}C^{-1}$.

During the experiments, the microgrippers were actuated either to the closed position or beyond, and Raman measurements were performed at all measurement points, sequentially. In order to eliminate the effect of drifting of the measured sample, the measurements were repeated twice (or three times if necessary) and the average of these measurements was used in calculating the temperature.

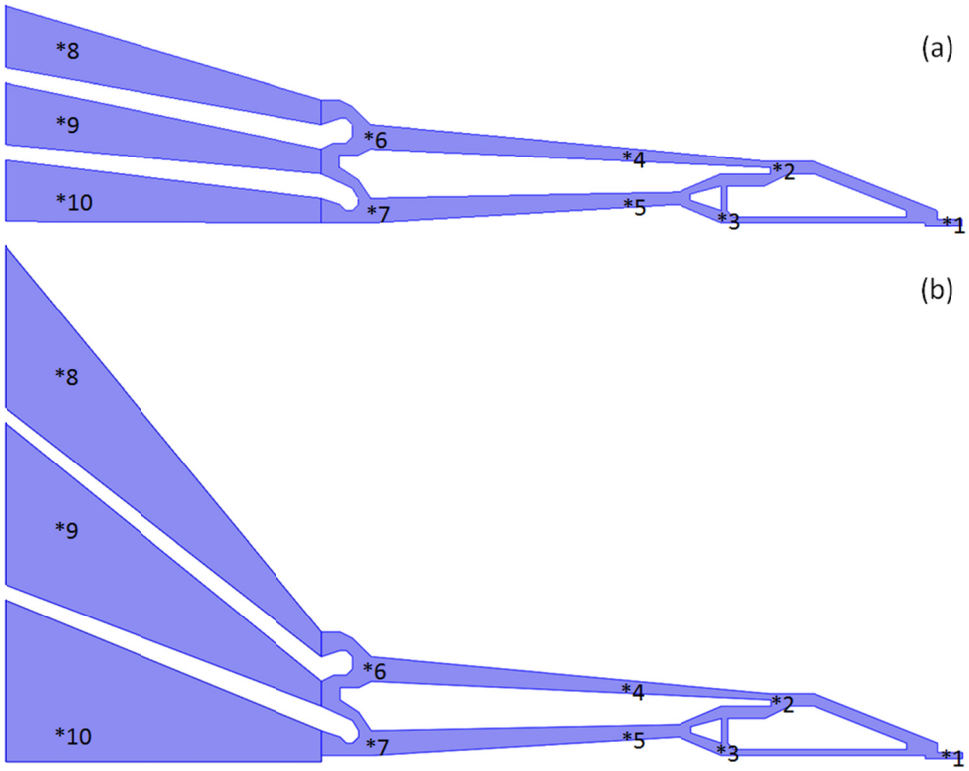

Figure 6.11 Points defined on smoothed Design B and the leads with (a) the initial lead design and (b) the improved, larger lead design.

Comparison of the temperature measurements with the non-ideal case finite element simulation results for smoothed Design B is plotted for in Figure 6.12. Note that, the results of the temperature measurements revealed that the carrier chip is excessively heating. In order to minimize chip heating, a new batch of topology optimized microgrippers was fabricated with a larger electrode design (Figure 2.20). A similar comparison for smoothed Design B with large electrodes can be seen in Figure 6.13.

Similar plots for the original and the tilted versions of Design B and all other designs can be found in APPENDIX H.

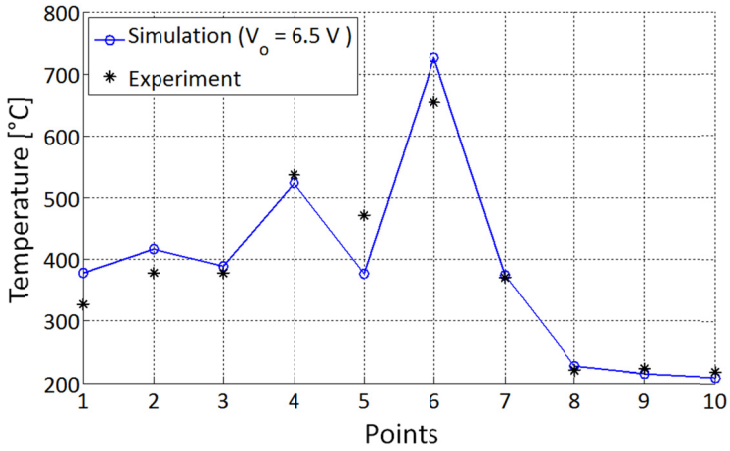

Figure 6.12 Comparison of the temperature measurement results with the finite element simulations for smoothed Design B with narrow leads ($V_o = 6.5\ V$, $y_{free} = 1.4\ \mu m$, $F_{blocking} = 302\ \mu N$, $F_{gripping} = 87\ \mu N$).

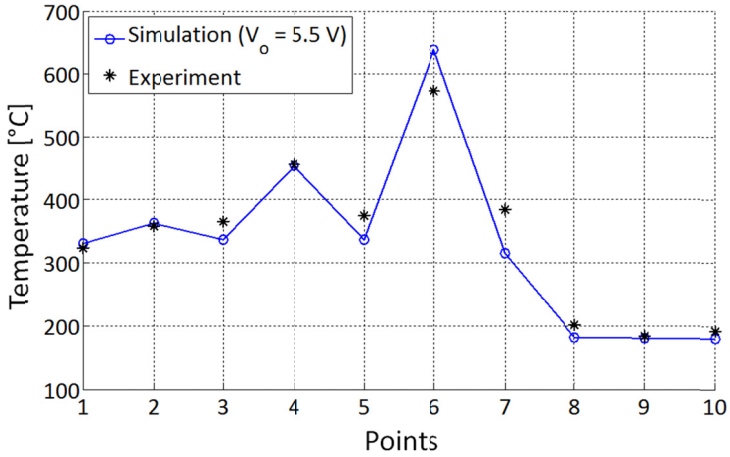

Figure 6.13 Comparison of the temperature measurement results with the finite element simulations for smoothed Design B with wide leads ($V_o = 5.5\ V$, $y_{free} = 1.324\ \mu m$, $F_{blocking} = 286\ \mu N$, $F_{gripping} = 70\ \mu N$).

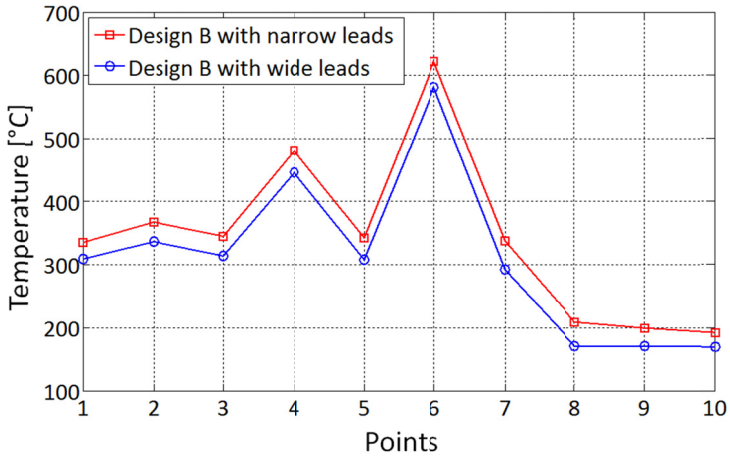

Figure 6.14 Comparison of the non-ideal case finite element simulation results for smoothed Design B with narrow and wide leads ($y_{free} = 1\ \mu m$).

The effect of lead size on chip heating can be determined by comparing the non-ideal case simulation results for smoothed Design B under same conditions (Figure 6.14).

6.4.5.2 Temperature Mapping

In addition to the point measurements, the temperature map of a microgripper (smoothed Design B with narrow electrodes) was also obtained through multiple measurements performed within a grid. Mapping measurements are rather time consuming experiments, which should be run over night. For this reason, the topology optimized microgripper was actuated only to the half-closed position, i.e. -0.5 µm actuator displacement, in order to reduce the risk of device failure during mapping.

The results of three mapping runs performed at different locations of the microgrippers are compared with the non-ideal case finite element simulations in Figure 6.15.

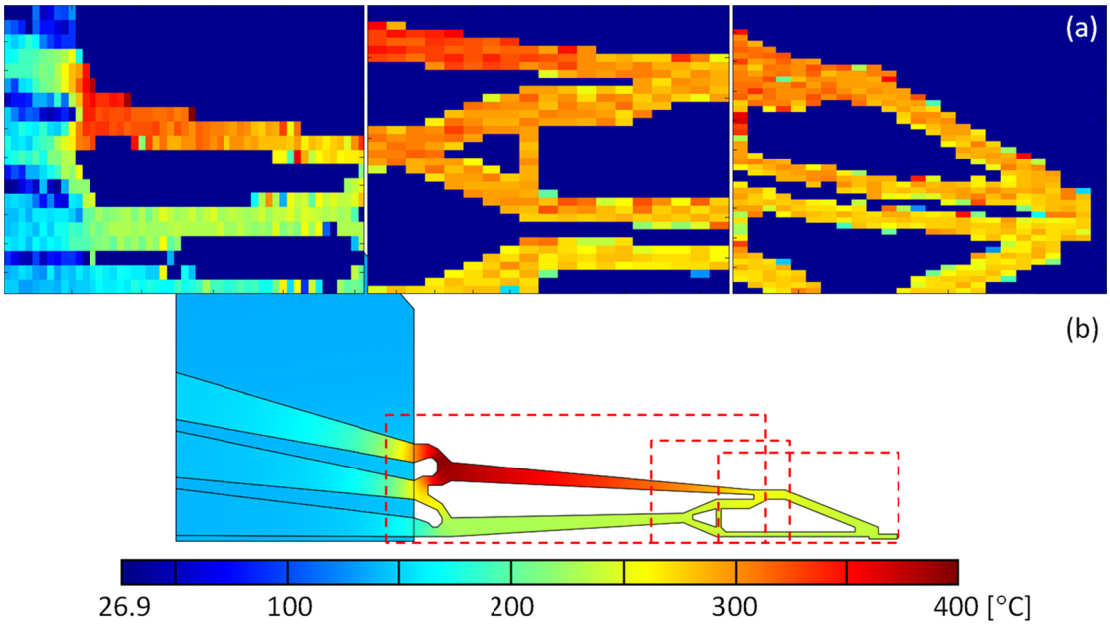

Figure 6.15 (a) Temperature mapping results for smoothed Design B with initial electrode design at the half closed position. (b) Non-ideal case finite element simulation results for the same design at the same position.

6.5 Discussion

This chapter described characterization of the topology optimized microgrippers. Setups, procedures and results of actuation, stiffness and temperature characterization experiments were explained in detail.

A high magnification optical manipulation setup was used for actuation characterization experiments of the topology optimized microgrippers. The stability of the setup was enhanced by mounting the hydraulic table on the wall and replacing the mechanical support with a new one, where the objective is clamped from both ends. Furthermore, the holder for the microgripper interface was also replaced with an all-metal holder, where the interface is supported from bottom. Hence, the bending of the PCB interface during actuation was eliminated to a great extent and the heat transfer away from the interface was enhanced.

Results of the actuation measurements are in correspondence with the results of the finite element simulations within 5-10 %. As well as the reliability of the measurements, this good agreement indicates that the finite element model is rather good. However, there are small deviations in the measurements of some devices (see APPENDIX G): Due to out-of-plane movement of the end-effectors during both opening and closing and since the end-effectors go out of the rectangular area of interest (see APPENDIX F) during opening.

Spring constants of the three-beam and topology optimized microgrippers were measured by AFM measurements. Although the experimental results for the three-beam microgrippers are in agreement with the results of the finite element simulations, there is a one order of magnitude difference between the experimental results for the topology optimized microgrippers and the results of the finite element simulations. Two sets of experiments were performed, where more than one device of the same kind was measured. However, the above mentioned variation was seen during both.

The reason behind this disagreement may be the misalignment of the actuators during the measurements: If the actuators are not aligned parallel to the AFM cantilever, the AFM measurements respond to the external force by out-of-plane bending, i.e. also along the y-axis in Figure 6.6. The measured spring constant is lowered since the stiffness of the topology optimized microgrippers is much lower along the y-axis than that in the z-axis (see Figure 6.6), e.g. for smoothed design B the values are 21 N/m vs. 234 N/m, respectively.

Misalignment of the three-beam microgrippers does not have a significant effect on the stiffness measurements since the stiffness of the topology optimized microgrippers along y-axis is not much different from that along z-axis, e.g. 10 N/m and 2.2 N/m, respectively.

The stiffness measurements can be improved by precise alignment of the actuators with respect to the AFM cantilever. This can be done by using a high-magnification camera instead of a low-magnification one. Also, the experiments can be performed inside an SEM,

where the force is calculated from the deflection of the AFM cantilever, by image processing [118].

Temperature measurements of the topology optimized microgrippers were performed at EMPA Materials Science and Technology, in Thun, Switzerland. The value of the linear coefficient of peak shift associated with temperature was determined as $d\Omega/dT = 0.035\ cm^{-1}{}^{\circ}C^{-1}$. However, this value is higher than the values in the literature [115]. The reason behind this may be the dopant concentration of poly-Si and the internal stresses in the microgrippers [112].

The results of the temperature measurements are in a good agreement with the non-ideal case finite element simulation results, with an accuracy in the range from 10 to 30 °C. This corresponds to an error on the order of 4-12 %, which is similar to the earlier reportings [112, 119].

However, measurements for some points on a few devices are rather different from the corresponding finite element results. One reason may be the mechanical stresses concentrated at these measurement points [112]. Another reason may be the out-of-plane movement of the microgrippers during the measurement due to the instability of the XYZ stage.

Furthermore, the experimental results for the lead temperatures of the devices with two-leads are much lower than the values expected by the finite element simulations. This may be the fact that the length of the leads included in the finite element model is not sufficient for simulating the heat transfer behavior of these devices. The agreement between the experimental results the finite element simulations can be achieved by improving the finite element model by extending the length of the leads and the carrier chip. However, this adds to the number of mesh elements, and hence, the analysis time.

The results of the mapping measurements are also in a good agreement with the finite element simulations. However, these measurements were performed only for one device due to the lack of time.

CHAPTER 7
Nanomanipulation and Assembly

7.1 Introduction

Topology optimized microgrippers are powerful tools for pick-and-place nanomanipulation of nanostructures, mainly CNTs, since they were especially designed for this purpose. In this chapter, nanomanipulation experiments performed with the topology optimized microgrippers will be explained.

Initially, the nanomanipulation setups used at different laboratories will be introduced. Then, the basic nanomanipulation procedure will be described. Finally, the results of various manipulation experiments performed will be presented.

7.2 Nanomanipulation Setups

During this work, various setups were used for manipulation and assembly of nanostructures. All these setups at different laboratories will be introduced in the following sections.

7.2.1 Setups at DTU

There are various nanorobotic systems at DTU Nanotech. During this thesis, two of them were used: A 2×3D system and a 13D system. Both these systems utilize SmarAct nanopositioners and can be integrated inside an SEM.

The first system at DTU is composed of two 3D SmarAct robots, each of which consists of three nanopositioners (SL-2040-S). Each nanopositioner has an integrated position sensor. Dimensions of the 3D robots are 40×70×58 mm^3 and they have a working area of 27×27×27 mm^3. The minimum and maximum step sizes are 50 nm and 500 nm, respectively, with a sub-nanometer resolution. The number of steps, the amplitude and the frequency of each 3D robot can be controlled through an individual control box.

The 2×3D system can either be placed under an optical microscope, or integrated inside a JEOL JSM-5500 SEM, using a special SEM door and a stage, i.e. the so-called “Catwalk” platform (Figure 7.1). Microgrippers can be mounted on the 3D robots, via a ZIF socket interface. The sample and the target substrates can be mounted on the SEM stage.

Details on how to use the 2×3D system can be found in [120].

The second system at DTU is based on a 13D SmarAct nanomanipulator, which consists of four 3D robots (SLC-1720) and a rotary positioner (SR-1908). Dimensions of the 13D system are 80×80×32.5 mm^3 and each 3D robot has a working area of 12×12×12 mm^3, where the working area of the rotary stage is unlimited. The minimum and maximum step sizes are 50 nm and 500 nm, respectively, with a sub-nanometer resolution. The number of steps, the amplitude and the frequency of all components can be controlled through a single control box.

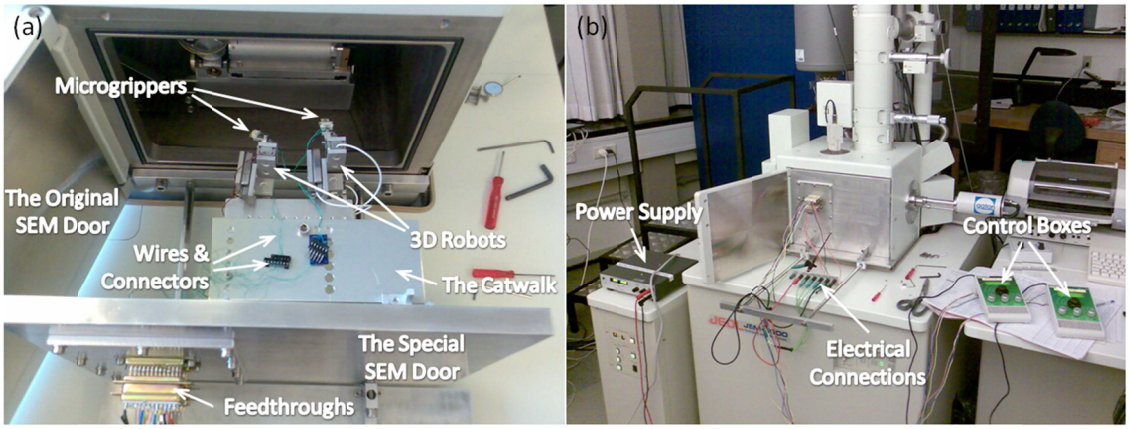

Figure 7.1 The 2×3D nanomanipulation system integrated inside a JEOL JSM-5500 SEM at DTU MEK when the SEM door is (a) open and (b) closed.

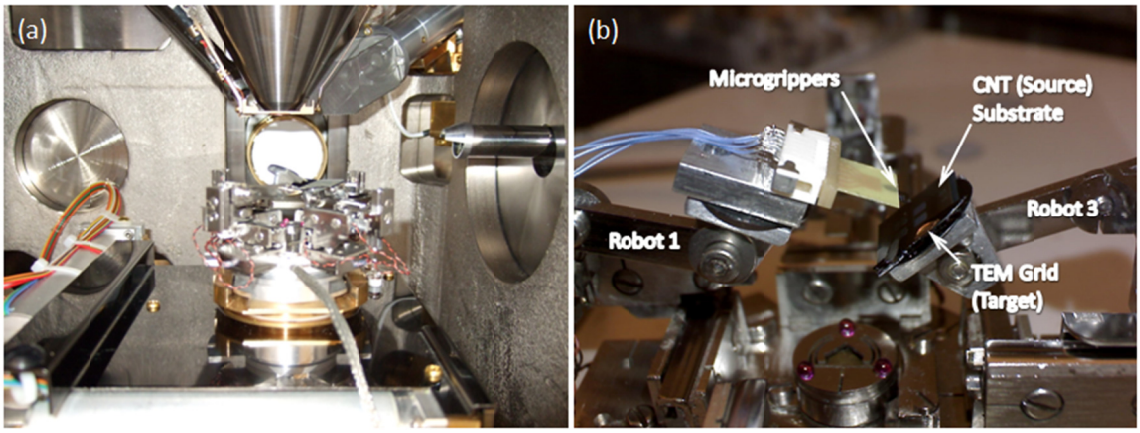

Figure 7.2 (a) The 13D nanomanipulation system integrated inside a JEOL JSM-5500 SEM at DTU MEK and (b) the orientation of the microgrippers and the source substrate and the target, where only two of the 3D robots are used.

The 13D system can also be used under an optical microscope or inside an SEM. However, for integration inside an SEM, the need for the special SEM door is eliminated since the system can simply be mounted on the SEM holder (Figure 7.2 (a)). This enables integration of the system inside different SEM models. The 3D robots can again be equipped with a ZIF socket interface. The sample and target substrates can either be mounted on the rotary stage or on individual 3D robots (Figure 7.2 (b)). Details on how to use the 2×3D system can be found in [121].

7.2.2 Setups at AMiR (University of Oldenburg, Germany)

The initial setup at the Division of Microrobotics and Control Engineering (AMiR) consists of two different manipulators: A 3D Kleindiek micromanipulator for coarse positioning and a 3D Physik Instrumente nanopositioning stage for fine positioning (Figure 7.3) [122].

The minimum step size of the Kleindiek manipulator is 5 nm for the two rotational axes and 0.25 nm for the linear axis. The microgrippers are mounted on the Kleindiek manipulator, which is equipped with a ZIF socket interface.

The full range of the nanopositioning stage is 50 µm, where the resolution of each linear axis is 1.55 nm, which is limited by the electronics (16-bit D/A converter of the control module). The target and the source substrates are placed on the nanopositioning stage.

Both manipulators are assembled on a special base plate, which can be mounted on the SEM stage.

During the project, the Kleindiek manipulator is replaced with a 4D SmarAct system, which enables rotation of the microgrippers during nanomanipulation (Figure 7.4) [123]. The 4D system consists of three (SL-2040-S) nanopositioners with integrated position sensors and one rotary nanopositioner (SR-1908). The properties of the 4D system are similar to those of the 3D robots mentioned in the previous section.

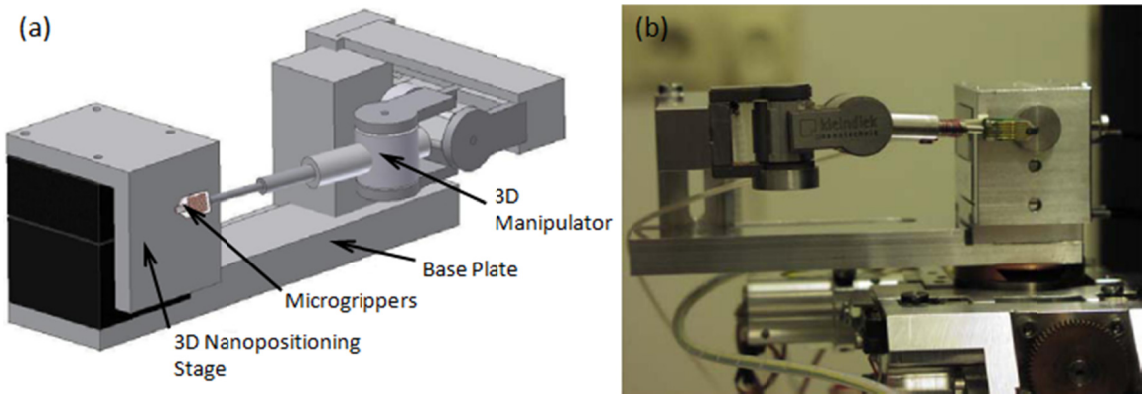

Figure 7.3 (a) Schematic illustration of the initial nanomanipulation setup at AMiR and (b) the actual setup mounted on the stage of a LEO 1450 SEM [122].

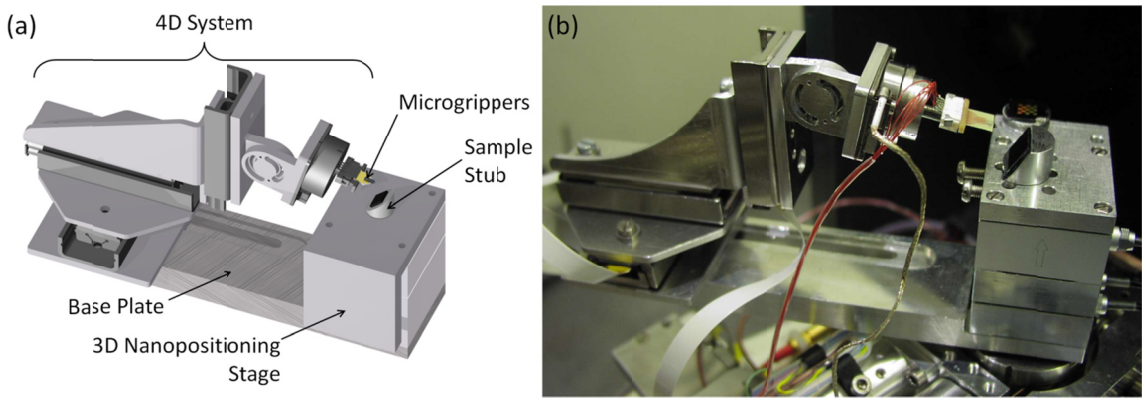

Figure 7.4 Schematic illustration of the improved nanomanipulation setup at AMiR and (b) the actual setup mounted on the stage of a LEO 1450 SEM [123].

7.2.3 Setup at Klocke Nanotechnik (Aachen, Germany)

The setup at Klocke Nanotechnik consists of four 3D nanomanipulators, which are mounted on the ceiling of the chamber of a TESCAN MIRA SEM, and a 5D sample stage, i.e. the SEM stage (Figure 5.1) [124].

The nanomanipulators have strokes of 20 mm in x- and y-directions and 10 mm in z-direction. They allow both coarse and fine positioning with close loop operation through integrated force sensors. The repeatability and the resolution of the nanomanipulators are 50 nm and 1 nm, respectively.

Microgrippers can be mounted on individual nanomanipulators, where a number of sample and target substrates can be mounted on various stubs on the sample stage. The nanomanipulators can be controlled manually using a keypad and via the Nanofab user interface.

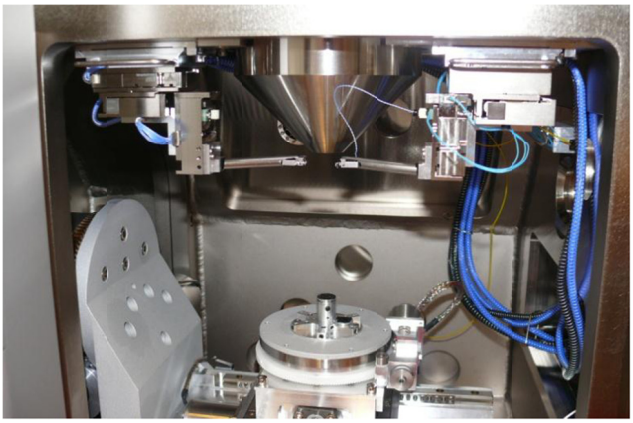

Figure 7.5 The nanomanipulation setup inside a Tescan MIRA SEM at Klocke Nanotechnik [124].

7.3 The Procedure

Initially the nanomanipulation tool, i.e. the microgrippers, and the sample and the target substrates should be mounted inside the SEM chamber with a proper alignment. Generally, the alignment should be as follows:

The sample substrate should be fixed on a 15-60° slanted sample stub, generally using a carbon pad. The target substrates, e.g. a TEM grid or a cantilever chip, can either be fixed near the edge of the sample stub or on a secondary stub, again using small pieces from a carbon pad. The stub(s) can be mounted either on a nanomanipulator or on the sample stage.

The microgrippers should be mounted on the arm of a nanomanipulator through a PCB-ZIF socket interface. Note that, the microgripper chip may face downwards, depending on the direction that the interface is mounted on the nanomanipulator arm.

Finally, the end-effectors of the microgrippers should be aligned perpendicular to the surface of the sample substrate and a few millimeters above it. Once all components are mounted inside the SEM chamber and the chamber is pumped down, the general procedure for nanomanipulation inside an SEM is explained in Table 7.1.

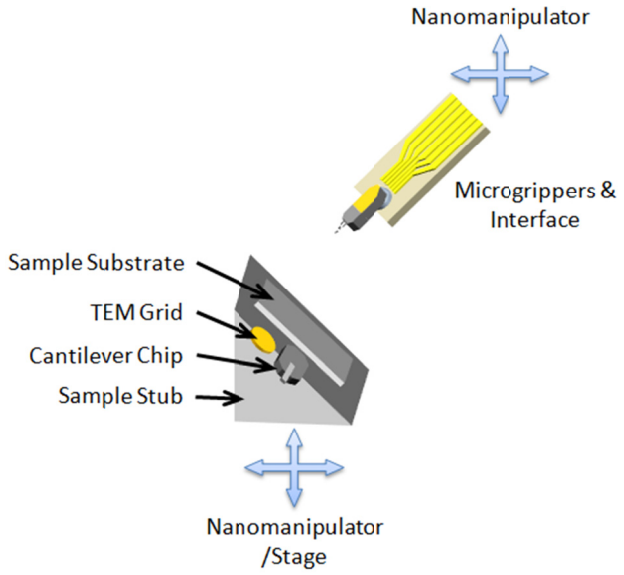

Figure 7.6 Schematic illustration showing the basic alignment of the components prior to nanomanipulation (see also Figure 7.2 (b)).

Table 7.1 The general procedure for nanomanipulation inside an SEM.

Step 1	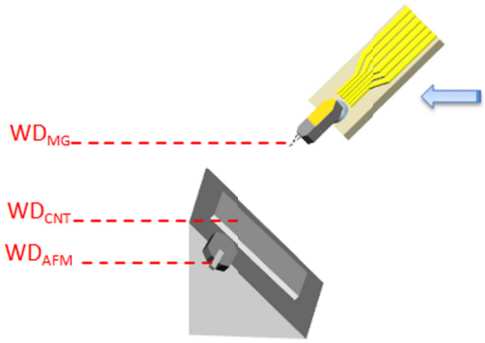		The microgrippers are brought into the field of view, the SEM image is adjusted properly and the working distance (WD) is noted. The same procedure is repeated for both the sample, e.g. the CNT, and the target structures, e.g. the tip of the AFM cantilever, respectively.
Step 2	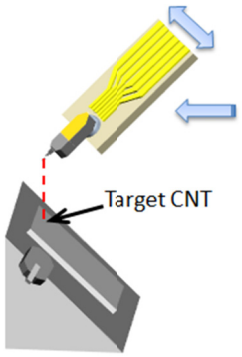		The microgripper chip is aligned over the sample structure.
Step 3	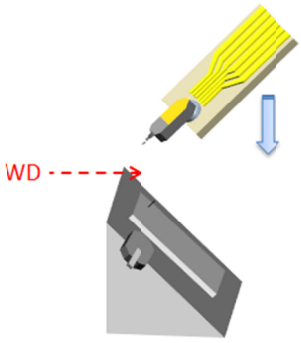	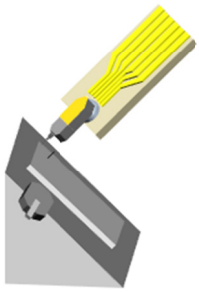	The WD is set to a value roughly corresponding to the mid-way between the microgrippers and the sample structure. Then, the microgripper is brought into focus by moving the nanomanipulator arm down with rough steps. The same procedure is repeated until there is less than 1 mm left between the microgrippers and the sample structure.

Table 7.1 Continued.

Step 4	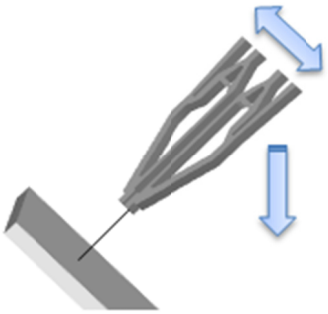	The sample structure is aligned in-between the end-effectors of the microgrippers with fine steps. The tip of the sample structure is shadowed as it is in-between the end-effectors. This happens since some of the secondary electrons scattered by the sample structure are emitted by the end-effectors. However, the alignment should be checked by moving the microgripper sideways prior to gripping.
Step 5	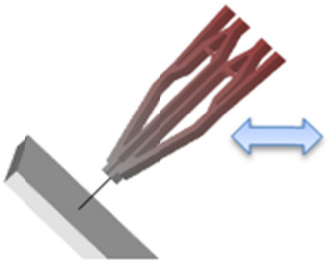	The microgripper is actuated slowly, in case there is a forward and/or out-of-plane motion due to the thermal expansion of the interface. Also any forward and/or out-of-plane motion should be compensated by moving the microgripper in the inverse direction.
Step 6	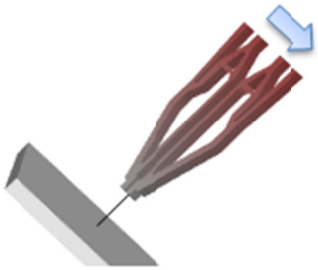	Once the end-effectors are completely closed, the sample structure should be detached by moving the microgripper sideways, i.e. shear gripping. In the case of a long CNT, the end-effectors should be aligned ~5 µm away from the CNT's base. If the length of the CNT is shorter, the end-effectors should be aligned at the mid-length of the CNT.

Table 7.1 Continued.

Step 7	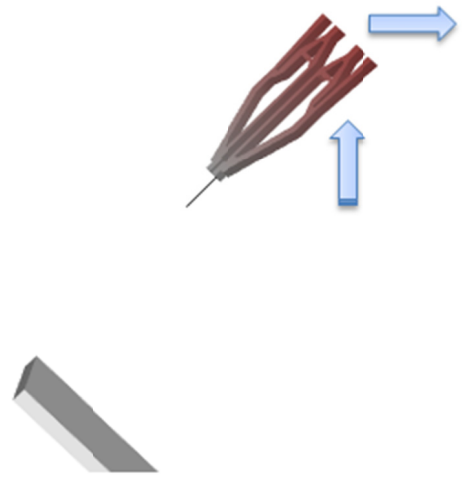	The micrograpper is moved away from the sample substrate and up until a safe position is reached.
Step 8	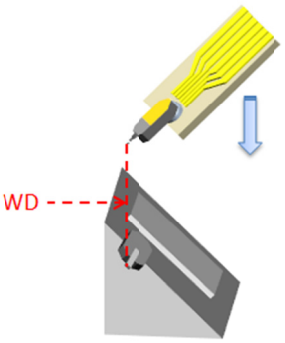 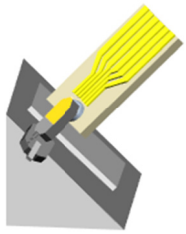	The WD is set to a value roughly corresponding to the mid-way between the micrograppers and the target structure. Then, the rough approach between the micrograpper and the target structure is performed similar to Step 3.
Step 9	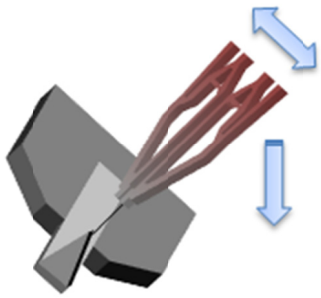	The free end of the gripped sample is properly aligned to the target structure, i.e. the tip of the AFM cantilever or one of the TEM grid beams. Then, contact is achieved by moving the micrograppers down with fine steps. Note that, the contact area between the gripped sample and the target structure should be as large as possible.

Table 7.1 Continued.

Step 10	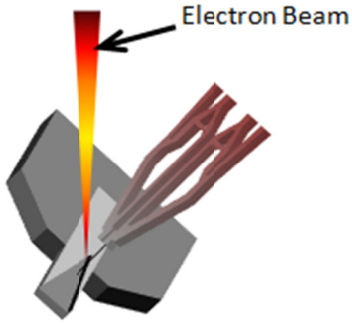	The sample structure is glued on the target surface by e-beam induced deposition (EBiD), i.e. deposition of a carbonaceous material by focusing the e-beam with a high current over the overlap area.
Step 11	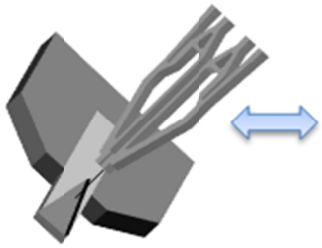	Once the contact is achieved, the voltage on the microgripper is released, again slowly, in order to be able to compensate any backward and/or out-of plane motion.
Step 12	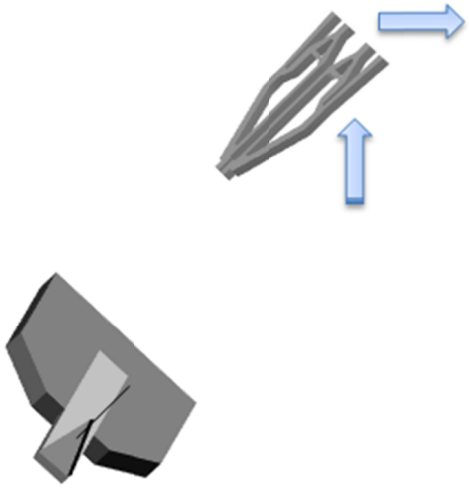	The microgripper is moved backwards and up with fine steps and the contact between the gripped sample and the end-effectors is broken.

Table 7.1 Continued.

Step 13	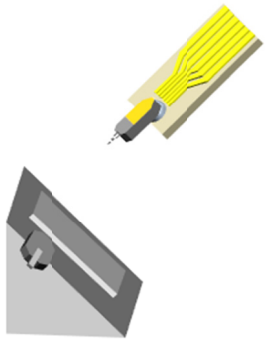	The micrograpper is moved away from the assembled target structure and up until a safe position is reached.

Note that, if the precision of the sample stage is better than that of the nanomanipualtor, which is equipped with the micrograpper, the sample can be moved instead of the micrograpper for the alignment purposes mentioned in steps 3-6, 8, 9 and 12 above; however, in reverse directions.

Furthermore, if the control software enables, safe positions near each component can be defined and stored through the user interface and the rough approaching steps, i.e. steps 3, 7, 8 and 13, can be performed automatically.

During the EU funded NanoHand project, an automated nanomanipulation system was developed at AMiR, where assembly of CNT-enhanced AFM super-tips is performed through a user interface and only by clicking a few buttons. Once a single CNT is found, the remaining steps are simply as follows:

1. A number of CNTs are found on the sample substrate and indexed.
2. Micrograppers are brought into the field of view, aligned with the CNT and actuated.
3. The CNT is gripped by shear-pulling and the voltage on the micrograppers is released.
4. AFM tip is brought into the field of view.
5. Micrograppers are brought into the field of view, aligned with the AFM tip and the CNT is assembled on the tip by retracting the micrograppers with fine steps.
6. The CNT is fixed on the AFM tip by EBiD.

As mentioned above, all these steps are automated and can be performed even by an inexperienced operator.

7.4 Nanomanipulation and Assembly with Topology Optimized Microgrippers

Topology optimized microgrippers were used in manipulation and assembly of PECVD–grown multi-walled (MW) CNTs, Si NWs and silicon dioxide/nitride NanoBITS. In addition to the microgrippers with original end-effectors, microgrippers with FIB-modified end-effectors were also used in the experiments. In the following sections, results of these nanomanipulation and assembly experiments will be presented.

7.4.1 Nanomanipulation and Assembly of CNTs

Topology optimized microgrippers were used for manipulation of CNTs onto TEM grids and electrodes, i.e. four-point probes (FPPs), for structural and electrical characterization, respectively. Also CNT-enhanced AFM super-tips were assembled, again using topology optimized microgrippers.

Relatively small MWCNTs, which are 1-2 µm-long and ~120 nm in diameter, were picked from a 5 µm 2D array and placed onto a TEM grid for structural characterization (Figure 7.7). A microgripper with tilted design B was used during the experiment, which was performed at DTU using the 13D nanomanipulation system.

Similar experiments with longer and larger diameter CNTs were performed together with Volkmar Eichhorn at AMiR using both setups, where ~20 µm-long and ~300 nm in diameter MWCNTs, were picked from a 50 µm 1D array. These CNTs were then, placed onto TEM grids for structural characterization (Figure 7.8) (see Section 7.6) and onto FPPs for electrical characterization (Figure 7.9). Smoothed and tilted versions of design B were used, respectively, during these experiments. Note that, when placing the CNTs on the TEM grid, the rotation feature of the 4D SmarAct system was used successfully.

Furthermore, assembly of CNT-enhanced AFM super-tips was performed at AMiR (Figure 7.10 (a)-(c)). AFM scans performed with the assembled super-tips reveal that their performance is much better than that of an ordinary AFM tip (see Section 7.7).

Electrical characterization of the samples manipulated onto FPPs was not yet successful due to the high contact resistance between the CNTs and the thin gold layer on the FPP beams. However, the efforts for achieving less contact resistance are still continuing at AMiR.

All experiments performed at AMiR were reproducible and multiple devices were assembled during most of these experiments without venting the SEM chamber (Figure 7.10 (d)-(f)).

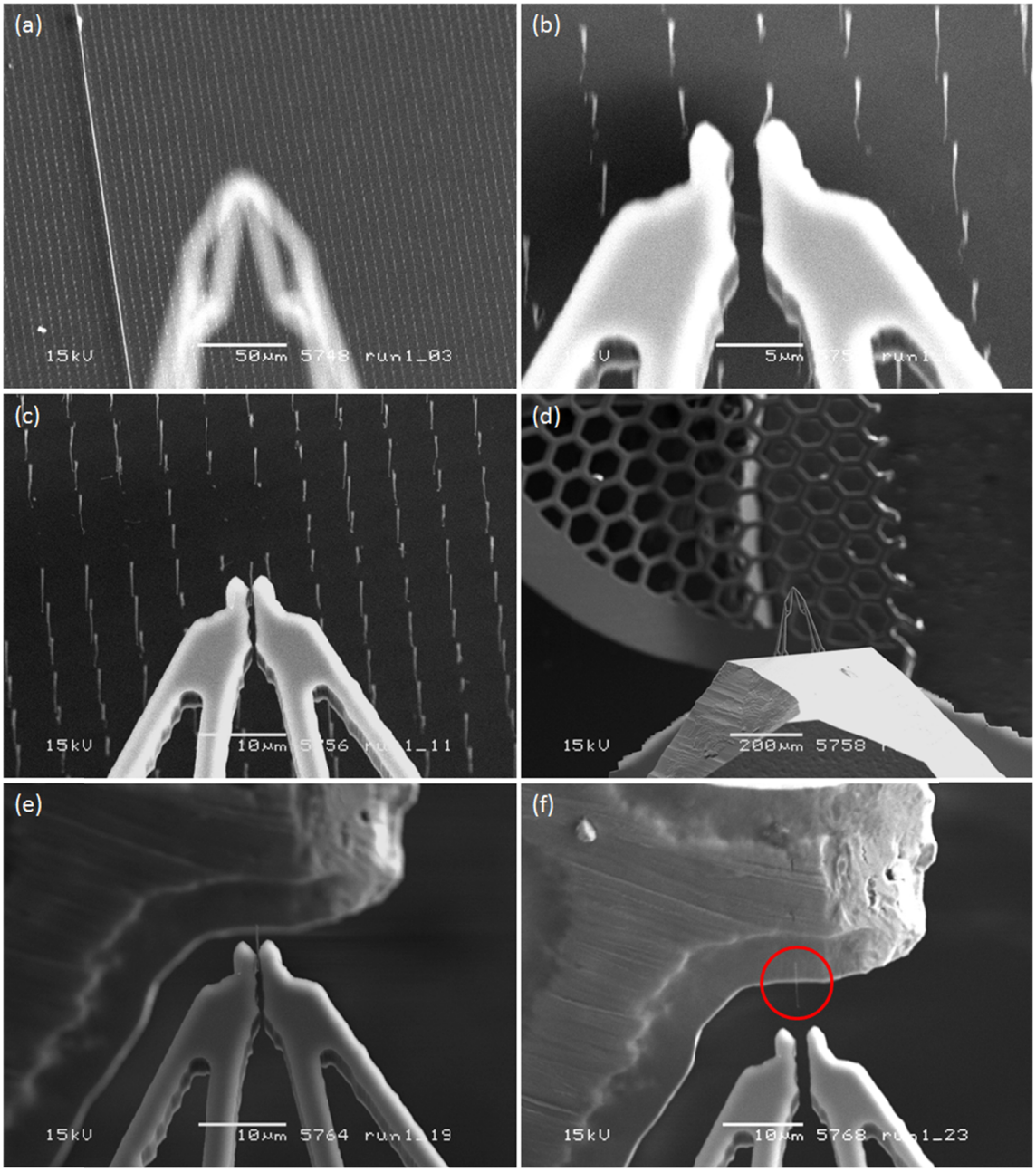

Figure 7.7 Nanomanipulation sequence showing pick-and-place of a 120 nm-diameter CNT onto a TEM grid (DTU): (a) Topology optimized microgrippers approaching the 5 µm 2D CNT array. (b) Bending a CNT with the microgrippers. (c) CNT picked from the array by actuating the microgrippers. (d) Microgrippers approaching the half-divided TEM grid with the gripped CNT between the end-effectors. (e) Proper alignment of the CNT with respect to the grid edge. (f) CNT placed on TEM grid and the microgrippers released.

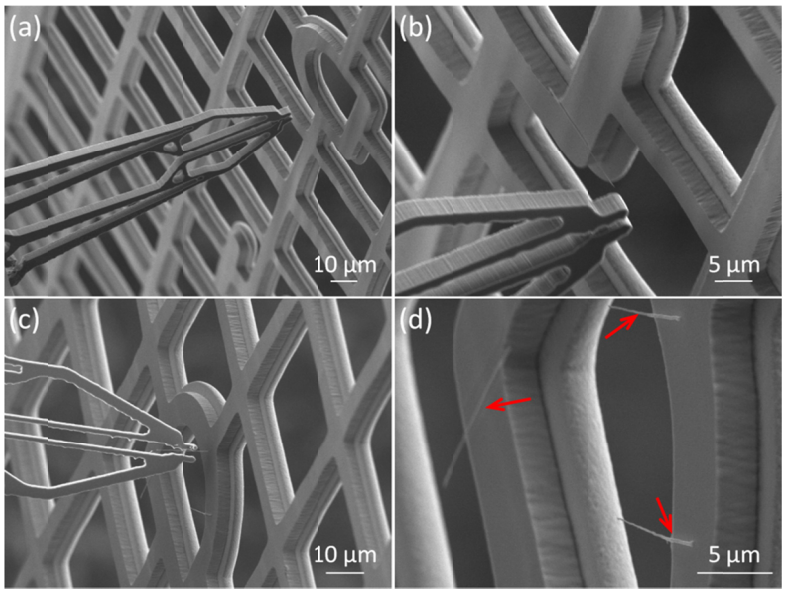

Figure 7.8 Pick-and-place of 300 nm-diameter CNTs onto a TEM grid (AMiR): (a) Approaching the TEM grid with the gripped CNT. (b)-(c) Placing the first and the third CNTs on the TEM grid. (d) Close-up view of the three CNTs placed on the TEM grid.

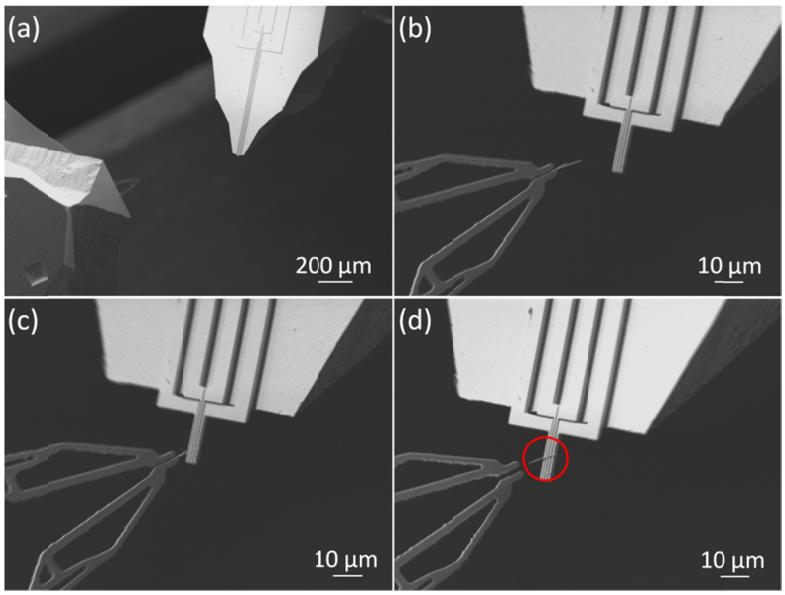

Figure 7.9 Pick-and-place of 300 nm-diameter CNTs onto FPPs (AMiR): (a) Overview and (b) close-up views of approaching the FPP with the gripped CNTs. (c) Aligning the CNTs over the FPP. (d) The CNTs placed on the FPP and the microgripper is moved away.

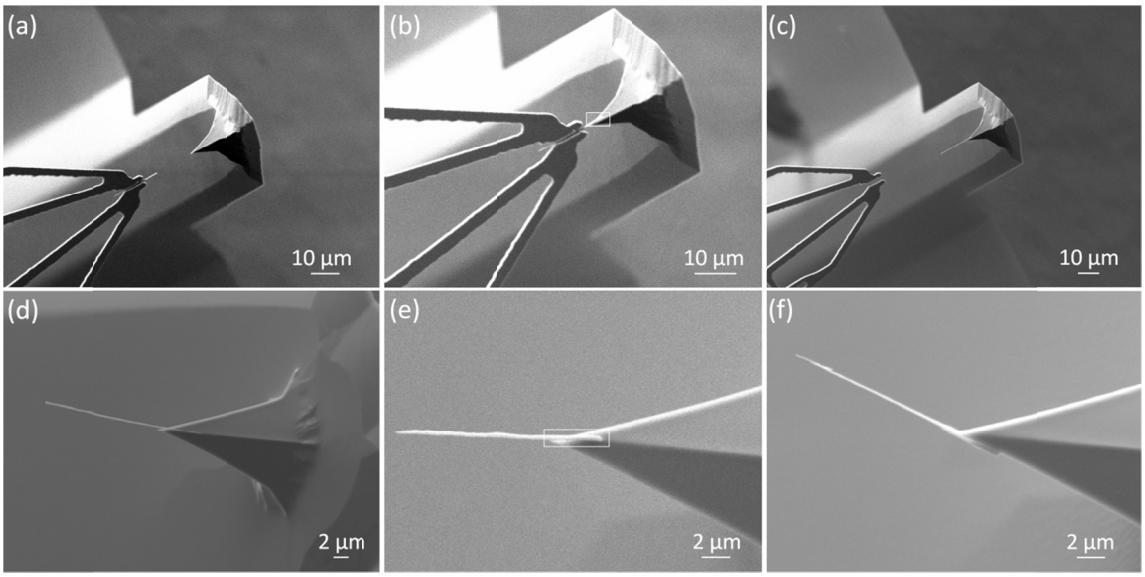

Figure 7.10 Assembly of CNT-enhanced AFM super-tips (AMiR): (a) Approaching the AFM tip. (b) Aligning the CNT to the AFM tip, achieving contact between the free end of the CNT and the AFM tip and gluing with EBiD. (c) The CNT assembled at the AFM tip and the microgripper is moved away. (d)-(f) Three super-tips assembled during the same experiment and without venting the SEM chamber.

The experiments performed together with Ralf Kauffman at Klocke Nanotechnik were not quite successful. The main reason for this was the condition of the CNTs, which were coated with an unknown, thick layer of material. This layer is most probably due to melting of the gold layer on the bonding pads, or due to melting the glue (see Section 5.3). Hence, instead of bending when contacted, they were easily detached from the substrate and disappeared (Figure 7.11).

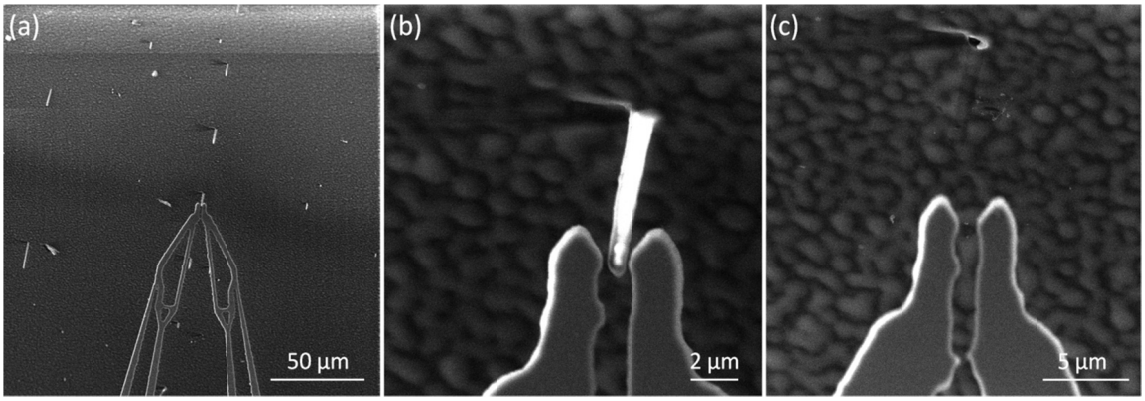

Figure 7.11 (a) Overview of the CNT sample used during the nanmanipulation experiments at Klocke Nanotechnik. (b) Approaching a CNT contaminated by an unknown, thick layer of material. (c) The CNT was easily detached and disappeared when contacted.

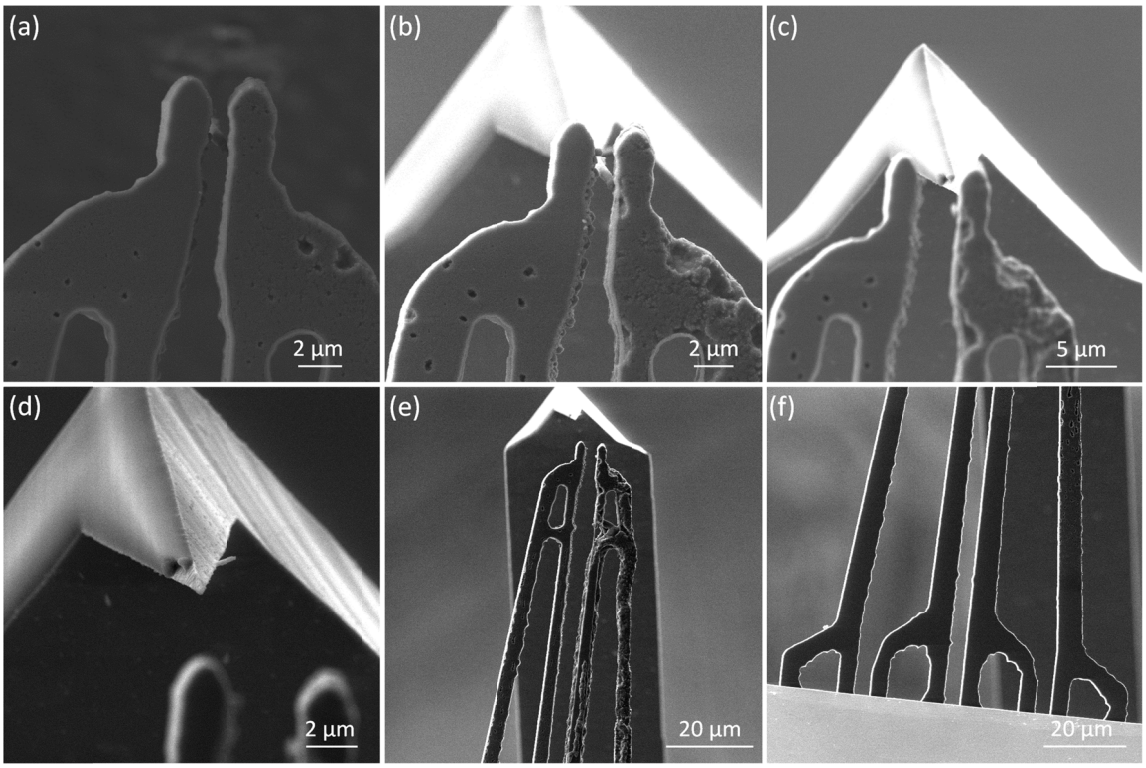

Figure 7.12 Gradual melting of the microgrippe with the divided electrode design during a nanomanipulation experiment (Klocke Nanotechnik): (a) Approaching a contaminated CNT. (b) The gripped CNT was vertically aligned between the end-effectors of the microgripper. (c) Approaching the AFM cantilever. The CNT was lost since the microgripper did not actuate properly anymore. (d) The AFM tip was damaged due to excess heating. (e)-(f) Overview of the melted microgripper after the experiment.

Another reason was that, microgrippers with the divided electrode design (Figure 2.19) were used during these experiments. These microgrippers were melting due to excess heating during the manipulation experiments (Figure D.49). Hence, although CNTs were successfully gripped, the microgrippers were becoming useless before their assembly (Figure 7.12).

7.4.2 Nanomanipulation and Assembly of NanoBITs

In addition to manipulation and assembly of 1D nanostructures, such as CNTs, topology optimized microgrippers were also used for manipulation and assembly of 2D nanostructures: NanoBITs (NanoBITs).

NanoBITs are exchangeable tool tips, which can be assembled on standard pyramidal AFM tips by direct manipulation (Figure 7.13). They enable realization of more complex tip shapes for various purposes, e.g. side-wall scan. NanoBITs can be fabricated from thin membranes of both silicon dioxide and silicon nitride by planar e-beam lithography (EBL) by R T Rajendra Kumar and S Uddin Hassan. More information on NanoBITs can be found in [125].

The procedure for nanomanipulation of the NanoBITs is slightly different than that of the CNTs (Figure 7.14). There are mainly two procedures: If the microgrippers have a 2 µm gap, they are not completely closed while gripping NanoBITs. Instead, they are actuated until the end-effectors apply a sufficient force to the NanoBITs 1 µm-wide handle without damaging it (Figure 7.15 (b)). If the microgrippers have rough end-effectors, and hence, an effective gap size less than 1 µm (Figure 7.14 (b)), they can be actuated in the opening mode and the gripping can be performed by releasing the voltage. The second approach is more advantageous since any possible damage due to the end-effector temperature is eliminated.

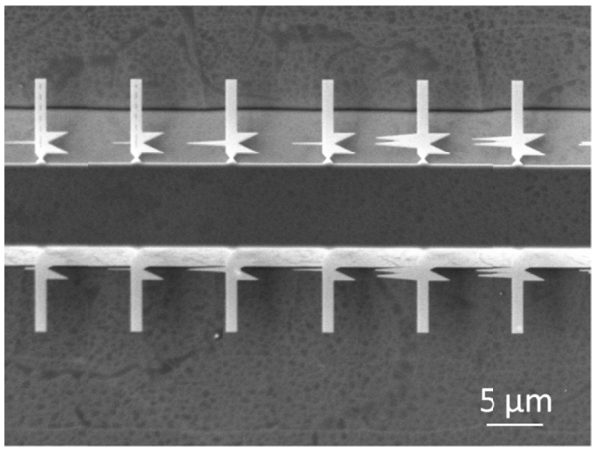

Figure 7.13 A library of Si_3N_4 NanoBITs with different tip shapes.

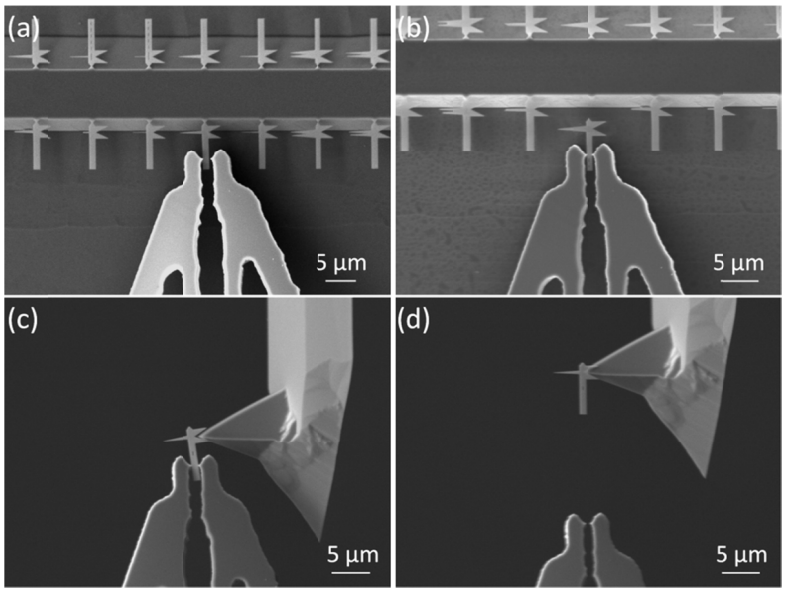

Figure 7.14 Assembly of NanoBITs on an AFM tip: (a) Approaching the selected NanoBIT while the microgripper is actuated in the opening mode. (b) Gripping the NanoBIT by releasing the voltage. (c) Proper alignment of the NanoBIT with the pyramidal tip. (d) The NanoBIT assembled at the AFM tip, using EBiD.

In addition to the assembly of NanoBITs on pyramidal AFM tips, an ordinary cantilever can be converted into a probe by inserting the NanoBITs into a FIB-cut slit at its front edge (Figure 7.15). This can be done by inserting the gripped NanoBIT into the slit by moving the microgrippers with fine steps. Once, the NanoBIT is completely inside the slit, the microgrippers are retracted, again with fine steps, by moving the microgrippers down and away (Figure 7.15 (d)). Here, the NanoBIT, itself, serves as the tip.

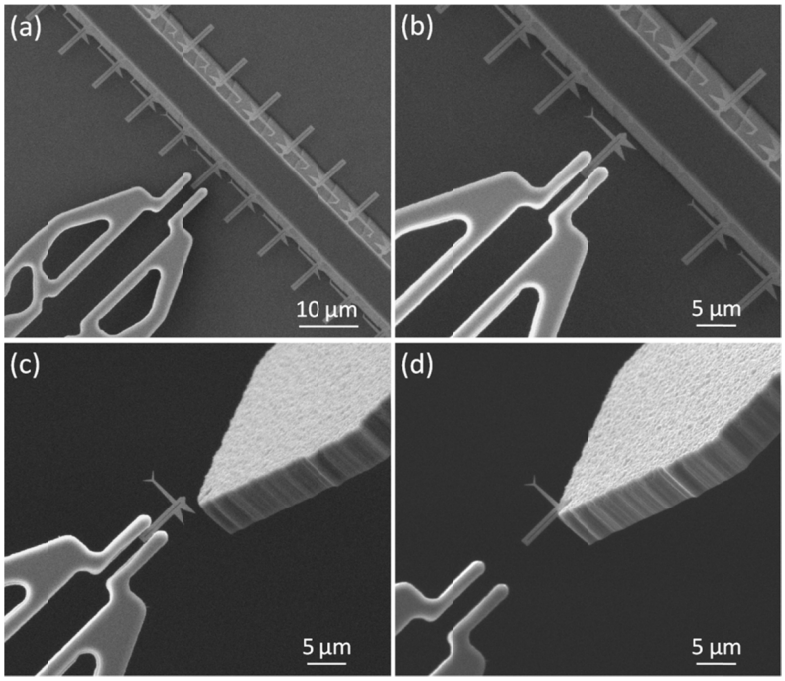

Figure 7.15 Assembly of NanoBITs on a tip-less cantilever: (a) Approaching the selected NanoBIT. (b) Gripping the NanoBIT by actuating the microgrippers slightly in the closing mode. (c) Approaching the cantilever with a FIB-cut slit. (d) The NanoBIT inserted into the slit by moving the microgrippers down and away.

7.5 Nanomanipulation with FIB Modified Microgrippers

Microgrippers with FIB-modified end-effectors were also used in manipulation of silicon NWs onto FPPs (Figure 7.16) and TEM grids (Figure 7.17) for electrical and structural characterization, respectively. In these experiments, the microgrippers were slightly actuated in the opening mode while picking and placing the NWs and let in the neutral position during transport.

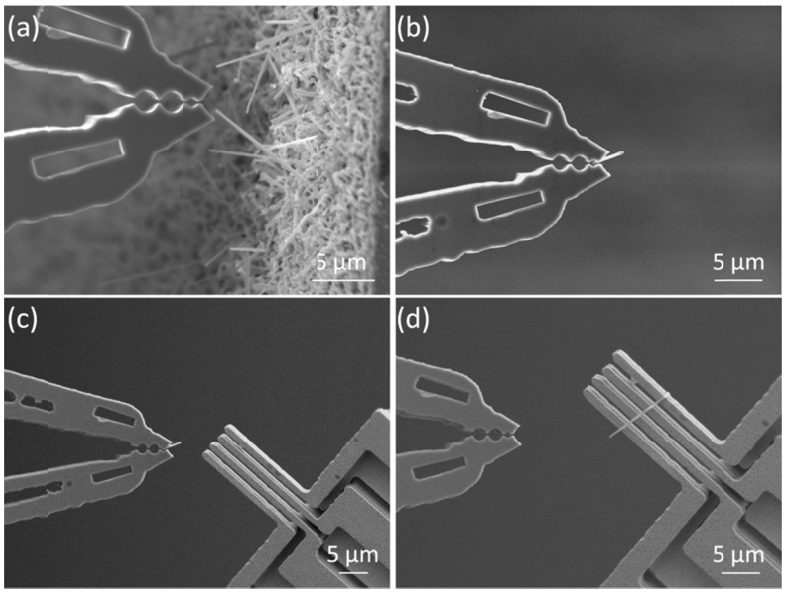

Figure 7.16 Pick-and-place of a silicon NW onto a FPP: (a) Approaching a protruding NW within the bundle. (b) The gripped NW between the end-effectors while the microgripper is in the neutral position. (c) Approaching the FPP. (d) The NW placed on the FPP.

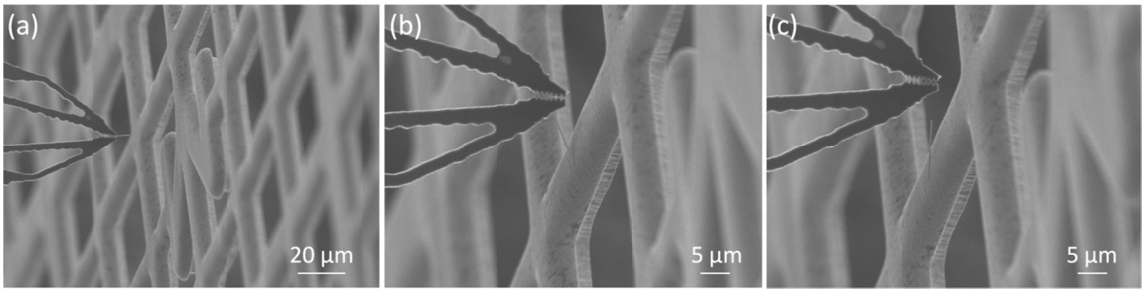

Figure 7.17 Pick-and-place of a silicon NW onto a TEM grid: (a) Approaching the TEM grid with the gripped NW. (b) Releasing the NW. (c) The NW placed on the TEM grid.

7.6 Results of the TEM Experiments

CNTs and NWs placed on TEM grids during various experiments (Figure 7.7, Figure 7.8 and Figure 7.17) were investigated together with Lionel Cervera Gontard, using two different FEI TEMs at DTUs Center for Electron Nanoscopy (CEN): A TECHNAI T20 and a TITAN Analytical.

The 120 nm-diameter CNT placed on the half-divided TEM grid at DTU Nanotech (Figure 7.7) as well as the 300 nm-diameter CNTs placed on a TEM grid at AMiR (Figure 7.8) were investigated using the two TEMs (Figure 7.18 & Figure 7.19).

The high magnification TEM images clearly reveal the layered structure of the multi-walled CNTs, where the multi-walled hollow CNTs are surrounded by an amorphous carbon layer, which may have been deposited at the end of the PECVD growth (Figure 7.18 (c) & Figure 7.19 (a, top)). These layers are coated with a second, thin layer of amorphous material, which according to EDS measurements contains a high amount of silicon. Also remains of the nickel catalyst were observed at the tip and in the interior of the CNT along the longitudinal axis (Figure 7.18 (b) & Figure 7.19 (a, bottom)).

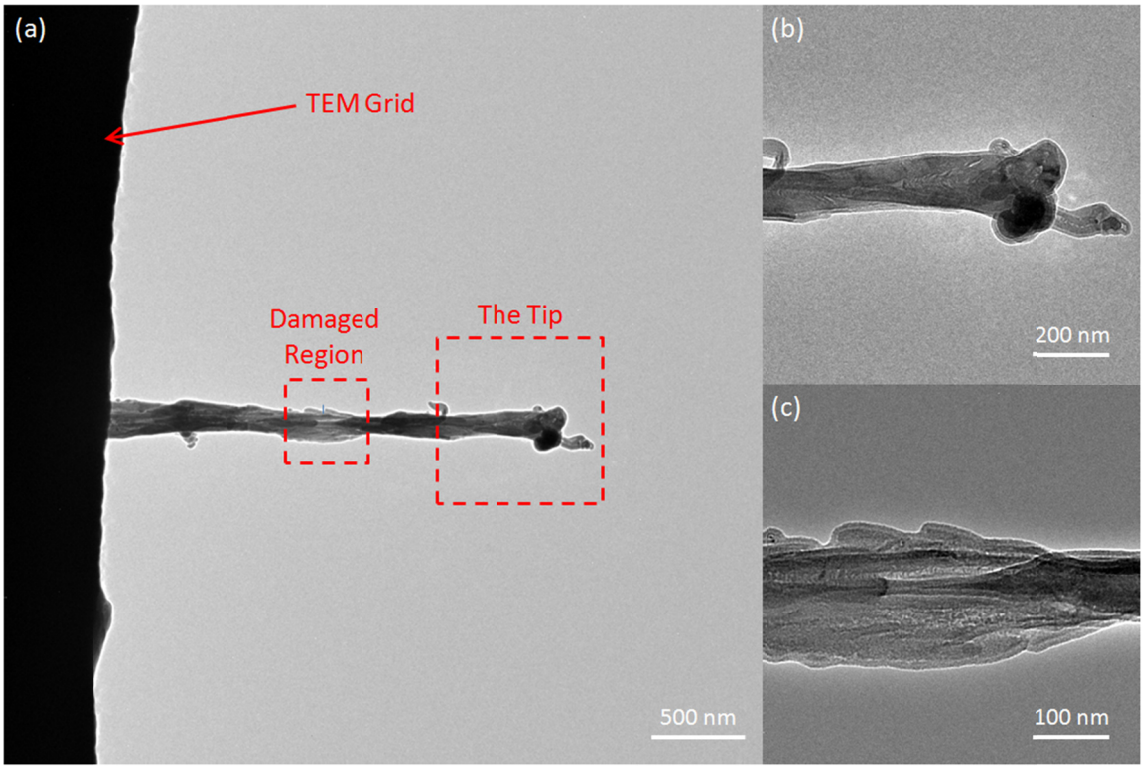

Figure 7.18 (a) Low magnification bright field (BF) TEM image of a 120 nm-diameter CNT (see Figure 7.7) with close up views of (b) the nickel catalyst at the tip and (c) the region damaged by the microgrippers at the centre.

Low magnification TEM images of the CNTs reveal that the CNTs were locally damaged along the CNTs' length (Figure 7.18 (a) & Figure 7.19 (a)). High-angle annular dark-field (HAADF) scanning transmission electron microscope (STEM) images of the CNT (Figure 7.19 (b))

clarify that the outer amorphous carbon layer is locally removed, with ~4.3 µm distance in-between.

However, it was not possible to investigate the silicon NWs placed on a TEM grid using FIB modified microgrippers (Figure 7.17) using a TEM. This was since the samples were lost during transportation or mounting, probably since they were not firmly fixed on the TEM grid. And the experiments could not be repeated due to time limitations.

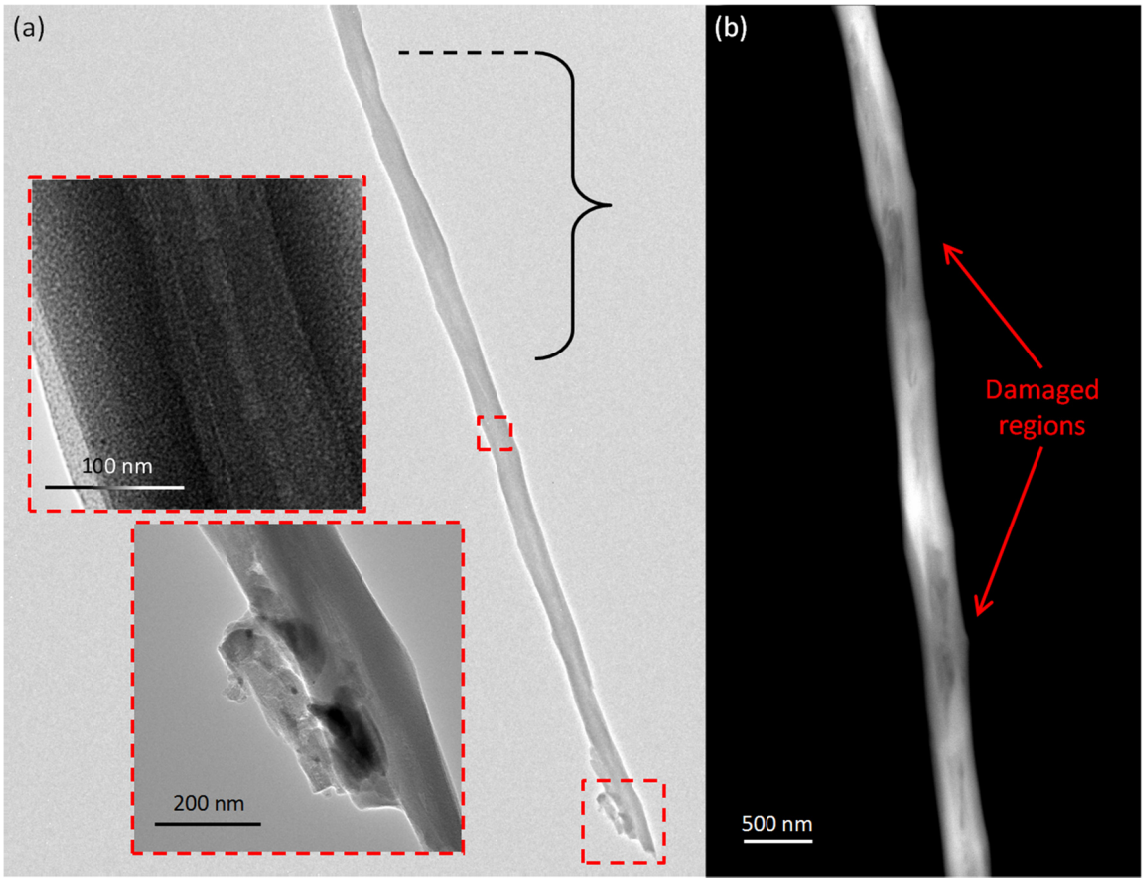

Figure 7.19 TEM images of a 300 nm-diameter CNT (see Figure 7.8) with (a) low-magnification BF image of the whole CNT with high-magnification views of the layered structure of the CNT (top) and the nickel catalyst at the tip (bottom) and (b) HAADF image clearly showing the damage caused by the microgrippers.

7.7 Results of the AFM Experiments

The CNT- (Figure 7.10) and NanoBIT-enhanced (Figure 7.14) AFM super-tips assembled using topology optimized microgrippers were used to perform AFM scans of high-aspect ratio microstructures, i.e. 2.5 µm-deep trenches etched in a silicon substrate (Figure 7.20).

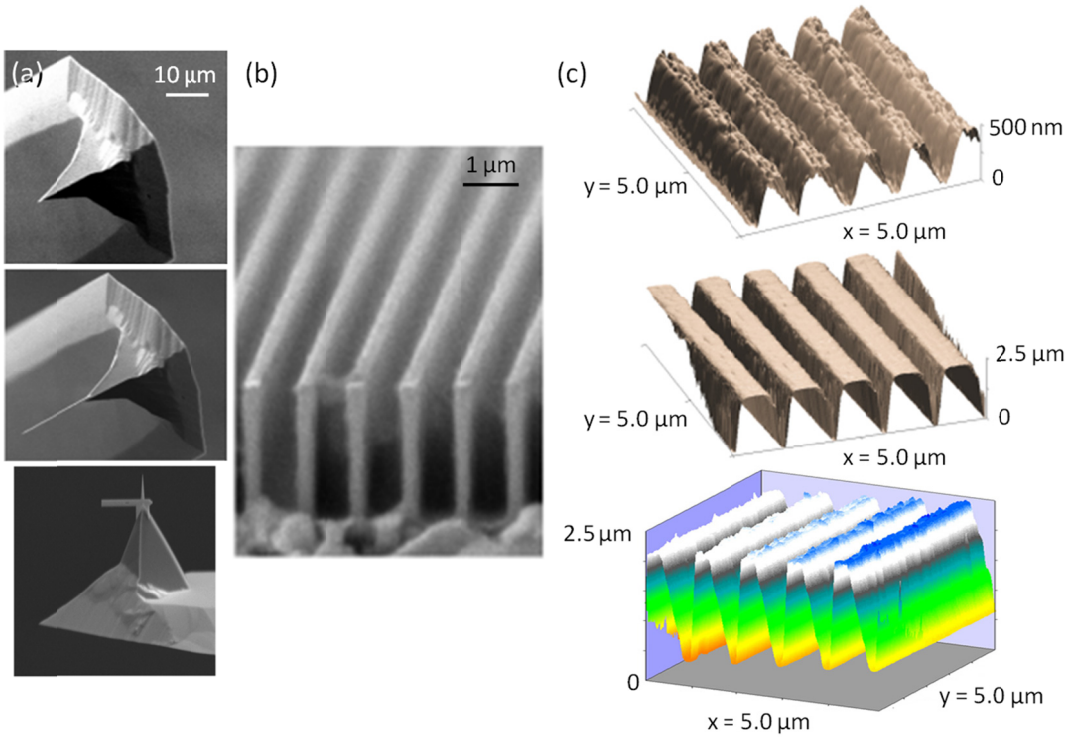

Figure 7.20 (a) A standard pyramidal AFM probe (top), a CNT-enhanced super-tip (middle) and a NanoBIT-enhanced super-tip (bottom) assembled during the experiments. (b) 2.5 µm-deep trenches etched in a silicon substrate. (c) Comparison of AFM scans of the deep trenches using the standard pyramidal AFM probe (top), the CNT-enhanced super-tip (middle) and the NanoBIT-enhanced super-tip (bottom).

7.8 Discussion

Reproducible and consecutive nanomanipulation experiments were performed inside SEM using the topology optimized microgrippers. These experiments include manipulation of CNTs and NWs onto TEM grids for structural analysis, assembly of CNT- and NanoBIT-enhanced AFM super-tips and manipulation of CNTs and NWs onto electrodes, i.e. FPPs, for electrical characterization.

TEM investigations of the CNTs reveal that an amorphous layer of mainly silicon was deposited on the CNTs during manipulation. Furthermore, it was observed that the amorphous carbon layer on the CNTs was damaged at locations contacted by the end-effectors and the amorphous carbon layer covering the multi-walled CNTs was locally removed. The reason behind the silicon contamination and the physical damage is most probably the high operation temperature of the microgrippers. However, the cause of the physical damage can also be only mechanical, or a combination.

In order to verify this, similar experiments were performed using devices with FIB modified end-effectors, where gripping was realized mechanically without actuating the microgrippers. Unfortunately, a comparison of the TEM results was not possible since the samples were lost during transportation or mounting. However, no damage would be expected on these samples if the reason is high-temperatures, where the damage would be at multiple points if the reason is the excessive mechanical forces.

The method used for assembly of CNT-enhanced AFM-super-tips in this project has various advantages over alternative methods, where the nanowires/tube is manipulated and assembled by the AFM tip itself with the help of Van de Waals forces [40, 41]. First of all, such methods are rather time consuming, where the reliability and the repeatability is rather poor. Hence, the assembled super-tips are rather rare and expensive. Secondly, there are significant constraints of large-scale fabrication on such devices and the automation of the nanomanipulation procedure. Furthermore, the control over the direction and orientation of the assembled nanostructures is also rather poor. Finally, the usage of an advanced nanomanipulation tool, such as microgrippers, rather than a passive tool enables manipulation of nanostructures with more complex geometries, such as NanoBITs, and hence, assembly of task-specific nanodevices.

AFM scans performed with the assembled CNT- and NanoBIT-enhanced AFM super-tips. As expected, the results for both kinds of devices turned out to be better than previous a reporting [52], where only 1.2 µm of the 2.5 µm-deep trenches was resolved. This is since the assembled structures were much longer. CNT-enhanced super-tips perform slightly better than the NanoBIT-enhanced super-tips due to the higher aspect ratio. However, with different shape geometries, NanoBIT enhanced super-tips will enable realization of more advanced experiments, e.g. side-wall or non-planar AFM scans.

When compared to the AFM super-tips assembled using single-walled CNTs [40], the resolution of the devices assembled in this work is lower. However, this is related to the CNTs used in the assembly. An the resolution can be enhanced by using nanotubes of similar size but with a tapered geometry [126].

CHAPTER 8
Conclusions and Outlook

During this Ph.D. thesis, electrothermal microgrippers were developed for nanomanipulation and assembly inside SEM. The microgrippers are compatible with the components of the nanorobotic systems developed during the NanoHand project and were successfully integrated into different systems available at the project partners. Furthermore, nanomanipulation of 300 nm-diameter CNTs was performed repeatedly, and in a reliable manner.

The details of the project and regarding conclusions are as follows:

Electrothermal actuation principle was selected for the microgrippers, mainly due to the availability of relatively high forces with a compact design. However, existing electrothermal microgripper designs were either rather bulky, or not strong enough.

In order to meet all requirements mentioned in Section 1.3 in one device, topology optimization was used in the design of the electrothermal microgrippers.

Initially, the conventional three-beam actuator design was taken as the basis and the design domain for the topology optimization was defined accordingly. However, since the optimization problem for the electrothermal actuators was highly non-linear, even a small change in the design parameters was resulting in a completely different design. For this reason, a number of analyses were performed using a range of different values for the most important design parameters. Three designs were selected among many others according to their performance, i.e. actuator force, actuation range and end-effector temperature, and feasibility for fabrication.

Then, actuators with two-electrodes were designed in a similar manner. However, instead of changing values of the design parameters, positions of electrodes were changed during the topology optimization analyses. Again, three high-performance designs were selected for further development.

Topology optimization results foresee that the designed microgrippers were one order of magnitude stronger than the conventional three-beam actuators. Since it is not possible to realize a structure with a variable material density as suggested by the topology optimization algorithm, the output should be processed prior to fabrication. For this purpose, the grey-scale bitmap image, i.e. the output, was converted into black & white and the beams were smoothed. As an optional step, some actuators were tilted in order to correct the line of motion. Note that, computer algorithms were not used during these

steps and all processing were manually performed by checking different parts of the actuators and considering fabricational limitations.

The performance of the post-processed designs was verified through the finite element simulations performed using COMSOL Multiphysics. Initially, the carrier chip was not included in the simulation model.

According to the results of these finite element simulations, the post-processed designs are 1-2 orders of magnitude stronger than the conventional three-beam design, which has a stiffness of 2.2 N/m. Hence, they are suitable for miniaturization.

The effects of design and fabrication variations on the performance of the topology optimized actuators were also investigated through finite element simulations. In order to compare the performance of different actuators from various aspects, a *robustness* parameter was introduced. Performance of a *robust* actuator is influenced less by fabricational variations.

The designed topology optimized actuators were fabricated through a sequence of conventional microfabrication processes. The fabrication yield was improved at each of the three batches, from 33 % to 90 %, and finally to 99 %. Also, side-wall profiles and dimensional accuracy of the devices were improved by using a fluorocarbon inhibited ASE process instead of an oxygen inhibited RIE process. The fabrication yield was further increased by functionalizing the devices with defects, e.g. merged end-effectors and/or missing design features, using FIB milling.

FIB milling was also used for achieving finer end-effectors, which enable easier access to small samples and do not have an influence on the quality of the image during manipulation inside an SEM. Furthermore, different end-effector designs with decreased contact area and a sub-micron gap were realized using FIB milling. Hence, the adhesion forces and the actuation necessary for completely closing the gap, consequently the temperature, were decreased, respectively. Finally, more advanced microgripper concepts, such as XY- and inverse microgrippers were realized, again, using FIB milling.

Actuation, stiffness and temperature of the fabricated devices were characterized using different setups.

For the actuation characterization, an optical manipulation setup with a LabView interface was used, where the gap-displacement was instantaneously calculated by image processing. The results of the actuation measurements are in agreement with the finite element simulation results for all designs within 5-10 %.

Stiffness of a selected design, its variations and three-beam actuators were determined through AFM force measurements. Although the experimental results for the three-beam actuators agreed rather well with the theory and the finite element simulations, there was

an order of magnitude difference between the two for the topology optimized actuators. The reason behind this was mainly the axial misalignment of the actuators with respect to the AFM cantilever. The effect of misalignment was not significant for the three-beam actuators since their lateral and out-of-plane spring constants were similar. However, the out-of-plane spring constants of topology optimized actuators were much smaller than their lateral spring constants. And hence, the experimental results were an order of magnitude less than expected.

A Raman spectroscopy setup was used for the temperature measurements of the microgrippers. In addition to the point measurements performed on along the topology optimized actuators, temperature mapping of a selected design was acquired by performing multiple measurements within a grid. Both the point measurements and the mapping results were in correspondence with the simulation results, however with an offset of 150-200 °C. This offset was mainly due to the assumption of constant temperature made in the non-ideal case finite element simulations. However, the carrier chip was heating up during actuation. In order to better estimate this behavior, a section of the carrier chip was also included in the finite element model and an agreement with the measurement results was achieved within 4-12 %.

Temperature measurements revealed that the carrier chip was excessively heating during actuation. This excess heat was resulting in elongation of the PCB interface, and hence out-of-plane movement of the microgrippers during actuation. Attempts were made in order to minimize this effect. Initially, the components of the package, such as the PCB interface and the glue, were replaced with those having high thermal conductivity and compatibility with high temperatures. Secondly, the lead design was improved, where the width of the electrodes was increased from 20 µm to 185 µm. With the new lead design a temperature drop of 50-100 °C was achieved. However, although the issues regarding the out-of-plane movement were considerably reduced, they have not been completely resolved

As mentioned in the beginning of this chapter, topology optimized microgrippers were successfully used in various nanomanipulation and assembly experiments inside an SEM. These experiments include manipulation of 300 nm-diameter CNTs and NWs onto TEM grids for structural characterization or onto electrodes for electrical characterization, and assembly of CNT- and NanoBIT-enhanced AFM super-tips. All these experiments were reproducible.

TEM investigations of the manipulated samples reveal silicon contamination and local damage on their outer layer. Assembled super-tips showed superior performance as compared to ordinary pyramidal AFM tips.

Being capable of supplying much higher forces than the conventional actuator designs, topology optimized microgrippers are suitable for miniaturization. First examples of sub-micron grippers, i.e. topology optimized designs scaled down by a factor of 4 or 5, were

fabricated by Alberto Cagliani. Mix-and-match fabrication technique was used for fabricating these devices, where fine structures, such as actuators, were defined by electron beam lithography and larger features, such as leads and bonding pads, were defined by conventional UV lithography. These down-scaled versions of the topology optimized microgrippers were used in the manipulation of 20-30 nm-diameter CNT bundles and ~7 nm-diameter single-walled CNTs by Rafal Wierzbicki.

As a further step, nanogrippers can be fabricated by FIB milling, as explained in Section 4.4. First prototypes of such devices, Gückel nanogrippers, were realized as a proof of concept. Next step would be designing better electrothermal actuators by performing topology optimization analyses in a nano-scale domain and fabrication of these devices by FIB milling.

Although it is a powerful design tool as it is now, the topology optimization software for the electrothermal actuators can be further improved to include new features. As an example the algorithm for considering the process variation during design presented in [75] can be implemented in the code. Furthermore, a temperature constraint can be introduced for controlling the maximum temperature or the temperature at a specific location within the domain. Also, the temperature dependency of the material properties can be considered by defining these as data files rather than constants.

Finally, taking advantage of the non-uniform material properties achieved by annealing the FIB milled nanostructures and implementing this into the topology optimization code for the electrothermal actuation more advanced actuators can be designed with non-uniform material properties.

APPENDIX A
Topology Optimization Software

A.1 Tutorial: "How to use Topology Optimization Software "TopOpt" with a Case Study of 3-beam Electro-thermal Actuators

Author: Ozlem Sardan Sukas

Date: 25/02/2009

Version: 5

A.1.1 Abstract

This document describes how to use the topology optimization software "TopOpt", developed by Ole Sigmund [53] through a case study for 3-beam electro-thermal actuators. Contents of the tutorial are as follows:

A.1.2 Contents

a) Overview
b) Getting Started
c) How to run the program?
d) Input file "konst.dat"
e) Input file "geom.dat"
f) How to perform a simple analysis with a current constraint?
g) How to add a cross displacement constraint?
h) How to perform an analysis with two load cases?
i) How to add an objective error constraint?
j) How to edit and display the results?

a) Overview

TopOpt is a topology optimization program, developed by Ole Sigmund. The program aims at solving a general topology optimization problem, by distributing a given amount of material within a predefined design domain, such that the displacement of a specific point is maximized. It can be used for the solution of thermal and electro-thermal problems, which include either one or two types of materials.

The program code is written in FORTRAN77 programming language. For more information, either visit www.topopt.dtu.dk or contact Ole Sigmund (sigmund@mek.dtu.dk). Also, there is a simpler online version of the program with a JAVA user interface available on the web page.

b) Getting Started

The TopOpt program can be run by logging on to the DTU GBar, using a proper client such as "ThinLinc" or "X-Win32". However, executables are required to be obtained from Ole Sigmund.

If you are using X-Win32 Client:

1. Start X-Win32 client,
2. Right click the program icon on the notification area and select "XConfig",
3. Click "Wizard",
4. Type a proper name for your session, eg. gbar, and click "Next",
5. Select "StartNetSSH" and click "Next",
6. Enter host name as "bohr.gbar.dtu.dk", click "Next", enter your login name and password and click "Next" again,
7. Select "SunOS (Solaris)" as the Unix command and click "Finish",
8. Launch the session you created and now you are connected to DTU Gbar!

If you are using ThinLinc Client:

- ✓ Start ThinLinc client,
- ✓ Enter server name as "thinlinc.gbar.dtu.dk", your login name and password, respectively,
- ✓ Click "Login" and "OK", respectively and now you are connected to DTU Gbar!

After logging on to DTU Gbar, open a terminal window by clicking on the "IceWM" button on the lower left corner, click "Terminal" and again "Terminal" or "Terminal on bohr" to open a command window.

Proper files and folders should have been created in your account. Contact Ole Sigmund (sigmund@mek.dtu.dk) for this purpose.

c) How to run the program?

- Open “fortran” folder by typing “cd fortran” and pressing “return” in the terminal window.
- Open “actu” folder in the “fortran” folder by typing “cd actu” and pressing “return”.

  Remark: The names of the above mentioned folders might differ!

- Open the two input files:
  - Open “konst.dat” by typing “nedit konst.dat&” and pressing ”return”,
  - Open “geom..dat” by typing “nedit geom.dat&” and pressing “return”.

  Remark: “nedit” is a text editor, which is used in editing the data files. Symbol “&” is put at the end of the file name in order to be able to continue on working.

- Run the program by typing “r1” and pressing “return”.
- The program will print the analysis type and ask:

```
LINEAR ANALYSIS!
begin new problem (1/2) ? :
```

  - Type either “1” for performing a new analysis or “2” for continuing a previous analysis and press “return”.

- If you start a new analysis by typing “1”, the program will ask you the number of discretization elements that you want to divide the domain in both x- and y-directions, i.e. “nelx” and “nely”, respectively:

```
enter nelx, nely
```

  - Enter “nelx”, press “return”, enter “nely” and press “return” again.

  Remark: Be careful not to use values less than 20! More is better but the solution becomes slower…

- Hence, analysis starts and two plot windows open:
  1. *Results window :* Includes 5 different graphs (Figure A.1), which are:
     - *Densities:* Shows the density distribution within the domain at each analysis step.
     - *Potential:* Shows the potential distribution within the domain at each analysis step.
     - *Current :* Shows the current distribution within the domain at each analysis step.
     - *Design changes :* Shows the density changes within the domain at each analysis step.
     - *Temperatures:* Shows the temperature distribution within the domain at each analysis step.

Remark: Analysis parameters, such as number of iterations, spring displacement, spring force, spring work, current and resistance, are also printed in the results window after each analysis step.

2. Convergence window : Shows the convergence of the algebraic function as a function of the number of iterations (Figure A.2).

- Analysis stops when the maximum number of iterations defined in the input file “konst.dat” is reached or the convergence criterion is satisfied (Input files will be explained in detail below.). Click on the terminal window and press “return”.

Remark: “ctrl+C” breaks the program before the maximum number of iterations is reached.

1. Be careful, not to break the program when it is writing the results to avoid data loss!
2. It is a good idea to always keep backup copies of all important files.

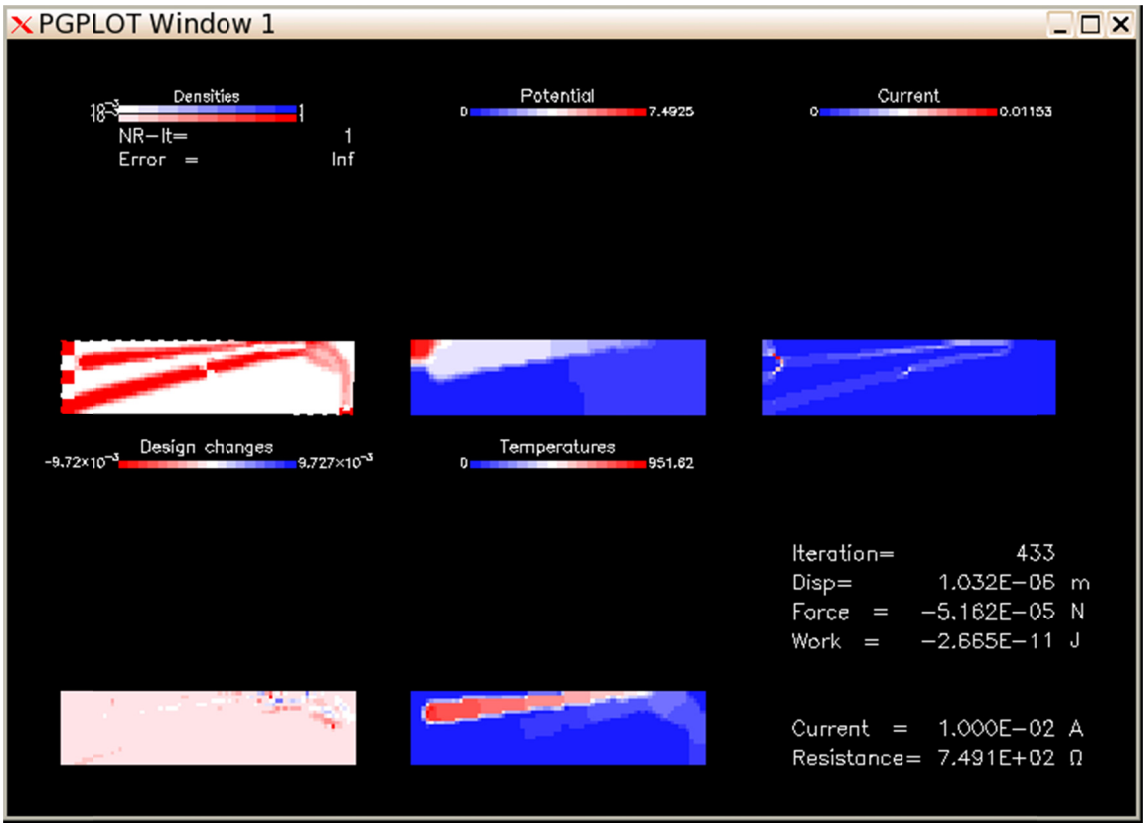

Figure A.1 Results window for the simplest analysis case with a current constraint.

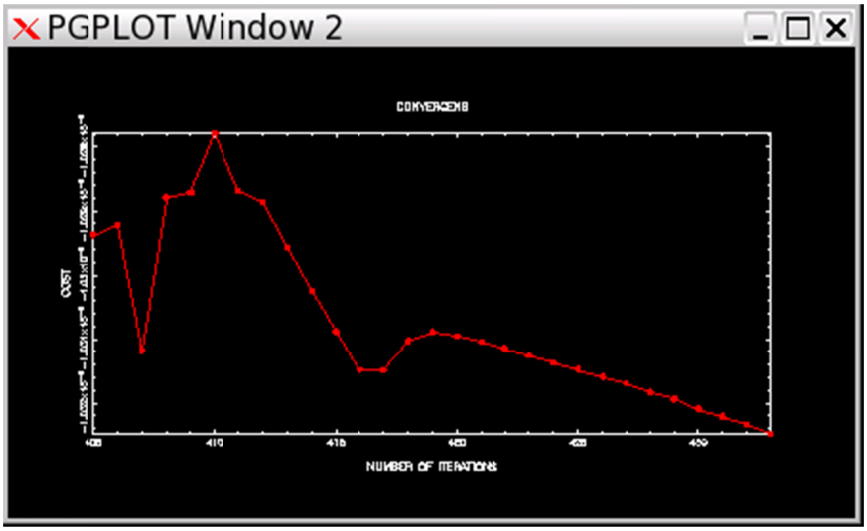

Figure A.2 Convergence window for the simplest analysis case with a current constraint.

d) Input File "konst.dat":

- An example input file "konst.dat" looks as follows:

```
---NORMAL/BATCH-(1/2)---
1
---LINEAR/NONLINEAR (1/2)
1
---COMMON---
move   .1
maxit  100
check  2    (1: gradient, 2:filter, 3:both)
rmin   2. 0.5 (half window size)
xmin   0.001
xmax   1.
penal  3.  1. (penalty1 and 2 or penalty 1 and HS (0 low))
igraph 1  (show graph every igraph iteration)
animate 1 (animate 1/2/3 = density/none/disptemp)
symm   0  (1:vert line, 2: hor line, 3: both)
```

- In this file, the type of the analysis to be performed is defined in the fourth line.
    1. A linear analysis
    2. A non-linear analysis.
- *maxit:* Number of maximum iterations.
- *rmin:* Filter radius for a filter, which is given in terms of the element size and makes the design mesh-independent.
    - Start with a large rmin value, such as 4, and gradually decrease it to 1 and even for optimization.
- *igraph:* Interval, with which the results are to be plotted in the plot windows.
- *animate:* Animation type.
    1. For animating the density changes within the domain.
    2. For a faster analysis with no animation.
    3. For animating the displacement of the structure together with the temperature distribution.
    - For animating the deformed and undeformed shapes of the structure sequentially, set maxit to 1 and animate to 3.

  Remark: It is recommended that other parameters, which are not mentioned in this manual, are not modified by the user.

e) Input File "geom.dat":

- An example input file "geom.dat" for the simplest analysis case with a current constraint looks as follows:

```
---Opt_prob--(therm1/electrotherm1/therm2/electrotherm2)-(1/2/3/4)---
oprob  2
---micelaneous---
lxly   200.e-6  50.e-6
vol   .3 .3
nreal  1
nadj   1
ncon   3
---SUPPORTS-ELAST-(xdir/ydir/both,xpos,ypos,radh,radv)
nsup   3

sup1   3  0.e-6  0.e-6  0.e-6 10.e-6

sup2   3  0.e-6 25.e-6  0.e-6  5.e-6

sup3   3  0.e-6 50.e-6  0.e-6 10.e-6

---SPRINGS----(load-case,xdir/ydir,stiffn,xpos,ypos,2nd-xpos,2nd-ypos)
nspr   1
s1     1 2 50. 195.e-6 5.e-6 -1. -1.
---ACTUATOR-FORCE-(load-case,potential,xpos,ypos,force)
nin   0
---ELECT.LOAD-(load-case,potential,xpos,ypos,radh,radv)
nsup   1

sup3   1  7.5  0.e-6 50.e-6  0.e-6 10.e-6

---ADJOINT-LOADS-(load-case,xdir/ydir, xpos,ypos)
nin    1

l1     1  -2 195.e-6  5.e-6

---PASSIVE-AREAS---0/1,x1,x3,y1,y3

npa    6

npa1   1  0.e-6 10.e-6  0.e-6 10.e-6

npa2   0  0.e-6 10.e-6 10.e-6 20.e-6
```

```
npa3   1  0.e-6 10.e-6 20.e-6 30.e-6

npa4   0  0.e-6 10.e-6 30.e-6 40.e-6

npa5   1  0.e-6 10.e-6 40.e-6 50.e-6

npa6   1 190.e-6 200.e-6 0.e-6 10.e-6


---Objective---(r_load,a_load,weight)----------
nobj   1
nmd1   1 1 1.
---current-constraints---(r_load,imax)
ncurre 1
ncur1  1 0.01
---obj-error---(r_load,r_load,constr)
nuerro 0
---U-cross---(r_load,a_load,constr)
nucros 0
--domain-data--(thickness,convec,temperature)
mat    5.e-6  18700.0  0.
---Material-Constants----(youngs,ny,alpha1,alpha2,econd,tcond)
mat1   169.e9  0.30  2.57e-6 2.57e-6  2.857e4 146.

mat2   200.e9  0.31  13.4e-6 13.4e-6  6.4e6    90.7
```

- oprob : Type of the optimization problem.
  1. A thermal problem containing a single kind of material,
  2. An electro-thermal problem containing a single kind of material,
  3. A thermal problem containing two different kinds of materials and
  4. An electro-thermal problem containing two different kinds of materials.
- *lxly:* Relative size in meters ([m]).
- *vol:* Volume fraction of first and second material types, respectively, i.e. the maximum volume fraction of the domain that can be filled with that type of material.

  Remark: "vol" counts for two constraints: Volume constraint for the first material and volume constraint for the second material.

- *nreal:* Number of real problems, i.e. input cases.
- *nadj:* Number of adjoint loads, i.e. output cases.
- *ncon:* Number of constraints.

Remark: There are three other constraint types other than volume constraints: Current constraint, objective error constraint and cross displacement constraint. (Details of all constraints will be explained in detail below.)

- *nsup:* Number of elastic supports.
    - *xdir/ydir/both:* Directions along which the support is fixed.
        1. A support fixed in x-direction.
        2. A support fixed in y-direction.
        3. A support fixed in both x- and y-directions.
    - *xpos:* x-axis coordinate of the center of the support in [m].
    - *ypos:* y-axis coordinate of the center of the support in [m].
    - *radh:* Horizontal dimension of the support in [m].
    - *radv:* Vertical dimension of the support in [m].
- *nspr:* Number of springs.
    - *load-case:* Input or output load case, such as an electric load or an adjoint load, to which the spring belongs to.
    - *xdir/ydir:* Defines the direction of the spring.
        1. A spring extending along x-direction.
        2. A spring extending along y-direction.

    Remark: (-) sign in front means the spring is grounded.

    - *stiffn:* Stiffness of the spring in [N/m], i.e. a workpiece.

    Remark 1: Stiffness should be increased for higher force and decreased for higher displacement.
    Remark 2: Generally, stiffness of the resulting structure will match the stiffness of the spring.

    - *xpos:* x-axis coordinate of the spring-end in [m].
    - *ypos:* y-axis coordinate of the spring-end in [m].
    - *2-nd xpos:* x-axis coordinate of the other spring-end in [m], if it is connected to another location within the domain.
    - *2-nd ypos:* y-axis coordinate of the other spring-end in [m], if it is connected to another location within the domain.

    Remark: "-1 -1" means that the spring is grounded.

- *nsup:* Defines the number of electric loads.
    - *potential:* Voltage at the electric supply in [V].

    Remark 1: "load-case" is defined similar to that of an elastic spring, where "xpos", "ypos", "radh" and "radv" are defined similar to those of an elastic support.
    Remark 2: Generally, electric loads are defined at elastic supports. If there is not a supply defined at an elastic support, it is grounded by default.

- *nin:* Number of adjoint loads.
    - *xpos:* x-axis coordinate of the point, at which the adjoint load acts, i.e. the displacement is to be minimized/maximized.
    - *ypos:* y-axis coordinate of the point, at which the adjoint load acts, i.e. the displacement is to be minimized/or maximized.

  Remark: "load-case" and "xdir/ydir" are defined similar to that of an elastic spring, where "radh" and "radv" are defined similar to those of an elastic support.

- *npa:* Number of passive areas, which are predefined as being either void or filled and do not change during the analysis.
    - *0/1:* Defines whether the defined area is void or filled.
    - *x1:* x-axis coordinate of the lower left corner of the area, in [m].
    - *x3:* x-axis coordinate of the upper right corner of the area, in [m].
    - *y1:* y-axis coordinate of the lower left corner of the area, in [m].
    - *y3:* y-axis coordinate of the upper right corner of the area, in [m].
- *nobj:* Number of objective functions to be satisfied.
    - *r_load:* Real load case, to which the objective function belongs.
    - *a_load:* Adjoint load case, to which the objective function belongs.
    - *weight:* Defines the weight of the objective function.
- *ncurre:* Number of current constraints.
    - *imax:* Defines magnitude of the maximum current that can pass through the structure, in Amps.

  Remark 1: Select a large value for "imax" in the beginning and define the upper limit afterwards according to the maximum current running through the resulting structure.
  Remark 2: "r_load" and "a_load" are defined similar to those of an objective function.
  Remark 3: "ncurre" adds to the number of constraints.

- *nuerro:* Number of objective error constraints.
    - constr: Maximum allowable difference of the cross displacement than the actual displacement as a fraction of the actual displacement.

  Remark 1: Select a large value for "constr" in the beginning and follow the same procedure as described in the current constraint.
  Remark 2: "r_load" and "a_load" are defined similar to those of an objective function and a current constraint.
  Remark 3: "nuerro" adds to the number of constraints.

- nucros : Number of cross displacement constraints.
    - constr : Magnitude of the maximum cross displacement as a fraction of the actual displacement.

Remark 1: Select a large value for “constr” in the beginning and follow the same procedure as described in the current and the objective error constraints.
Remark 2: “r_load” and “a_load” are defined similar to those of an objective function, a current constraint and an objective error constraint.
Remark 3: “nucros” adds to the number of constraints.

- *mat:* Domain properties.
  - *thickness:* Thickness of the structure in [m].
  - *convec:* Convection coefficient of the surroundings in [W/m2K].
  - *Temperature:* Initial temperature of the domain in [°C].
- *mat1:* Material properties of the first material.
- *mat2:* Material properties of the second material.
  - “youngs”, “ny”, “alpha1”, “alpha2”, “econd”, “tcond” define the modulus of elasticity in Pa, Poisson’s ratio, coefficients of thermal expansion along x- and y-directions in 1/K, electrical conductivity in Ω/m and thermal conductivity in W/mK, respectively.

f) How to perform a simple electro-thermal analysis with a current constraint?

- The example input file “geom.dat” given above is for a simple electro-thermal analysis with a current constraint as stated above.
- The domain is defined as shown in Figure A.3.
- The problem is an electro-thermal problem with only one material type and “oprob” is set to “2”.
- Width and height of the domain are defined as 200 µm and 50 µm, respectively.
- Volume constraints both materials are defined as 30%.

  Remark 1: The aim of defining volume constraints is to ensure the convergence of the analysis.
  Remark 2: Since the second material is not involved in the analysis, second volume constraint will not be active.

- Since there is only one load case, only one input voltage is defined by setting “nreal” to “1”.
- Displacement of only a single point is to be maximized and hence only a single adjoint load defined by setting “nadj” to “1”.
- The problem includes a total of three constraints: Two volume constraints and a current constraint, and hence “ncon” is set to “3”.
- Three elastic supports are defined, all of which are fixed in both x- and y-directions. Coordinates of the supports are (0, 0), (0, 25) and (0, 50) in µm’s and they are extending only along (+) and (-) y-directions, by amounts of 10 µm, 5 µm and 10 µm, respectively.

  Remark: Although the extensions of first and third supports outside the domain limits are not considered during the analysis.

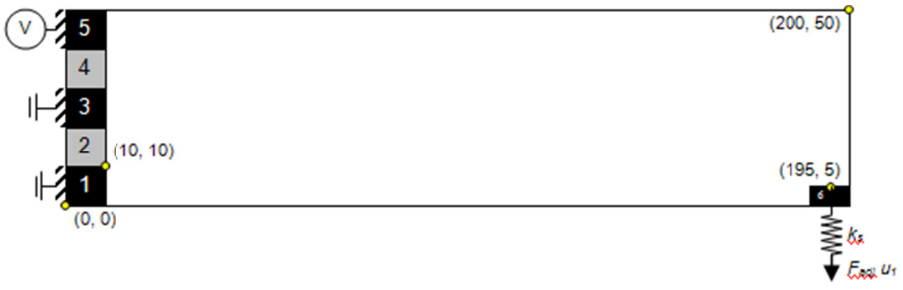

Figure A.3 Illustration of the domain defined for a simple electro-thermal analysis with a current constraint.

- One spring is defined at the point, where the displacement is to be maximized, i.e. at coordinates (195, 5) in [μm]. The spring is extending along y-direction and it is desired to have a stiffness of 50 N/m. Since the second end of the spring is connected to a point outside the domain, both “2nd-xpos” and “2nd-ypos” are set to -1”.
- There is no actuator forces defined.
- Only one electric load, which is equal to 7.5 V, is defined at the same location and with the same dimensions as the third elastic support.

  Remark: Elastic supports, at which no electric load is defined, are set to ground by default.

- One adjoint load is defined at the point, where the displacement is to be maximized, i.e. at the same location as the spring, but along (-) y-direction.
- Six passive areas are defined, either to be filled, i.e. areas 1, 3, 5 and 6 or void, i.e. areas 2 and 4.

  Remark: Filled areas are represented with black in Figure A.3, where void areas are represented with grey.

- There is only one objective function to be satisfied, where the displacement, u1, along
  (-) y-direction is to be maximized according to:

$$\boldsymbol{\varphi_1 = W_1 \cdot U_1} \tag{A.1}$$

- Only one current constraint is defined, where the maximum current that can pass through the structure is 0.01 A.

$$i_1 \leq i_{max,1} \tag{A.2}$$

- There are no objective error or cross displacement constraints defined.
- The thickness of the structure is defined as 5 μm and the convection coefficient of the surroundings is defined as 18.7 kW/m2/K.
- The material properties of the structure are defined as follows:
  - Modulus of elasticity : 169 GPa
  - Poisson’s ratio : 0.30
  - x- and y-axis coefficients of thermal expansion : 2.57 10-6/K
  - Electrical conductivity : 2.857 104 Ω/m
  - Thermal conductivity : 146 W/mK

  Remark: Although a second material is defined, it will not be considered during the analysis since “oprob” is set to be “2” initially.

- The analysis is run as usual and two display windows are opened: One results window and one convergence window. Figure A.1 and Figure A.2 show these display windows corresponding to the simple analysis case with a current constraint.
- As the analysis continues, the results are also printed in the terminal window after each iteration, as follows:

```
1   Power=          7.51106E-02   Cond.=          4.24727E-02   Conv.=          2.57020E-02
(0.907658)(0.565469)
1 Heat capacity=     1.78000E-07J/K, Heat=    2.44651E-05 J
 disp       (m) =     8.96580E-07
 cross disp (m) =   0.
 f_out      (N) =    -4.48290E-05
 Work       (J) =    -2.00964E-11
 Stiffness (N/m)=     133.282
 Bl0. force (N) =     7.46690E-05
 Free disp  (m) =     5.60233E-07
 current    (A) =     1.00147E-02
 Work/Power     =    -2.67557E-10
Constraint violation  1.00  0.00  1.00

it.= 100 V= 0.3000 0.0000  ch= 0.0356 npas=  935 CO= -0.89658E-06
 dual variables    0.386400  0.   0.568136  0.
```

g) How to add a cross displacement constraint?

- A cross displacement constraint can be added to the problem, if the displacement of the structure is to be maximized along one direction, i.e. u1 in Figure A.4, while the displacement of the structure along its cross direction, i.e. û1 in Figure A.4, is to be kept below a certain limit according to:

$$\hat{u}_1{}^2 = \varepsilon^2 \cdot u_1{}^2 \qquad \text{(A.3)}$$

- Addition of a cross displacement constraint adds to the number of adjoint loads and the number constraints. Hence, “nadj” ıs set to “2” and “ncon” is set to “4”.
- As stated above, an adjoint load, which acts at the same point as the original load, but along the cross displacement direction, should be defined.

  Remark: The load case for the new adjoint load is “2”.

- Finally, the number of cross displacement constraints should be set to “1” the constraint should be defined as a fraction of the original displacement.
- The real load case for the cross displacement constraint is “1”, where the adjoint load case is “2”.

  Remark: The constraint should be set to a relatively high value, i.e. 0.5, in the beginning. After a few iterations, according to the constraint violation value corresponding to the cross displacement sensitivity printed on the terminal window.

- Hence, the input file “geom.dat” should be modified as follows:

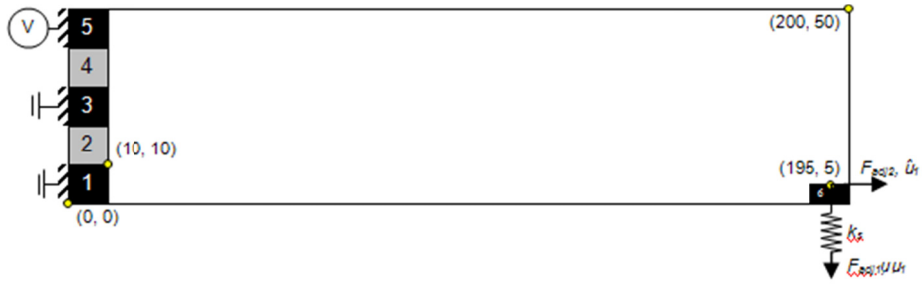

Figure A.4 Illustration of the domain for the analysis case with a cross displacement constraint.

```
 ...
nadj   2
ncon   4
...
---ADJOINT-LOADS-(load-case,xdir/ydir, xpos,ypos)
nin    2
l1     1  -2 195.e-6  5.e-6
l2     2   1 195.e-6  5.e-6
...
---U-cross---(r_load,a_load,constr)
nucros 1
nucr1  1  2  0.5
...
```

- The analysis is run as usual and two display windows are opened, similarly. Figure A.5 shows the display window, in which the results are plotted, corresponding to the analysis case, with a cross displacement constraint.

  Remark: It is easily observed that the resulting structure is different than that obtained in the previous case.

  - Furthermore, the displacement is decreased due to the addition of one more constraint. Other values have also changed.

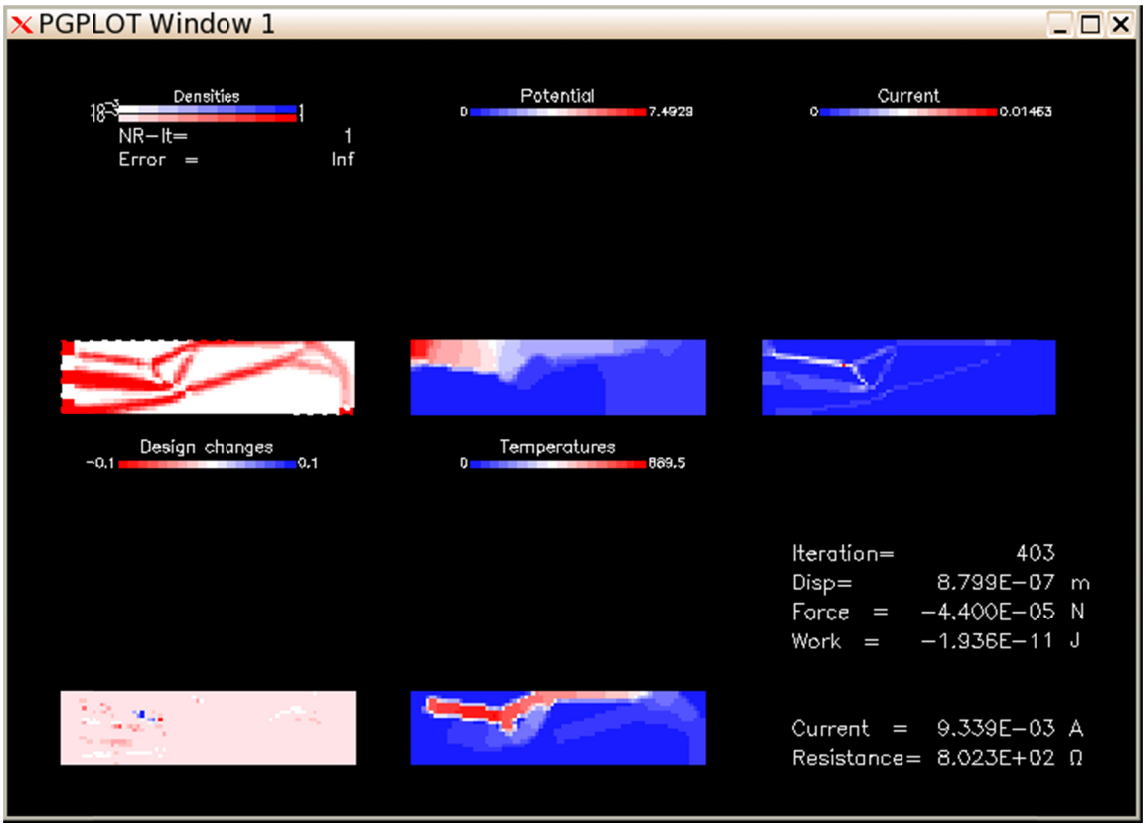

Figure A.5 Results window for the analysis case with a cross displacement constraint.

h) How to perform an analysis with two load cases?

- More than one load cases can be analyzed at the same time, such as the cases where the displacement of another point in a specific direction, or the same point in a different direction, is to be maximized.
- A second load case for the domain, given in the above analysis case is shown in Figure A.6.
- The objective function to be maximized for the second load case is as follows, where the displacement, u2, along (+) y-direction is to be maximized according to:

$$\boldsymbol{\varphi_2 = W_2 \cdot U_2} \tag{A.4}$$

- Hence, the overall objective function can be written by combining the two objective functions. Note that, increasing the importance of one over the other is possible, according to w1/w2 ratio.

$$\boldsymbol{\varphi = W_1 \cdot U_1 + W_2 \cdot U_2} \tag{A.5}$$

- A current constraint is also defined for the second load case similarly, where the maximum current that can pass through the structure is 0.01 A.

$$i_2 \leq i_{max,2} \tag{A.6}$$

- A cross displacement constraint is also defined for the second load case similarly, where the displacement of the structure is to be maximized in one axis, i.e. u2 in Figure A.6, while the displacement of the structure in the other axis, i.e. û2 in Figure A.6, is to be kept below a certain limit according to:

$$\hat{u}_2{}^2 = \varepsilon \cdot {u_2}^2 \tag{A.7}$$

- Addition of a second load case doubles both the number of real loads and the number of adjacent load. Hence, “nreal” is set to “2” and “nadj” is set to “4”.

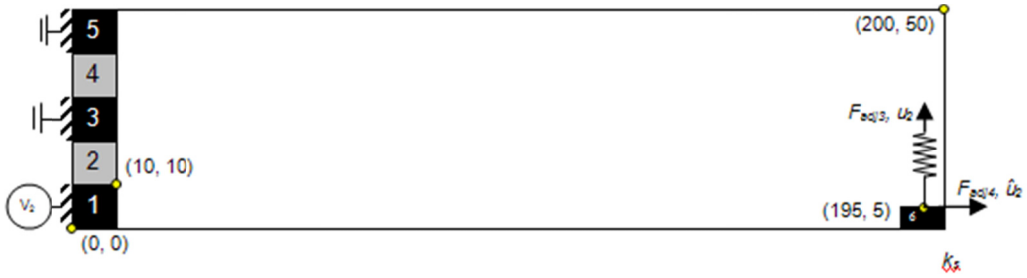

Figure A.6 Illustration of the domain for the second load case of the analysis case with two load cases.

- Addition of a second load case also doubles the number of constraints other than volume constraints. Hence, “ncon” is set to “6”.

- One more spring should be defined for the second load case, which has the same properties as the spring of the first load case.
- Similarly, one more electric load should be defined for the second load case, which has the same properties as the electric load of the first load case, but at the same location as the first elastic support.
- Two more adjoint loads should be defined at the same point as the first two: One along (+) y-direction and another along its cross displacement direction, i.e. (+) x-direction.
    - Pay attention to the definition of the load cases for the adjoint load pairs!
- One more objective function and one more current constraint should be defined belonging to the second load case, in a similar manner as explained above.
- There are no objective error functions defined yet.
- Finally, one more cross displacement constraint should be defined as a percent of the original displacement for the second load case.
    - Again pay attention to the definition of the load cases for the cross displacement constraints.
- Hence, the input file “geom.dat” should be modified as follows:

```
...
nreal  2
nadj   4
ncon   6
...
---SPRINGS----(load-case,xdir/ydir,stiffn,xpos,ypos,2nd-xpos,2nd-ypos)
nspr   1

s1     1 2 50. 195.e-6 5.e-6 -1. -1.

S2     2 2 50. 195.e-6 5.e-6 -1. -1.

...
---ELECT.LOAD-(load-case,potential,xpos,ypos,radh,radv)
nsup   2

sup3   1  7.5  0.e-6 50.e-6  0.e-6 10.e-6

sup1   2  7.5  0.e-6  0.e-6  0.e-6 10.e-6
---ADJOINT-LOADS-(load-case,xdir/ydir, xpos,ypos)
nin    4

l1     1  -2 195.e-6  5.e-6
```

```
l2    3   1 195.e-6  5.e-6

l3    2   2 195.e-6  5.e-6

l4    4   1 195.e-6  5.e-6
...
---Objective---(r_load,a_load,weight)----------
nobj   2
nmd1   1 1 1.
Nmd2   2 2 1.
---current-constraints---(r_load,imax)
ncurre 2
ncur1  1 0.01
ncur2  2 0.01
---obj-error---(r_load,r_load,constr)
nuerro 0
---U-cross---(r_load,a_load,constr)
nucros 2
nucr1  1  3  0.1
nucr2  2  4  0.1
...
```

- The analysis is run as usual; however, three display windows are opened: Two results window, one for the first load case and one for the second, and a convergence window. Figure A.7 and Figure A.8 show the results display windows, corresponding to first and second analysis cases, respectively.

  Remark: It is easily observed that the resulting structure is more symmetrical.

  - However, displacement values of the two load cases as well as most of the other parameters are different.
- Furthermore, as the analysis continues, the results for the second load case are also printed in the terminal window after each iteration, as well as those for the first load case.

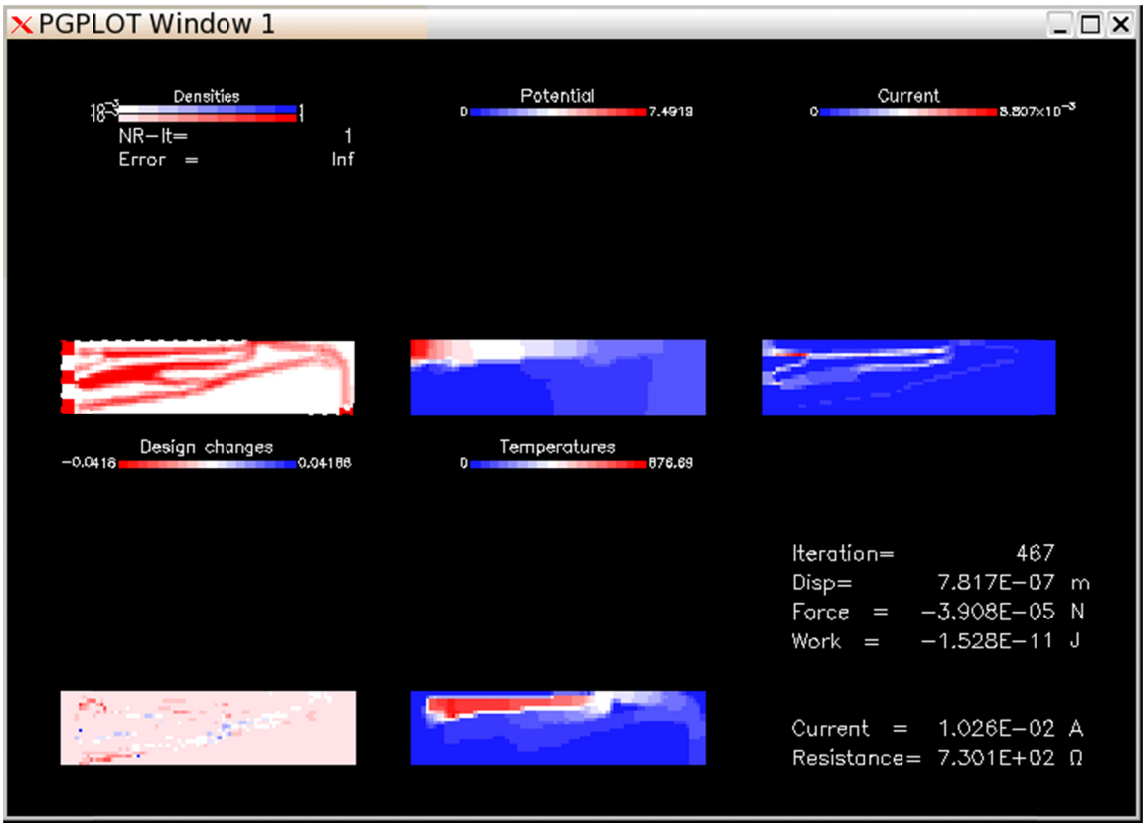

Figure A.7 Results window for the first load case of the analysis case with two different load cases.

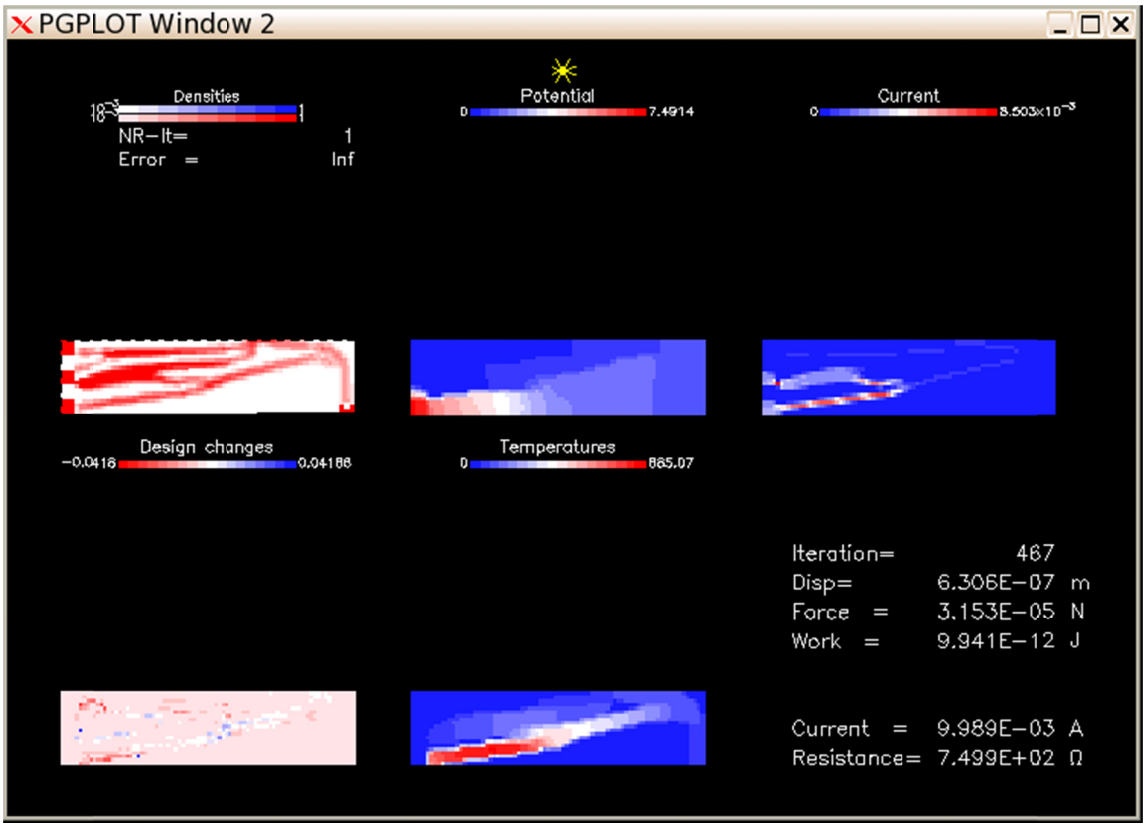

Figure A.8 Results window for the second load case of the analysis case with two different load cases.

i) How to add an objective error constraint?

- An objective error constraint can be added to the problems with more than one load cases, if displacements of two different load cases are to be equalized, or one should be within a certain percent of the other, according to:

$$\frac{(u_1-u_2)^2}{(u_1+u_2)^2} \leq \epsilon^2 \qquad \text{(A.8)}$$

- Addition of an objective error constraint adds to the number of constraints, hence "ncon" is set to "7".
- Finally, the number of objective error constraints should be set to "1" the constraint should be defined as a percent of the original displacement for the first load case.
    - The real load case for the objective error case is "1", where the adjoint load case is "2".

  Remark: The constraint should be set to a relatively high value, i.e. 50%, in the beginning, similar to other constraints.

- Hence, the input file "geom.dat" should be modified as follows:

```
...
ncon   7
...
---obj-error---(r_load,r_load,constr)
nuerro 1
nuer1  1 2 0.5
...
```

- The analysis is run as usual and four display windows are opened, similar to the previous analysis case. Figure A.9 and Figure A.10 show the display windows, in which the results are plotted, corresponding to first and second analysis cases for this analysis case, respectively.

- **Remark 1:** Displacement values of the two load cases are closer to each other.
- **Remark 2:** Addition of a constraint costs more than that of another component, such as an adjoint load, an electric supply or a spring, in terms or the computation time.
- **Remark 3:** In order for a more stable analysis, start with the simplest case and add constraints afterwards.

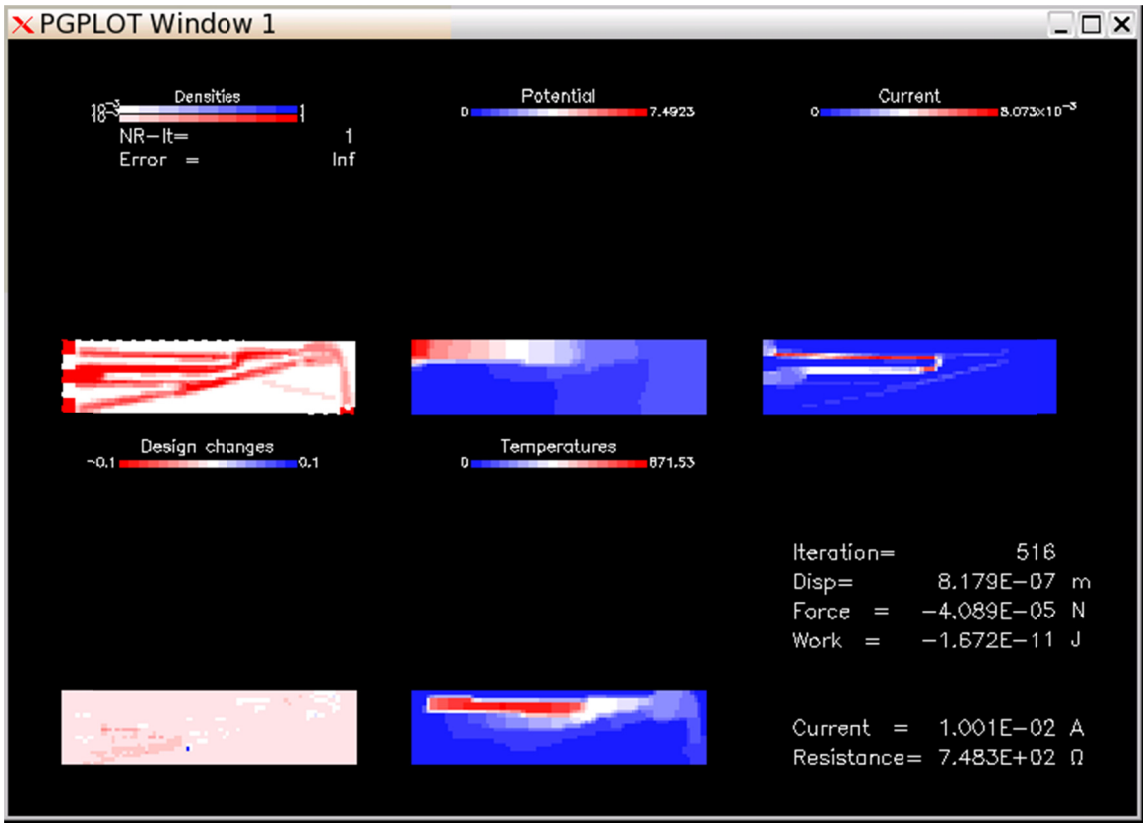

Figure A.9 Results window for the first load case of the analysis case with two different load cases and an objective error constraint.

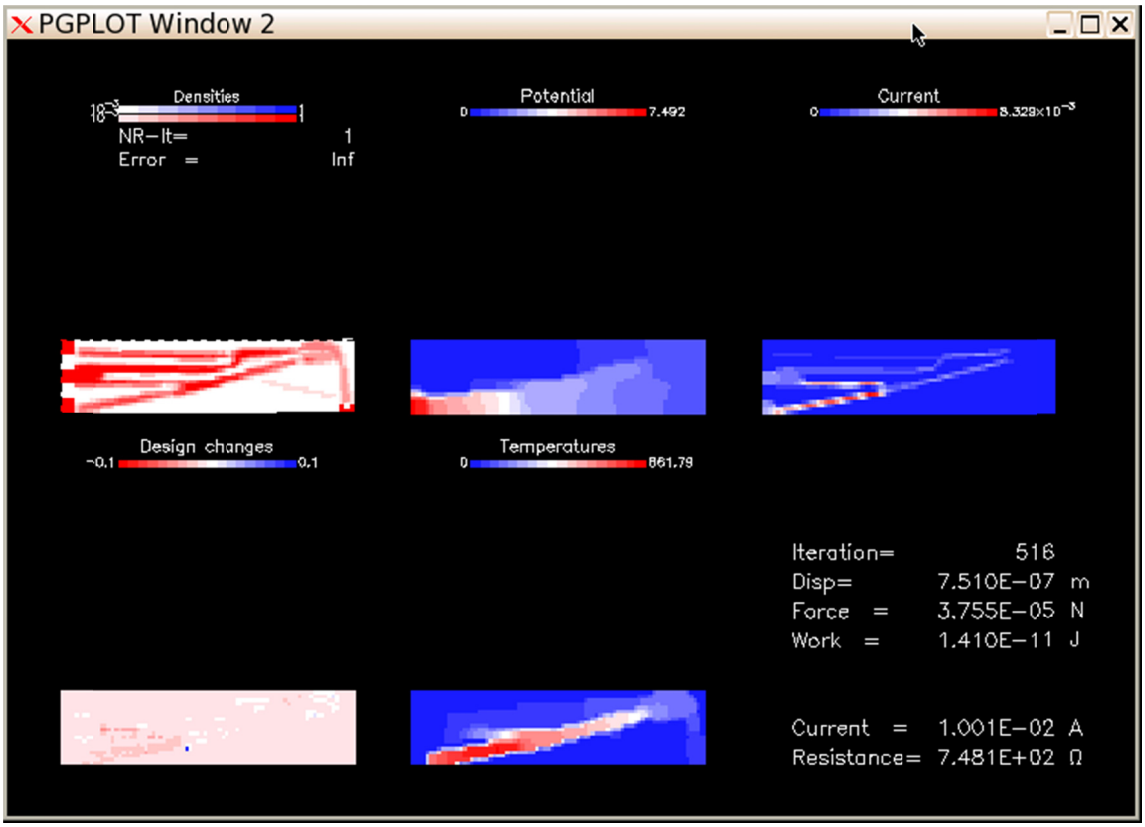

Figure A.10 Results window for the second load case of the analysis case with two different load cases and an objective error constraint.

j) How to edit and display the results?

- Open the results folder by typing “cd results” and pressing “return”.
    - This folder includes the following files and programs:
      “aa, ac, ai, ai2, bitmap.gif, contour.gif, current.gif, dens1.gif, dens2.gif, dens3.gif, dens4.gif, dens5.eps, dens6.eps, dens7.eps, dens8.eps, disp.gif, dispc.gif, disptemp1.gif, disptemp2.gif, imag, out.gif, pgm, temp.gif”
- “imag” is an image editor, which is used in displaying and processing image files. To open the program, type “imag” and press “return”. The program will print the following lines:

```
Read input from:
1: ai
2: ai (second variable)
3: in.gif
4: new graphics (with XPaint)
5: Exit
```

- “ai” is a design file, which contains the results.
    - You can either open the image in the design file “ai” by typing “1” and “return” or load another image file, “in.gif” by typing “3” and “return”.
- After the program reads the image files it will print the following lines:

```
1: Conversion
2: Image Processing
3: Thresholding
4: Symmetrize picture
5: Display out.gif picture
6: Manipulate out.gif picture
7: Contour plot
8: Restart
9: Exit without saving
10: Exit and Save
```

- For changing the image resolution, select “Conversion” by typing “1” and pressing “return”. The program will print the resolution of the old image in both x- and y-directions, i.e. “nex” and “ney”, respectively, and ask you the new values as follows, for example:

```
old nex and ney are 80 20
```

```
enter new ones:
```

- Enter new “nex”, press “return”, enter new “ney” and press “return” again. The program will ask whether to perform filtering, or not as follows:

```
want filtering? (1/2)
```

- Type “1” for filtering.

- For processing the image, select “Image Processing” by typing “2” and pressing “return”. The program will print the following lines:

```
1: Dilate
2: Erode
3: Close
4: Open
5: Thin
6: Skellet
7: Nothing
```

- Note that, this feature has not been used yet!

- For changing the threshold of the image, select “Thresholding” by typing “3” and pressing “return”. The program will ask the threshold value:

```
enter thresh-hold value? (0..1)
```

- Enter a proper threshold value between “0” and “1” and press “return”.
  - Note that, this feature has not also been used yet!
- For symmetrizing the image, i.e. combining the original image with its mirror image along either x- or y-directions, select “Symmetrize” by typing “4” and pressing “return”.
- For seeing the resulting image after processing, select “Display out.gif picture” by typing “5” and pressing “return”. “out.gif” file will be opened in a new window.
- For editing the image “6”, select “Manipulate out.gif picture” by typing “6” and pressing “return”. An image editor will open, which is similar to “Paint”. Note the following, when editing an image:
  - Always draw with black and white. Behavior of the program is indeterminate if colors other than black and white are used!
  - Draw by selecting the brush.

- For obtaining the contours of the image, select “Contour” by typing “7” and pressing “return”.

enter new number of elements (nelx, nely):

- For restarting the “imag” program and loading a new image file, select “Restart” by typing “8” and pressing “return”.
- For exiting the program without saving your changes, select “Exit without saving” by typing “9” and pressing “return”.
- For exiting the program and saving your changes, select “Exit and Save” by typing “10” and pressing “return”.
    - Now the modified file is contained in the design file “ai2”, in “out.gif”.
- In order to continue topology optimization using the file you modified, you should copy “ai2” to “ai” by typing “cp ai2 ai” and pressing “return”.
    - Then, exit the results folder by typing “cd ..” and pressing “return”.
    - Run program “r1” as usual.
    - Be careful to continue from the previous analysis by typing “2” and “return” and the program will analyze staring from the modified image you loaded.
- “xv” is a command for displaying image files and an image file can be opened by typing “xv filename.ext”. Note that you can add the symbol “&” at the end for the same purpose mentioned above.
- After closing all command windows and open files, click “Logout” and then “OK” to close your connection to the DTU Gbar.

A.2 Example Input Files for the Topology Optimization Software used for the Analysis Summarized in Section 2.3

A.2.1 "konst.dat"

```
---NORMAL/BATCH-(1/2)---
1
---LINEAR/NONLINEAR (1/2)
1
---COMMON---
move   .1
maxit  250
check  2    (1: gradient, 2:filter, 3:both)
rmin   3. 0.5 (half window size)
xmin   0.001
xmax   1.
penal  3.  1. (penalty1 and 2 or penalty 1 and HS (0 low))
igraph 5  (show graph every igraph iteration)
animate 2 (animate 1/2/3 = density/none/disptemp)
symm   0  (1:vert line, 2: hor line, 3: both)
```

A.2.2 "geom.dat"

```
---Opt_prob--(therm1/electrotherm1/therm2/electrotherm2)-(1/2/3/4)---
oprob  2
---micelaneous---
lxly   200.e-6  40.e-6
vol   .15 .01
nreal  2
nadj   4
ncon   2
---SUPPORTS-ELAST-(xdir/ydir/both,xpos,ypos,radh,radv)
nsup   3

sup1   3  0.e-6  0.e-6  0.e-6  8.e-6

sup2   3  0.e-6 20.e-6  0.e-6  4.e-6

sup3   3  0.e-6 40.e-6  0.e-6  8.e-6

---SPRINGS----(load-case,xdir/ydir,stiffn,xpos,ypos,2nd-xpos,2nd-ypos)
nspr   2

s1     1 2 25. 200.e-6 0.e-6 -1. -1.

s2     2 2 25. 200.e-6 0.e-6 -1. -1.

---ACTUATOR-FORCE-(load-case,potential,xpos,ypos,force)
nin   0
---ELECT.LOAD-(load-case,potential,xpos,ypos,radh,radv)
nsup   2

sup3   1  8.  0.e-6 40.e-6  0.e-6 8.e-6

sup1   2  8.  0.e-6  0.e-6  0.e-6 8.e-6
---ADJOINT-LOADS-(load-case,xdir/ydir, xpos,ypos)
nin    4

l1     1  -2 200.e-6 0.e-6

l2     3   1 200.e-6 0.e-6

l3     2   2 200.e-6 0.e-6

l4     4   1 200.e-6 0.e-6

---PASSIVE-AREAS---0/1,x1,x3,y1,y3
```

```
npa    7

npa1   1  0.e-6  5.e-6  0.e-6   8.e-6

npa2   0  0.e-6  5.e-6  8.e-6  16.e-6

npa3   0  5.e-6 10.e-6 11.e-6  13.e-6

npa4   1  0.e-6  5.e-6 16.e-6  24.e-6

npa5   0  0.e-6  5.e-6 24.e-6  32.e-6

npa6   0  5.e-6 10.e-6 27.e-6  29.e-6

npa7   1  0.e-6  5.e-6 32.e-6  40.e-6

---Objective---(r_load,a_load,weight)----------
nobj   2
nmd1   1 1 1.
nmd2   2 2 1.
---current-constraints---(r_load,imax)
ncurre 0 ncur1  1 0.005 ncur2  2 0.005
---obj-error---(r_load,r_load,constr)
nuerro 0 nuer1  1 2  0.5
---U-cross---(r_load,a_load,constr)
nucros 0 nucr1 1 3 0.5 nucr2 2 4 0.5
--domain-data--(thickness,convec,temperature)
mat    5.e-6  0.0  0.
---Material-Constants----(youngs,ny,alpha1,alpha2,econd,tcond)
mat1   169.e9  0.30  2.57e-6 2.57e-6  1.125e4  148

mat2   200.e9  0.31  13.4e-6 13.4e-6  6.4e6  90.7
```

APPENDIX B
Topology Optimization Results

B.1 Results for the Three-beam-based Designs

Table B.1 Topology optimization results for the three-beam-based designs in a 100 µm × 20 µm domain.

I	k_s = 10 N/m		
	No I^*	I^* = 5 mA	I^* = 10 mA
V^* = 0.30	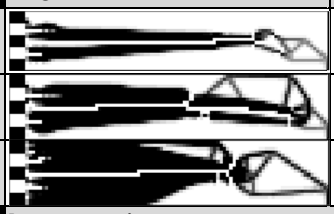		
V^* = 0.45			
V^* = 0.60			
II	k_s = 25 N/m		
	No I^*	I^* = 5 mA	I^* = 10 mA
V^* = 0.30	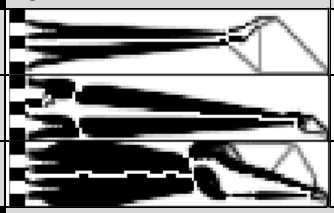		
V^* = 0.45			
V^* = 0.60			
III	k_s = 40 N/m		
	No I^*	I^* = 5 mA	I^* = 10 mA
V^* = 0.30			
V^* = 0.45			
V^* = 0.60			

Table B.2 Topology optimization results for the three-beam-based designs in a 150 µm × 30 µm domain.

IV	k_s = 10 N/m	k_s = 25 N/m	k_s = 40 N/m
V^* = 0.20	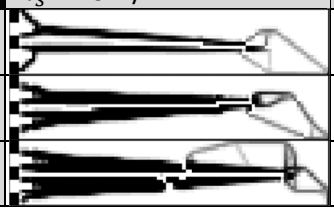		
V^* = 0.30			
V^* = 0.40			

Table B.3 Topology optimization results for the three-beam-based designs in a 200 µm × 40 µm domain.

V	V^* = 0.150	V^* = 0.225	V^* = 0.300
k_s = 25 N/m		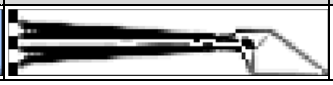	

Table B.4 Performance summary of the topology optimized designs in Table B.1.

		Closing					Opening				
		u_{out}	F_{out}	T	k	I	u_{out}	F_{out}	T	k	I
		µm	µN	°C	N/m	mA	µm	µN	°C	N/m	mA
I	k_s = 10 N/m										
V^* = 0.30	No I^*	0.750	7.50	606	27.90	22	0.815	8.15	620	27.90	14
	I^* = 5 mA	0.757	7.57	711	20.96	5	0.720	7.20	680	20.96	5
	I^* = 10 mA	0.743	7.43	643	26.63	10	0.720	7.20	642	26.63	10
V^* = 0.45	No I^*	0.700	7.00	603	33.70	25	0.848	8.48	640	33.70	14
	I^* = 5 mA	0.700	7.00	707	29.49	5	0.666	6.66	699	29.49	5
	I^* = 10 mA	0.749	7.49	641	37.84	10	0.705	7.05	656	37.84	10
V^* = 0.60	No I^*	0.858	8.58	607	31.22	29	0.855	8.55	604	31.22	31
	I^* = 5 mA	0.712	7.12	699	26.06	5	0.692	6.92	686	26.06	5
	I^* = 10 mA	0.717	7.17	647	46.43	10	0.689	6.89	633	46.43	10
II	k_s = 25 N/m										
V^* = 0.30	No I^*	0.583	14.57	605	48.03	26	0.559	13.97	604	48.03	26
	I^* = 5 mA	0.504	12.61	699	26.26	5	0.489	12.21	680	26.26	5
	I^* = 10 mA	0.552	13.80	656	34.65	10	0.533	13.32	637	34.65	10
V^* = 0.45	No I^*	0.580	14.50	617	88.10	18	0.546	13.65	605	88.10	21
	I^* = 5 mA	0.502	12.56	695	44.33	5	0.492	12.30	673	44.33	5
	I^* = 10 mA	0.569	14.22	654	63.75	10	0.541	13.54	638	63.75	10
V^* = 0.60	No I^*	0.592	14.80	605	75.94	29	0.584	14.61	603	75.94	29
	I^* = 5 mA	0.540	13.50	712	36.44	5	0.452	11.30	625	36.44	5
	I^* = 10 mA	0.497	12.43	637	68.34	10	0.543	13.56	646	68.34	10

Table B.4 Continued.

		Closing					Opening				
		u_{out}	F_{out}	T	k	I	u_{out}	F_{out}	T	k	I
		µm	µN	°C	N/m	mA	µm	µN	°C	N/m	mA
III	k_s = 40 N/m										
V^* = 0.30	No I^*	0.474	18.97	605	70.58	25	0.460	18.41	605	70.58	25
	I^* = 5 mA	0.365	14.59	613	45.36	5	0.417	16.68	681	45.36	5
	I^* = 10 mA	0.422	16.90	609	63.49	10	0.450	18.01	638	63.49	10
V^* = 0.45	No I^*	0.497	19.88	606	117.98	26	0.482	19.28	605	117.98	26
	I^* = 5 mA	0.431	17.25	614	73.88	5	0.364	14.56	515	73.88	5
	I^* = 10 mA	0.451	18.05	608	84.87	10	0.491	19.64	642	84.87	10
V^* = 0.60	No I^*	0.500	20.00	608	139.99	28	0.490	19.60	607	139.99	27
	I^* = 5 mA	0.427	17.08	683	56.90	5	0.350	14.01	608	56.90	5
	I^* = 10 mA	0.508	20.32	656	70.52	10	0.464	18.55	615	70.52	10

Table B.5 Performance summary of the topology optimized designs in Table B.2.

		Closing					Opening				
IV		u_{out}	F_{out}	T	k	I	u_{out}	F_{out}	T	k	I
		µm	µN	°C	N/m	mA	µm	µN	°C	N/m	mA
V^* = 0.20	k_s =10 N/m	1.162	11.62	605	19.27	24	1.112	11.12	605	19.27	29
	k_s = 25 N/m	0.708	19.52	604	33.67	26	0.762	19.05	604	33.67	25
	k_s = 40 N/m	0.670	26.79	606	63.00	22	0.620	24.80	604	63.00	21
V^* = 0.30	k_s =10 N/m	1.265	12.65	605	29.27	31	1.258	12.58	606	29.27	29
	k_s = 25 N/m	0.953	23.81	604	42.84	36	0.915	22.87	602	42.84	39
	k_s = 40 N/m	0.769	30.08	603	68.89	39	0.744	29.77	603	68.89	39
V^* = 0.40	k_s =10 N/m	1.409	14.09	606	33.60	28	1.413	14.13	611	33.60	25
	k_s = 25 N/m	1.003	25.07	604	66.74	40	0.982	24.56	605	66.74	40
	k_s = 40 N/m	0.866	34.66	603	81.24	44	0.818	32.72	603	81.24	47

Table B.6 Performance summary of the topology optimized designs in Table B.3.

V		Closing					Opening				
		u_{out}	F_{out}	T	k	I	u_{out}	F_{out}	T	k	I
		µm	µN	°C	N/m	mA	µm	µN	°C	N/m	mA
k_s = 25 N/m	V^* = 0.15	0.789	19.72	621	37.17	14	0.733	18.33	606	37.17	15
	V^* = 0.225	1.112	27.79	605	41.88	32	1.067	26.66	601	41.88	33
	V^* = 0.30	1.268	31.70	607	48.43	37	1.217	30.42	604	48.43	37

B.2 Results for the Gückel-based Designs

Table B.7 Topology optimization results for the Gückel-based designs with V^* = 0.40.

VI	k_s = 10 N/m	k_s = 25 N/m	k_s = 40 N/m
l_x = 160 µm l_y = 20 µm	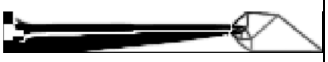	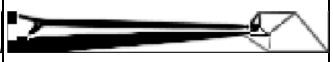	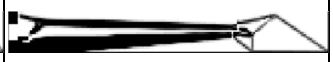
l_x = 240 µm l_y = 30 µm	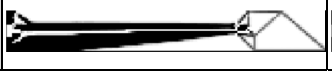	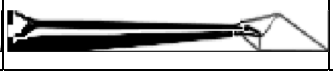	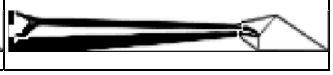

Table B.8 Performance summary of the topology optimized designs in Table B.7.

VI		Closing				
		u_{out}	F_{out}	T	k	I
		µm	µN	°C	N/m	mA
l_x = 160 µm l_y = 20 µm	k_s = 10 N/m	1.494	14.94	680	22.69	6
	k_s = 25 N/m	1.071	26.79	657	37.02	7
	k_s = 40 N/m	0.850	34.01	649	50.06	8
l_x = 240 µm l_y = 30 µm	k_s = 10 N/m	2.496	24.96	679	22.64	10
	k_s = 25 N/m	1.681	42.02	657	41.67	12
	k_s = 40 N/m	1.383	55.32	624	52.64	13

B.3 Results of the Analyses with Different Two-electrode Configurations

Table B.9 Topology optimization results with different two-electrode configurations.

VII		2nd position					
		2	3	4	5	6	7
1st position	1						
	2	X	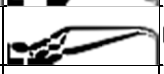				
	3	X	X	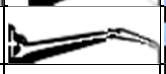		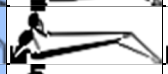	
	4	X	X	X			
	5	X	X	X	X		
	6	X	X	X	X	X	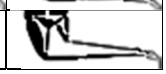

Table B.10 Performance summary of the topology optimized designs in Table B.9.

VII		Closing				
		u_{out}	F_{out}	T	k	I
1st pos.	2nd pos.	µm	µN	°C	N/m	mA
1	2	0.800	19.99	641	80.36	5
	3	1.187	29.67	627	68.76	6
	4	0.968	24.20	614	86.87	4
	5	1.391	34.76	589	76.57	2
	6	0.937	23.44	652	106.72	7
	7	1.289	32.23	600	93.39	38
2	3	1.017	25.44	605	102.50	18
	4	1.162	29.04	646	55.81	7
	5	1.151	28.78	612	66.50	15
	6	0.606	15.14	667	138.45	2
	7	1.278	31.96	596	54.18	42

VII		Closing				
		u_{out}	F_{out}	T	k	I
1st pos.	2nd pos.	µm	µN	°C	N/m	mA
3	4	1.310	32.75	607	53.41	41
	5	1.221	30.53	596	44.73	40
	6	1.332	33.29	599	54.71	32
	7	1.081	27.02	569	86.56	25
4	5	1.121	28.02	599	52.37	50
	6	1.145	28.64	603	45.12	39
	7	1.271	31.78	595	40.25	38
5	6	0.929	23.22	599	50.65	62
	7	1.007	26.18	594	44.58	40
6	7	0.868	21.69	598	48.93	-

APPENDIX C
Material Properties Used in the Finite Element Simulations

C.1 Material Properties for Poly-Si

C.1.1 Constant Properties

Table C.1 Constant material properties of poly-Si.

Heat Capacity, Q	712	J/(kg·K)
Young's Modulus, E	169	GPa
Poisson's Ratio, ν	0.3	

C.1.2 Temperature Dependent Properties

Table C.2 Temperature dependent material properties of poly-Si [99].

Temperature, T [K]	Thermal Conductivity, k [W/(m·K)]	Coefficient of Thermal Expansion, α [1/K]
300	65.00	2.5×10^{-6}
400	53.75	3.1×10^{-6}
500	46.54	3.5×10^{-6}
600	40.00	3.8×10^{-6}
700	35.00	4.1×10^{-6}
800	32.08	4.3×10^{-6}

Table C.3 Temperature dependent electrical resistivity of poly-Si [99].

Electrical Resistivity, ρ [Ω·m]	
$\frac{1}{\rho} = \alpha_1 + \alpha_2 \cdot T^{\alpha_3}$	
Coefficient	Value
α_1	2.6×10^{-3}
α_2	8.16×10^{-9}
α_3	1.946

C.2 Material Properties for SiO_2

Table C.4 Material properties of SiO_2.

Heat Capacity, Q	1000	J/(kg·K)
Young's Modulus, E	70	GPa
Poisson's Ratio, ν	0.17	
Thermal Conductivity, k	1.423	W/(m·K)
Coefficient of Thermal Expansion, α	0.5×10^{-6}	1/K
Electrical Resistivity, ρ	1×10^{10}	Ω·m

C.3 Air Properties

Table C.5 Heat transfer coefficient for air [99].

Temperature,T	Heat Transfer Coefficient, h
K	W/(m^2·K)
300	1101.7
400	1214.3
500	1381.0
600	1520.7
700	1660.3
800	1799.9

APPENDIX D
Finite Element Analysis Results

D.1 Ideal Case Simulations

D.1.1 Temperature Distribution

Simulation results for the ideal case, showing the temperature distribution within the topology optimized actuators at 1 µm displacement.

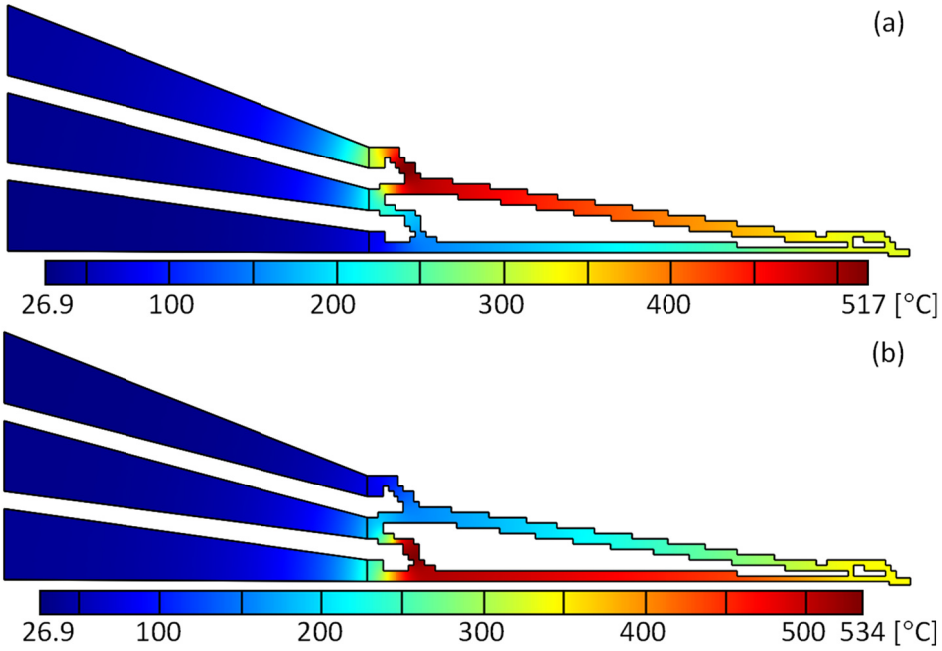

Figure D.1 Results for original Design A for (a) closing and (b) opening modes.

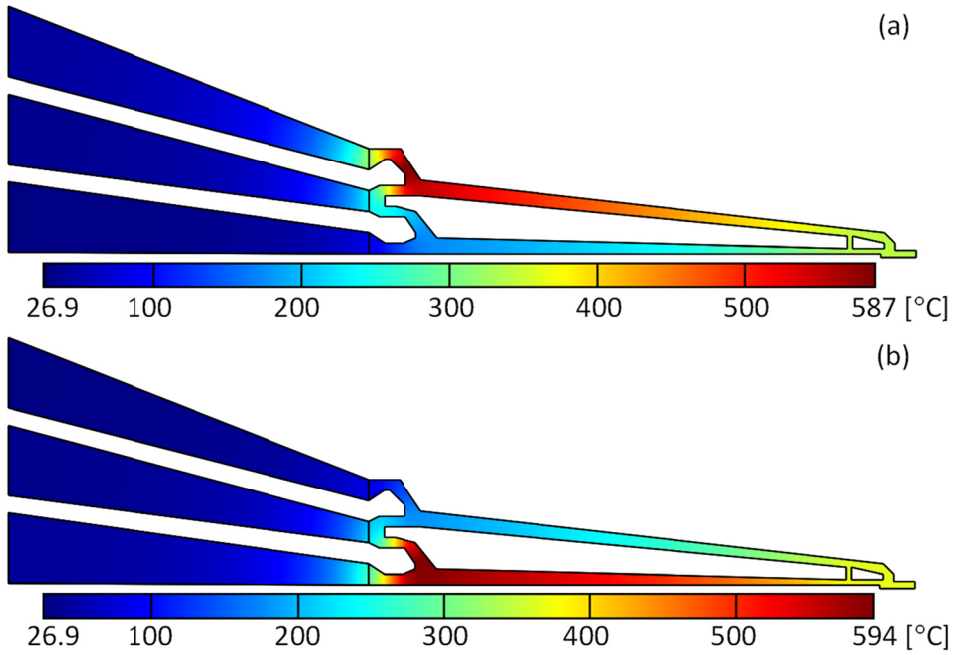

Figure D.2 Results for smoothed Design A for (a) closing and (b) opening modes.

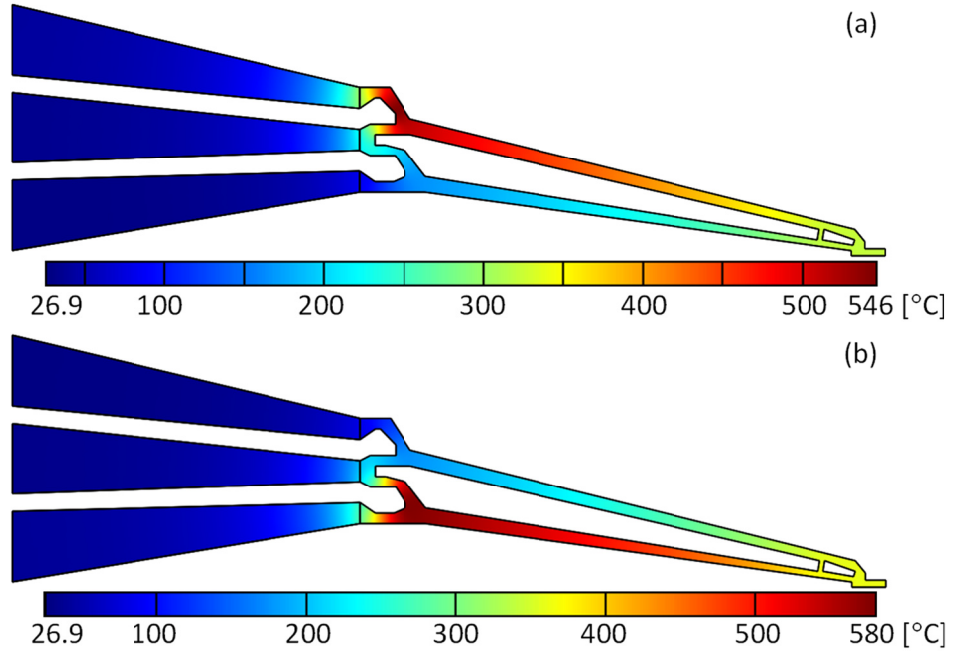

Figure D.3 Results for tilted Design A for (a) closing and (b) opening modes.

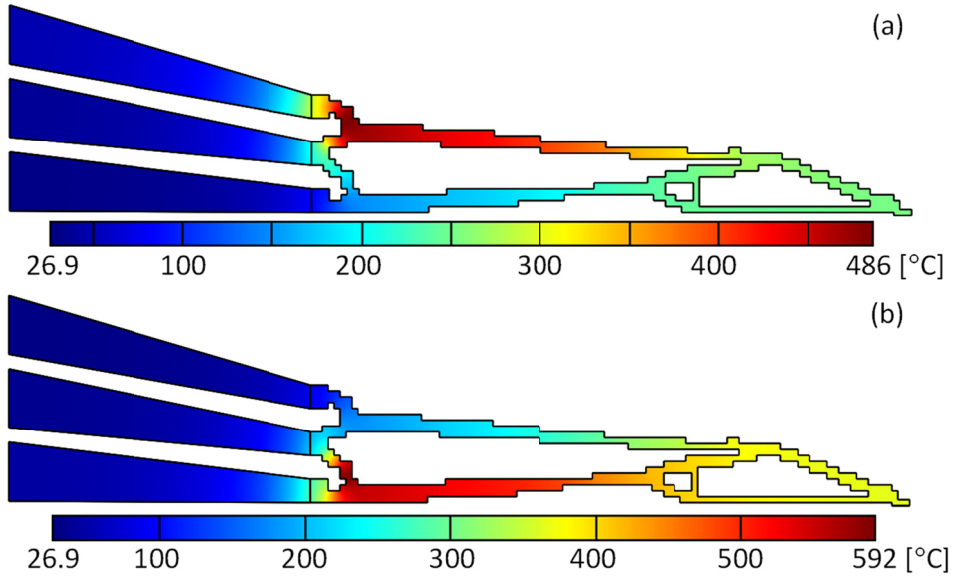

Figure D.4 Results for original Design B for (a) closing and (b) opening modes.

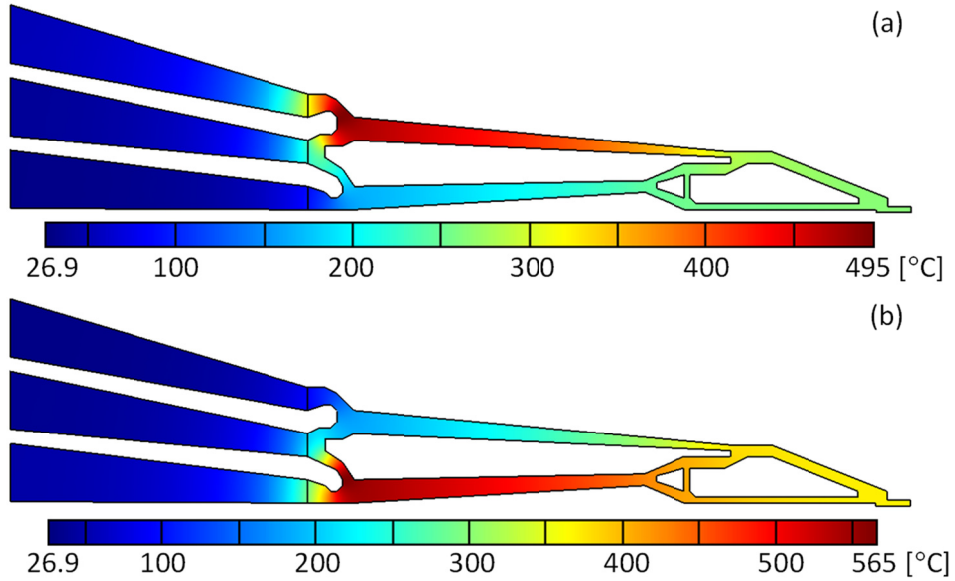

Figure D.5 Results for smoothed Design B for (a) closing and (b) opening modes.

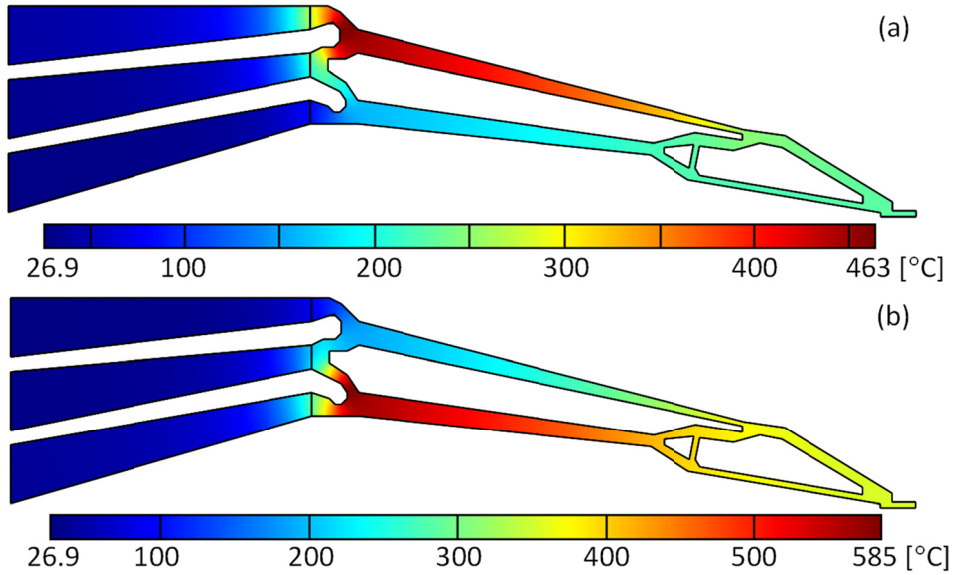

Figure D.6 Results for tilted Design B for (a) closing and (b) opening modes.

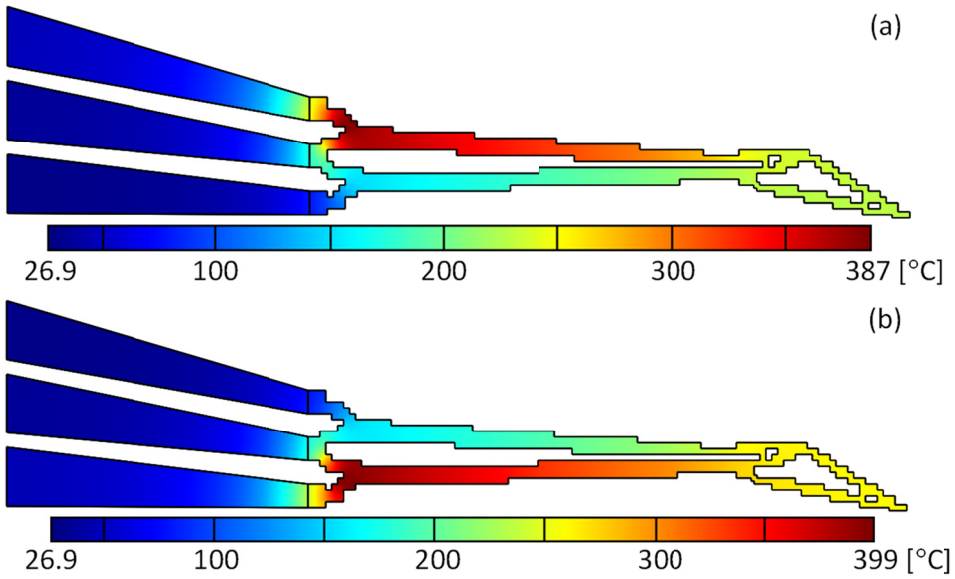

Figure D.7 Results for original Design C for (a) closing and (b) opening modes.

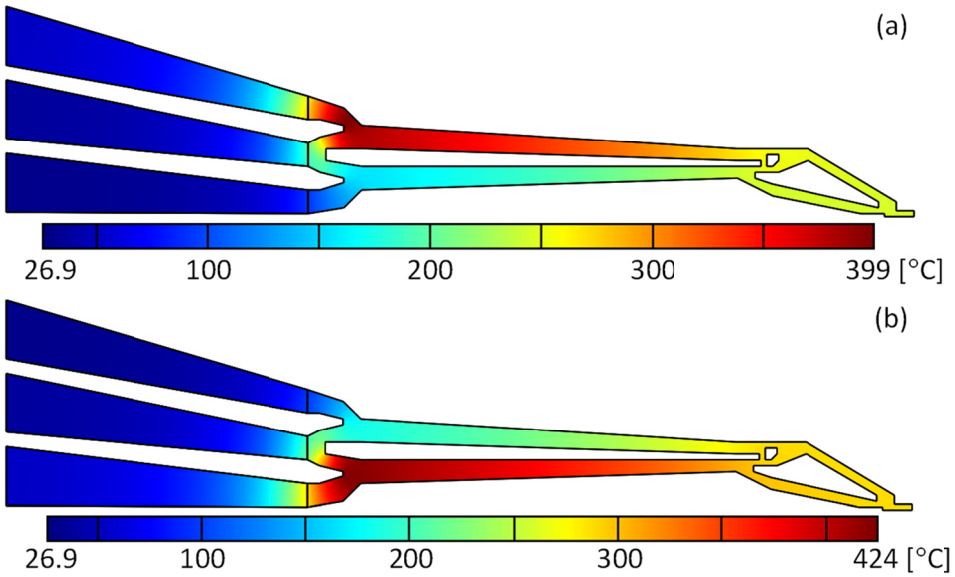

Figure D.8 Results for smoothed Design C for (a) closing and (b) opening modes.

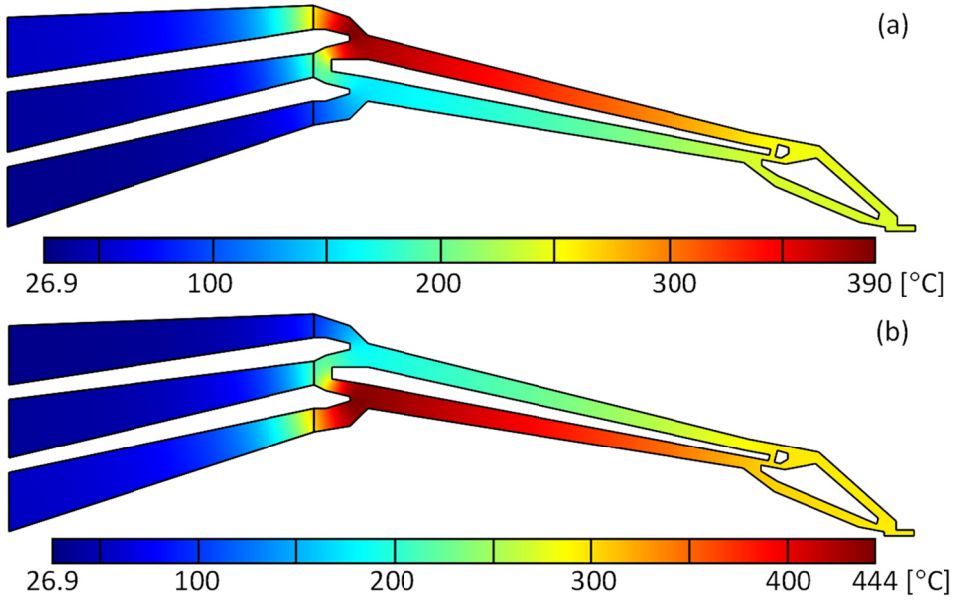

Figure D.9 Results for tilted Design C for (a) closing and (b) opening modes.

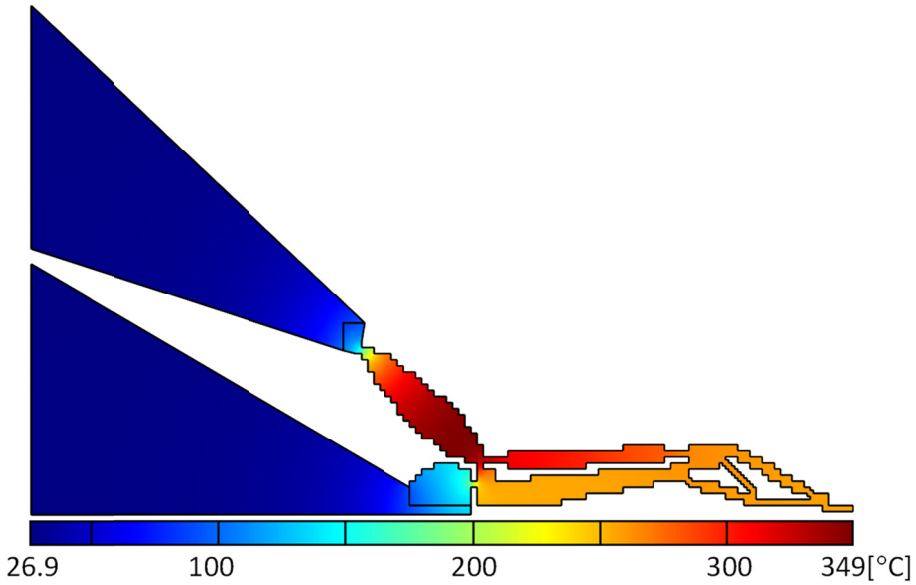

Figure D.10 Results for original Design D for closing mode.

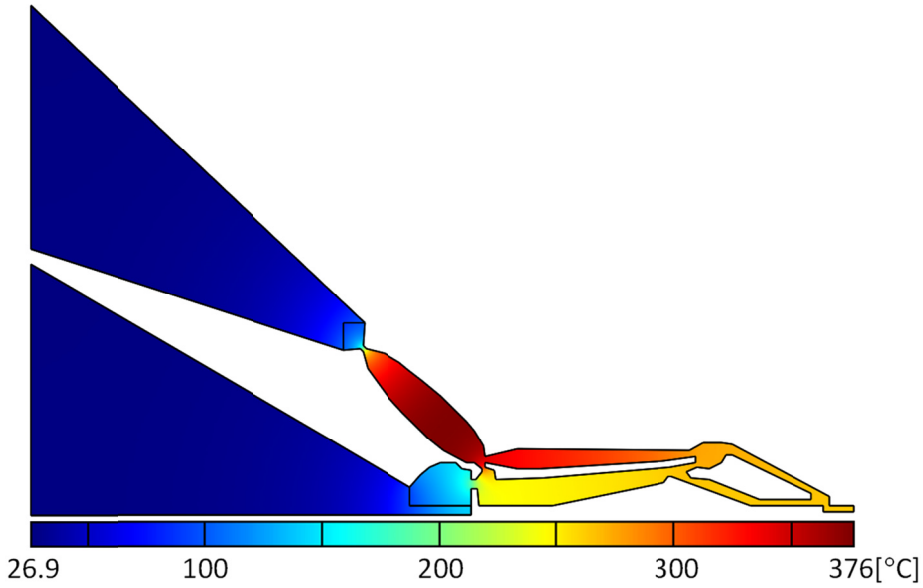

Figure D.11 Results for smoothed Design D for closing mode.

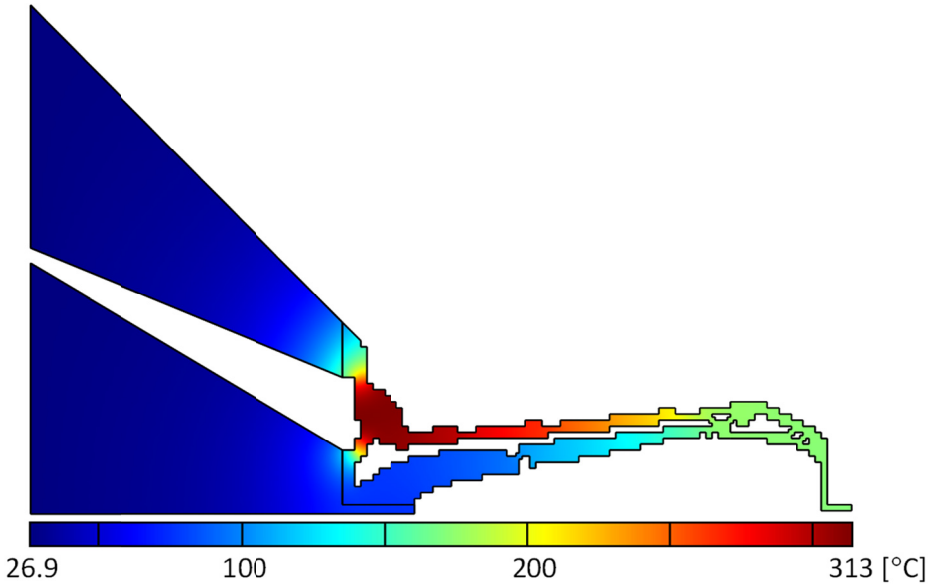

Figure D.12 Results for original Design E for closing mode.

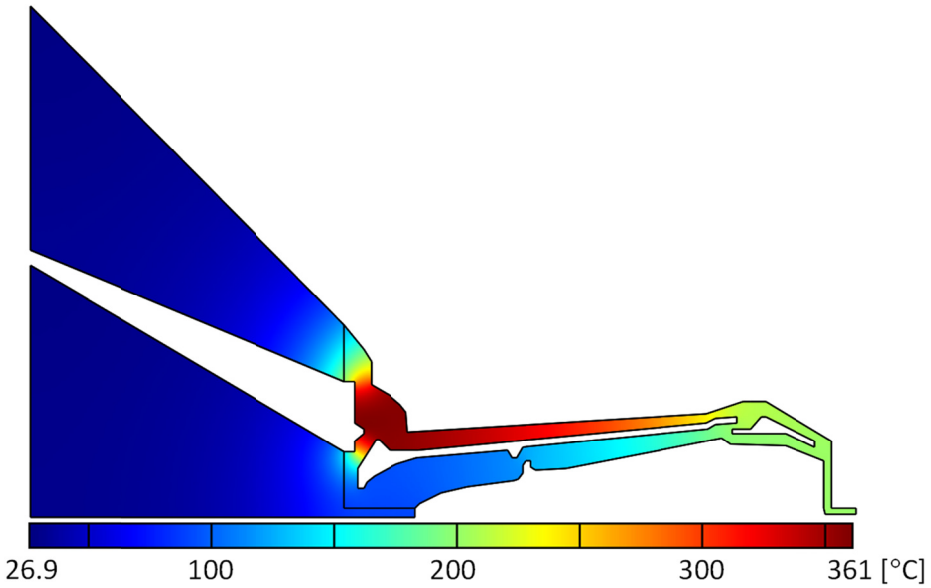

Figure D.13 Results for smoothed Design E for closing mode.

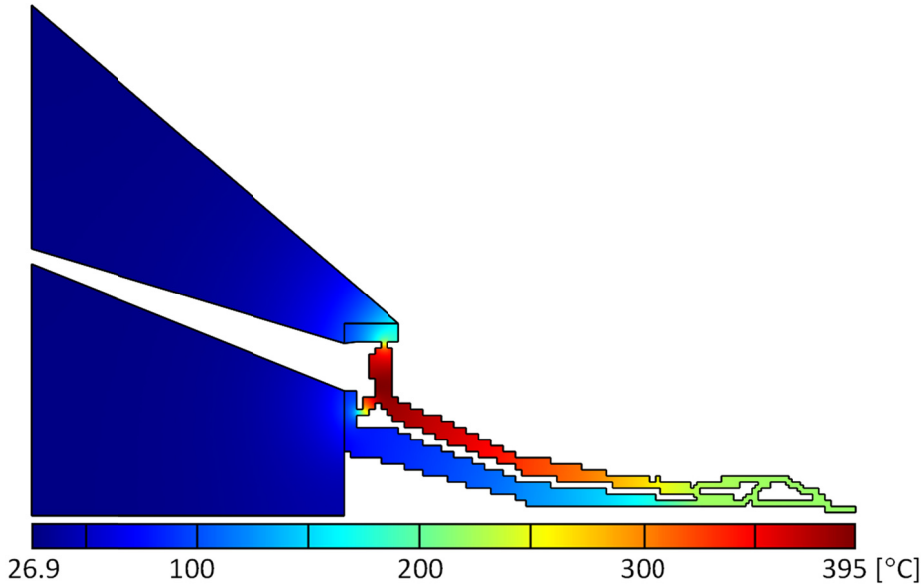

Figure D.14 Results for original Design F for closing mode.

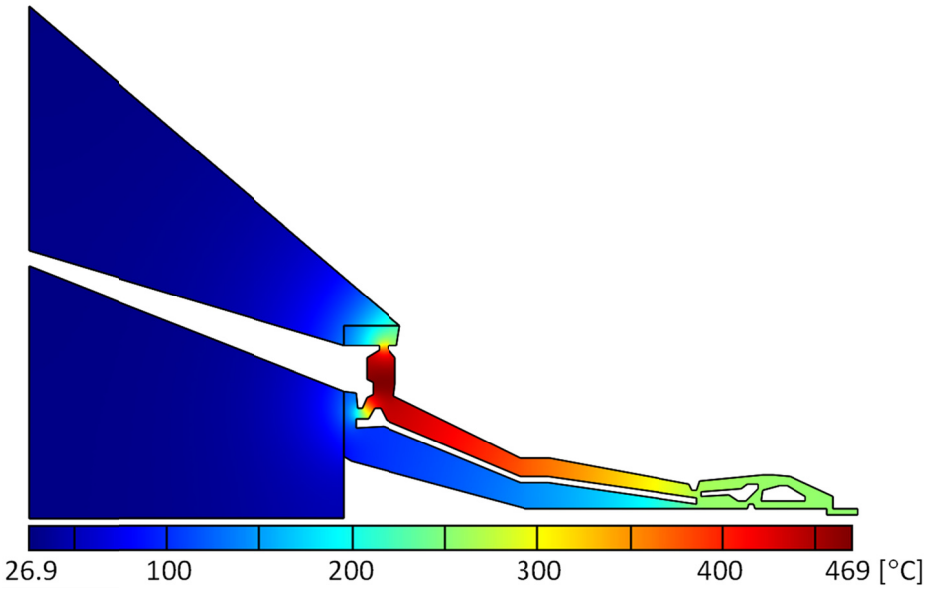

Figure D.15 Results for smoothed Design F for closing mode.

D.1.2 Sensitivity to Design Variations

Finite element analysis showing the effect of design variations for the topology optimized designs, with the color bar showing the maximum temperature: *Dashed lines.* Using the topology optimization software for the initial, grey-scale design (black) and the original, black & white design (blue). *Solid lines.* Ideal case analyses using COMSOL for the original, black & white design (blue), smoothed design (red) and tilted design (green).

In the three plots below, the left side corresponds to the closing mode of the microgrippers, where the right side corresponds to the opening mode.

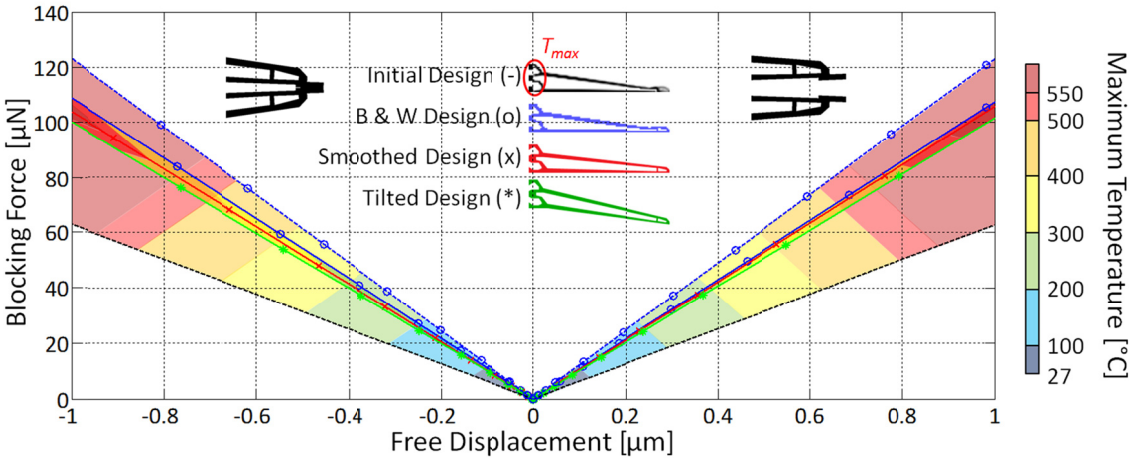

Figure D.16 For Design A.

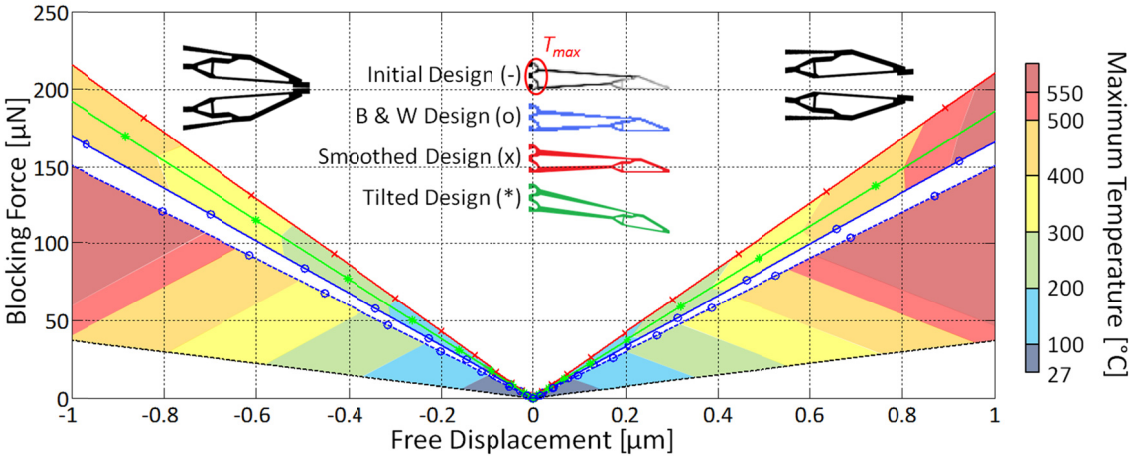

Figure D.17 For Design B.

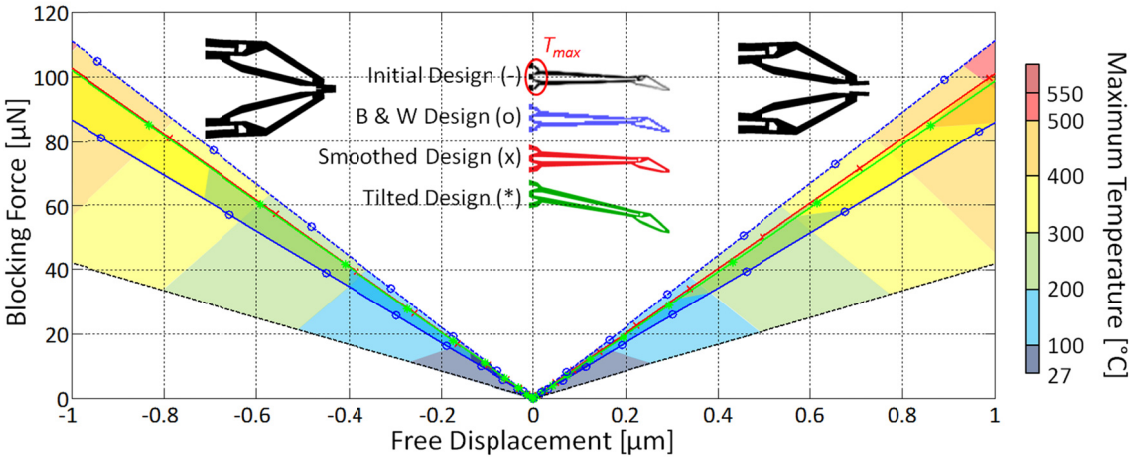

Figure D.18 For Design C.

In the following three plots below, there is only the left side since the microgrippers were designed for only closing.

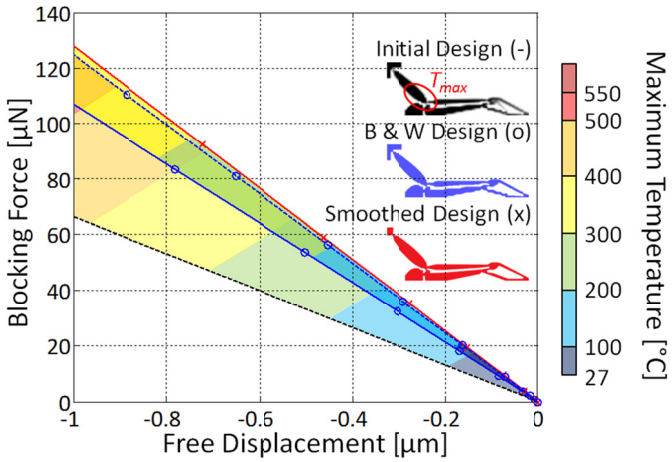

Figure D.19 For Design D.

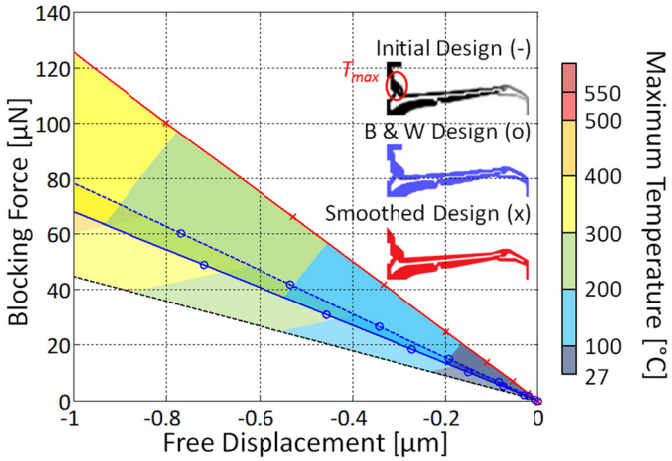

Figure D.20 For Design E.

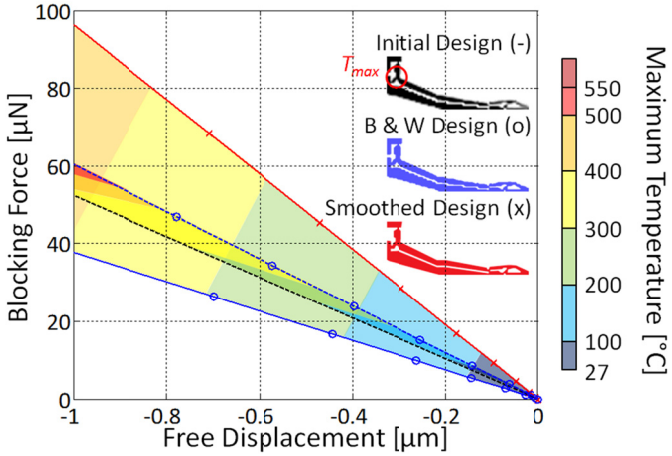

Figure D.21 For Design F.

Finite element analysis showing the effect of design variations for the topology optimized designs, with the color bar showing the end-effector temperature: *Dashed lines.* Using the topology optimization software for the initial, grey-scale design (black) and the original, black & white design (blue). *Solid lines.* Ideal case analyses using COMSOL for the original, black & white design (blue), smoothed design (red) and tilted design (green).

In the three plots below, the left side corresponds to the closing mode of the microgrippers, where the right side corresponds to the opening mode.

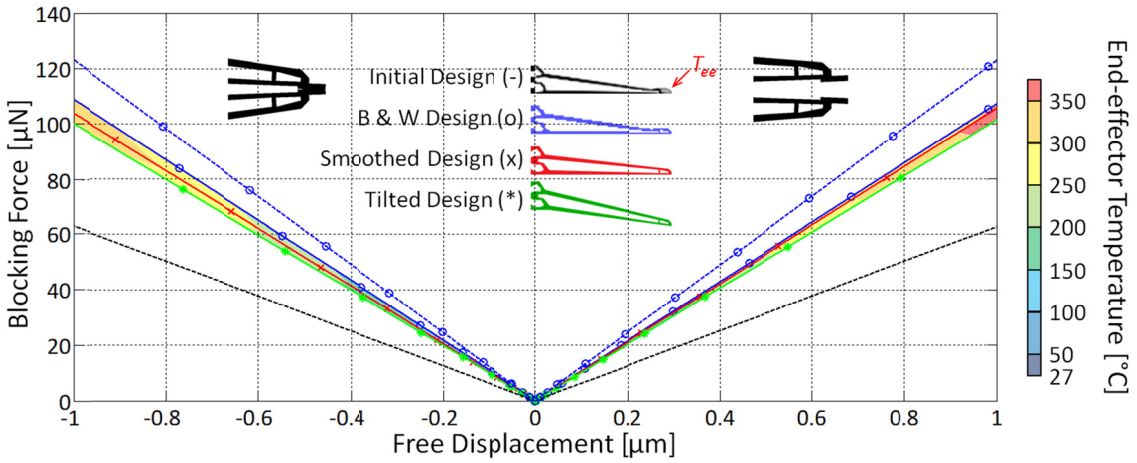

Figure D.22 For Design A.

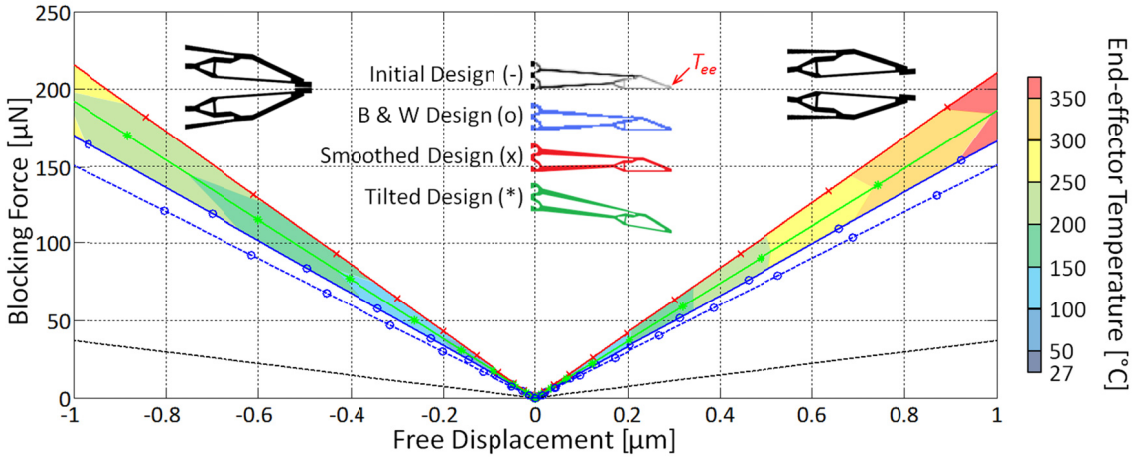

Figure D.23 For Design B.

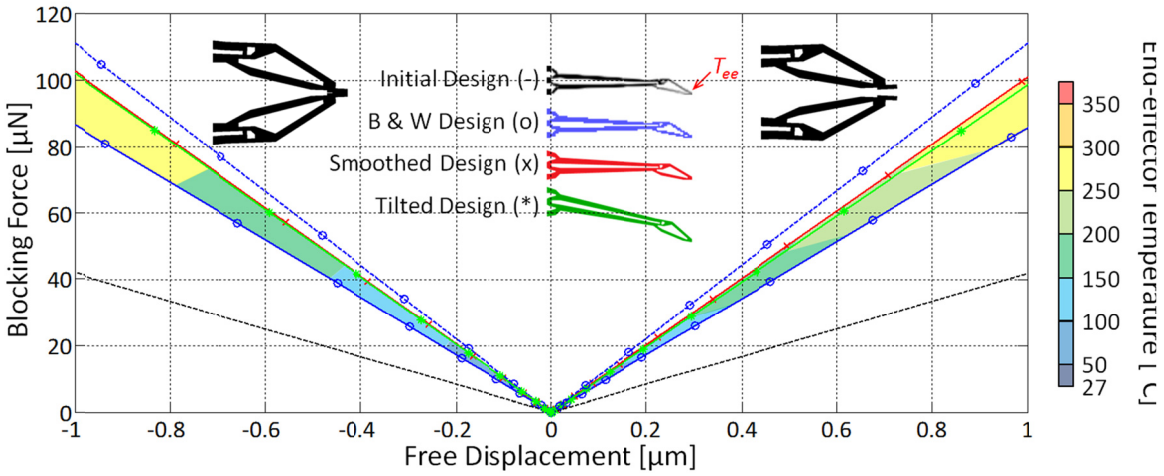

Figure D.24 For Design C.

In the following three plots below, there is only the left side since the microgrippers were designed for only closing.

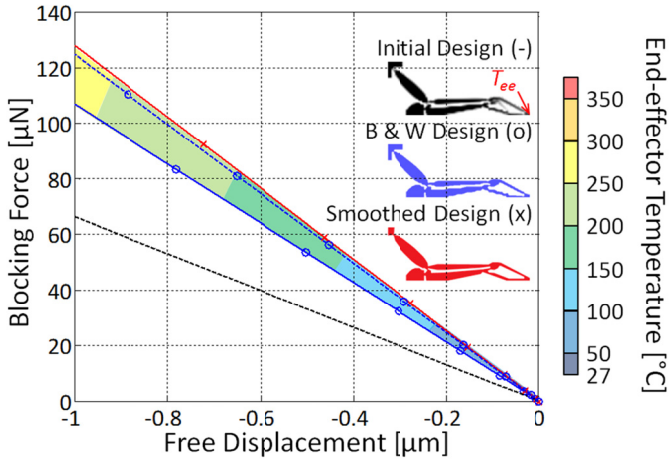

Figure D.25 For Design D.

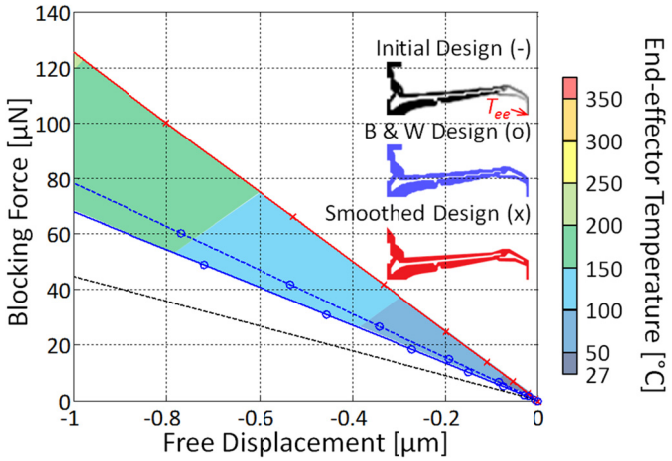

Figure D.26 For Design E.

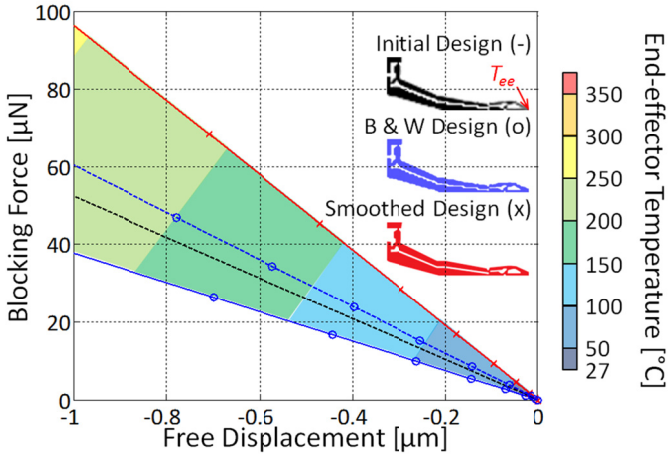

Figure D.27 For Design F.

Results for the mechanical simulations performed for determining the stiffness and the maximum gripping force applied to a 300 nm nanotube/wire at T_max = 550 °C for the topology optimized actuators at different design phases. Note that, the best (green) and the worst (red) performances at each column are highlighted.

Table D.1 Summary of the effect of design variations on the actuator performance, where the most favorable and unfavorable values are highlighted with green and red, respectively.

		Stiffness [N/m]	Gripping Force, F_{grip} [μN] @ T_{max} = 550 °C	End-effector Temperature, T_{ee} [°C]	
				@ contact, i.e. F_{grip} = 0	@ T_{max} = 550 °C
A	Original, B & W Version	119	14.6	307	332
	Smoothed Version	91.0	18.3	288	325
	Tilted Version	91.7	22.2	280	322
B	Original, B & W Version	177	38.5	244	270
	Smoothed Version	234	33.3	261	281
	Tilted Version	219	55.3	226	255
C	Original, B & W Version	102	46.6	228	283
	Smoothed Version	130	41.4	256	302
	Tilted Version	130	43.8	252	302
D	Original, B & W Version	127	72.5	260	361
	Smoothed Version	148	71.6	264	349
E	Original, B & W Version	79	63.4	172	248
	Smoothed Version	149	77.6	204	268
F	Original, B & W Version	61.8	2.5	265	272
	Smoothed Version	146	N/A (contact @ 591 °C)	295	282
Three-Beam Actuator (with 2 μm × 200 μm beams)		2.2	10.2	294	387

D.1.3 Sensitivity to Fabrication Variations

Ideal case actuator force vs. y-axis displacement curves for the smoothed topology optimized actuators and their variations with increased and decreased line-widths, where the color map shows the maximum temperature.

In the three plots below, the left side corresponds to the closing mode of the microgrippers, where the right side corresponds to the opening mode.

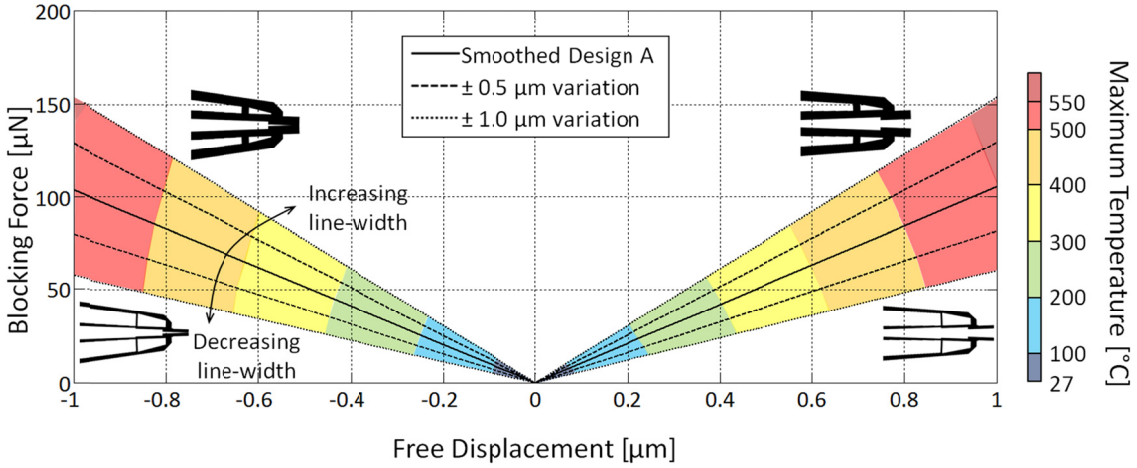

Figure D.28 For smoothed Design A.

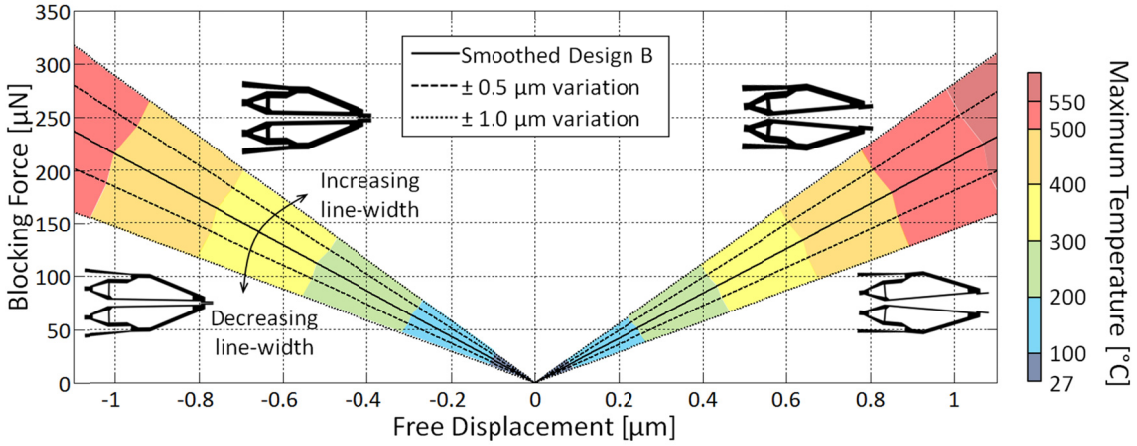

Figure D.29 For smoothed Design B.

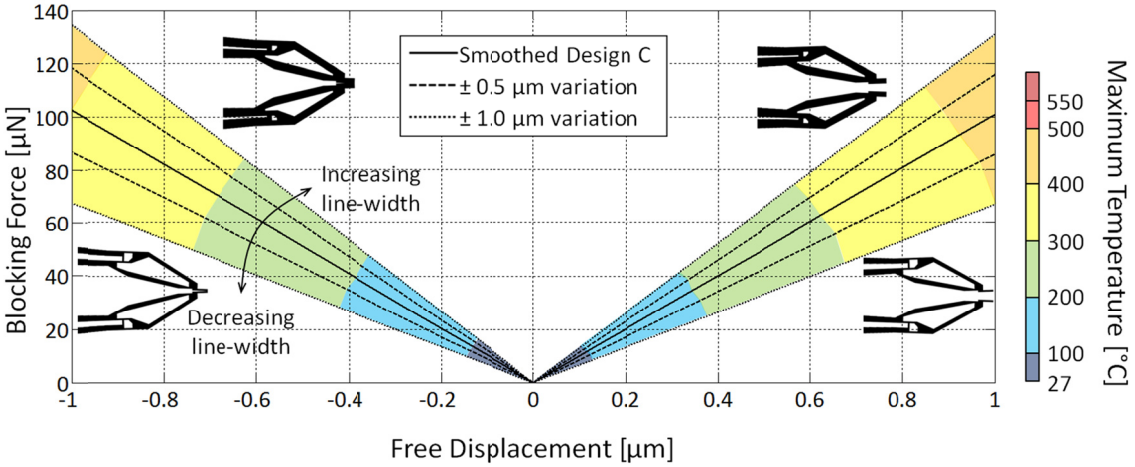

Figure D.30 For smoothed Design C.

In the following three plots below, there is only the left side since the microgrippers were designed for only closing.

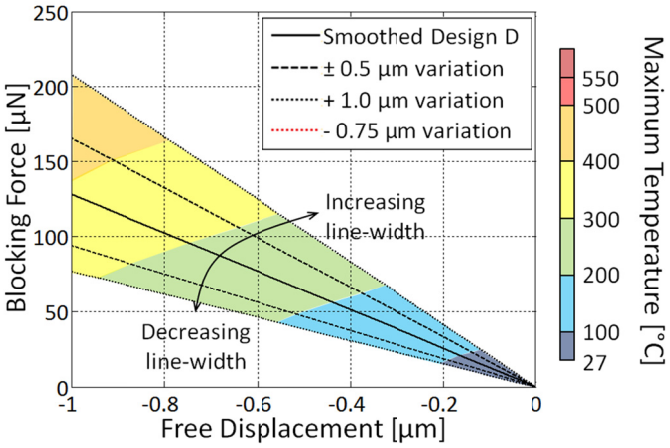

Figure D.31 For smoothed Design D.

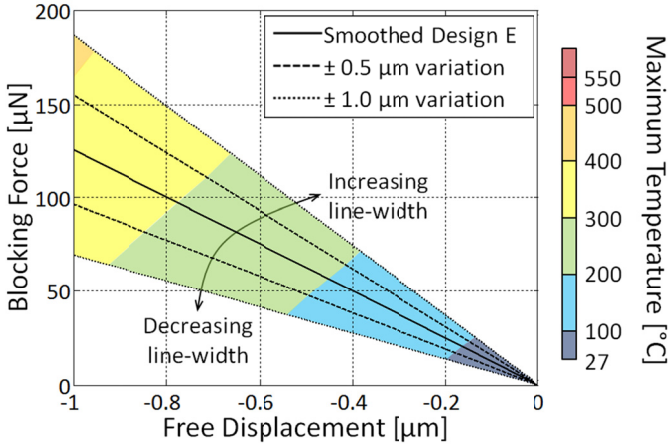

Figure D.32 For smoothed Design E.

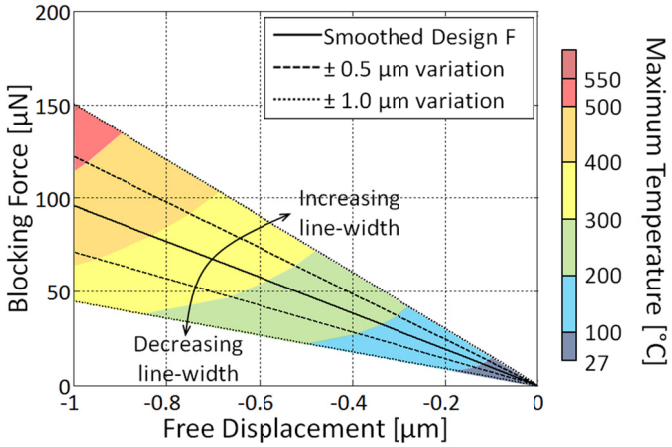

Figure D.33 For smoothed Design F.

Ideal case actuator force vs. y-axis displacement curves for the smoothed topology optimized actuators and their variations with increased and decreased line-widths, where the color map shows the end-effector temperature.

In the three plots below, the left side corresponds to the closing mode of the microgrippers, where the right side corresponds to the opening mode.

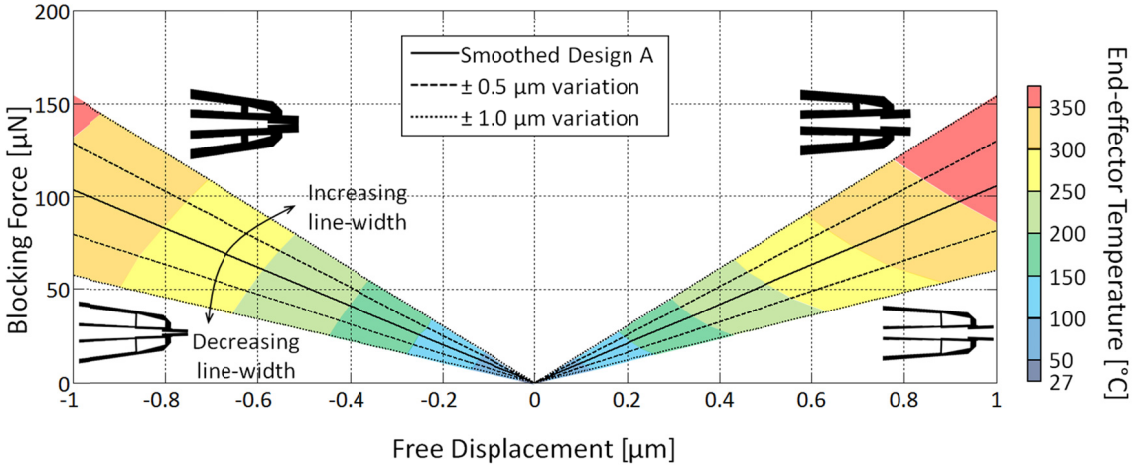

Figure D.34 For smoothed Design A.

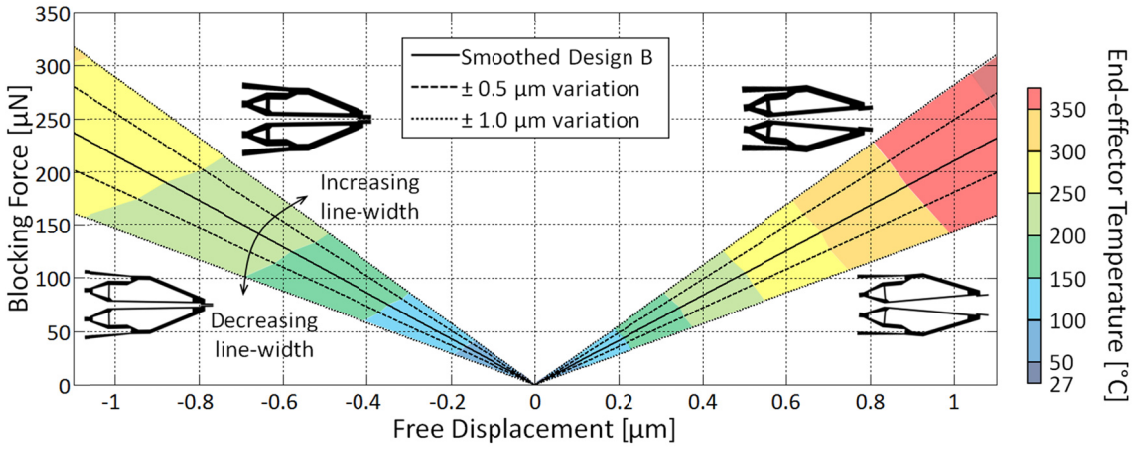

Figure D.35 For smoothed Design B.

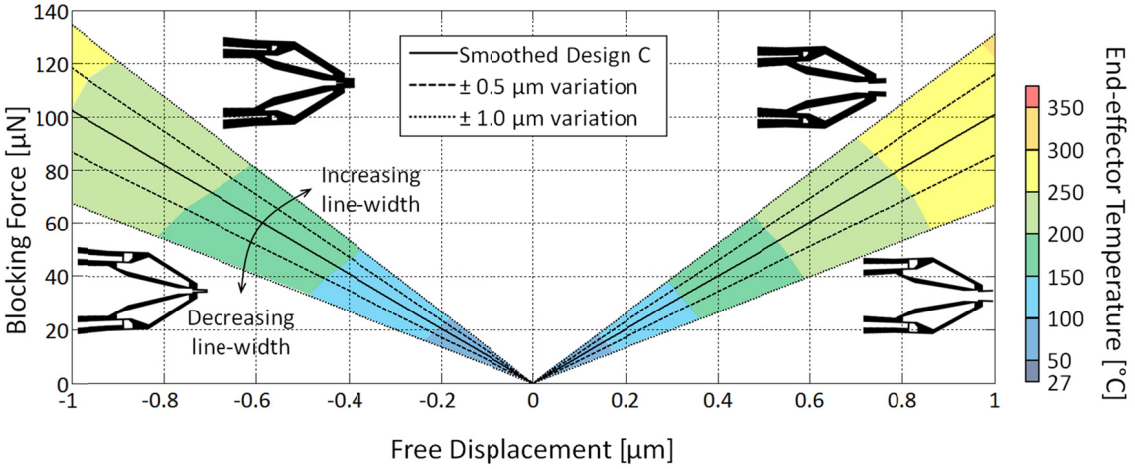

Figure D.36 For smoothed Design C.

In the three plots below, there is only the left side since the microgrippers were designed for only closing.

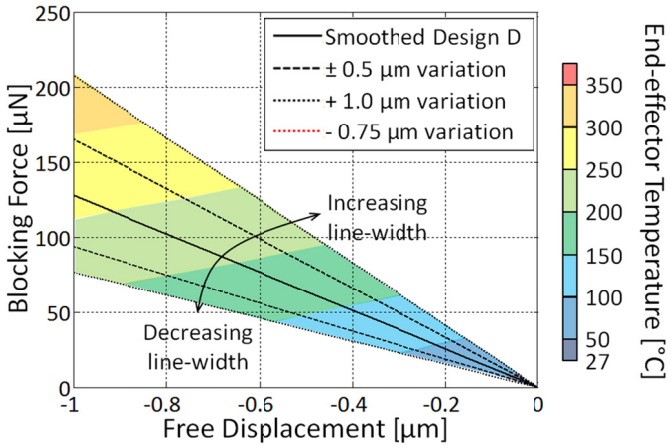

Figure D.37 For smoothed Design D.

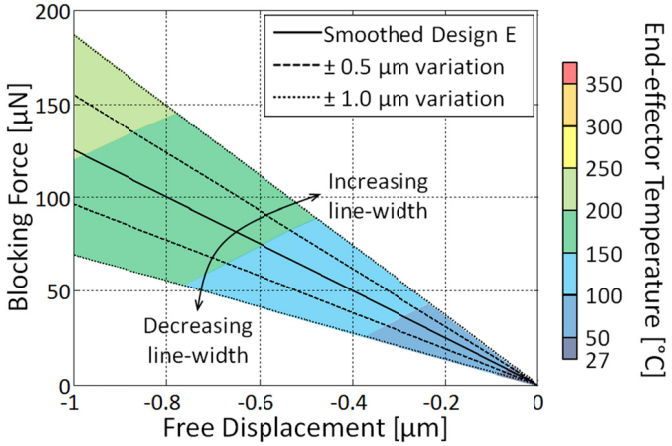

Figure D.38 For smoothed Design E.

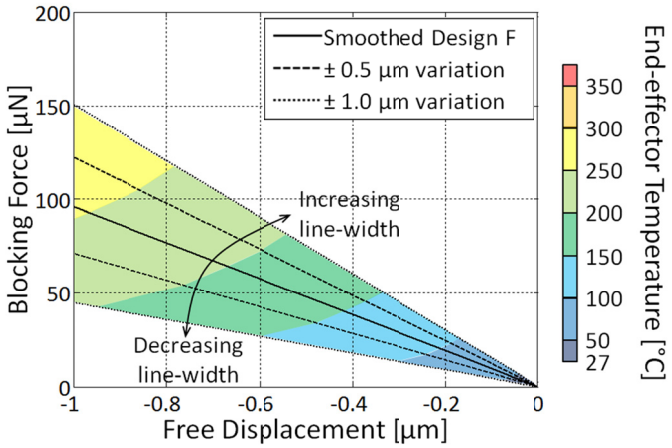

Figure D.39 For smoothed Design F.

Results for the mechanical simulations performed for determining the stiffness and the maximum gripping force applied to a 300 nm nanotube/wire at T_{max} = 550 °C for the topology optimized actuators with variable line-width.

Table D.2 Summary of the effect of fabrication variations on the actuator performance, where the most favorable and unfavorable values are highlighted with green and red, respectively.

		Stiffness [N/m]	Gripping Force, F_{grip} [μN] @ T_{max} = 550 °C	End-effector Temperature, T_{ee} [°C]	
				@ contact, i.e. F_{grip} = 0	@ T_{max} = 550 °C
A	-1 μm variation	41.1	19.6	240	308
	-0.5 μm variation	63.9	20.2	265	316
	Smoothed Design	91.0	18.3	288	325
	+0.5 μm variation	122	12.9	312	331
	+1 μm variation	156	3.4	334	339
B	-1 μm variation	153	36.5	232	260
	-0.5 μm variation	194	36.8	249	273
	Smoothed Design	234	33.2	261	281
	+0.5 μm variation	277	23.9	277	290
	+1 μm variation	320	13.4	289	296
C	-1 μm variation	78.5	40.4	223	285
	-0.5 μm variation	105	44.2	238	294
	Smoothed Design	130	41.4	256	302
	+0.5 μm variation	157	35.8	271	307
	+1 μm variation	185	27.5	289	312
D	-0.75 μm variation	86.3	78.4	209	327
	-0.5 μm variation	107	79.8	228	336
	Smoothed Design	148	71.6	264	349
	+0.5 μm variation	198	51.5	302	357
	+1 μm variation	254	22.8	342	363
E	-1 μm variation	80.5	64.9	174	253
	-0.5 μm variation	113	74.4	188	260
	Smoothed Design	149	77.6	204	268
	+0.5 μm variation	187	74.8	221	274
	+1 μm variation	229	66.8	237	280

Table D.2 Continued.

		Stiffness [N/m]	Gripping Force, F_{grip} [µN] @ T_{max} = 550 °C	End-effector Temperature, T_{ee} [°C]	
				@ contact, i.e. F_{grip} = 0	@ T_{max} = 550 °C
F	-1 µm variation	77.0	13	259	289
	-0.5 µm variation	110	3.4	277	283
	Smoothed Design	146	N/A (contact @ 591 °C)	295	282
	+0.5 µm variation	183	N/A (contact @ 641 °C)	312	284
	+1 µm variation	224	N/A (contact @ 691 °C)	328	287

D.1.4 Elongation (x-Axis Displacement)

Elongation vs. actuation curves for different versions of the topology optimized actuators.

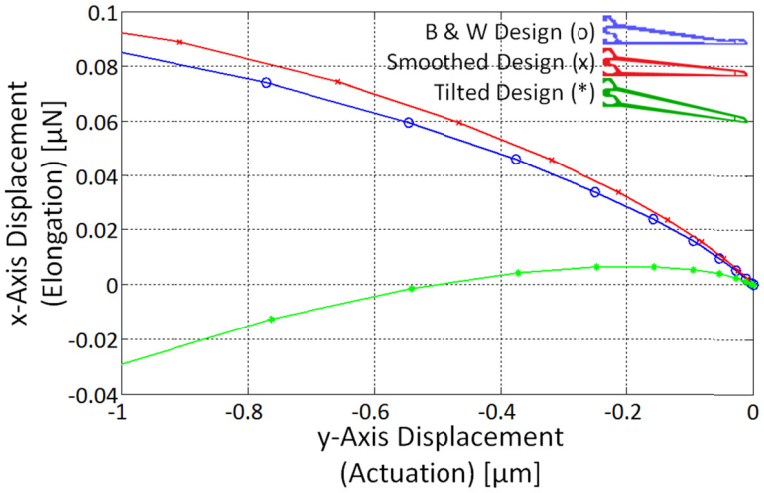

Figure D.40 For Design A.

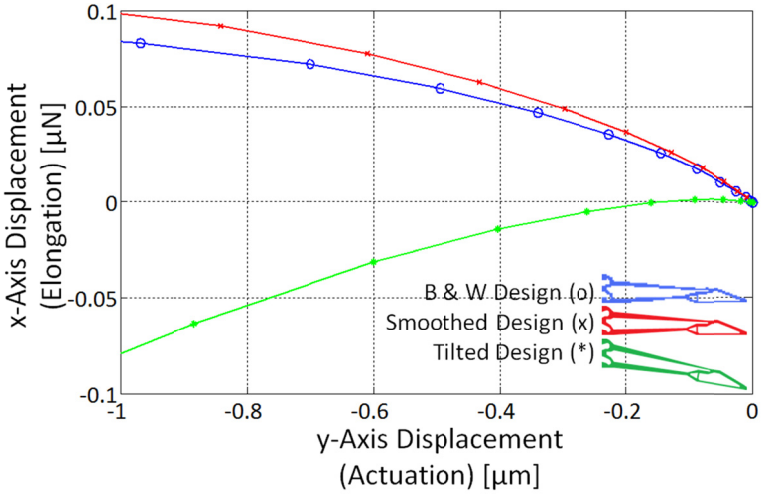

Figure D.41 For Design B.

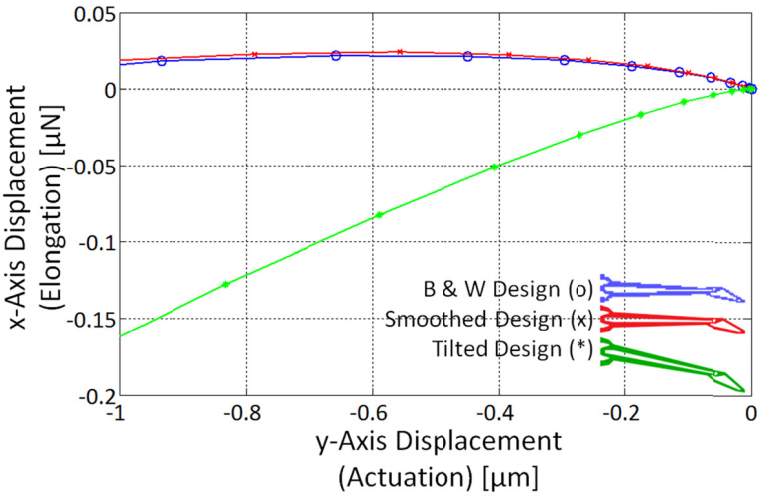

Figure D.42 For Design C.

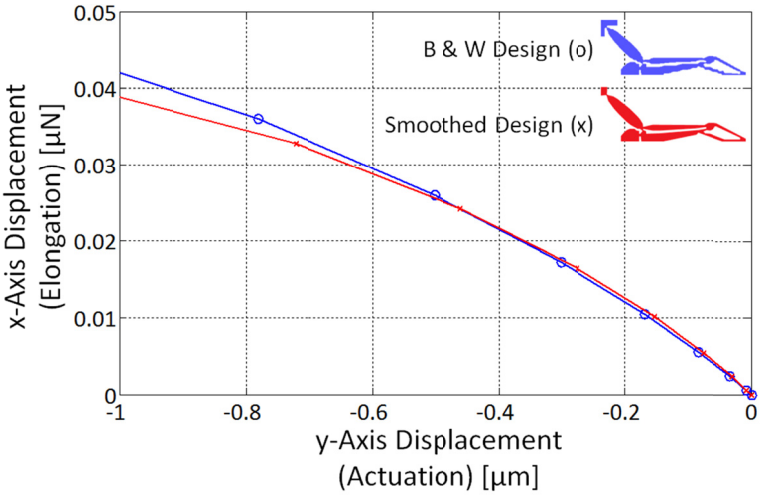

Figure D.43 For Design D.

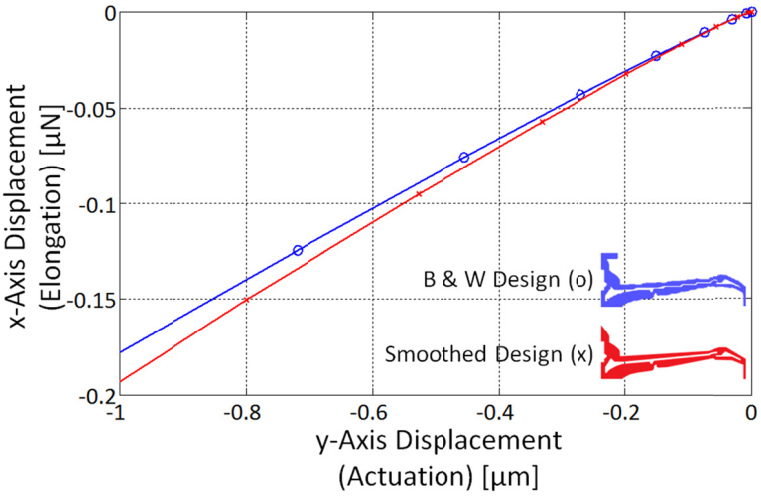

Figure D.44 For Design E.

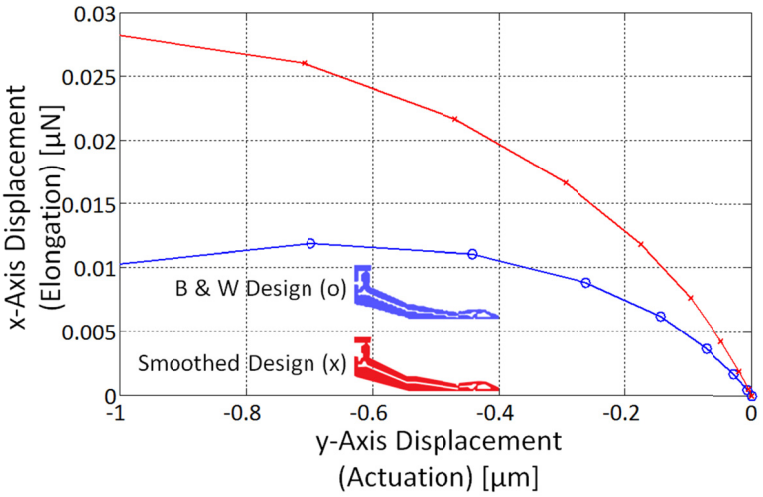

Figure D.45 For Design F.

D.2 Non-ideal Case Simulations

Simulation results for the non-ideal case, showing the temperature distribution within the topology optimized actuators at 1 µm displacement at the closing mode.

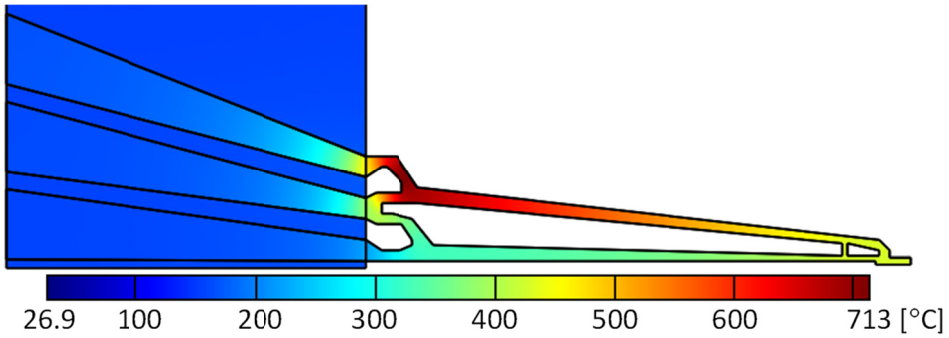

Figure D.46 Results for smoothed Design A with narrow electrodes.

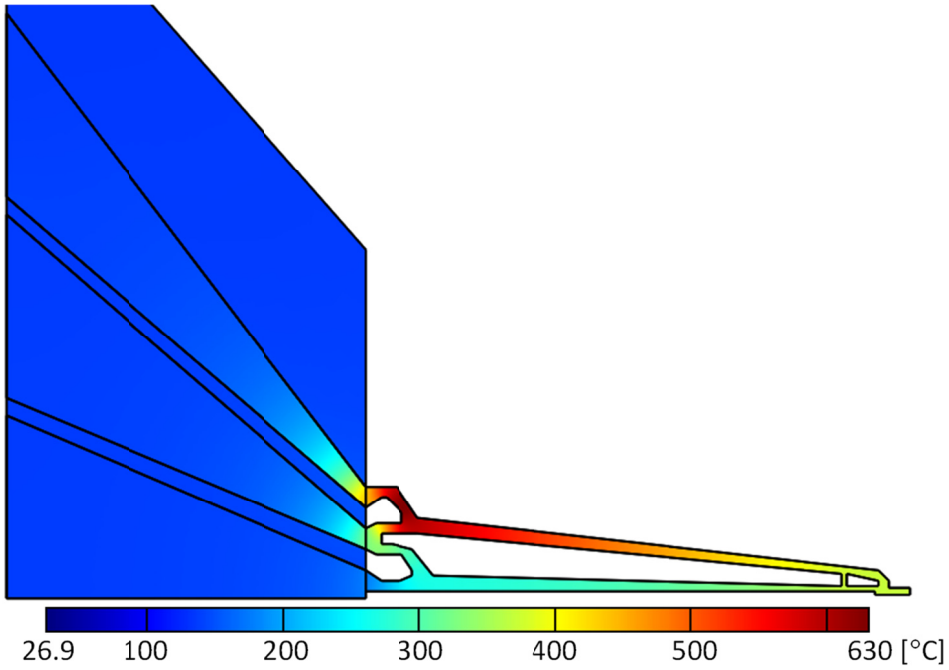

Figure D.47 Results for smoothed Design A with wide electrodes.

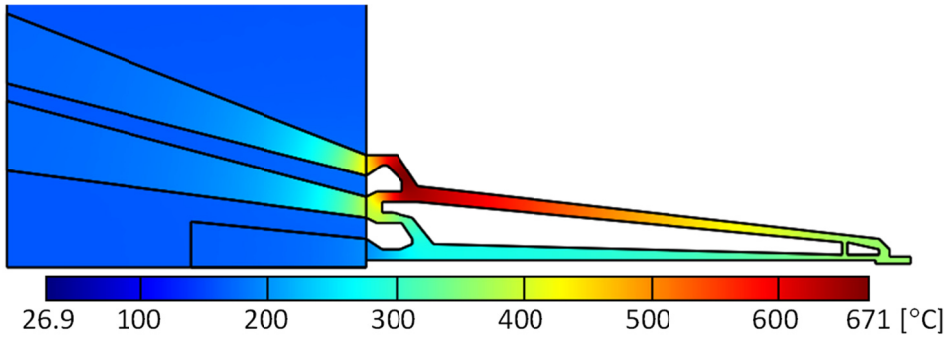

Figure D.48 Results for smoothed Design A with two electrodes.

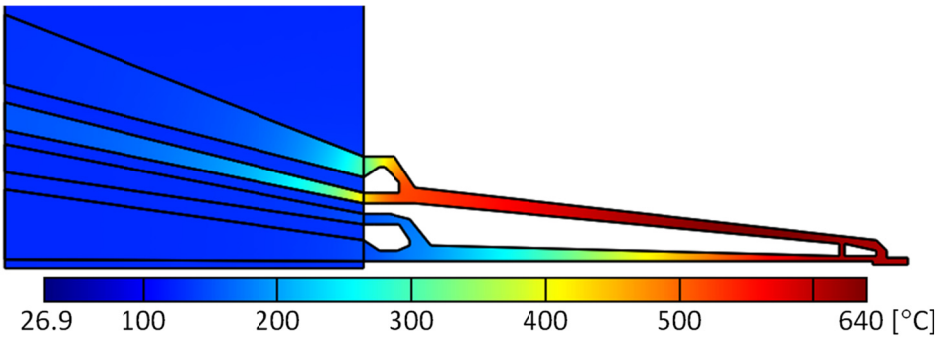

Figure D.49 Results for smoothed Design A with divided electrodes.

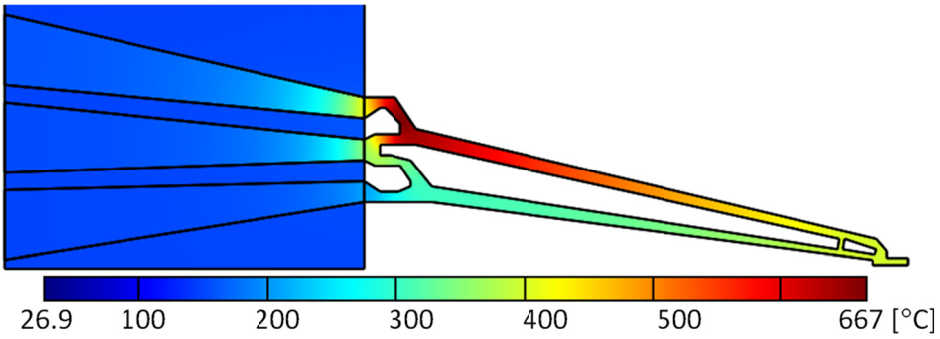

Figure D.50 Results for tilted Design A with narrow electrodes for closing mode.

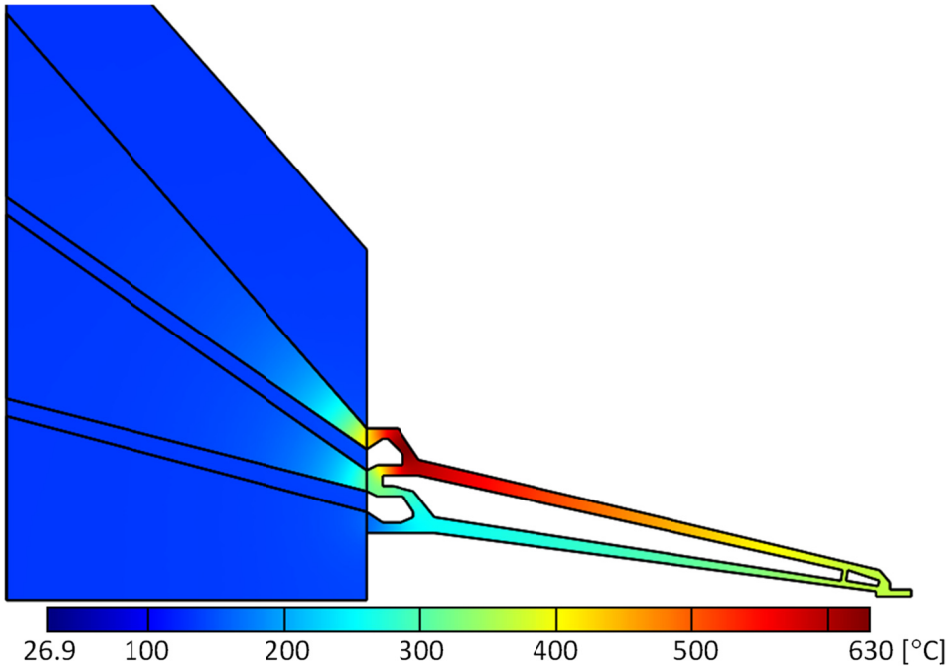

Figure D.51 Results for tilted Design A with wide electrodes.

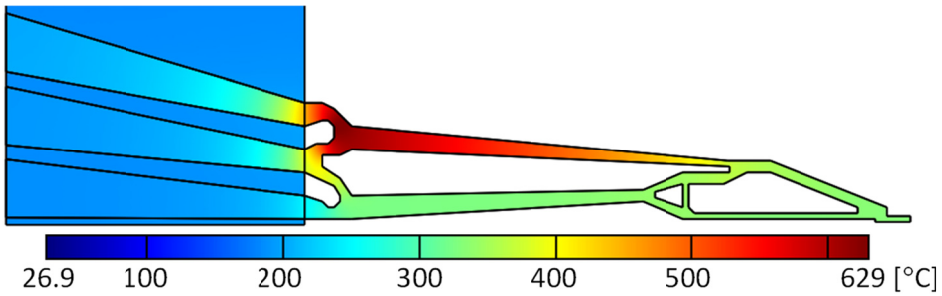

Figure D.52 Results for smoothed Design B with narrow electrodes.

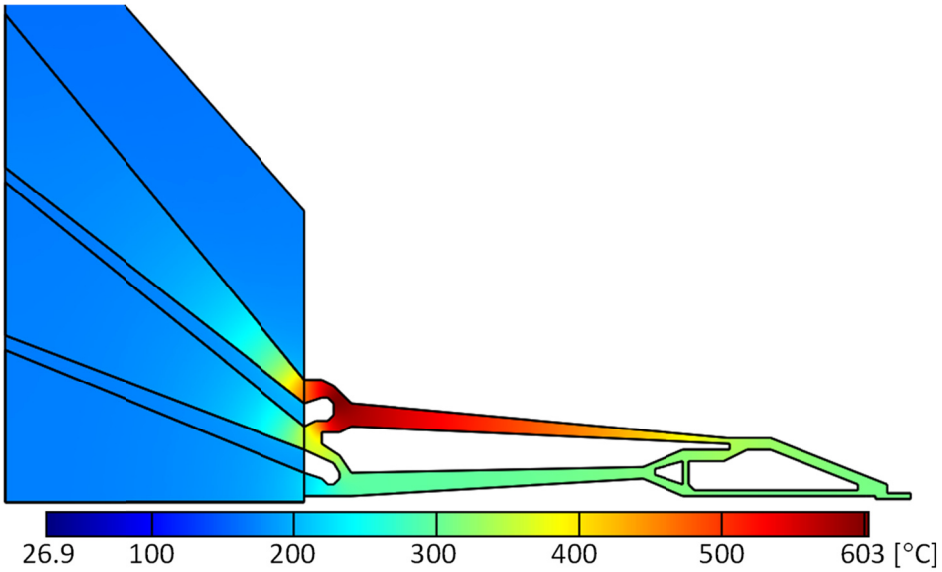

Figure D.53 Results for smoothed Design B with wide electrodes.

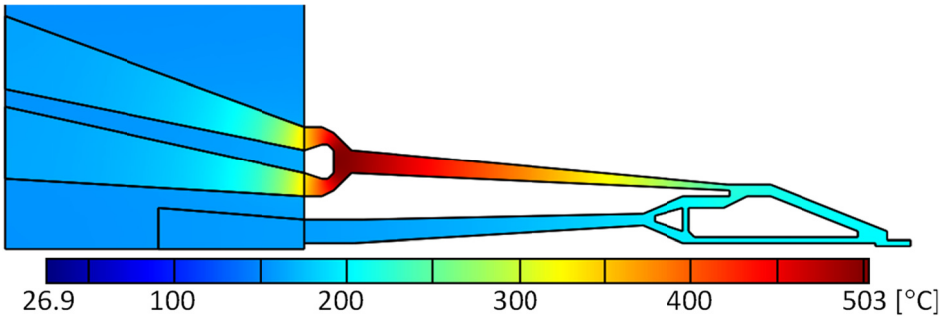

Figure D.54 Results for smoothed Design B with two electrodes.

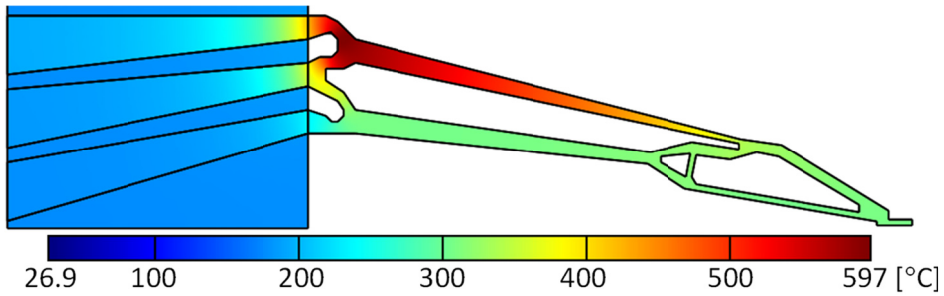

Figure D.55 Results for tilted Design B with narrow electrodes.

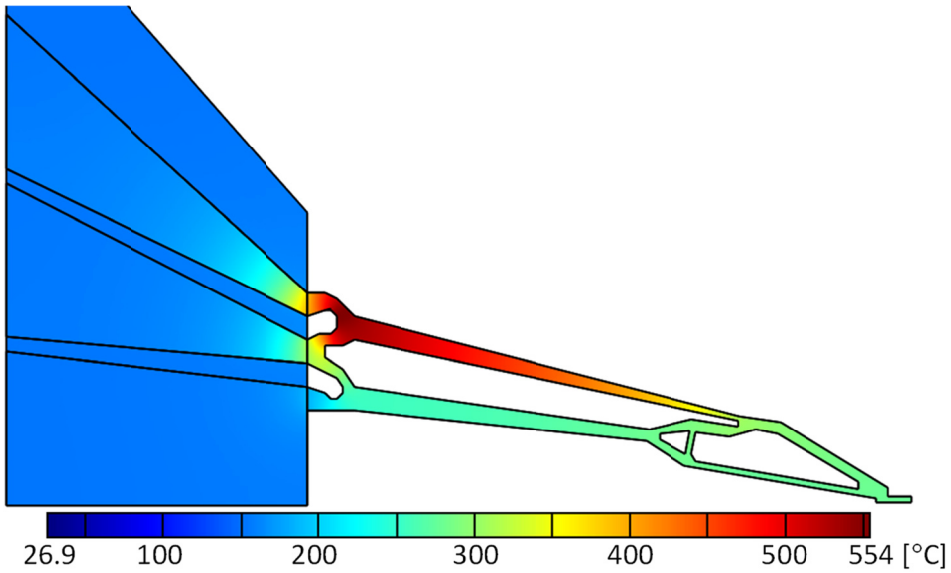

Figure D.56 Results for tilted Design B with wide electrodes.

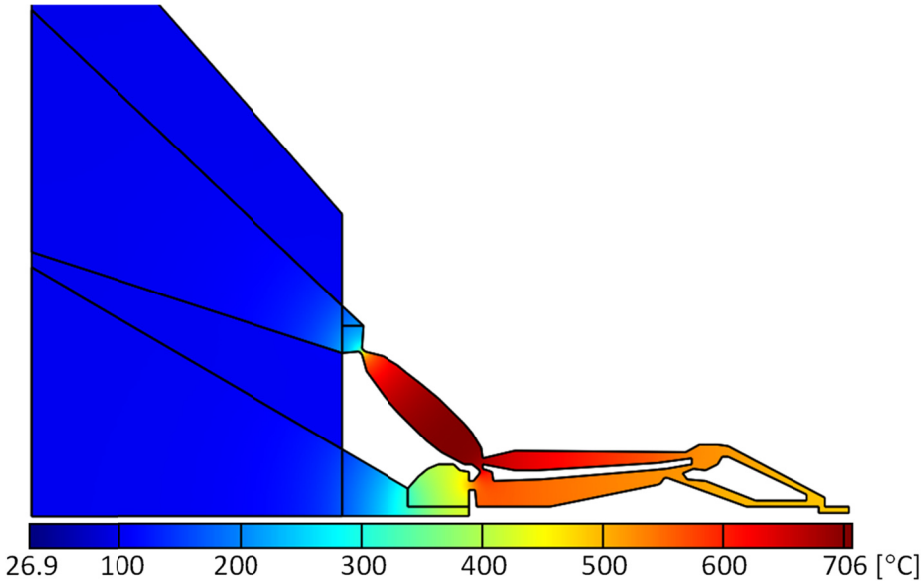

Figure D.57 Results for Design D.

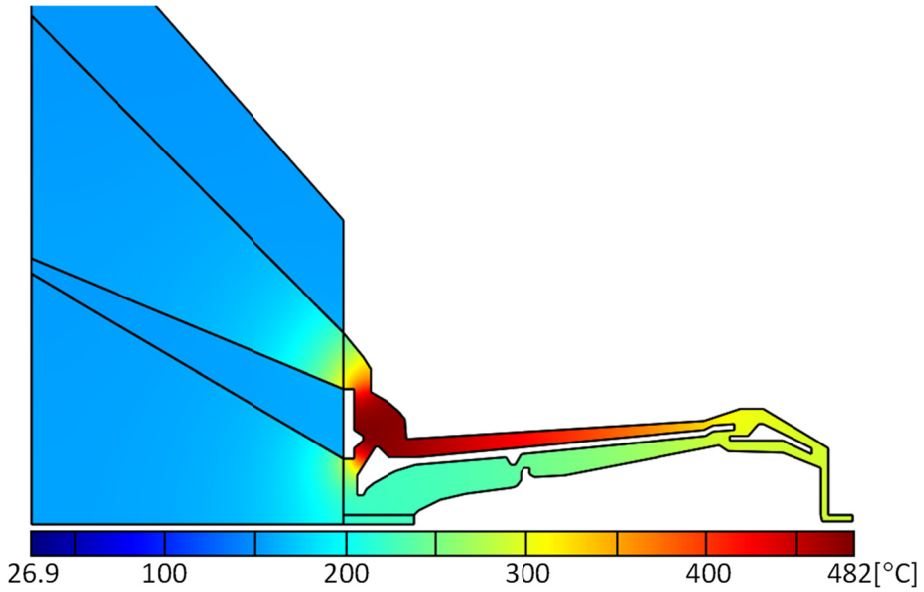

Figure D.58 Results for Design E.

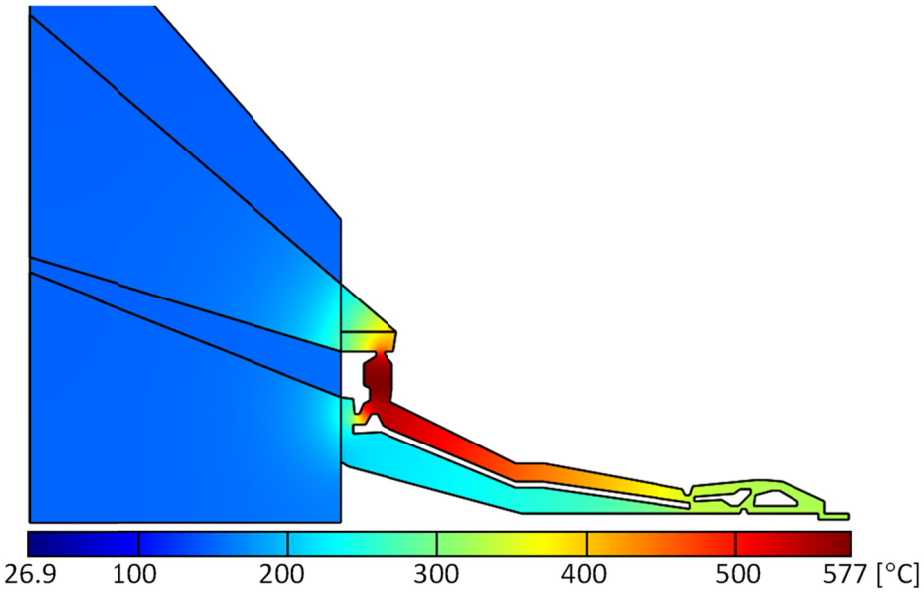

Figure D.59 Results for Design F.

APPENDIX E The Fabrication Process

Table E.1 Fabrication process for the topology optimized microgrippers.

Process Step	Details	Comments	Cross-section
1.a. Handle wafer	Si(100), n-type (phosphor) **Resistivity:** 1-30 Ω-cm **Thickness:** 501-503 µm	✓ Use numbered wafers. ✓ Process 25 wafers from the same box. ✓ Measure thickness of one wafer from the same batch. ✓ t_{wafer}: ..... µm	
1.b. Deposition of the buried SiO_2 layer	**Furnace:** Phosphor drive-in **Recipe:** wet1000 **Thickness:** 750 nm-1 µm	✓ Measure thickness of the oxide layer using Filmtek. ✓ t_{oxide}: ..... nm	
1.c. Deposition of the Poly-Si device layer (p-type (boron), 0.01-0.16 Ω-cm)	**Furnace:** LPCVD-PolySi **Recipe:** pol620px **Thickness:** 5±0.5 µm **Boat speed:** 150 mm/min **SiH_4 flow:** 80 sccm **B_2H_6 flow:** 7 sccm **Pressure:** 250 mTorr	Boat speed is important. Wafers break if it is fast!	

Table E.1 Continued.

Process Step	Details	Comments	Cross-section
1.d. Annealing	**Furnace:** Anneal 1 **Recipe:** ann1000 **N_2 flow:** 6 sccm **O_2 flow:** 0 sccm **Time:** 1 h	✓ Measure thickness of the PolySi layer in SEM. ✓ $t_{poly-Si}$: ..... nm	
1.e. Removal of the backside poly-Si	**Machine:** RIE1 **Recipe:** dhp_soi **Time:** Continue until the end point is reached!	✓ Process 10 wafers. ✓ Process the back side! ✓ (A faster RIE etch or ASE can also be used.)	
2.a. Oxide etch (bHF)	**Time:** Until the oxide layer at the back is removed!		
2.b. Resist spin	**Machine:** Track1 **Resist Type:** AZ5214E **Thickness:** 1.5 µm		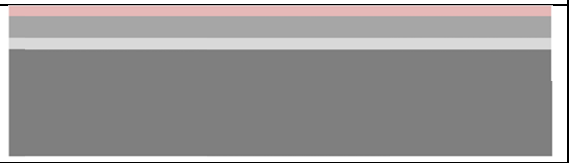
2.c. First exposure (Device Mask)	**Machine:** KS Aligner **Exposure Mode:** Hard contact **Exposure Time:** 3.3 s	✓ Align to major flat.	
2.d. Reversal bake	**Machine:** Track1 **Recipe:** rev120s **Temperature:** 120 °C **Time:** 120 s		

Table E.1 Continued.

Process Step	Details	Comments	Cross-section
2.e. Flood exposure	**Machine:** KS Aligner **Exposure Time:** ~ 35 s		
2.f. Develop	**Time:** ~ 65 s	✓ Prepare a fresh developer bath.	
2.g. Spin dry	**Machine:** Spin Drier 1		
3.a. Device layer etch	**Machine:** ASE **Recipe:** nanointegration/sar_soi (Process has an O_2 etch step for descum before etch step!) **Time:** ~24-25 min **C_4F_8 flow:** 90 sccm **SF_6 flow:** 40 sccm **Pressure:** 15 mTorr **Coil power:** 800 W **Platen power:** 10 W **Mode:** Unswitched, auto APC **Temperature:** 20 ^{o}C **Pressure (He):** 9.8 Torr	✓ Process has an O_2 etch step, i.e. descum, before the etch step! ✓ Start watching the wafer from the mirror after the 20th minute of the etch step. ✓ Poly-Si slowly disappears starting from the wafer edge. ✓ Continue the process ~2 min 30 s more after the poly-Si is completely removed from the wafer and abort the process.	
✓ Check if the poly-Si between the beams is completely etched using the optical microscope. Continue ASE ~1 min. more if not.			

Table E.1 Continued.

Process Step	Details	Comments	Cross-section
3.b. Resist removal	**Machine:** Plasma asher **Recipe:** 1 **Time:** 30 min **Pressure:** 0.5 mbar **Power:** 1000 W **O_2 flow:** 210 ml/min **N_2 flow:** 70 ml/min	T ~ 130 °C	
4.a. RCA clean		✓ 10 s HF dip at 1st step No HF dip 2nd step	
4.b. Low-stress Si-rich silicon nitride deposition	**Furnace:** LPCVD Nitrid **Recipe:** SIRICH **Temperature:** 835 °C **Pressure:** 112 mTorr **DCS flow:** 93 sccm **NH_3 flow:** 13 sccm **Time:** 1 h 35 min **Thickness:** ~350 nm	✓ Measure nitride thickness. ✓ $t_{nitride}$: ..... m	
✓ This step can also be performed at the in the Nanofabrication Laboratory at the Department of Microtechnology and Nanoscience at the Chalmers University of Technology in Sweden.			
5.a. HMDS treatment	**Time:** 32 min 30 s		
5.b. Resist spin	**Machine:** KS Spinner **Resist Type:** AZ5214E **Thickness:** 2.2 µm	Use chuck with no vacuum!	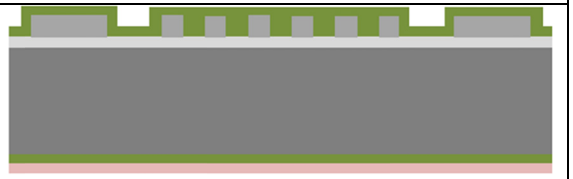

Table E.1 Continued.

Process Step	Details	Comments	Cross-section
5.c. Oven bake	**Temperature:** 90 °C **Time:** 30 min		
5.d. Exposure (Mask 2)	**Machine:** KS aligner **Exposure:** 8 s at CI **Mode:** Hard contact	Use special holder! Misalign the mask vertically, if the thickness of the wafer is different than 500 µm.	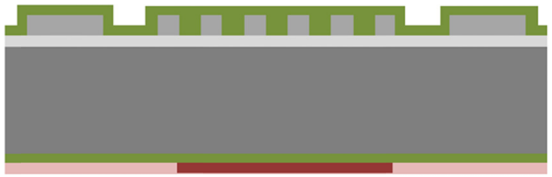
Alignment Marks:		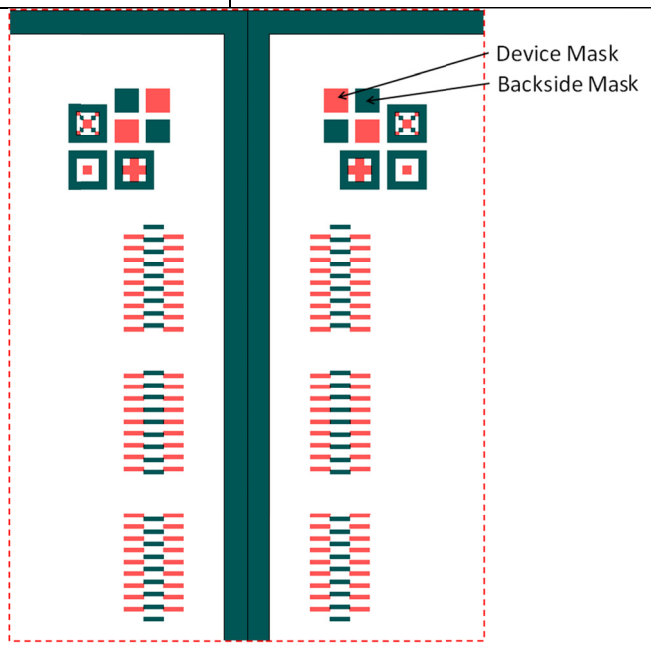	

Table E.1 Continued.

Process Step	Details	Comments	Cross-section
5.e. Develop	**Time:** 70 s	✓ Prepare a fresh developer bath.	
5.f. Hard bake	**Temperature:** 120 °C **Time:** 30 min	Use oven.	
6.a. Nitride etch	**Machine:** RIE1 **Recipe 1:** dp_koh **Step 1:** Descum (To remove residual resist) **Pressure:** 100 mTorr **Power:** 150 W **O_2 flow:** 20 sccm **N_2 flow:** 99 sccm **Time:** 30 s **Step 2:** Nitride etch **Pressure:** 40 mTorr **Power:** 60 W **CHF_3 flow:** 10 sccm **C_2F_6 flow:** 20 sccm **Time:** 12 min	✓ Process only one wafer initially! Use special aluminum chuck! ✓ No edge protection. ✓ Average etch rate: ~120 nm/min ✓ Etch rate not measured: ✓ Nitride = ~40 nm/min ✓ Resist(hard) = ~100nm/min ✓ Resist(soft) = ~200 nm/min	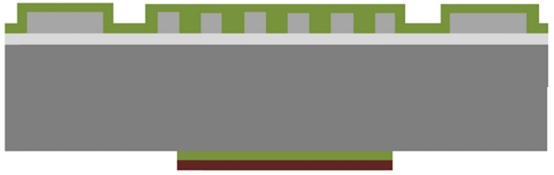

Table E.1 Continued.

Process Step	Details	Comments	Cross-section
6.b. Resist removal	**Machine:** Plasma asher **Recipe:** 1 **Time:** 30 min **Pressure:** 0.5 mbar **Power:** 1000 W **O_2 flow:** 210 ml/min **N_2 flow:** 70 ml/min	✓ T ~ 130 °C	
7.a. Silicon etch (KOH)	**Temperature:** 80 °C **Time:** ~6 hours **Weight %:** ~28 % **Etch Rates** **<100>:** ~1300 nm/min **<110>:** ~2000 nm/min **<111>:** ~3 nm/min **SiO_2:** ~4 nm/min	✓ 30 s BHF before KOH. No bubbles during wafer rinse! ✓ Etch 502 µm + 5 µm overetch ✓ Time: …..h …..min	
7.b. Nitride etch (Phosphoric acid bath)	**Temperature:** 180 °C **Time:** > 90 min **Etch rate:** ~ 8 nm/min	✓ Does not etch Si and SiO_2. No bubbles during wafer rinse! ✓ Assume 4nm/min to calculate etching time ✓ Time: …..	

Table E.1 Continued.

Process Step	Details	Comments	Cross-section
7.c. Oxide etch (bHF)	**Etch rate:** ~ 700-800 Å/min **Time:** ~10 min	No bubbles during wafer rinse!	
8.a. Metal evaporation (Ti/Pt)	**Machine:** Alcatel **Ti thickness:** 100 Å **Pt thickness:** 1900 Å	✓ Use the Al shadow mask!	

APPENDIX F
Nanostation Software

F.1 The User Interface

The components of the optical manipulation setup can be controlled via the LabView user interface, Nanostation for Microgrippers written by Kristian Mølhave and Peter Bøggild.

A screenshot from the user interface can be seen in Figure F.1 and Figure F.2. Most important parts of the user interface can be listed as:

1. Image window: Shows the image from the CCD camera (Figure F.1). For actuation measurements, a rectangular area of interest should be defined on this image. Then, the relative gap position is calculated from the average intensity of the pixels as follows:
    i. According to the direction of the measurement (horizontal/vertical), the intensities of the pixels in each row/column of the area of interest are averaged.
    ii. The averaged intensities are plotted as a function of the column/row position (see 3 in Figure F.2).
    iii. Gaussian curves are fitted to the peaks of the intensity plot. Hence, the relative peak positions can be measured with a sub-pixel, i.e. 2-3 nm, precision.

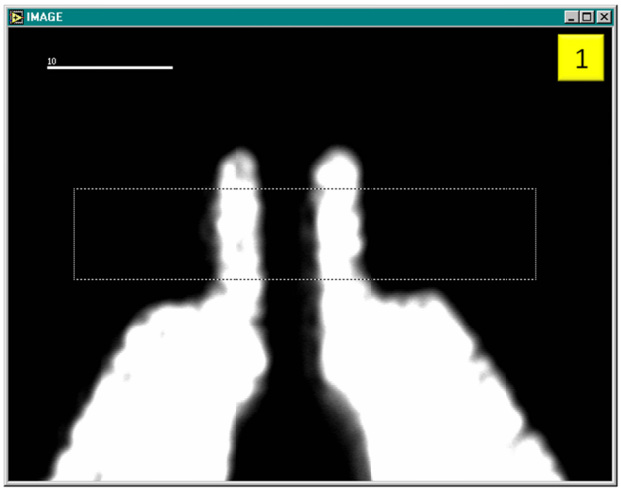

Figure F.1 A screenshot of the image window.

2. Stage control: Enables control of the XYZ stage with 0.1, 1, 10 or 100 µm precision. Note that, the smallest and the largest step sizes are 0.1 µm and 500 µm, respectively.
3. Image adjust: The horizontally/vertically averaged intensity of the rectangular area of interest is plotted here. The remaining buttons enable selection of the measurement direction and optimization of the image.
4. Image properties: The properties of the image, e.g. scale, size, etc., can be selected here. Also, the image can be saved here.
5. Peak adjust/position: The threshold and the peak width for the intensity plot (Part 3) can be adjusted here. The number of tips, i.e. end-effectors, can be selected and their position can be reset. Also, the variation of the peak positions, i.e. mean, is plotted here.
6. Scan parameters: Scan parameters for the measurement are selected here.
7. Save data: The name and the destination of the data file can be defined and comments can be written for each scan here.

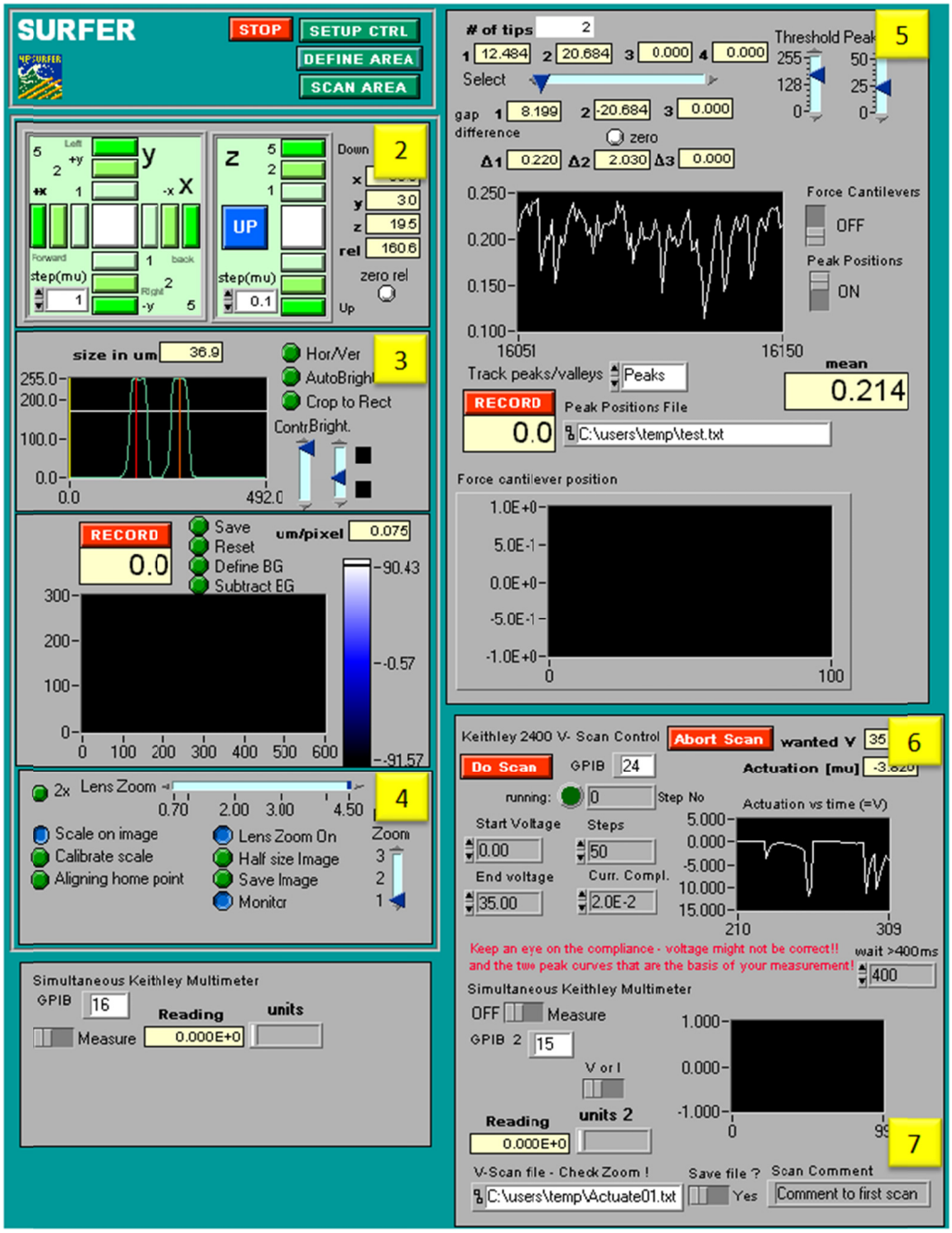

Figure F.2 A screen shot from the user interface.

F.2 The Procedure for Actuation Measurements

The procedure for actuation measurements using the Nanostation software and the optical manipulation setup is as follows:

1. Make sure that the connections between the setup components are all correct. Turn the computer, the sourcemeter and the motion controller on.
2. Slowly turn on the light source.
3. Run the Labview user interface.
4. Insert the microgripper interface into the ZIF socket of the holder.
5. Firmly mount the holder firmly on the stage.
6. Arrange the connection between the banana plugs on the hydraulic table and the sourcemeter according to the measured device and the operating mode.
7. Connect the microgrippers to the banana plugs and hence, to the sourcemeter.
8. Bring the microgrippers into the field of view (Part 1) at the lowest magnification of the lens system by moving the XYZ stage through the user interface (Part 2).
9. Increase the magnification to the maximum and bring the end-effectors to the center of the camera image.
10. Adjust the intensity of the light source.
11. Adjust the focus, the brightness and the contrast of the image through the user interface to obtain a sharp black & white image (Part 3).
12. Select the number of tips as 2 and turn the peak positions on (Part 5).
13. Select a rectangular region, which covers both end-effectors (Part 1).
14. Adjust the threshold and the peak width according to the intensity curve (Part 5).
15. Select start and end voltages, the number of steps and the compliance current according to the measured device and the operating mode (Part 6).
16. Turn saving data on, write comments if necessary and select a destination folder and a file name for the data (Part 7).
17. Reset the distance between the end-effectors by clicking “Zero” (Part 3).
18. Start the measurement by clicking “Do Scan” (Part 6).
19. Repeat steps 17-18 a few times more or until you get reliable data.
20. Disconnect the microgrippers, dismount the holder from the stage and the microgripper interface from the holder
21. Insert a new microgripper interface and repeat steps 5-20. When finished proceed with step 22.
22. Stop the user interface.
23. Turn the computer, the sourcemeter and the motion controller off.

APPENDIX G
Actuation Results

Gap displacement vs. bias voltage curves for the topology optimized designs and their variations.

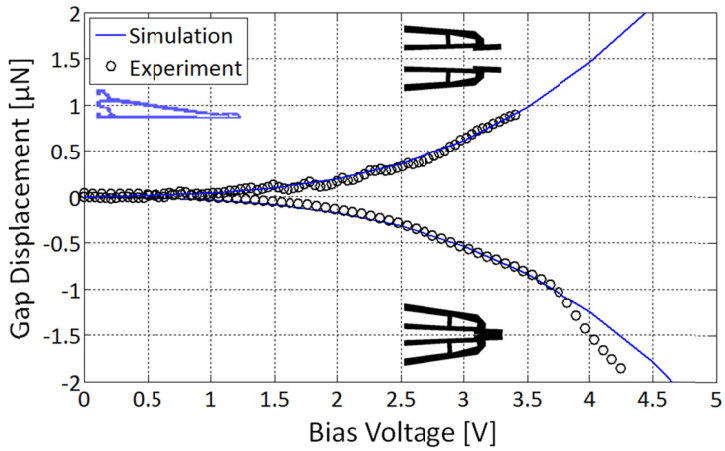

Figure G.1 Results for original Design A with a line-width variation of -1 µm.

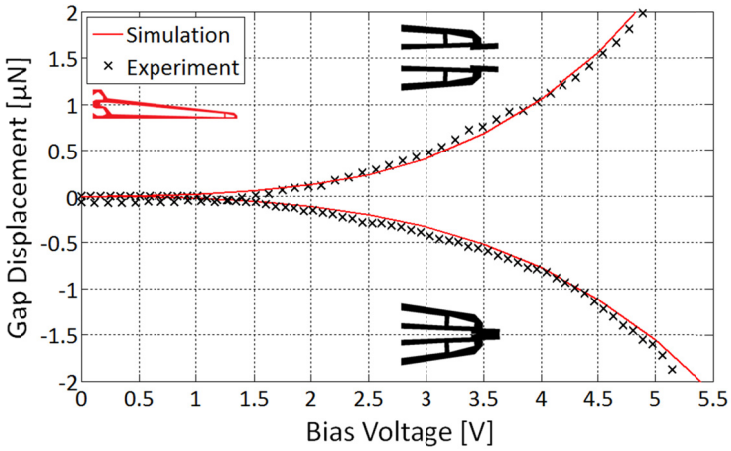

Figure G.2 Results for smoothed Design A with large electrodes.

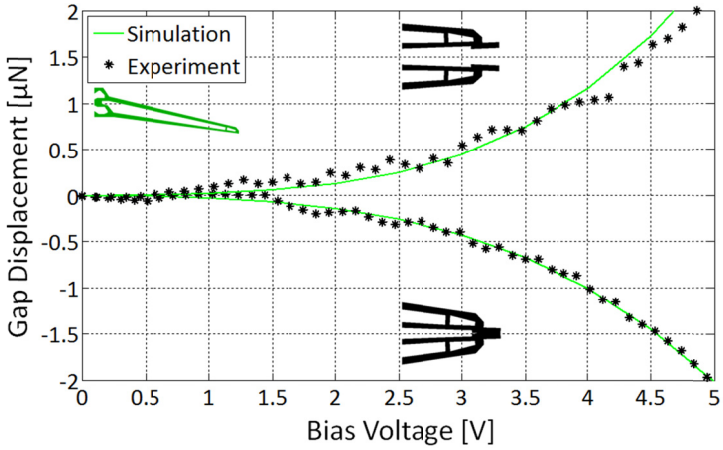

Figure G.3 Results for tilted Design A with large electrodes.

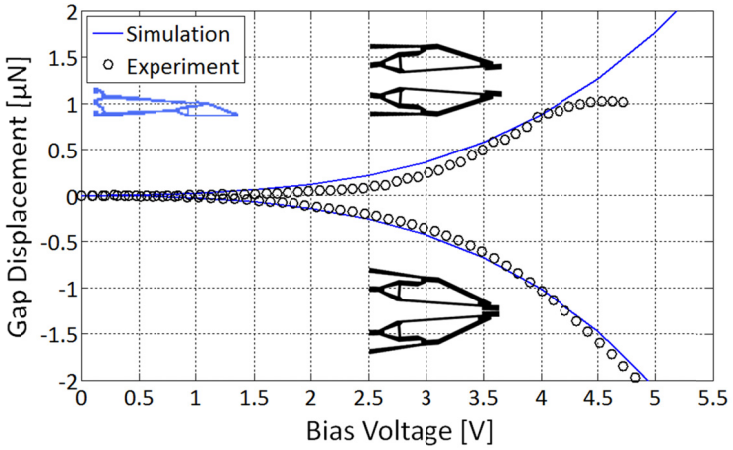

Figure G.4 Results for original Design B with a line-width variation of -1 µm.

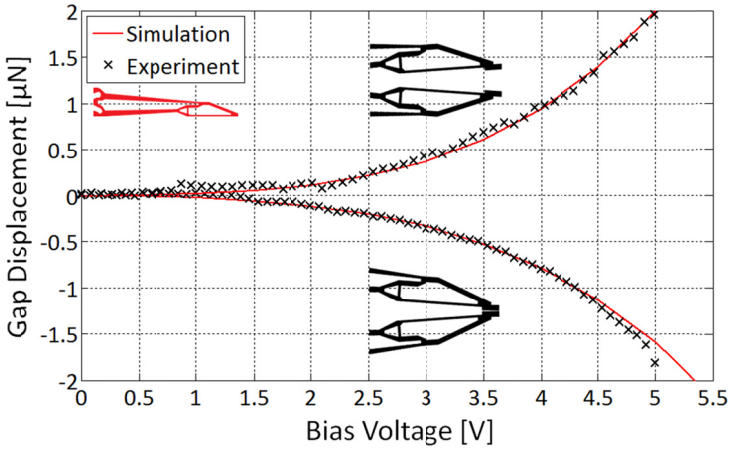

Figure G.5 Results for smoothed Design B with large electrodes.

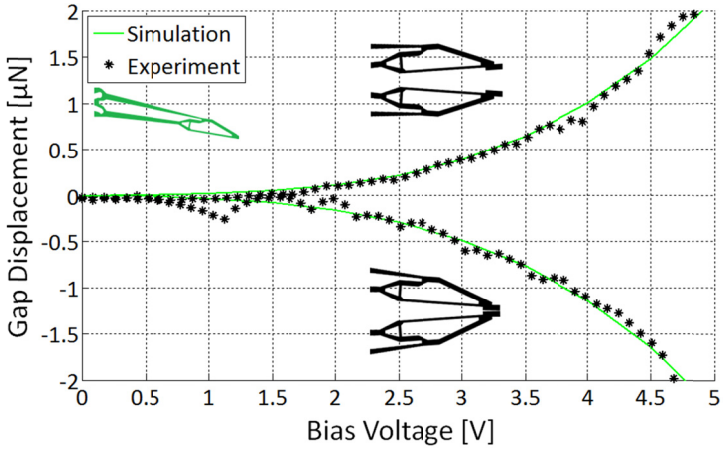

Figure G.6 Results for tilted Design B with large electrodes.

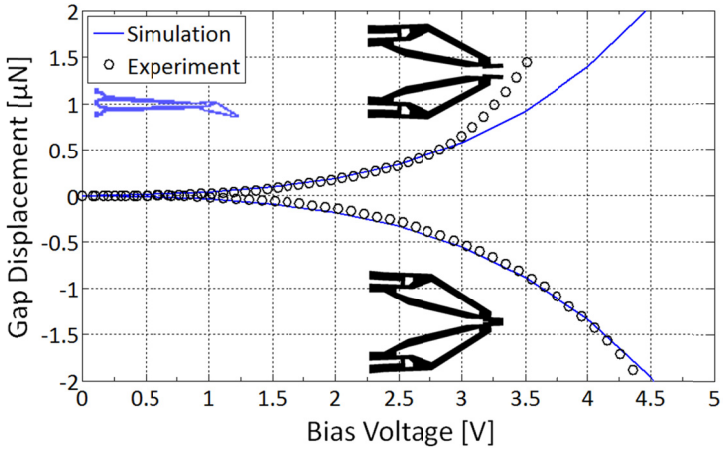

Figure G.7 Results for original Design C with a line-width variation of -1 µm.

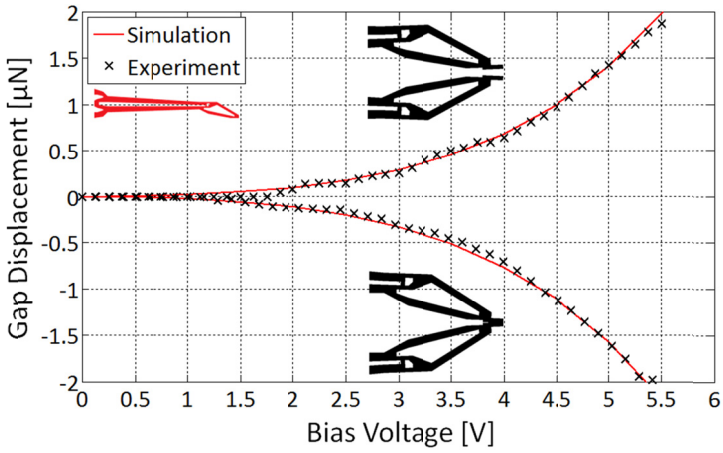

Figure G.8 Results for smoothed Design C.

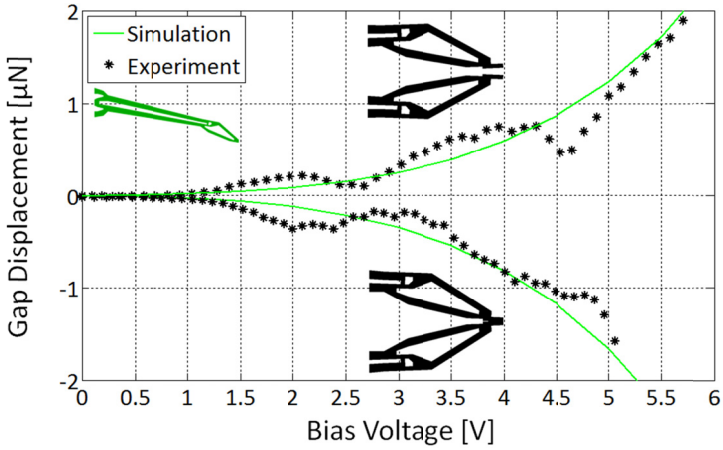

Figure G.9 Results for tilted Design C (Note that this data was taken from a microgripper with FIB modified end-effectors. Hence, experimental curves are not smooth due to the non-uniform shape of the end-effectors).

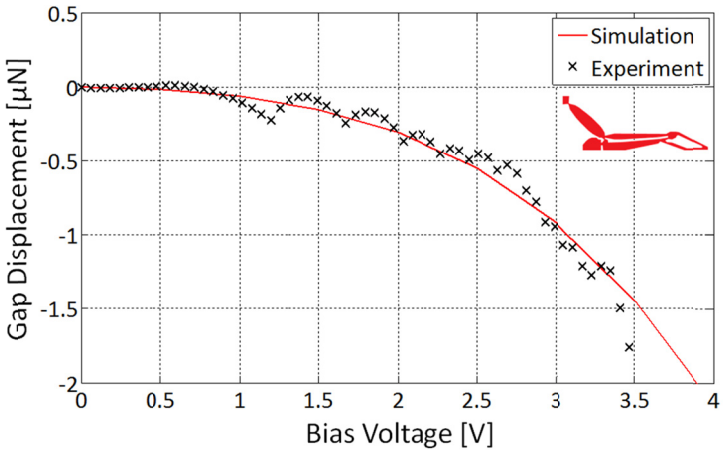

Figure G.10 Results for smoothed Design D.

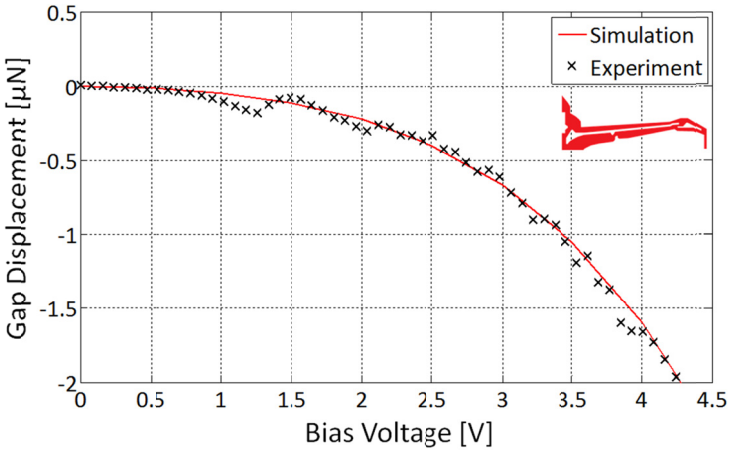

Figure G.11 Results for smoothed Design E.

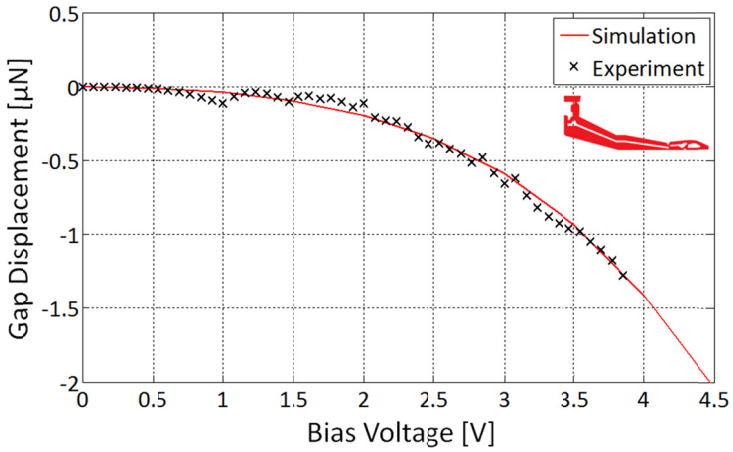

Figure G.12 Results for smoothed Design F.

APPENDIX H
Raman Spectroscopy Results

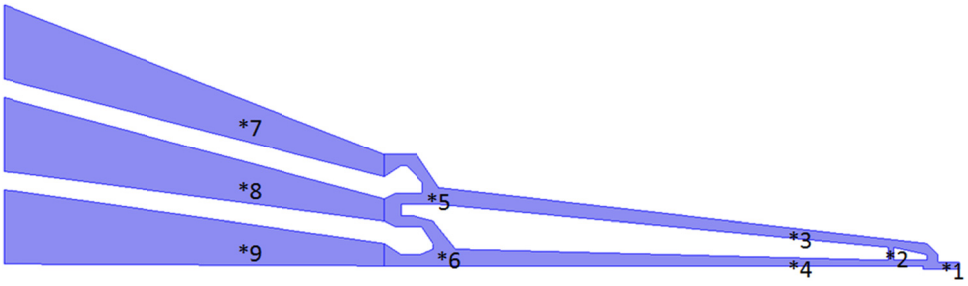

Figure H.1 Points defined on smoothed Design A with narrow leads.

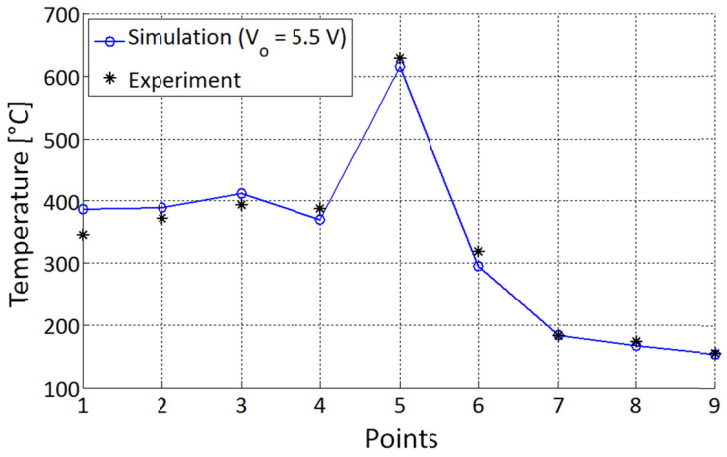

Figure H.2 Comparison of the temperature measurement results with the finite element simulations for smoothed Design A with narrow leads ($V_o = 5.5\,V$, $y_{free} = 1.025\ \mu m$, $F_{blocking} = 107\ \mu N$, $F_{gripping} = 3\ \mu N$).

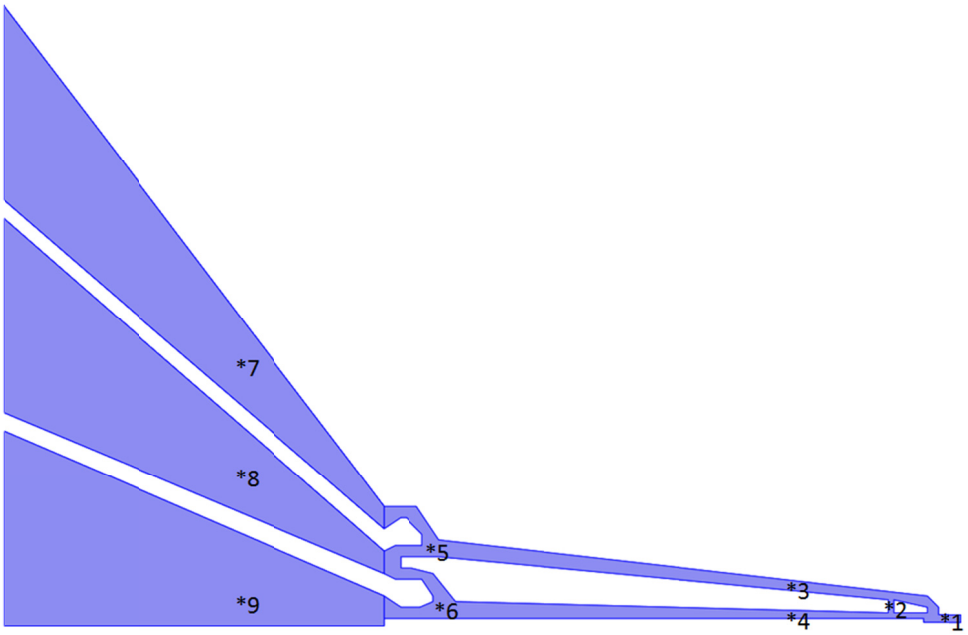

Figure H.3 Points defined on smoothed Design A with wide leads.

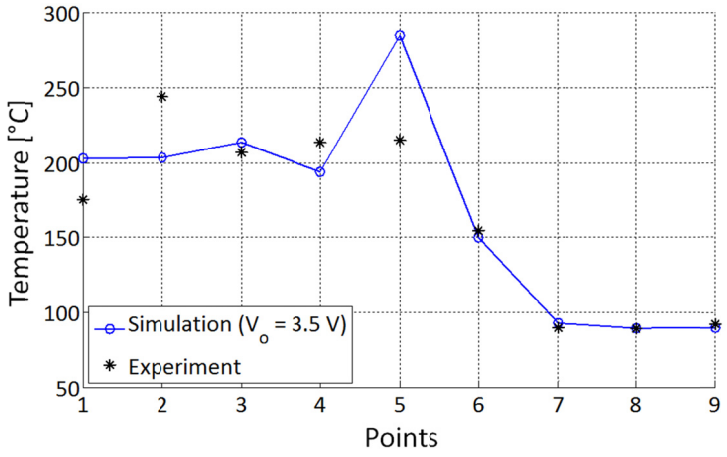

Figure H.4 Comparison of the temperature measurement results with the finite element simulations for smoothed Design A with wide leads ($V_o = 3.5\ V$, $y_{free} = 0.514\ \mu m$, $F_{blocking} = 53\ \mu N$, $F_{gripping} = 0$). Note that, measurements for point 2 and point 5 may be confused.

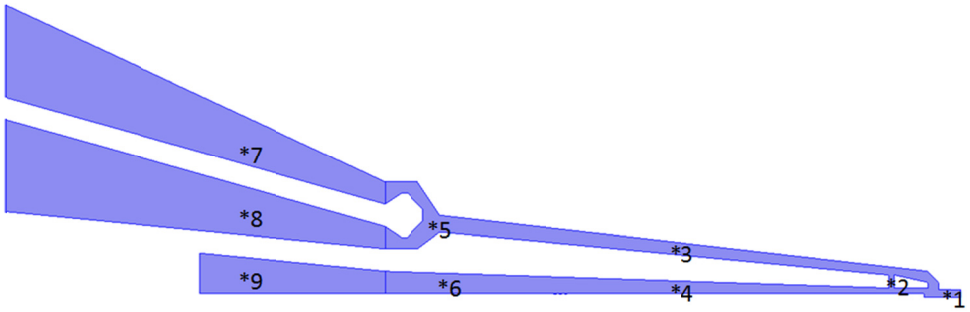

Figure H.5 Points defined on smoothed Design A with two leads.

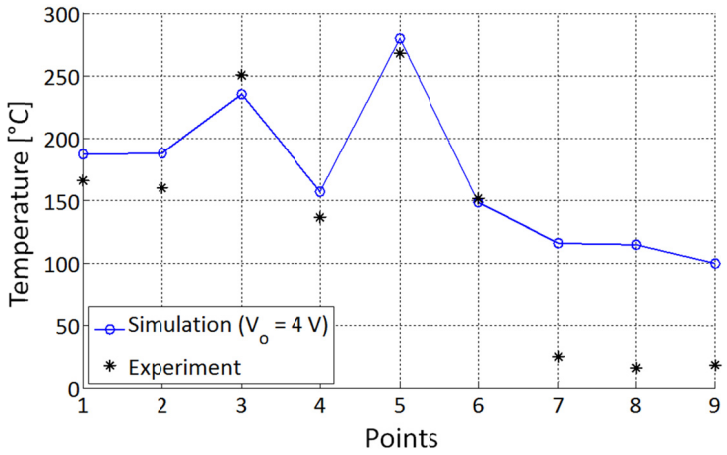

Figure H.6 Comparison of the temperature measurement results with the finite element simulations for smoothed Design A with two leads ($V_o = 4\,V$, $y_{free} = 0.335\ \mu m$, $F_{blocking} = 35\ \mu N$, $F_{gripping} = 0$).

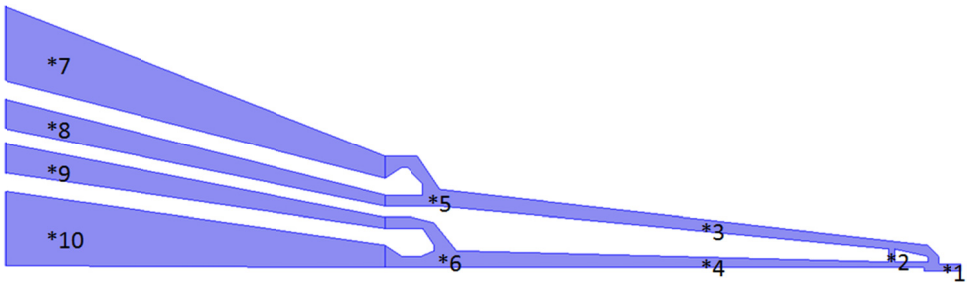

Figure H.7 Points defined on smoothed Design A with divided leads.

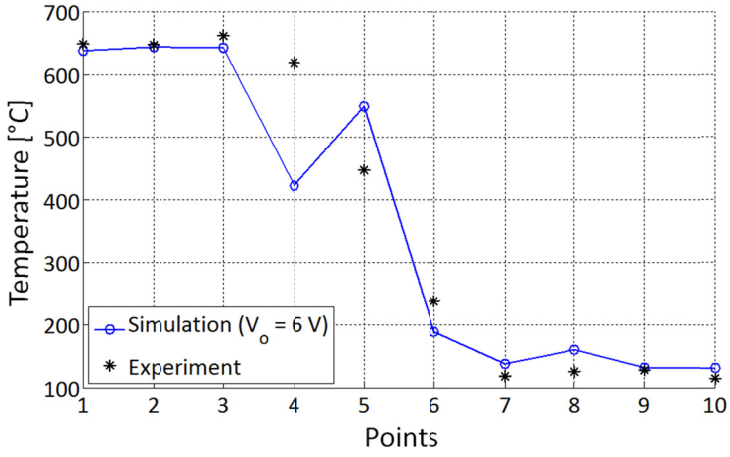

Figure H.8 Comparison of the temperature measurement results with the finite element simulations for smoothed Design A with divided leads ($V_o = 6\,V$, $y_{free} = 1.214\ \mu m$, $F_{blocking} = 128\ \mu N$, $F_{gripping} = 23\ \mu N$).

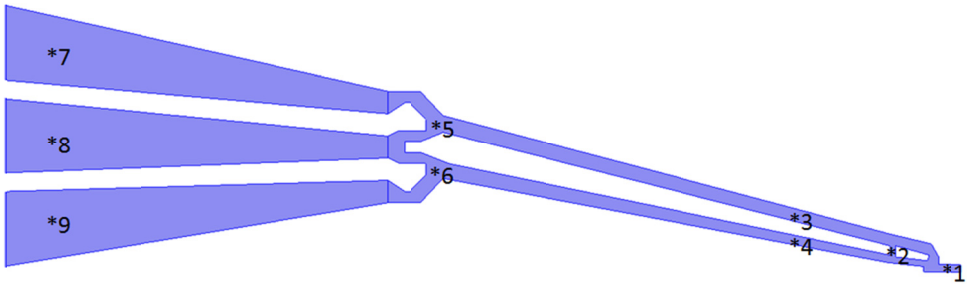

Figure H.9 Points defined on tilted Design A with narrow leads.

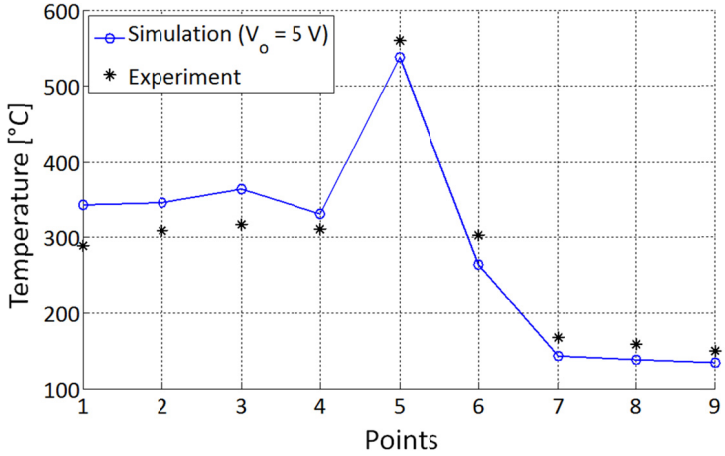

Figure H.10 Comparison of the temperature measurement results with the finite element simulations for tilted Design A with narrow leads ($V_o = 5\ V$, $y_{free} = 0.975\ \mu m$, $F_{blocking} = 98\ \mu N$, $F_{gripping} = 0$).

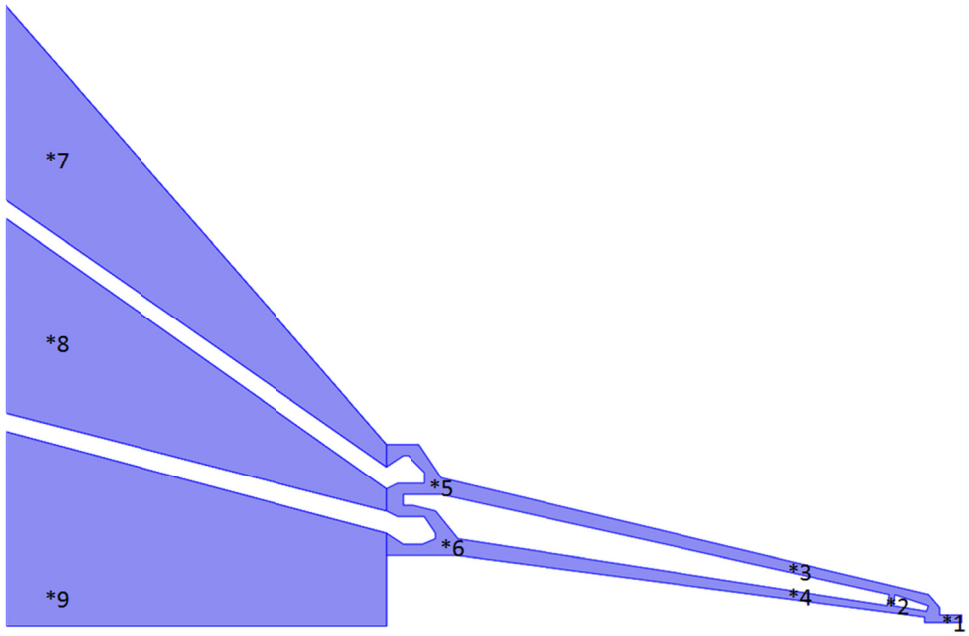

Figure H.11 Points defined on tilted Design A with wide leads.

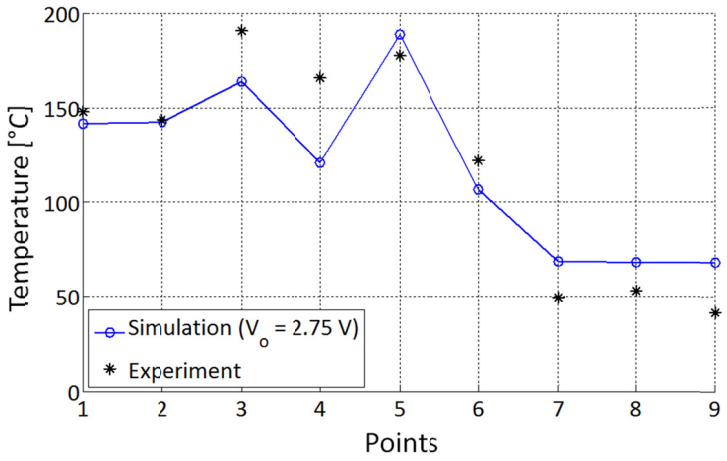

Figure H.12 Comparison of the temperature measurement results with the finite element simulations for tilted Design A with wide leads ($V_o = 2.75\ V$, $y_{free} = 0.355\ \mu m$, $F_{blocking} = 35\ \mu N$, $F_{gripping} = 0$).

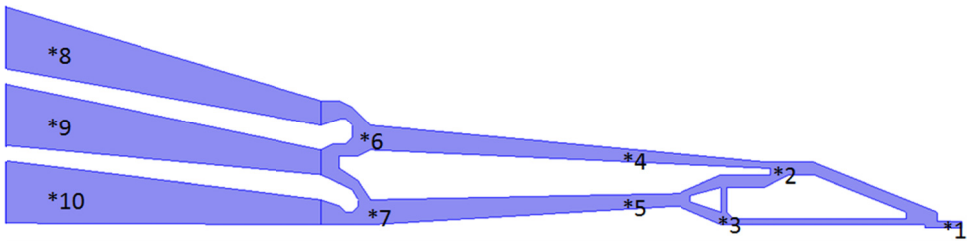

Figure H.13 Points defined on smoothed Design B with narrow leads.

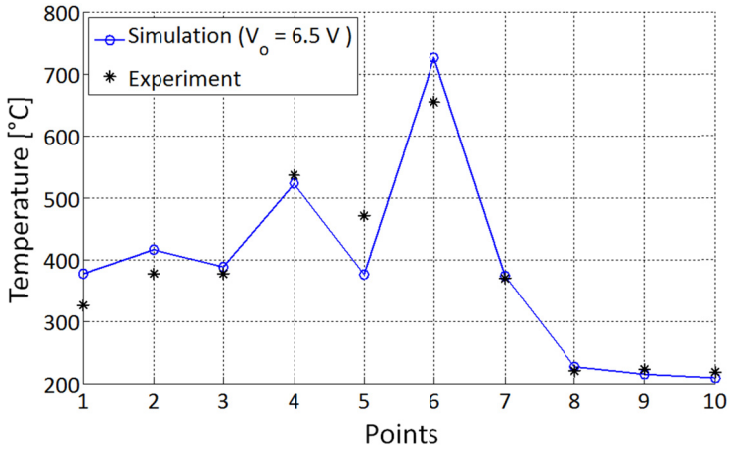

Figure H.14 Comparison of the temperature measurement results with the finite element simulations for smoothed Design B with narrow leads ($V_o = 6.5\ V$, $y_{free} = 1.4\ \mu m$, $F_{blocking} = 302\ \mu N$, $F_{gripping} = 87\ \mu N$).

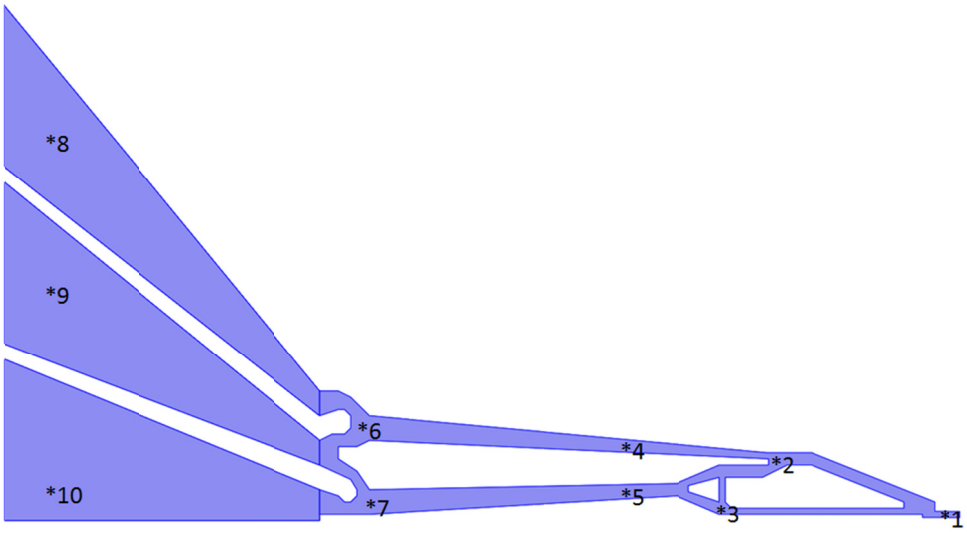

Figure H.15 Points defined on smoothed Design B with wide leads.

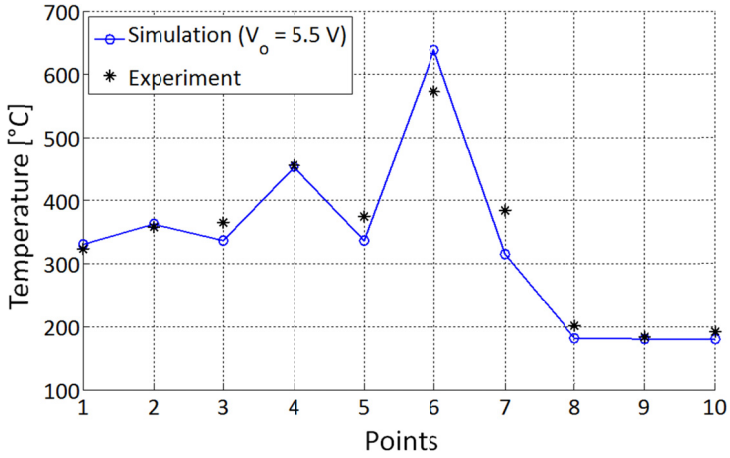

Figure H.16 Comparison of the temperature measurement results with the finite element simulations for smoothed Design B with wide leads ($V_o = 5.5\,V$, $y_{free} = 1.324\ \mu m$, $F_{blocking} = 286\ \mu N$, $F_{gripping} = 70\ \mu N$).

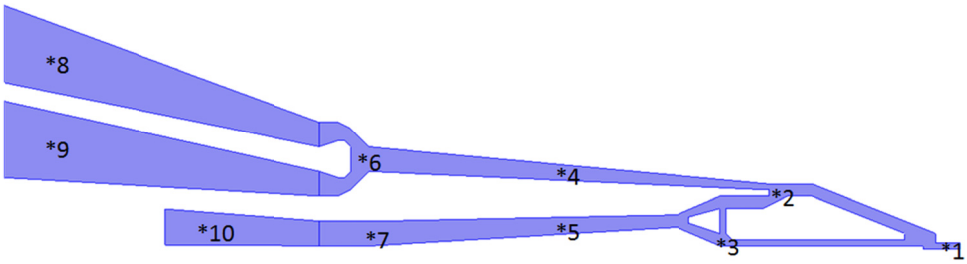

Figure H.17 Points defined on smoothed Design B with two leads.

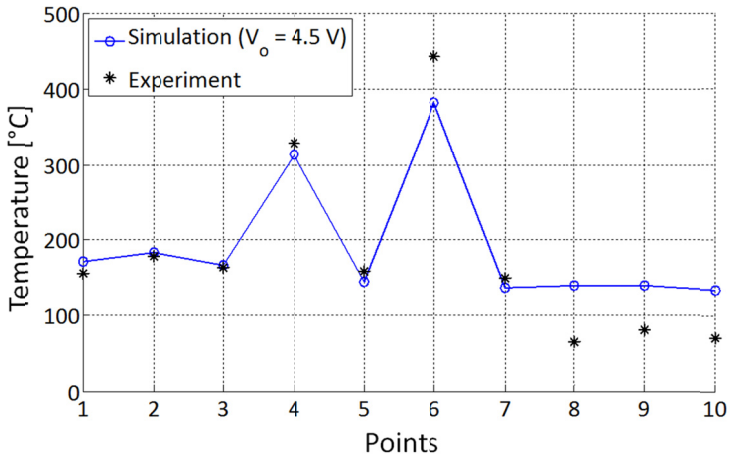

Figure H.18 Comparison of the temperature measurement results with the finite element simulations for smoothed Design B with two leads ($V_o = 4.5\,V$, $y_{free} = 0.925\ \mu m$, $F_{blocking} = 76\ \mu N$, $F_{gripping} = 0$).

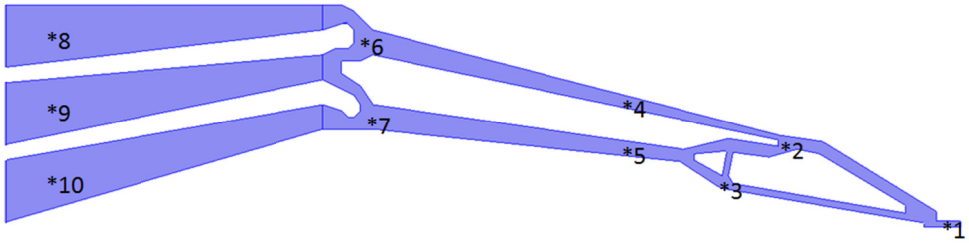

Figure H.19 Points defined on tilted Design B with narrow leads.

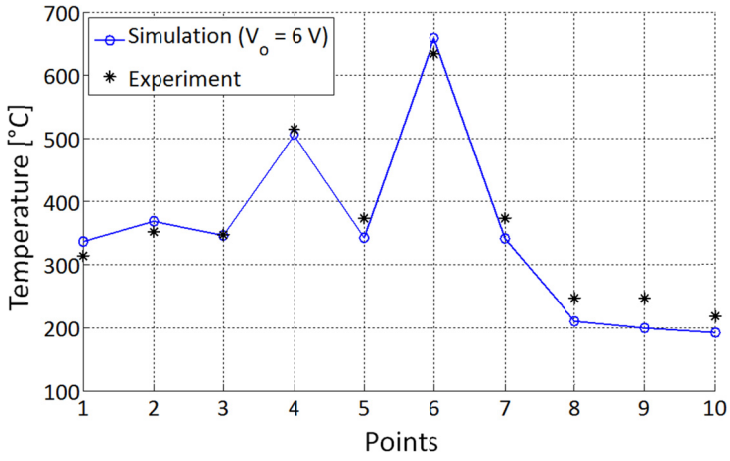

Figure H.20 Comparison of the temperature measurement results with the finite element simulations for tilted Design B with narrow leads ($V_o = 6\,V$, $y_{free} = 1.355\ \mu m$, $F_{blocking} = 260\ \mu N$, $F_{gripping} = 68$).

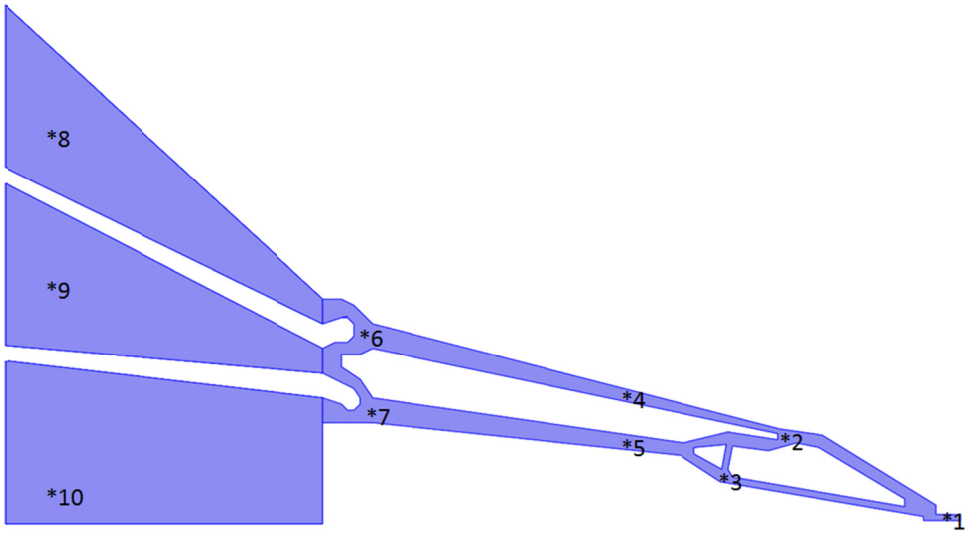

Figure H.21 Points defined on tilted Design B with wide leads.

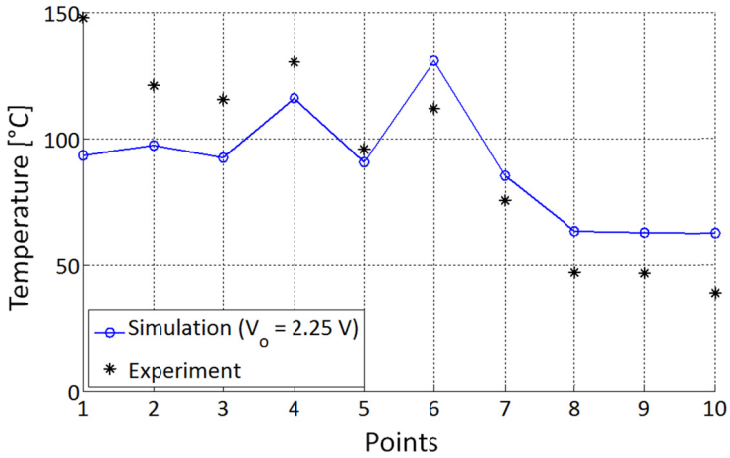

Figure H.22 Comparison of the temperature measurement results with the finite element simulations for tilted Design B with wide leads ($V_o = 2.25\ V$, $y_{free} = 0.262\ \mu m$, $F_{blocking} = 51\ \mu N$, $F_{gripping} = 0$).

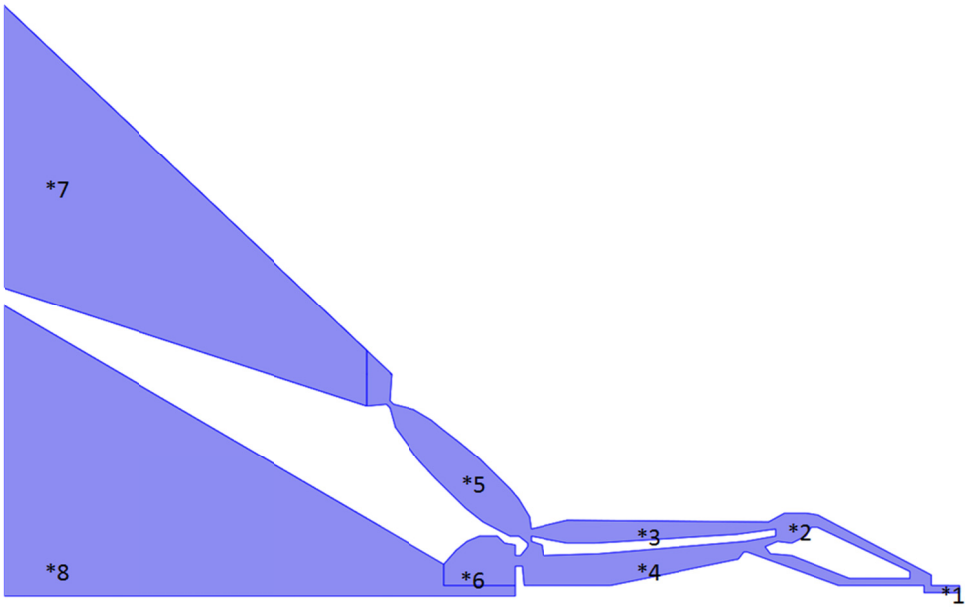

Figure H.23 Points defined on Design D.

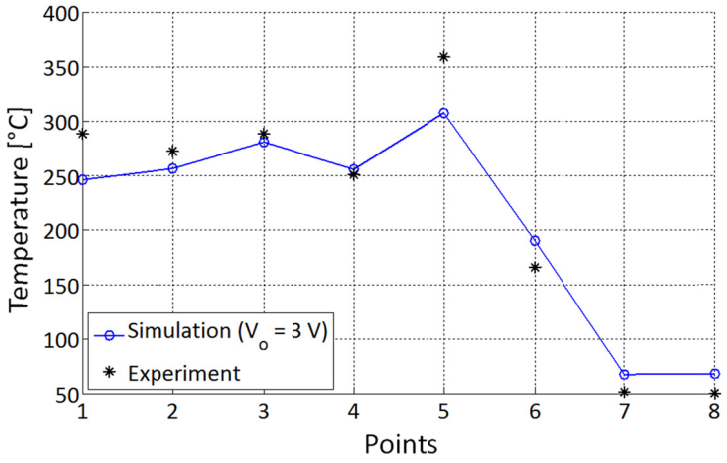

Figure H.24 Comparison of the temperature measurement results with the finite element simulations for Design D ($V_o = 3\,V$, $y_{free} = 0.544\ \mu m$, $F_{blocking} = 70\ \mu N$, $F_{gripping} = 0\ \mu N$).

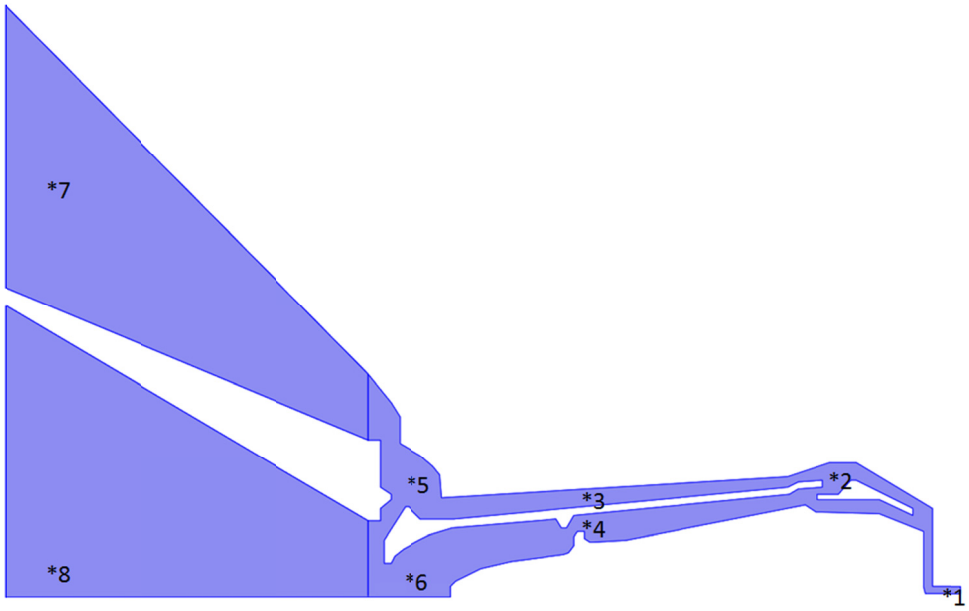

Figure H.25 Points defined on Design E.

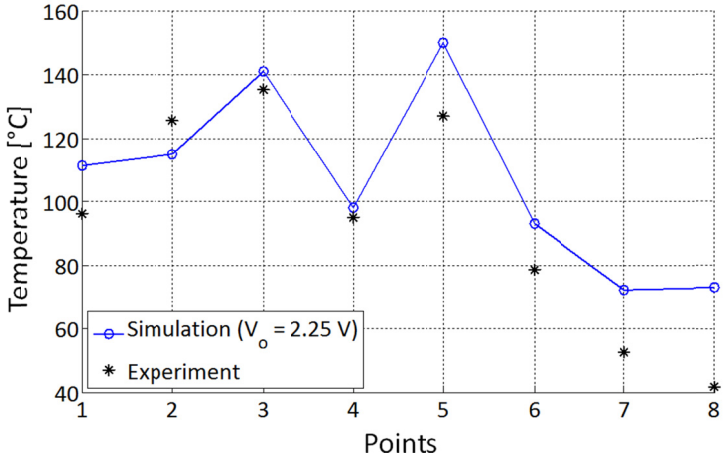

Figure H.26 Comparison of the temperature measurement results with the finite element simulations for Design E ($V_o = 2.25\,V$, $y_{free} = 0.361\ \mu m$, $F_{blocking} = 45\ \mu N$, $F_{gripping} = 0$).

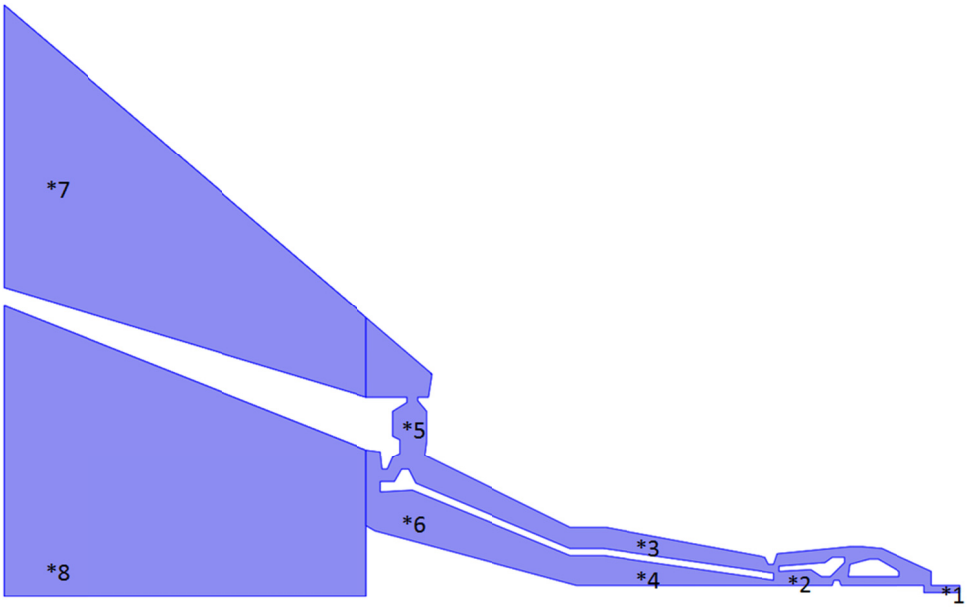

Figure H.27 Points defined on Design F.

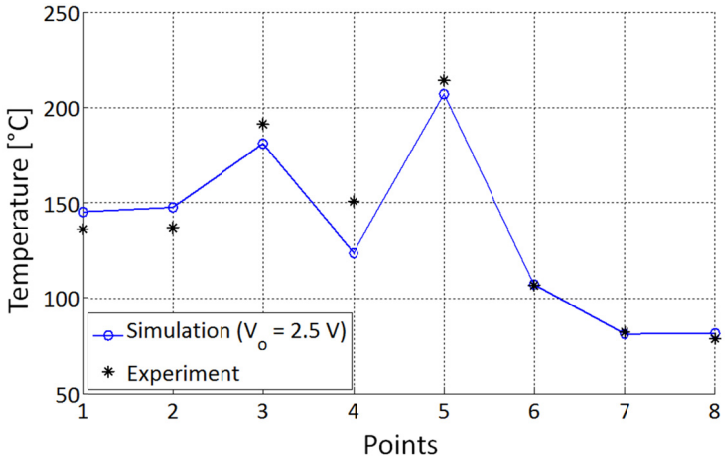

Figure H.28 Comparison of the temperature measurement results with the finite element simulations for Design F ($V_o = 2.5\ V$, $y_{free} = 0.447\ \mu m$, $F_{blocking} = 43\ \mu N$, $F_{gripping} = 0$).

Bibliography

[1] R. P. Feynman, "There's Plenty of Room at the Bottom," *Journal of Microelectromechanical Systems,* vol. 1, pp. 60-66, 1992.

[2] C. Baur, B. C. Gazen, B. Koel, T. R. Ramachandran, A. A. G. Requicha, and L. Zini, "Robotic Nanomanipulation with a Scanning Probe Microscope in a Networked Computing Environment," *Journal of Vacuum Science & Technology B: Microelectronics and Nanometer Structures,* vol. 15, pp. 1577-1580, 1997.

[3] www.fei.com.

[4] www.intel.com.

[5] www.nanohand.com.

[6] K. Drexler and R. Whitaker, *Engines of Creation: The Coming Era of Nanotechnology*: Doubleday/Anchor Press, 1986.

[7] K. Drexler, *Nanosystems: Molecular Machinery, Manufacturing, and Computation*: John Wiley & Sons, Inc. New York, NY, USA, 1992.

[8] G. Binnig, H. Rohrer, C. Gerber, and E. Weibel, "Surface Studies by Scanning Tunneling Microscopy," *Physical Review Letters,* vol. 49, pp. 57-61, 1982.

[9] G. Binnig and C. Quate, "Atomic Force Microscope," *Physical Review Letters,* vol. 56, pp. 930-933, 1986.

[10] H. Kroto, J. Heath, S. O'Brien, R. Curl, and R. Smalley, "C 60: Buckminsterfullerene," *Nature,* vol. 318, pp. 162-163, 1985.

[11] S. Iijima, "Helical Microtubules of Graphitic Carbon," *Nature,* vol. 354, pp. 56-58, 1991.

[12] P. Marquardt, L. Borngen, G. Nimtz, R. Sonnberger, H. Gleiter, and J. Zhu, "Microwave Absorption by Small Metal Particles," *Physics Letters. A,* vol. 114, pp. 39-42, 1986.

[13] C. Knoedler, "Helium-ion Damage and Nanowire Fabrication in GaAs/AlGaAs Heterostructures," *Journal of Applied Physics,* vol. 68, pp. 1129-1136, 1990.

[14] V. Varadan, "The Role of Nanotechnology and Nano and Micro-electronics in Monitoring and Control of Cardiovascular Diseases and Neurological Disorders," in *Nanosensors, Microsensors and Biosensors and Systems*, 2007, p. 652813.

[15] H. Zhang, J. Bei, and S. Wang, "Multi-morphological Biodegradable PLGE Nanoparticles and Their Drug Release Behavior," *Biomaterials,* vol. 30, pp. 100-107, 2009.

[16] T. Ntho, J. Anderson, and M. Scurrell, "CO Oxidation Over Titanate Nanotube Supported Au: Deactivation due to Bicarbonate," *Journal of Catalysis,* vol. 261, pp. 94-100, 2008.

[17] X. Li, D. Zhang, Z. Sun, Y. Chen, and S. Huang, "Metal-free Indoline-dye-sensitized TiO2 Nanotube Solar Cells," *Microelectronics Journal,* vol. 40, pp. 108-114, 2008.

[18] A. Cuche, B. Masenelli, G. Ledoux, D. Amans, C. Dujardin, Y. Sonnefraud, P. Mélinon, and S. Huant, "Fluorescent Oxide Nanoparticles Adapted to Active Tips for Near-field Optics," *Nanotechnology,* vol. 20, p. 6, 2008.

[19] C. Hsiao, C. Lin, C. Hung, C. Su, Y. Lo, C. Lee, H. Lin, F. Ko, T. Huang, and Y. Yang, "Novel Poly-silicon Nanowire Field Effect Transistor for Biosensing Application," *Biosensors and Bioelectronics,* vol. 24, pp. 1223-1229, 2009.

[20] B. Witkamp, M. Poot, and H. van der Zant, "Bending-Mode Vibration of a Suspended Nanotube Resonator," *Nano Letters,* vol. 6, pp. 2904-2908, 2006.

[21] H. Soh, C. Quate, A. Morpurgo, C. Marcus, J. Kong, and H. Dai, "Integrated Nanotube Circuits: Controlled Growth and Ohmic Contacting of Single-walled Carbon Nanotubes," *Applied Physics Letters,* vol. 75, pp. 627-629, 1999.

[22] J. Jang, S. Cha, Y. Choi, D. Kang, D. Hasko, J. Jung, J. Kim, and G. Amaratunga, "A Nanogripper Employing Aligned Multiwall Carbon Nanotubes," *IEEE Transactions on Nanotechnology,* vol. 7, pp. 389-393, 2008.

[23] M. Casavant, D. Walters, J. Schmidt, and R. Smalley, "Neat Macroscopic Membranes of Aligned Carbon Nanotubes," *Journal of Applied Physics,* vol. 93, pp. 2153-2156, 2003.

[24] C. Hangarter and N. Myung, "Magnetic Alignment of Nanowires," *Chemistry of Materials,* vol. 17, pp. 1320-1324, 2005.

[25] K. W. C. Lai, N. Xi, and U. C. Wejinya, "Automated process for selection of carbon nanotube by electronic property using dielectrophoretic manipulation," *Journal of Micro-Nano Mechanics,* vol. 4, p. 12, 2008.

[26] H. Ko, S. Peleshanko, and V. Tsukruk, "Combing and Bending of Carbon Nanotube Arrays with Confined Microfluidic Flow on Patterned Surfaces," *Journal of Physical Chemistry B,* vol. 108, pp. 4385-4393, 2004.

[27] X. Sun, J. Zhang, X. Li, D. Gong, and H. Lee, "Optical Rotation and Manipulation of Micro-sized LiNbO3 Crystals and Single-walled Carbon Nanotubes Bundles," *Colloids and Surfaces A: Physicochemical and Engineering Aspects,* vol. 313-314, pp. 488-491, 2008.

[28] W. Lim, K. Yao, and Y. Chen, "Alignment of Carbon Nanotubes by Acoustic Manipulation in a Fluidic Medium," *Journal of Physical Chemistry B,* vol. 111, p. 16802, 2007.

[29] S. Fatikow, V. Eichhorn, T. Wich, T. Sievers, O. HanBler, and K. Andersen, "Depth-Detection Methods for CNT Manipulation and Characterization in a Scanning Electron Microscope," in *2007 IEEE International Conference on Mechatronics and Automation*, 2007, pp. 45-50.

[30] P. Williams, S. Papadakis, M. Falvo, A. Patel, M. Sinclair, A. Seeger, A. Helser, R. II, S. Washburn, and R. Superfine, "Controlled Placement of an Individual Carbon Nanotube onto a Microelectromechanical Structure," *Applied Physics Letters,* vol. 80, pp. 2574-2576, 2002.

[31] T. Fukuda, F. Arai, and L. Dong, "Assembly of Nanodevices with Carbon Nanotubes Through Nanorobotic Manipulations," *Proceedings of the IEEE,* vol. 91, pp. 1803-1818, 2003.

[32] K. Svensson, H. Olin, and E. Olsson, "Nanopipettes for Metal Transport," *Physical Review Letters,* vol. 93, p. 145901, 2004.

[33] S. Lim, K. Kim, I. Lee, S. Jeong, S. Cho, J. Yoo, and Y. Lee, "Nanomanipulator-assisted Fabrication and Characterization of Carbon Nanotubes Inside Scanning Electron Microscope," *Micron,* vol. 36, pp. 471-476, 2005.

[34] Y. Nakayama and S. Akita, "Nanoengineering of Carbon Nanotubes for Nanotools," *New Journal of Physics,* vol. 5, p. 128, 2003.

[35] S. Fahlbusch, S. Mazerolle, J. Breguet, A. Steinecker, J. Agnus, R. Pérez, and J. Michler, "Nanomanipulation in a Scanning Electron Microscope," *Journal of Materials Processing Technology,* vol. 167, pp. 371-382, 2005.

[36] V. Eichhorn, K. Carlson, K. Andersen, S. Fatikow, and P. Boggild, "Nanorobotic Manipulation Setup for Pick-and-place Handling and Nondestructive Characterization of Carbon Nanotubes," in *2007 IEEE/RSJ, International Conference on Intelligent Robots and Systems*, 2007, pp. 291-296.

[37] T. Kuzumaki and Y. Mitsuda, "Dynamic Measurement of Electrical Conductivity of Carbon Nanotubes During Mechanical Deformation by Nanoprobe Manipulation in Transmission Electron Microscopy," *Applied Physics Letters,* vol. 85, p. 12501252, 2004.

[38] M. Falvo, J. Steele, R. Taylor, and R. Superfine, "Evidence of Commensurate Contact and Rolling Motion: AFM Manipulation Studies of Carbon Nanotubes on HOPG," *Tribology Letters,* vol. 9, pp. 73-76, 2000.

[39] Q. Li, S. Koo, C. Richter, M. Edelstein, J. Bonevich, J. Kopanski, J. Suehle, and E. Vogel, "Precise Alignment of Single Nanowires and Fabrication of Nanoelectromechanical Switch and Other Test Structures," *IEEE Transactions on Nanotechnology,* vol. 6, pp. 256-262, 2007.

[40] J. Hafner, C. Cheung, T. Oosterkamp, and C. Lieber, "High-Yield Assembly of Individual Single-Walled Carbon Nanotube Tips for Scanning Probe Microscopies," *Journal of Physical Chemistry B,* vol. 105, pp. 743-746, 2001.

[41] S. Christiansen, M. Becker, S. Fahlbusch, J. Michler, V. Sivakov, G. Andra, and R. Geiger, "Signal Enhancement in Nano-Raman Spectroscopy by Gold Caps on Silicon Nanowires Obtained by Vapour-liquid-solid Growth," *Nanotechnology,* vol. 18, p. 35503, 2007.

[42] C. J. Kim, A. P. Pisano, and R. S. Muller, "Silicon-processed Overhanging Microgripper," *Journal of Microelectromechanical Systems,* vol. 1, pp. 31-36, 1992.

[43] N. Chronis and L. Lee, "Electrothermally Activated SU-8 Microgripper for Single Cell Manipulation in Solution," *Journal of Microelectromechanical Systems,* vol. 14, p. 857, 2005.

[44] K. Mølhave and O. Hansen, "Electro-thermally Actuated Microgrippers with Integrated Force-feedback," *Journal of Micromechanics & Microengineering,* vol. 15, pp. 1265-1270, 2005.

[45] www.nascatec.com.

[46] www.zyvex.com.

[47] R. Wierzbicki, C. Adda, and H. Hotzendorfer, "Electrostatic Silicon Microgripper with Low Voltage of Actuation," in *18th International Symposium on Micro-NanoMechatronics and Human Science*, 2007, pp. 344-349.

[48] M. Mita, H. Kawara, H. Toshiyoshi, M. Ataka, and H. Fujita, "An Electrostatic 2-dimensional Micro-gripper for Nano Structure," in *TRANSDUCERS 2003, 12th International Conference on Solid-State Sensors, Actuators and Microsystems*, 2003, pp. 272-275.

[49] K. Molhave, T. Hansen, D. Madsen, and P. Boggild, "Towards Pick-and-place Assembly of Nanostructures," *Journal of Nanoscience & Nanotechnology,* vol. 4, pp. 279–282, 2004.

[50] J. Comtois and V. Bright, "Applications for Surface-micromachined Polysilicon Thermal Actuators and Arrays," *Sensors & Actuators A: Physical,* vol. 58, pp. 19-25, 1997.

[51] L. Que, J. Park, and Y. Gianchandani, "Bent-beam Electro-thermal Actuators for High Force Applications," in *MEMS 1999, 12th IEEE International Conference on Micro Electro Mechanical Systems*, 1999, pp. 31-36.

[52] K. Carlson, K. Andersen, V. Eichhorn, D. Petersen, K. Molhave, I. Bu, K. Teo, W. Milne, S. Fatikow, and P. Boggild, "A Carbon Nanofibre Scanning Probe Assembled Using an Electrothermal Microgripper," *Nanotechnology,* vol. 18, p. 345501, 2007.

[53] O. Sigmund, "Design of Multiphysics Actuators Using Topology Optimization–Part I: One-material Structures," *Computer Methods in Applied Mechanics and Engineering,* vol. 190, pp. 6577-6604, 2001.

[54] C. G. Keller and R. T. Howe, "Nickel-filled hexsil thermally actuated tweezers," 1995.

[55] C. G. Keller and R. T. Howe, "Hexsil tweezers for teleoperated micro-assembly," 1997, pp. 72-77.

[56] X. Wang, L. Vincent, M. Yu, Y. Huang, and C. Liu, "Architecture of a Three-probe MEMS Nanomanipulator with Nanoscale End-effectors," in *AIM 2003, IEEE/ASME International Conference on Advanced Intelligent Mechatronics*, 2003, pp. 891-896.

[57] D. Kim, M. Lee, B. Kim, and Y. Sun, "A Superelastic Alloy Microgripper with Embedded Electromagnetic Actuators and Piezoelectric Force Sensors: A Numerical and Experimental Study," *Smart Materials and Structures,* vol. 14, pp. 1265-1272, 2005.

[58] S. Jericho, M. Jericho, T. Hubbard, and M. Kujath, "Micro-electro-mechanical Systems Microtweezers for the Manipulation of Bacteria and Small Particles," *Review of Scientific Instruments,* vol. 75, pp. 1280-1282, 2004.

[59] P. Kim and C. Lieber, "Nanotube Nanotweezers," *Science,* vol. 286, pp. 2148-2150, 1999.

[60] S. Akita, Y. Nakayama, S. Mizooka, Y. Takano, T. Okawa, Y. Miyatake, S. Yamanaka, M. Tsuji, and T. Nosaka, "Nanotweezers Consisting of Carbon Nanotubes Operating in an Atomic Force Microscope," *Applied Physics Letters,* vol. 79, pp. 1691-1693, 2001.

[61] P. Boggild, T. Hansen, C. Tanasa, and F. Grey, "Fabrication and Actuation of Customized Nanotweezers with a 25 nm Gap," *Nanotechnology,* vol. 12, pp. 331-335, 2001.

[62] O. Sardan, B. Alaca, A. Yalcinkaya, P. Boggild, P. Tang, and O. Hansen, "Microgrippers: A Case Study for Batch-compatible Integration of MEMS with Nanostructures," *Nanotechnology,* vol. 18, p. 375501, 2007.

[63] P. Rai-Choudhury, *Handbook of Microlithography, Micromachining, and Microfabrication*: SPIE, 1997.

[64] S. Chou, "Nanoimprint Lithography and Lithographically Induced Self-Assembly," *MRS Bulletin-Materials Research Society,* vol. 26, pp. 512-518, 2001.

[65] I. Bargatin, I. Kozinsky, and M. Roukes, "Efficient Electrothermal Actuation of Multiple Modes of High-frequency Nanoelectromechanical Resonators," *Applied Physics Letters,* vol. 90, p. 093116, 2007.

[66] J. Lee, D. Park, A. Nallani, Y. Cui, A. Skoyles, and J. Lee, "High-Aspect Ratio Metallic Nano Grippers," in *2006 1st IEEE International Conference on Nano/Micro Engineered Molecular Systems*, 2006, pp. 682-686.

[67] M. Bendsoe and O. Sigmund, *Topology Optimization: Theory, Methods, and Applications*: Springer, 2003.

[68] M. Bendsoe and N. Kikuchi, "Generating Optimal Topologies in Structural Design Using a Homogenization Method," *Computer Methods in Applied Mechanics and Engineering,* vol. 71, pp. 197-224, 1988.

[69] Z. Luo, J. Yang, and L. Chen, "A New Procedure for Aerodynamic Missile Designs Using Topological Optimization Approach of Continuum Structures," *Aerospace Science and Technology,* vol. 10, pp. 364-373, 2006.

[70] R. Yang and A. Chahande, "Automotive Applications of Topology Optimization," *Structural and Multidisciplinary Optimization,* vol. 9, pp. 245-249, 1995.

[71] O. Sigmund and S. Torquato, "Design of Smart Composite Materials Using Topology Optimization," *Smart Materials and Structures,* vol. 8, pp. 365-379, 1999.

[72] J. Jonsmann, O. Sigmund, and S. Bouwstra, "Compliant Thermal Microactuators," *Sensors & Actuators A: Physical,* vol. 76, pp. 463-469, 1999.

[73] G. Yoon and O. Sigmund, "A Monolithic Approach for Topology Optimization of Electrostatically Actuated Devices," *Computer Methods in Applied Mechanics and Engineering,* vol. 197, pp. 4062-4075, 2008.

[74] C. Pedersen, T. Buhl, and O. Sigmund, "Topology synthesis of large-displacement compliant mechanisms," *Int. J. Numer. Methods Eng,* vol. 50, pp. 2683–2705, 2001.

[75] O. Sigmund, "Manufacturing tolerant topology optimization," *Acta Mechanica Sinica,* vol. 25, pp. 227-239, 2009.

[76] J. Melngailis, "Focused Ion Beam Technology and Applications," *Journal of Vacuum Science & Technology B: Microelectronics and Nanometer Structures,* vol. 5, pp. 469-495, 1987.

[77] S. Reyntjens and R. Puers, "A Review of Focused Ion Beam Applications in Microsystem Technology," *Journal of Micromechanics and Microengineering,* vol. 11, pp. 287-300, 2001.

[78] J. Daniel and D. Moore, "A Microaccelerometer Structure Fabricated in Silicon-on-insulator Using a Focused Ion Beam Process," *Sensors & Actuators A: Physical,* vol. 73, pp. 201-209, 1999.

[79] S. Reyntjens and R. Puers, "Focused Ion Beam Induced Deposition: Fabrication of Three-dimensional Microstructures and Young's Modulus of the Deposited Material," *Journal of Micromechanics and Microengineering,* vol. 10, pp. 181-188, 2000.

[80] M. Bendsøe, "Optimal shape design as a material distribution problem," *Structural and Multidisciplinary Optimization,* vol. 1, pp. 193-202, 1989.

[81] P. Michaleris, D. Tortorelli, and C. Vidal, "Tangent operators and design sensitivity formulations for transient non-linear coupled problems with applications to elastoplasticity," *International Journal for Numerical Methods in Engineering,* vol. 37, pp. 2471-2499, 1994.

[82] J. Luo, J. He, A. Flewitt, D. Moore, S. Spearing, N. Fleck, and W. Milne, "Development of all metal electrothermal actuator and its applications," *Journal of Microlithography, Microfabrication, and Microsystems,* vol. 4, p. 023012, 2005.

[83] Q. Huang and N. Lee, "Analytical modeling and optimization for a laterally-driven polysilicon thermal actuator," *Microsystem Technologies,* vol. 5, pp. 133-137, 1999.

[84] W. Fulkerson, J. Moore, R. Williams, R. Graves, and D. McElroy, "Thermal Conductivity, Electrical Resistivity, and Seebeck Coefficient of Silicon from 100 to 1300° K," *Physical Review,* vol. 167, pp. 765-782, 1968.

[85] J. Israelachvili, "Intermolecular and surface forces," 1992.

[86] S. Senturia, *Microsystem design*: Kluwer Academic Publishers, 2001.

[87] B. Bhushan, *Springer handbook of nanotechnology*: Springer, 2006.

[88] H. Casimir and D. Polder, "Influence of retardation on the london-van der waals forces," *Nature,* vol. 158, p. 787, 1946.

[89] N. Tas, T. Sonnenberg, H. Jansen, R. Legtenberg, and M. Elwenspoek, "Stiction in surface micromachining," *Journal of Micromechanics and Microengineering,* vol. 6, pp. 385-397, 1996.

[90] E. Bhattacharya, U. Babu, L. Rani, P. Pradeep, P. Rao, and K. Bhat, "Contact angle measurements on polysilicon for surface micromachining applications," 2003, p. 367.

[91] S. Lee, D. Oh, I. Jung, K. Bae, P. Jung, K. Chung, S. Cho, and J. Ko, "Fabrication of nickel micromesh sheets and evaluation of their water-repellent and water-proof abilities," *International Journal of Precision Engineering and Manufacturing,* vol. 10, pp. 161-166, 2009.

[92] Y. Zhuang, O. Hansen, T. Knieling, C. Wang, P. Rombach, W. Lang, W. Benecke, M. Kehlenbeck, and J. Koblitz, "Thermal stability of vapor phase deposited self-assembled monolayers for MEMS anti-stiction," *Journal of Micromechanics and Microengineering,* vol. 16, pp. 2259-2264, 2006.

[93] X. Li, C. Zhang, and J. Liu, "DLC films as anti-stiction coatings for MEMS," 2008, p. 713346.

[94] N. Balabanava, R. Wierzbicki, M. Zielecka, and Z. Rymuza, "Effect of roughness on adhesion of polymeric coatings used for microgrippers," *Microelectronic Engineering,* vol. 84, pp. 1227-1230, 2007.

[95] E. M. Chow, A. Partridge, C. F. Quate, and T. W. Kenny, "Through-wafer electrical interconnects compatible with standard semiconductor processing," in *Solid-State Sensor and Actuator Workshop* Hilton Head Island: S.C.: Transducers Research Foundation, 2000, pp. 343-46.

[96] J. Li, C. Lu, X. Hu, X. Yang, A. Loboda, and R. Lipson, "Nanostructured porous silicon by laser assisted electrochemical etching," *International Journal of Mass Spectrometry,* vol. 285, pp. 137-142, 2009.

[97] A. Slimani, A. Iratni, J. Chazalviel, N. Gabouze, and F. Ozanam, "Experimental study of macropore formation in p-type silicon in a fluoride solution and the transition between macropore formation and electropolishing," *Electrochimica Acta,* vol. 54, pp. 3139-3144, 2009.

[98] D. H. Petersen, "High aspect ratio silicon beam fabrication and large scale nanowire integration," in *Department of Micro and Nanotechnology* Kgs. Lyngby: Technical University of Denmark, 2006.

[99] A. Geisberger, N. Sarkar, M. Ellis, and G. Skidmore, "Electrothermal properties and modeling of polysilicon microthermal actuators," *Microelectromechanical Systems, Journal of,* vol. 12, pp. 513-523, 2003.

[100] K. Andersen, D. Petersen, K. Carlson, K. Molhave, O. Sardan, A. Horsewell, V. Eichhorn, S. Fatikow, and P. Boggild, "Multimodal Electrothermal Silicon Microgrippers for Nanotube Manipulation," *IEEE Transactions on Nanotechnology,* vol. 8, pp. 76-85, 2009.

[101] A. Cagliani, R. Wierzbicki, D. H. Petersen, K. Nordstrøm Dyvelkov, O. Sardan, B. G. Herstrøm, T. Booth, and P. Bøggild, "Manipulation and insitu TEM characterisation of sub-100 nm nanostructures using microfabricated nanogripper," 2009.
[102] A. Lei, "Focused Ion Beam Shaped Nanotools," in *Department of Micro and Nanotechnology* Kgs. Lyngby: Technical University of Denmark, 2009.
[103] H. V. Jansen, M. J. de Boer, S. Unnikrishnan, M. C. Louwerse, and M. C. Elwenspoek, "Black silicon method X: a review on high speed and selective plasma etching of silicon with profile control: an in-depth comparison between Bosch and cryostat DRIE processes as a roadmap to next generation equipment," *Journal of Micromechanics and Microengineering,* vol. 19, 2009.
[104] www.technolam.de.
[105] www.rogerscorp.com.
[106] www.asuzac.jp.
[107] G. Binnig, C. Gerber, E. Stoll, T. Albrecht, and C. Quate, "Atomic resolution with atomic force microscope," *Europhys. Lett,* vol. 3, pp. 1281-1286, 1987.
[108] E. Wong, P. Sheehan, and C. Lieber, "Nanobeam mechanics: elasticity, strength, and toughness of nanorods and nanotubes," *Science,* vol. 277, p. 1971, 1997.
[109] K. Mølhave, "Using the AFM to measure mechanical properties of nanowires," Kgs. Lyngby: Department of Micro and Nanotechnology, DTU, 2008.
[110] I. Lewis and H. Edwards, *Handbook of Raman spectroscopy: from the research laboratory to the process line*: CRC, 2001.
[111] C. Raman and K. Krishnan, "A new type of secondary radiation," *Nature,* vol. 121, p. 501, 1928.
[112] M. Abel, T. Wright, W. King, and S. Graham, "Thermal metrology of silicon microstructures using Raman spectroscopy," *IEEE Transactions on Components and Packaging Technologies,* vol. 30, pp. 200-208, 2007.
[113] I. De Wolf, H. Maes, and S. Jones, "Stress measurements in silicon devices through Raman spectroscopy: Bridging the gap between theory and experiment," *Journal of Applied Physics,* vol. 79, p. 7148, 1996.
[114] J. Ferraro, K. Nakamoto, and C. Brown, *Introductory Raman Spectroscopy*: Academic Pr, 2003.
[115] S. Kearney, L. Phinney, and M. Baker, "Spatially resolved temperature mapping of electrothermal actuators by surface Raman scattering," *Microelectromechanical Systems, Journal of,* vol. 15, pp. 314-321, 2006.
[116] M. Bowden, D. Gardiner, A. Parr, R. Carline, R. Bozeat, R. Bunyan, and M. Ward, "Temperature mapping of polysilicon microheaters using Raman micro-spectroscopy," 1997, pp. 439-442.
[117] R. Ostermeir, K. Brunner, G. Abstreiter, and W. Weber, "Temperature distribution in Si-MOSFETs studied by micro-Ramanspectroscopy," *IEEE Transactions on Electron Devices,* vol. 39, pp. 858-863, 1992.
[118] D. Jasper, "Force control for nanohandling inside Scanning Electron Microscopes," 2009.
[119] J. Serrano, L. Phinney, and S. Kearney, "Micro-Raman thermometry of thermal flexure actuators," *Journal of Micromechanics and Microengineering,* vol. 16, pp. 1128-1134, 2006.
[120] K. N. Andersen, "Manipulation with the 2x3D SmarAct robots in the IPL SEM," Kgs. Lyngby: Department of Micro and Nanotechnology, DTU, 2008.

[121] K. N. Andersen, "Manipulation with the 13D SmarAct robots in the IPL SEM," Kgs. Lyngby: Department of Micro and Nanotechnology, DTU, 2008.
[122] S. Fatikow, S. Kray, V. Eichhorn, and S. Tautz, "Development of a nanohandling robot station for nanocharacterization by an AFM probe," 2006, pp. 1-6.
[123] O. Sardan, V. Eichhorn, D. Petersen, S. Fatikow, O. Sigmund, and P. Bøggild, "Rapid Prototyping of Nanotube-based Devices Using Topology-optimized Microgrippers," *Nanotechnology,* vol. 19, p. 495503, 2008.
[124] www.nanohand.eu.
[125] R. T. R. Kumar, S. U. Hassan, O. Sardan, V. Eichhorn, F. Krohs, S. Fatikow, and P. Boggild, "Nanobits: customizable scanning probe tips," *Nanotechnology,* vol. 20, p. 395703, 2009.
[126] J. Hu, Z. Chen, H. Jiang, Y. Sun, Y. Bando, and D. Golberg, "Rectangular or square, tapered, and single-crystal PbTe nanotubes," *Journal of Materials Chemistry,* vol. 19, pp. 3063-3068, 2009.

Publications

A. Peer Reviewed Journals *(Attached in full-text to the end)*

1. Sardan, V Eicchorn, D H Petersen, S Fatikow, O Sigmund and P Bøggild, "Rapid Prototyping of Nanotube-based Devices Using Topology-optimized Microgrippers", *Featured Article and Cover Page, Nanotechnology* 19 (49) (2008) 495503.
2. Sardan, D H Petersen, K Mølhave, O Sigmund and P Bøggild, "Topology Optimized Electrothermal Polysilicon Microgrippers", *Microelectronic Engineering* 85 (2008) 1096-1099.

B. Conference Proceedings (Attached in full-text to the end)

1. Sardan Sukas, J Liu and P Bøggild, "Measuring The Temperature Of Topology Optimized Electrothermal Microgrippers Using Raman Spectroscopy", *Proceedings of IMECE2009, 2009 ASME International Mechanical Engineering Congress and Exposition,* November 13-19, Lake Buena Vista, FL, USA.
2. Sardan, D H Petersen, O Sigmund and P Bøggild, "Simulation of Topology Optimized Electrothermal Microgrippers", *Proceedings of 2008 Comsol Conference*, November 4-6, 2008, Hannover, Germany.
3. Sardan, V Eichhorn, D H Petersen, S Fatikow, O Sigmund and P Bøggild, "Topology Optimized Microgrippers for Nanomanipulation of Carbon Nanotubes", *Proceedings of MNS 2008, ASME 2nd International Conference on Micro- and Nanosystems*, August 3-6, 2008, New York City, NY, USA.
4. Sardan K N Andersen, A N MacDonald, O Sigmund, P Bøggild and A Horsewell, "Focused Ion Beam (FIB) Modification of Topology Optimized Polysilicon Microgrippers", *Proceedings of MNS 2008, ASME 2nd International Conference on Micro- and Nanosystems*, August 3-6, 2008, New York City, NY, USA.

C. Co-authored Publications

1. R T R Kumar, S U Hassan, O Sardan, V Eichhorn, F Krohs, S Fatikow, and P Boggild, "Nanobits: customizable scanning probe tips", *Nanotechnology* 20 (39) (2009) 395703.
2. K N Andersen, D H Petersen, K Carlson, K Molhave, O Sardan, A Horsewell, V Eichhorn, S Fatikow and P Boggild, “Multimodal Silicon Microgrippers for Nanotube Manipulation”, *IEEE Transactions on Nanotechnology* 8 (1) (2009) 76-85.
3. V Eichhorn, S Fatikow, T Wortmann, C Stolle, C Edeler, D Jasper, O Sardan, P Boggild, G Boetsch, C Canales and R Clavel, “NanoLab: A nanorobotic system for automated pick-and-place handling and characterization of CNTs”, *Proceedings of ICRA 2009, 2009 IEEE International Conference on Robotics and Automation*, May 12-17, 2009, Kobe, Japan.

ISSN 0957-4484

NANOTECHNOLOGY

VOLUME 19 NUMBER 49 10 DECEMBER 2008

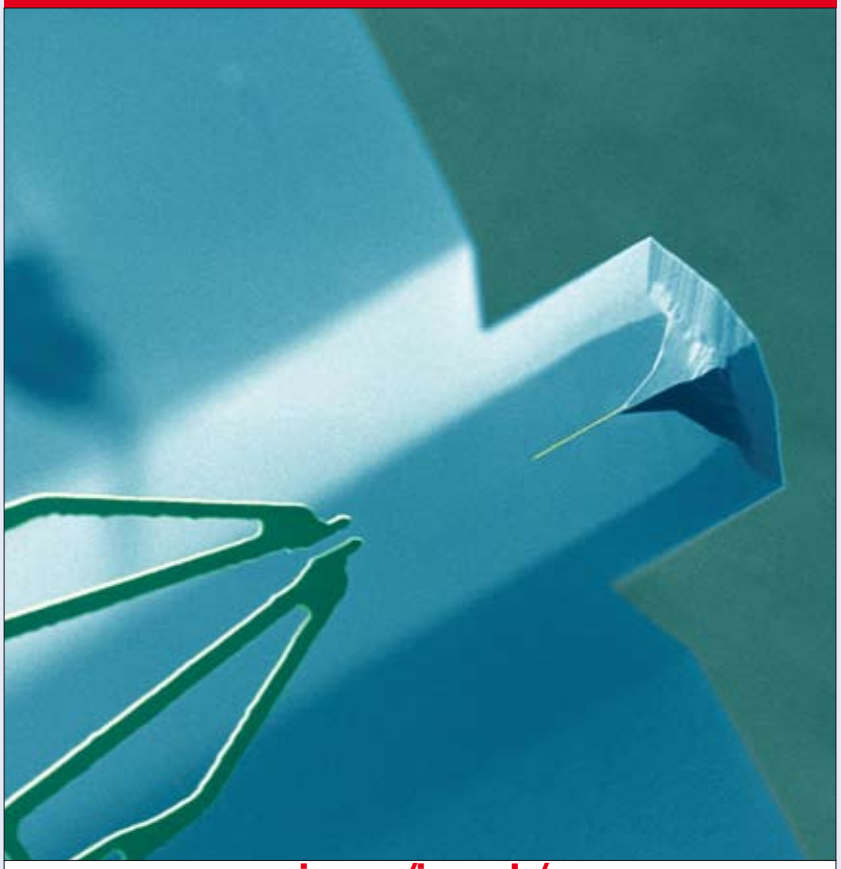

www.iop.org/journals/nano

Featured article

Rapid prototyping of nanotube-based devices using topology-optimized microgrippers

O Sardan, V Eichhorn, D H Petersen, S Fatikow, O Sigmund and P Bøggild

IOP Publishing

Nanotechnology **19** (2008) 495503 (9pp) doi:10.1088/0957-4484/19/49/495503

Rapid prototyping of nanotube-based devices using topology-optimized microgrippers

O Sardan[1], V Eichhorn[2], D H Petersen[1], S Fatikow[2], O Sigmund[3] and P Bøggild[1]

[1] Nanotech-Department of Micro and Nanotechnology, Technical University of Denmark, DK-2800 Kongens Lyngby, Denmark
[2] Division of Microrobotics and Control Engineering, University of Oldenburg, 26111 Oldenburg, Germany
[3] Department of Mechanical Engineering, Technical University of Denmark, DK-2800 Kongens Lyngby, Denmark

E-mail: oezlem.sardan@nanotech.dtu.dk

Received 8 October 2008, in final form 20 October 2008
Published 18 November 2008
Online at stacks.iop.org/Nano/19/495503

Abstract
Nanorobotic handling of carbon nanotubes (CNTs) using microgrippers is one of the most promising approaches for the rapid characterization of the CNTs and also for the assembly of prototypic nanotube-based devices. In this paper, we present pick-and-place nanomanipulation of multi-walled CNTs in a rapid and a reproducible manner. We placed CNTs on copper TEM grids for structural analysis and on AFM probes for the assembly of AFM super-tips. We used electrothermally actuated polysilicon microgrippers designed using topology optimization in the experiments. The microgrippers are able to open as well as close. Topology optimization leads to a 10–100 times improvement of the gripping force compared to conventional designs of similar size. Furthermore, we improved our nanorobotic system to offer more degrees of freedom. TEM investigation of the CNTs shows that the multi-walled tubes are coated with an amorphous carbon layer, which is locally removed at the contact points with the microgripper. The assembled AFM super-tips are used for AFM measurements of microstructures with high aspect ratios.

(Some figures in this article are in colour only in the electronic version)

1. Introduction

Handling and manipulation of nanostructures in three dimensions is challenging due to the need for small, accurate, yet mechanically stable manipulation tools. In situations in which the nanostructure is initially fastened to a surface, such as vertically aligned CNTs [1] or epitaxial nanowires [2], grippers and tweezers are useful due to their ability to apply opposing forces of adjustable magnitude, allowing the nanostructures to be detached controllably. Most practical methods of fabricating nanowires and nanotubes with well-defined orientation, location and dimensions suitable for device assembly involve electron-beam lithography (EBL) followed by a chemical or physical vapor deposition process (CVD or PVD) [1, 3].

During the past years, various nanorobotic systems that can be integrated into the vacuum chamber of scanning electron microscopes (SEMs) have been developed for micromanipulation and nanomanipulation purposes [4–10]. In this paper, we present a further development of the system presented in [11]. The newly designed nanorobotic system offers novel degrees of freedom, such as a rotational axis for the microgripper, and integrated sensors of all linear axes, resulting in closed-loop actuation, providing the basis for automated nanohandling sequences.

The performance of the manipulation tool is the most important factor for successive nanorobotic manipulation. Starting from early 1990s, various groups have fabricated grippers for manipulation of sub-micron objects, based on different actuation mechanisms and materials [12–15].

 © 2008 IOP Publishing Ltd Printed in the UK

Commercial suppliers, such as Nascatec and Zyvex [16, 17], also manufacture grippers for micron to sub-micron manipulation purposes. However, only a few examples of reproducible transfer of nanostructures from a well-defined starting point to a well-defined end point, i.e. a pick-and-place process suitable for implementation in an assembly line system, have been published so far.

Electrothermal expansion is an actuation principle which allows for rather large forces to be applied, using a gripper of relatively small size [15, 18]. Two common types of electrothermal actuator which have been used for nanomanipulation are parallel-beam [15, 18, 19] and rib-cage [20] actuators; the parallel-beam actuator is a variant of the Guckel actuator [19]. Parallel-beam microgrippers are advantageous due to their compact and flexible design, allowing both closing and opening action, and availability of piezoresistive force feed-back [15]. However, for the manipulation of plasma-enhanced (PE)CVD grown carbon nanofibres with diameters of several hundred nanometers [1], parallel-beam actuators delivered insufficient gripping force to safely detach the carbon nanotubes. The investigated microgrippers with rib-cage actuators [20] were more powerful, providing 10–20 times larger forces, at the cost of a more bulky form factor, and less flexibility in the design compared to the parallel-beam gripper. In order to manipulate nanowires and carbon nanotubes with smaller diameters, the overall size of the gripper should be reduced accordingly, to reduce blocking of the line of sight, and to allow increasingly delicate manipulation to be carried out. With the conventional design mentioned, the actuation range and the gripping force, which is the actual force that can be applied when the gripper is fully closed, would be significantly reduced [18]. For example, scaling the dimensions of the conventional three-parallel-beam actuator down by a factor of 2 results in an ∼6 times reduction in its in-plane stiffness.

To avoid these shortcomings a small gripper with narrow beams, able to generate a large force without leading to high temperatures at the end-effector, is required. Furthermore, the motion of the end-effectors should be stable, i.e. out-of-plane bending should be avoided. We use topology optimization to modify the parallel-beam actuator design for larger gripping force, without increasing the overall size and the operating temperature, or sacrificing the dual-direction ability (open/close).

Topology optimization is a finite-element-based method, which relies on the redistribution of a given amount of material in a well-defined design domain [21, 22], using gradient-based deterministic optimization algorithms, which often leads to vastly different topologies than conventional approaches, and with superior performance [23]. The two-dimensional (2D) topology optimization procedure used is here based on the approach described in [24].

Compared to previously reported work [23], we introduce several design improvements and demonstrate that the gripper is capable of picking and placing carbon nanotubes with great predictability. Mounting the CNTs on a TEM grid allows us to investigate structural damage effects caused by manipulation with nanometer resolution. Furthermore, AFM

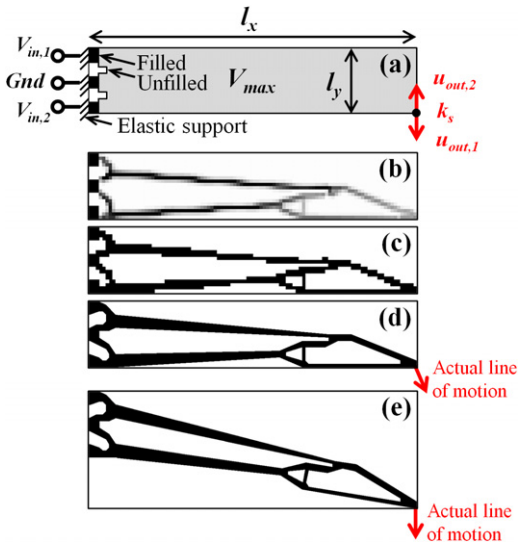

Figure 1. (a) Illustration of the design domain and boundary conditions for the topology optimization problem. (b) Grayscale output of the topology optimization program. (c) Conversion to a binary image. (d) Smoothing the design. (e) Tilting the actuator to change the line of motion.

super-tips assembled with thinner and sharper CNTs allow better AFM measurements of high aspect ratio structures compared to [20]. We find that the performance of the topology-optimized actuator is considerably better than that of the three-beam design and that the actuator force is increased by at least one order of magnitude, and discuss the further miniaturization of the design. For the structures used in this work, a considerable gripping force in the 10–100 μN range is required to detach the nanostructure in a predictable way [20].

2. Design

The first step of the topology optimization process is the definition of the design domain. This includes the definition of parameters such as domain size, material properties, force/displacement ratio, operating voltage and number of discretization elements, and setting up boundary conditions and constraints, such as the position of supports or the volume constraint, which is the maximum amount of material to be distributed within the domain.

The design domain and boundary conditions for topology optimization can be seen in figure 1(a), and all design parameters and material properties are given in table 1.

For practical reasons polysilicon was selected as the actuator material. The domain size was chosen to be slightly wider than the design space occupied by the three-beam actuator [15], which is composed of 200 μm × 2 μm × 5 μm beams. The volume constraint was set to the volume occupied by the same three-beam actuator within this domain. The positions of the elastic supports, voltage boundary conditions, and two load cases were defined by taking the electrothermal actuation principle of the three-beam design as a reference, to be able to directly compare the conventional design with the topology-optimized design. Note that the first load case

Table 1. Topology optimization design parameters and material properties.

Parameter/property	Value	Unit
Domain length, l_x	200	μm
Domain width, l_y	40	μm
Device thickness, h	5	μm
Volume constraint, $V_{\max}$	15	%
Force/displacement ratio, k_s	25	N m^{-1}
Input voltages, V_1 and V_2	8	V
Number of elements in x-direction	100	
Number of elements in y-direction	20	
Young's modulus	169	GPa
Poisson's ratio	0.3	
Coefficient of thermal expansion	2.57×10^{-6}	K^{-1}
Electrical conductivity	1.125×10^{4}	S m^{-1}
Thermal conductivity	148	W (m^{-1} K^{-1})

corresponds to closing of the microgripper whereas the second load case corresponds to its opening.

The target value for the gripping force/displacement ratio was set to 25 N m^{-1}, matching the rib-cage actuator presented in [20]. The input voltages with these parameters was adjusted to give a maximum temperature less than 700 °C, corresponding roughly to the temperature at which polysilicon undergoes permanent deformation. In the algorithm used, only fixed values of the thermal expansion coefficient, the electrical resistance, carrier density and thermal conductivity can be incorporated. We used values for the temperature-dependent material properties reported for 500 °C [25], representing the average temperature at a relatively large force/deflection.

The topology optimization problem, which implies maximization of the output displacements for the two load cases, i.e. work-pieces $u_{\text{out},1}$ and $u_{\text{out},2}$, simultaneously, is given by

$$\begin{aligned} &\underset{\rho}{\text{maximize}} \quad u_{\text{out},1}(\rho) + u_{\text{out},2}(\rho) \\ &\text{such that} \quad \begin{array}{l} \sum_{e=1}^{N} \rho^e V^e \leqslant V_{\max} \\ 0 < \rho_{\min} \leqslant \rho \leqslant 1 \end{array} . \end{aligned} \tag{1}$$

Here, ρ is the element relative density vector corresponding to the design variables, ρ^e is the element relative density, $\rho_{\min}$ is a lower bound on the relative material densities (1×10^{-3}), V^e is the element volume, and $V_{\max}$ is the volume constraint.

After proper discretization of the design domain, the above-stated optimization problem is solved through a number of iterations. To have reasonable computation times, we limited the total number of discretization elements to 2000, arranged in a 100 by 20 grid of elements, each 2 μm $\times$ 2 μm in size. This corresponds to the minimum line width that can be fabricated reproducibly using optical lithography. Each calculation ran a total of 1000 iterations, starting with a relatively large filter radius, $r_{\min}$, as 3 and gradually decreasing it to 2, 1.5 and 1.2, respectively. This method is described in detail in [24].

The output of the topology optimization is a grayscale bitmap image with the intensity of each pixel representing the element relative material density, ρ^e (figure 1(b)). The topology optimization results are given in table 2.

Table 2. Topology optimization results.

Parameter	Case 1 (close)	Case 2 (open)	Unit
Deformation, $u_{\text{out},i}$	0.789	0.733	μm
Force, $F_{\text{out},i}$	19.7	18.3	μN
Maximum temperature, $T_{\max,i}$	620.8	605.8	°C
Free deformation, $u_{\text{free},i}$	1.32	1.23	μm
Blocking force, $F_{\text{blo},i}$	49	45.6	μN
Maximum current, $I_{\max,i}$	13.7	15.1	mA
In-plane stiffness, k_y	37.17	37.17	N m^{-1}

Since it is not possible to fabricate a structure with a variable material density in practice, we converted the grayscale output of the topology optimization into a binary, i.e. black and white, image (figure 1(c)).

High stress concentration and high temperature at thin beams can lead to high local temperatures and mechanical failure. The topology-optimized actuator design was refined to avoid this, by replacing the pixelated structure with straight, smoothed beams (figure 1(d)). Although the topology-optimized actuator is designed to displace along the y-direction, we observed that it also slightly elongates, i.e. displaces along $+x$-axis. In order to reduce this cross-displacement, we calculated the angle between the actual line of motion and the y-axis and tilted the actuators by 9.5° accordingly when constructing the microgrippers (figure 1(e)). This will also result in an increase in the applied force.

3. Microfabrication

Polysilicon microgrippers were fabricated using polysilicon-on-insulator (pSOI) wafers (figure 2(a)). Such wafers were prepared by growth of 650 nm thick thermal oxide (SiO_2) on 4 inch (100) silicon wafers, followed by low-pressure chemical vapor deposition (LPCVD) of 5 μm thick highly B-doped polysilicon and subsequent furnace anneal at 1000 °C for 1 h in order to reduce film stress. The polysilicon and oxide layers were then removed from the backside first, by reactive-ion etching (RIE) using a pure SF_6 plasma and second, by a wet etch in buffered hydrofluoric acid (bHF).

Initially, the front side of the wafer is masked with a 1.5 μm thick AZ5214E photoresist layer using a negative UV lithography process. The polysilicon device layer can then be etched anisotropically until the buried oxide layer is reached using the plasma-based silicon etch (figure 2(b)).

RIE was used for this purpose in [23]. However, the actuator beams had a trapezoidal cross-section due to non-uniform etching during this step. This slanted sidewall profile prevents the microgripper end-effectors from closing completely. In addition, the mechanical performance of the design was also considerably influenced by variation of the line width of the beams due to the non-uniform RIE step [23]. For this reason we replaced the parallel plate RIE step with a single-step inductively coupled plasma (ICP) etch (unswitched process, C_4F_8 flow = 90 sccm, SF_6 flow = 40 sccm, pressure = 15 mT, coil power = 800 W, platen power = 10 W, temperature = 20 °C). The lateral etch rate during the ICP process is almost negligible, and hence the sidewalls of the resulting structures were quite uniform.

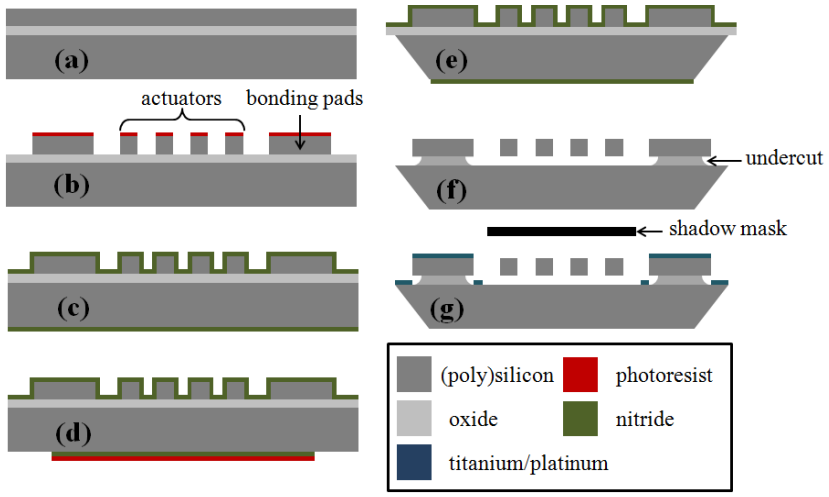

Figure 2. Fabrication steps for the polysilicon microgrippers.

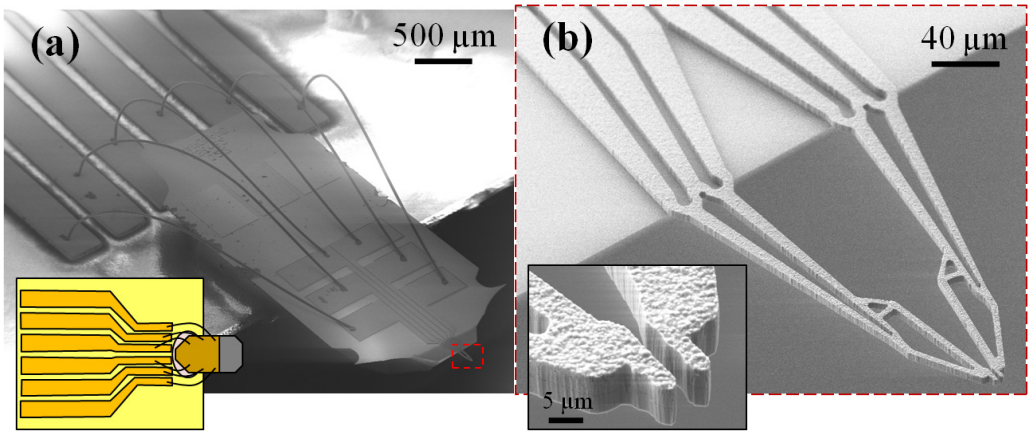

Figure 3. (a) A microgripper chip glued and wire-bonded to a PCB interface. A schematic illustration of the interface is shown in the inset. (b) Overview of the free-hanging topology-optimized microgripper pointing out from the front edge of the chip (the dashed rectangle in (a)). A detailed view of the end-effectors is shown in the inset.

After removal of the remaining photoresist in oxygen plasma, the wafer was RCA cleaned and coated with 350 nm thick low-stress, silicon-rich silicon nitride (Si_3N_4) on both sides, by LPCVD (figure 2(c)). The backside of the wafer was masked by a 2.2 μm thick layer using a positive UV lithography process, and then the unmasked nitride on this side was etched using RIE (figure 2(d)). Following the removal of the remaining photoresist in an oxygen plasma, individual microgripper chips were released by etching the silicon wafer through in a potassium hydroxide (KOH) solution at 80 °C (figure 2(e)). Afterward, nitride layers on both sides of the wafer were removed by wet etching in a 180 °C phosphoric acid (H_3PO_4) bath, and the microgrippers were released by underetching the oxide layer in bHF (figure 2(f)). Finally, a thin layer of metal, e.g. 10/190 nm Ti/Pt, was evaporated on the bonding pads in order to enable wire bonding. The actuators are protected with a mechanical shadow mask to prevent unwanted metal deposition (figure 2(g)). Short-circuits between bonding pads were eliminated due to the undercut of the oxide layer resulting from the isotropic bHF etch.

After the microgripper chip is released and removed from the wafer, it is glued onto a custom-made printed circuit board (PCB) interface. Then, electrical contact is achieved by wire bonding the metal-coated bonding pads on the chip to gold leads on the PCB (figure 3).

4. Finite-element analysis of the post processed design

Three-dimensional (3D) finite-element models of the actuators were created and coupled thermo-electro-mechanical analyses were performed using a COMSOL MEMS module. The models also include the first 100 μm length of the silicon leads connecting the actuators to the bonding pads, together with the 650 nm thick oxide layers underneath them. The temperature dependence of the coefficient of thermal expansion and the thermal and electrical conductivities of polysilicon were considered when defining the material properties [26]. In addition to these, the effect of air convection was taken into account since characterization was carried out in ambient conditions.

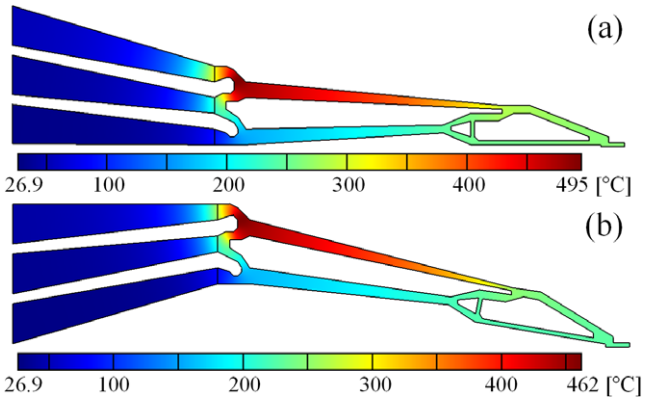

Figure 4. Simulation results for the temperature distribution within the topology-optimized actuators, including the first 100 μm long portion of the leads on the chip: (a) the smoothed design and (b) the tilted design.

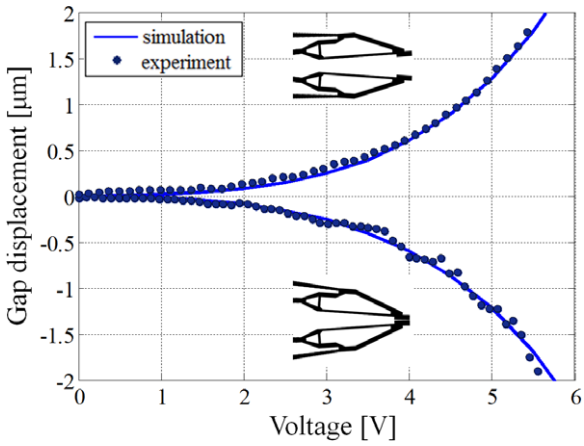

Figure 6. Comparison of the experiment results with finite-element simulations for the gap displacement versus bias curves for the topology-optimized microgrippers (smoothed design).

Simulation results for the temperature distribution within the actuators can be seen in figure 4. The in-plane spring constant of the topology-optimized actuator with smoothed beams was found to be 234 N m^{-1}, which is significantly more rigid than earlier reportings [15, 23]. Despite the larger stiffness, the maximum temperature in the topology-optimized actuator reaches just 495 °C, while the end-effector temperature is 265 °C, at the point where the 2 μm gap is completely closed (figure 4(a)). Hence, similar temperature maxima and actuation ranges can be reached with far higher stiffness and gripping force using the design shown. The value for the in-plane stiffness of the tilted design is slightly smaller than that of the smoothed design, being 219 N m^{-1}. However, there is a considerable improvement in the end-effector temperature, which drops to 229 °C (figure 4(b)).

The nonlinear y-axis displacement versus bias voltage curves for the topology-optimized actuator design at three different stages is plotted in figure 5(a). Although smoothing the design affects the maximal temperature and rigidity of the actuator, only small deviations less than 10% are observed in the actuation versus bias voltage characteristics. The x-axis displacement versus bias voltage curves for the topology-optimized actuator design at three different stages are plotted in figure 5(b). In the tilted design, the end-effectors move away from the sample rather than moving towards it during the actuation, which enhances gripping.

5. Characterization

The gap displacement versus bias voltage was measured in ambient conditions, for both open and close modes of the microgrippers. Simultaneous filtering and image processing data from a high-magnification optical lens system (Navitar) enable measuring the relative gap distance with a nanometric precision [20]. The experimental data agree quite well with the results of the finite-element simulations (figure 6).

The y-axis stiffness values of the actuators were measured by pushing the end-effectors sideways using an AFM cantilever under a low-magnification optical microscope. Stiffness values of 10.7 N m^{-1} and 11.9 N m^{-1} were measured for the smoothed and tilted designs, respectively. Although these

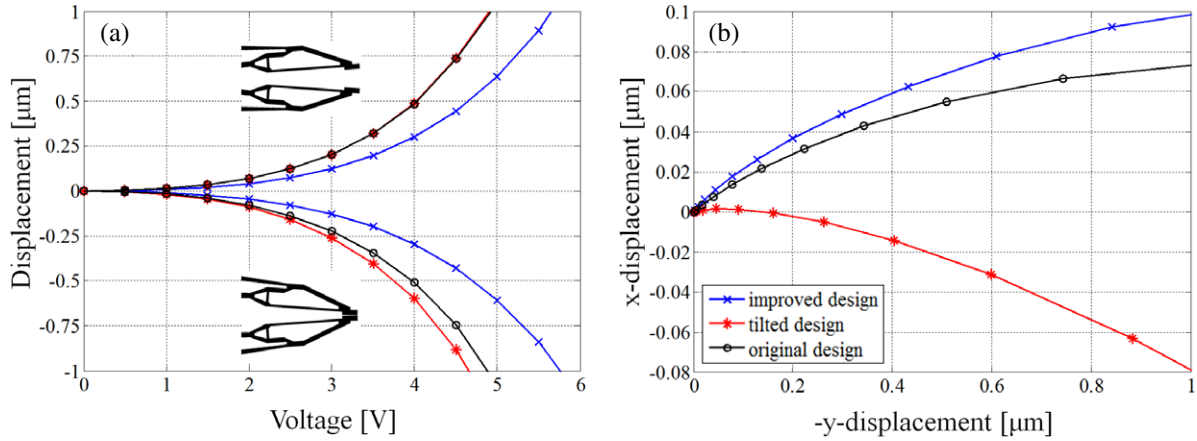

Figure 5. (a) The y-axis displacement versus bias voltage and (b) the x-axis displacement versus y-axis elongation curves for the topology-optimized design at three different stages: original design with a pixelated structure (circles), improved design with smoothed beams (crosses) and tilted version of the improved design (stars).

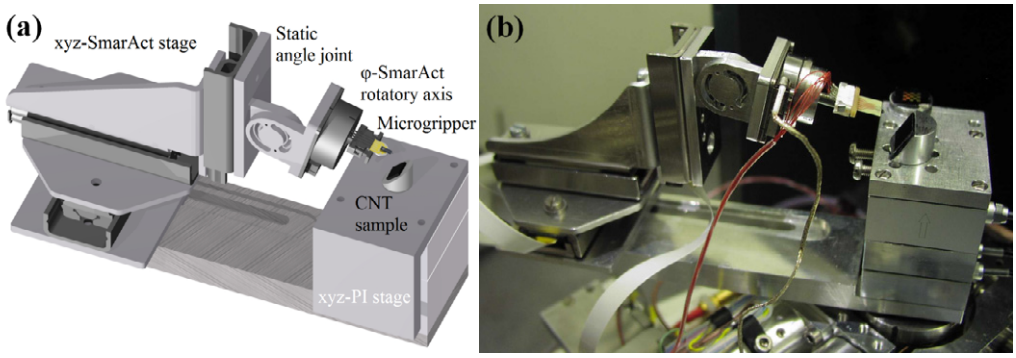

Figure 7. (a) CAD drawing of the novel nanorobotic system and (b) integrated setup on the motorized stage of the SEM.

values are higher than that of the original design, which was 9.1 N m^{-1} [23], a deviation of the experimental data from simulation results still exists. One possible explanation is that the grippers during AFM measurement respond to the external force by out-of-plane bending (z-axis), which lowers the measured spring constant.

6. Nanomanipulation results

For the nanomanipulation experiments the nanorobotic system reported in [11] has been further developed. Figure 7 shows the modified nanorobotic setup. A micromanipulator unit and a nanomanipulator unit are mounted on a base plate that can be integrated into the vacuum chamber of a LEO 1450 SEM. The microgripper is fixed to the micromanipulation unit, which is made up of three linear SmarAct micropositioners and one rotatory axis allowing coarse positioning between the gripper and the CNT. The linear SmarAct positioners offer an overall stroke of about 30 mm with minimal step widths between 50 and 500 nm. The microgripper interface is inserted in a zero insertion force (ZIF) socket, which is placed on the integrated holder. The static angle joint is used to adjust the attack angle of the gripper and the CNT, aligning the gripper almost parallel to the normal of the CNT substrate. The sample of vertically aligned CNTs is mounted on a 60°- or 75°-tilted sample holder using a carbon pad, while a copper TEM grid (Maxtaform, Type NH7C) is inserted into the thin slit of a special holder and clamped mechanically to enable easy exchange. Both sample holders are placed on the nanomanipulation unit which consists of three linear Physik Instrumente (PI) piezoactuators with a stroke of 50 μm and a minimal step width of only 1.5 nm. The indexed TEM grids used in the experiments are supplied by Maxtaform. The thickness, bar width and hole width of the copper grids are about 15 μm, 23 μm and 41 μm, respectively.

The CNT sample used in the experiments was supplied by Cambridge University and consists of multi-walled tapered CNTs, which are arranged in a linear array with a 50 μm distance in between. The CNT sample is similar to those presented in [1], however with lengths in the range 10–20 μm and upper and lower diameters around 150 nm and 350 nm, respectively.

The motorized SEM stage is used to bring the CNT sample into microscope view and to select a target CNT. After aligning the microgripper to the CNT (figure 8(a)), the CNT is detached by actuating the microgripper and moving sideways. The shear stress (shear pulling) caused by the sideways movement leads to breaking of the CNT near the base rather than close to the gripper in all cases. This was previously explained by finite-element simulation of the shear stress distribution in a CNT [18]. By using the rotational axis of the 4D manipulator, the microgripper is brought close to the TEM grid (figure 8(b)). The CNT is then released by opening the microgripper by removing the applied voltage and using the adhesion forces between the CNT and the grid surface to release the CNT controllably (figure 8(c)). In order to improve the bonding of the CNTs on the TEM grid, all CNTs are immediately fixed on the grid by carbonaceous electron-beam-induced deposition (EBiD), in which the electron beam is focused on the CNT–grid interface for 30 min, carefully avoiding irradiation of the suspended section of the CNTs. Three CNTs were put on the TEM grid in succession (figure 8(d)).

Combined TEM and energy dispersive spectroscopy (EDS) analyses of the manipulated CNTs were performed using two different microscopes: an FEI TECNAI T20 and an FEI TITAN Analytical.

Bright-field (BF) TEM images of the second CNT shown in figure 9 reveal that the CNT has a layered structure, with a multi-walled hollow CNT surrounded by an amorphous carbon layer, which may have been deposited at the end of the PECVD growth (figure 9(a), top) [1]. These layers are furthermore coated with a thin layer of amorphous material, which according to EDS measurements contains a high amount of silicon. Remains of the nickel catalyst particle are also observed at the tip and in the interior of the CNT along the longitudinal axis (figure 9(b), bottom). Similar results were obtained for the other two CNTs.

High-angle annular dark-field (HAADF) scanning transmission electron microscope (STEM) images of the CNT clearly reveal that the outer amorphous carbon layer is removed locally at two regions along the CNT length (figure 9(b)). The distance between these regions is about 4.3 μm (the microgripper thickness is 5 μm), which correspond to the positions of the end-effectors. Similar regions are also observed in the other two CNTs.

In addition to manipulation of CNTs onto a TEM grid, topology-optimized microgrippers were used in the

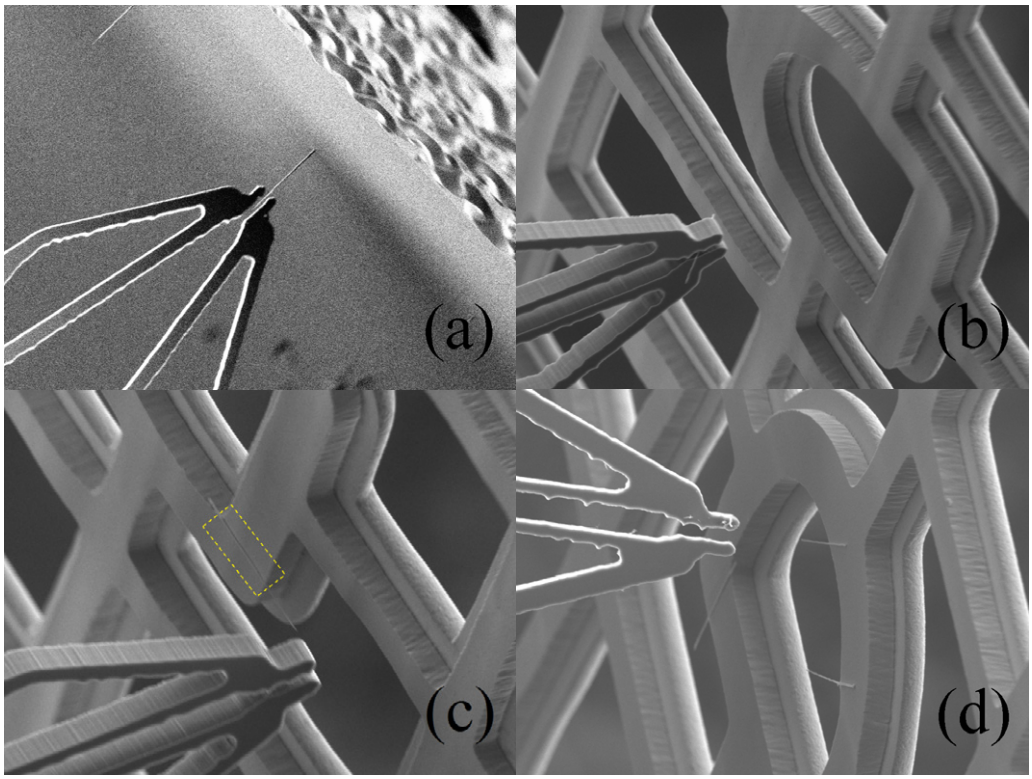

Figure 8. Pick-and-place sequence demonstrating manipulation of a CNT from the source substrate onto a TEM grid: (a) alignment of the end-effectors of the gripper to the CNT, (b) microgrippers approaching the TEM grid with the picked CNT. (c) The CNT released on the TEM grid and performing EBiD on the rectangular region. (d) Overview of the microgrippers and the three CNTs placed on the TEM grid.

assembly of CNT-enhanced AFM super-tips (figure 10). The repeatability of these experiments was verified by multiple, successive repetitions (figures 10 (a)–(d)).

The assembled AFM super-tip shown in figure 10(a) was used to perform AFM scans of microstructures with high aspect ratios. The first gripper-based assembly of a CNT-enhanced AFM super-tip and first AFM scans on deep trenches etched in a silicon substrate were reported in [20]. The CNT used to build up this former AFM super-tip was still too thick to completely resolve the high aspect ratio grooves having a depth of about 2.5 μm. The reported AFM scans provided a groove depth of only 1.2 μm. These new results were again performed on the same test structure but using a JPK NanoWizard II AFM with almost the same AFM parameters to acquire comparable AFM scans. This time the CNT used was thin and long enough to correctly scan the Si grooves. The CNT-enhanced AFM super-tip provides a groove depth of the correct 2.5 μm while a standard pyramidal AFM probe leads to a groove depth of only 500 nm (figure 11).

7. Discussion

The possibility of using electrothermal grippers for repeated assembly of carbon nanotubes has been investigated. First, the topology-optimized electrothermal actuator design reported in [23] was further modified by smoothing the pixelated output from the topology optimization algorithm, without changing the actuation behavior and temperature distribution significantly. By tilting the two gripper arms, elongation was largely eliminated, while at the same time an ∼200% improvement of the lateral stiffness was obtained. In fact, the tilted actuators retract instead of elongating along the x-direction, which may improve the gripping process by pulling the nanotubes away from the sample. Furthermore, improvement of the RIE process, previously used in the fabrication of the microgrippers [23], resulted in more uniform sidewalls and dimensional accuracy.

Finite-element simulations of the actuation characteristics agree quite well with the experimental data. However, an order of magnitude difference between the stiffness values predicted by the simulations and AFM measurements was found, which we expect is caused by out-of-plane bending of the actuators as a result of a misalignment between the AFM cantilever and the actuators. Such out-of-plane distortion was not observed during manipulation experiments.

Using the topology-optimized microgrippers in our further developed nanorobotic system, we demonstrated reproducible and consecutive nanomanipulation and assembly of CNTs for two different purposes. In the first experiment three CNTs were picked from the source substrate and placed on a TEM grid in one manipulation session and investigated using transmission electron microscopy. BF TEM images reveal the layered structure of the CNTs, where HAADF STEM images clearly showed changes to the outer, amorphous carbon crust at the positions of the end-effectors. In the second experiment, three high aspect ratio AFM probes were assembled also in the same session; such devices have widespread uses for the

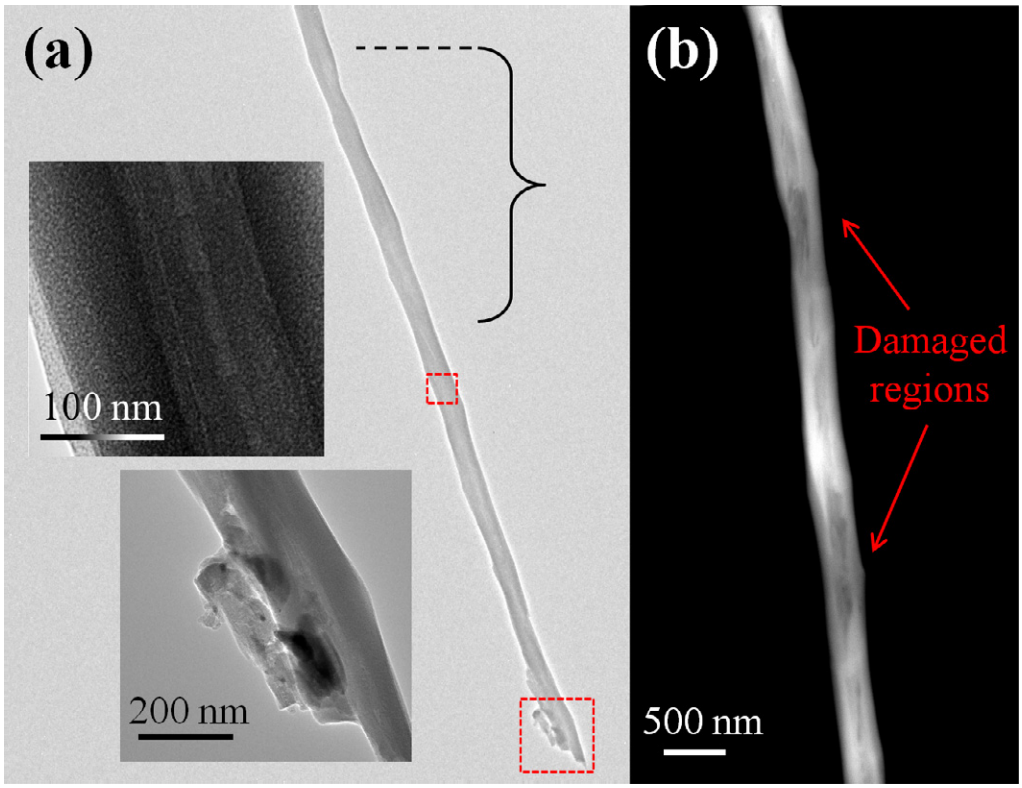

Figure 9. HAADF TEM images of the second CNT: (a) low-magnification BF image of the whole CNT with high-magnification views of the layered structure of the CNT (top) and the nickel catalyst at the tip (bottom). (b) HAADF image clearly showing the damage caused by the microgrippers.

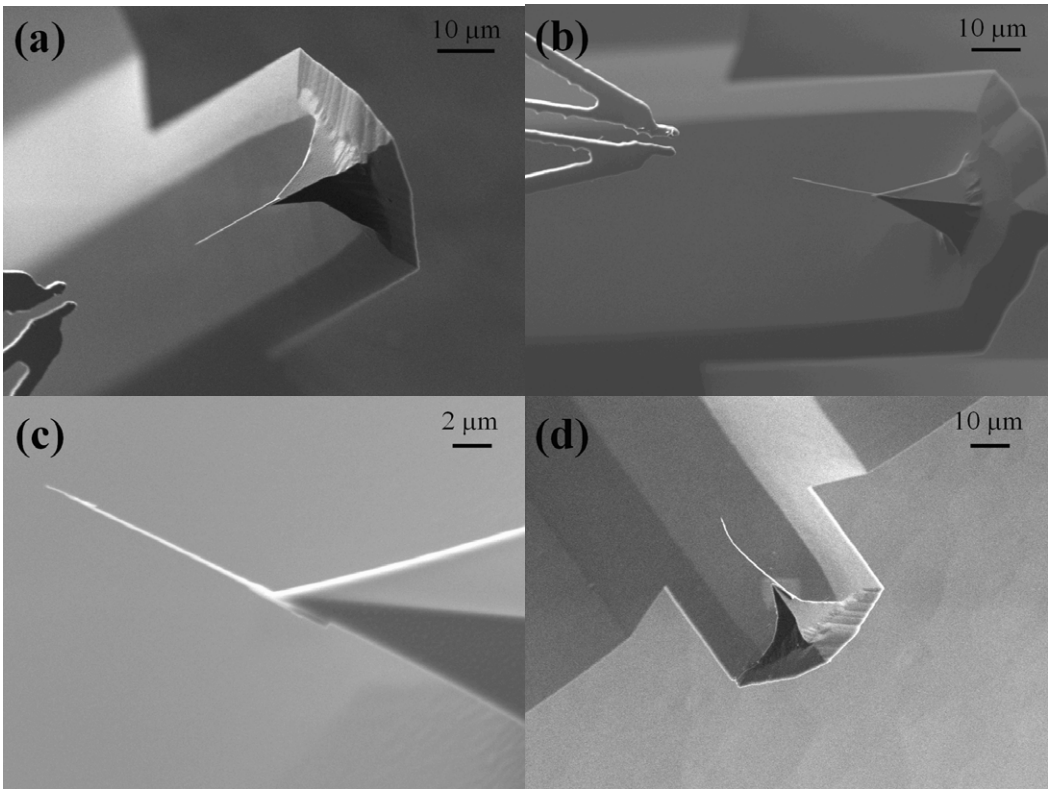

Figure 10. (a)–(d) Reproducible assembly of CNT-enhanced AFM super-tips using topology-optimized microgrippers.

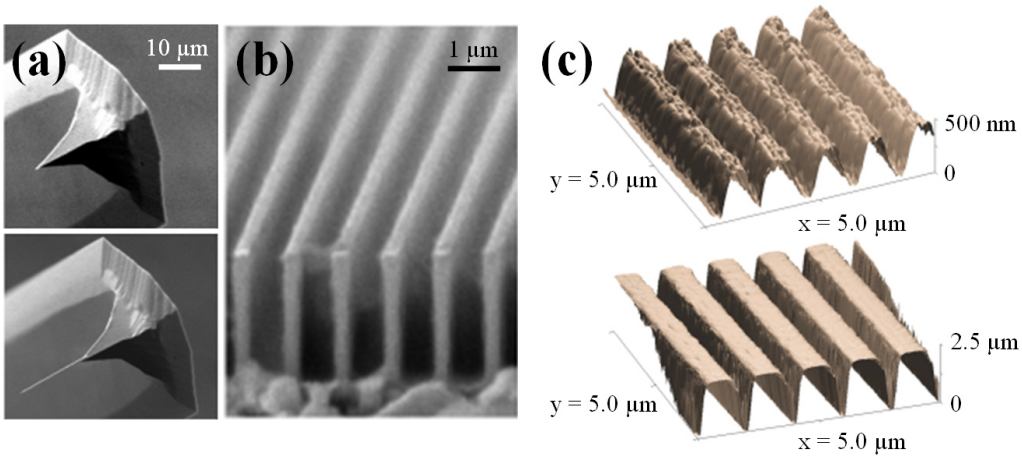

Figure 11. (a) A standard pyramidal AFM probe (top) and a CNT-enhanced AFM super-tip (bottom) assembled during the experiments. (b) 2.5 μm deep trenches etched in a silicon substrate. (c) Comparison of AFM scans of the deep trenches using the standard pyramidal AFM probe (top) and the CNT-enhanced AFM super-tip (bottom).

characterization of sidewalls, via, feedthroughs and trenches in the semiconductor industry and in research.

Issues like carbon and silicon contamination and physical damage during gripping will be investigated further. We suspect that the high temperatures of the actuators are responsible for both the silicon contamination of the outer crust and the physical damage to the nanotubes. Topology optimization is a rational and effective route for further optimization of the temperature distribution. We have demonstrated that electrothermal microgrippers integrated to a nanorobotic system can be used for serial device assembly, and can provide a viable route to fast prototyping and even small-scale manufacturing of nanotube-based devices, resembling industrial macroscale robotic assembly lines.

Acknowledgments

The vertically aligned CNT samples used in the nanomanipulation experiments were supplied by the Engineering Department at the University of Cambridge, UK. The TEM analyses were performed at the Center for Electron Nanoscopy (CEN) at the Technical University of Denmark. The authors would like to thank Lionel Cervera Gontard for his assistance with the TEM analysis. This project was supported by the EU grants NANOHAND (IP 034274) and NANORAC (STREP 013680).

References

[1] Teo K B K *et al* 2003 *Nanotechnology* **14** 204–11
[2] Seifert W *et al* 2004 *J. Cryst. Growth* **272** 211–20
[3] Samuelson L *et al* 2004 *Physica* E **25** 313–8
[4] Fukuda T, Arai F and Dong L 2003 *Proc. IEEE* **91** 1803–18
[5] Williams P A, Papadakis S J, Falvo M R, Patel A M, Sinclair M, Seeger A, Helser A, Taylor R M II, Washburn S and Superfine R 2002 *Appl. Phys. Lett.* **80** 2574–6
[6] Yu M, Dyer M J, Skidmore G D, Rohrs H W, Lu X, Ausman K D, Von Ehr J R and Ruoff R S 1999 *Nanotechnology* **10** 244–52
[7] Lim S C, Kim K S, Lee I B, Jeong S Y, Cho S, Yoo J-E and Lee Y E 2005 *Micron* **36** 471–6
[8] Nakayama Y and Akita S 2003 *New J. Phys.* **5** 128.1–23
[9] Fahlbusch S, Mazerolle S, Breguet J M, Steinecker A, Agnus J, Pérez R and Michler J 2005 *J. Mater. Process. Technol.* **167** 371–82
[10] Fatikow S 2008 *Automated Nanohandling by Microrobots* (*Springer Series in Advanced Manufacturing*) (London: Springer)
[11] Eichhorn V, Carlson K, Andersen K N, Fatikow S and Boggild P 2007 *Proc. 2007 IEEE/RSJ Int. Conf. on Intelligent Robots and Systems* pp 291–6
[12] Kim C-J, Pisano A P, Muller R S and Lim M G 1992 *Sensors Actuators* **33** 221–7
[13] Kim P and Lieber C M 1999 *Science* **286** 2148–50
[14] Bøggild P, Hansen T M, Tanasa C and Grey F 2001 *Nanotechnology* **12** 331–5
[15] Mølhave K and Hansen O 2005 *J. Micromech. Microeng.* **15** 1265–70
[16] www.nascatec.com
[17] www.zyvex.com
[18] Andersen K N, Petersen D H, Carlson K, Mølhave K, Sardan O, Horsewell A, Eichhorn V, Fatikow S and Bøggild P 2008 *IEEE Trans. Nanotechnol.* at press (doi:10.1109/TNANO.2008.2006558)
[19] Guckel H, Klein J, Christenson T, Skrobis K, Laudon M and Lovell E G 1992 *Solid-State Sensor and Actuator Workshop, 5th Technical Digest, IEEE* pp 73–5
[20] Carlson K, Andersen K N, Eichhorn V, Petersen D H, Mølhave K, Bu I Y Y, Teo K B K, Milne W I, Fatikow S and Bøggild P 2007 *Nanotechnology* **18** 345501
[21] Bendsøe M P and Kikuchi N 1988 *Comput. Methods Appl. Mech. Eng.* **71** 197–224
[22] Bendsøe M P and Sigmund O 2003 *Topology Optimization, Theory Methods and Applications* 2nd edn (Berlin: Springer)
[23] Sardan O, Petersen D H, Mølhave K, Sigmund O and Bøggild P 2008 *Microelectron. Eng.* **85** 1096–9
[24] Sigmund O 2001 *Comput. Methods Appl. Mech. Eng.* **190** 6577–604
[25] Fulkerson W, Moore J P, Williams R K, Graves R S and McElroy D L 1968 *Phys. Rev.* **167** 765–82
[26] Geisberger A A, Sarkar N, Ellis M and Skidmore G D 2003 *J. Microelectromech. Syst.* **12** 513–22

Available online at www.sciencedirect.com
ScienceDirect
Microelectronic Engineering 85 (2008) 1096–1099
MICROELECTRONIC ENGINEERING
www.elsevier.com/locate/mee

Topology optimized electrothermal polysilicon microgrippers

Ozlem Sardan [a,*], Dirch H. Petersen [a], Kristian Mølhave [a], Ole Sigmund [b], Peter Bøggild [a]

[a] MIC – Department of Micro and Nanotechnology, Technical University of Denmark, Building 345E, DK-2800 Kgs. Lyngby, Denmark
[b] MEK – Department of Mechanical Engineering, Technical University of Denmark, Building 404, DK-2800 Kgs. Lyngby, Denmark

Received 7 October 2007; received in revised form 12 January 2008; accepted 15 January 2008
Available online 26 January 2008

Abstract

This paper presents the topology optimized design procedure and fabrication of electrothermal polysilicon microgrippers for nanomanipulation purposes. Performance of the optimized microactuators is compared with a conventional three-beam microactuator design through finite element analysis. The accuracy of the finite element model is verified by comparison of simulated and measured displacement vs. bias voltage curves. A considerable improvement in the mechanical stiffness is indicated by AFM force measurements, being 9 times higher compared to the conventional three-beam actuator.
© 2008 Elsevier B.V. All rights reserved.

Keywords: Microgrippers; Electrothermal actuation; Topology optimization; Polysilicon; High-aspect-ratio; Nanomanipulation

1. Introduction

Microgrippers driven by three-parallel-beam electrothermal actuators are promising tools for nanomanipulation due to their compactness, design flexibility, ease of fabrication, mechanical stability and the possibility of force feedback [1,2]. This design allows both opening and closing of the gap.

While carbon nanofibers with diameters of several 100 nm's have been successfully picked up from a fixed position on a substrate [3], further miniaturization of the actuators is necessary for pick-and-place of nanotubes and nanowires with diameters in the sub-100 nm range. Nanolithography techniques such as electron beam lithography (EBL) enable fabrication of nano-scale structures. However, a linear reduction of all dimensions, i.e. length L, width w and height h, results in a linear decrease in the spring constant, $k_s = (11/4)Ehw^3/L^3$, and the actuation range will also be reduced accordingly.

Since the gripping force supplied by such microgrippers is just at the lower limit of the requirement for manipulation of samples [4], which are firmly attached to the substrate, e.g. carbon nanotubes (CNTs) grown by chemical vapor deposition (CVD) [5], simple down-scaling of the conventional three-beam design is not a possible solution for miniaturization.

Furthermore, the relatively high end-effector temperature during operation [1] restricts available fields of use. All in all, a different approach to the actuator design is necessary for efficient nano-scale pick-and-place.

Topology optimization is a promising method for efficient microactuator design [6,7]. In this paper, we present topology optimized electrothermal microgrippers and compare these to conventional three-beam design of similar overall dimensions.

2. Design

Topology optimization is a method for finding the optimum structural layout in a well-defined design domain by solving mathematical algorithms. It is a finite element based approach, which relies on finding the optimal distribution of a given amount of material within the design domain [6].

Initially, the design domain, i.e. size, shape and boundary conditions, is defined (Fig. 1a, Table 1). The volume

* Corresponding author. Tel.: +45 4525 6843; fax: +45 4525 7762.
E-mail address: sar@mic.dtu.dk (O. Sardan).

0167-9317/$ - see front matter © 2008 Elsevier B.V. All rights reserved.
doi:10.1016/j.mee.2008.01.049

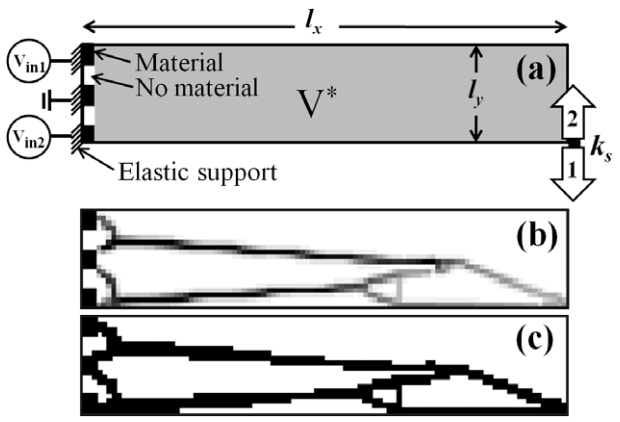

Fig. 1. (a) Illustration of the design domain and boundary conditions for the two load cases of the optimization problem, (b) grey-scale result of topology optimization and (c) conversion of the result to a binary image, ready for fabrication.

Table 1
Design parameters for topology optimization

Parameter	Unit	Value
Domain length, l_x	μm	200
Domain height, l_y	μm	40
Volume constraint, V^*	%	15
Stiffness, k_s	N/m	25
Input voltage, $V_{in,1}$ & $V_{in,2}$	V	8
Thickness, h	μm	5
Material properties	[8] @ 500 °C	

constraint corresponds to the volume occupied by a three-beam actuator with 2 μm × 200 μm beams in the same domain.

With proper discretization, the optimization problem given by (1), which implies simultaneous maximization of the two work-pieces, $u_{out,1}$ and $u_{out,2}$, of stiffness, k_s. Note that, displacements $u_{out,1}$ and $u_{out,2}$ correspond to close and open modes of the microgrippers, respectively:

$$\begin{aligned} &\max_{\rho} && u_{out,1}(\rho) - u_{out,2}(\rho) \\ &\text{such that} && \sum_{e=1}^{N} \rho^e V^e \leqslant V^* \\ & && 0 < \rho_{min} \leqslant \rho \leqslant 1 \end{aligned} \tag{1}$$

In the above expression, ρ is the element relative density vector, ρ^e is element relative density, ρ_{min} is the lower bound on relative material densities (1×10^{-3}), V^e is element volume and V^* is the volume constraint.

The number of discretization elements used is 2000 corresponding to 2 μm × 2 μm square elements, which was found to be optimal considering the aspect ratio limitations and minimum lithographic line-width. Iterations are initiated with a filter radius, r_{min}, [6,7] of 3 and decreased to 2, 1.5 and 1.2, respectively, after 250 iterations with each value.

The output of topology optimization is a grey-scale bitmap image with intensity representing the relative material density (Fig. 1b, Table 2).

Table 2
Results of topology optimization

Parameter	Unit	(1) Close	(2) Open
Deformation, u_{out}	μm	0.789	0.733
Force, F_{out}	μN	19.7	18.3
Max. temperature, T_{max}	°C	620.8	605.8
Free deformation, u_{free}	μm	1.32	1.23
Blocking force, F_{blo}	μN	49	45.6
Max. current, I_{max}	mA	13.7	15.1
Structural stiffness, $k_{s,st}$	N/m	37.17	

Since fabrication of a microstructure with a variable material density is not possible, the grey-tone output is converted into a binary image seen in Fig. 1c. The pixelated structure is retained in the fabricated structure to enable direct comparison of the experimental results with those predicted by topology optimization. The design procedure briefly summarized above is the same as the linear approach, which is explained in detail in [7].

3. Fabrication and characterization

The fabrication process, shown in Fig. 2 was initially optimized for three-beam microgrippers [2]. A polysilicon-on-insulator (polySOI) wafer with a 650 nm SiO_2 layer and a 5 μm p-type polycrystalline silicon (polySi) device layer is used. Due to lateral etching of the polySi structures during reactive ion etching (RIE) (Fig. 2b), the line-width of the resulting structures had a 1 μm decrease in the line-width on their upper surface, compared to the designed dimensions (Fig. 3).

Actuation curves of the topology optimized microgrippers are obtained by measuring the displacement of the gap between the end-effectors under an optical microscope (Fig. 4a).

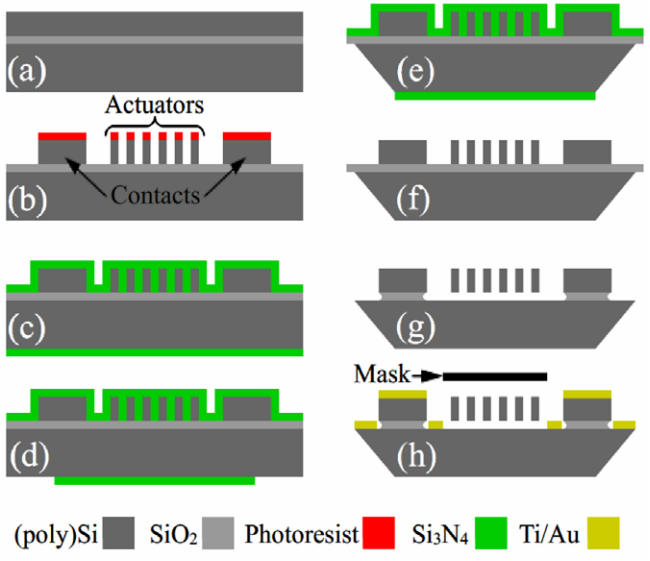

Fig. 2. Fabrication sequence for the polySi microgrippers.

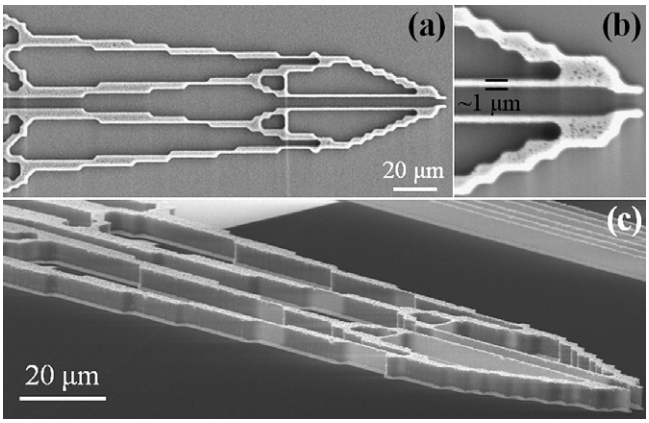

Fig. 3. SEM image of the topology optimized microgrippers: (a) Top view after RIE step with (b) a close-up view of the end-effectors and (c) isometric view after complete release, showing non-uniform side walls.

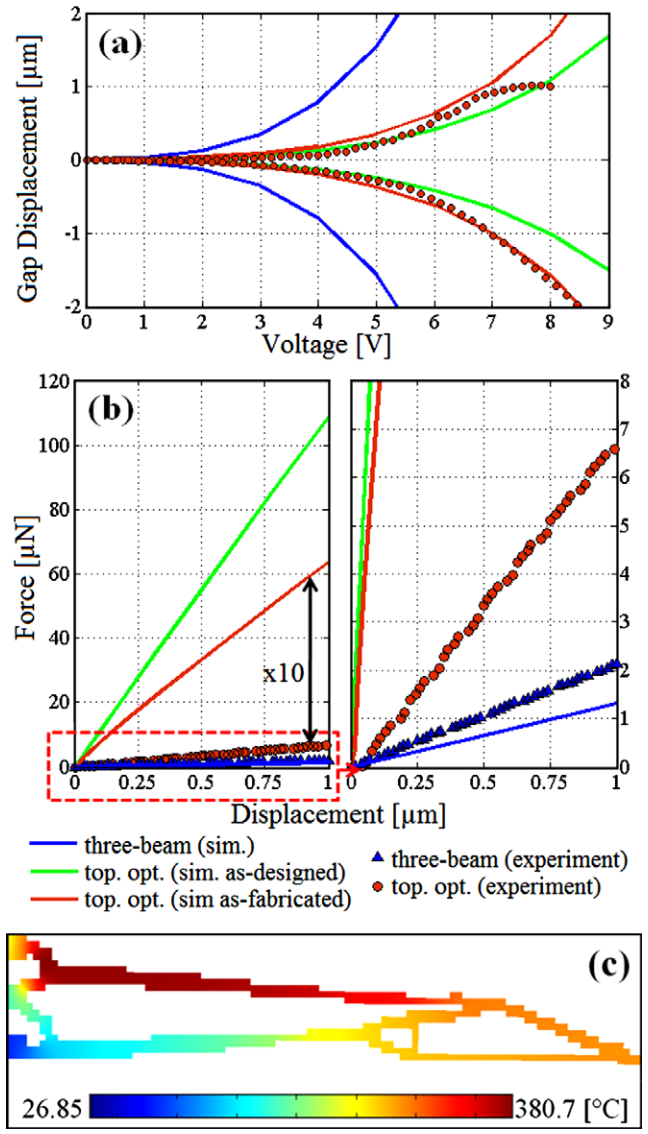

Fig. 4. Simulation and experiment results for (a) bias voltage-gap displacement for open and close modes and (b) force–displacement (left) with a detailed plot of the experiment results (right). (c) Simulation of the temperature distribution within actuator at 9 V.

Force vs. displacement curves of both topology optimized and three-beam actuators are obtained through AFM measurements (Fig. 4b) and stiffness of both actuators are calculated, by taking the stiffness of the AFM cantilever into account, as 9.1 N/m and 1.1 N/m, respectively.

4. Finite element analysis

Finite element simulations of both the topology optimized and the three-beam actuators are performed using COMSOL as software.

Models also include the initial 100 μm length of the contacts on the silicon wafer together with the underlying SiO_2 layer since heat conduction through these regions is considerable. Also the heat convection through air is also taken into account, with convection coefficient of 100 J/m^2 K. Temperature dependent material properties are used for polySi [8].

Since there is a 1 μm deviation in the line-width of the fabricated actuators from the original design, finite element simulations are performed for both topology optimized actuators with 2 μm line-width (designed) and 1 μm line-width (fabricated).

Simulation results are plotted in Fig. 4a and b. The end-effector temperatures for designed and fabricated optimized actuators are 334 °C (Fig. 4c) and 286 °C, respectively, at 1 μm displacement, being slightly higher than that of a three-beamactuator, which is 282 °C.

5. Conclusion

A conventional three-beam electrothermal microgripper design was improved by topology optimization and topology optimized microgrippers were fabricated using silicon microfabrication. A considerable improvement in the gripping force, compared to the three-beam design was shown. The 10 fold improvement should make a 10 fold size reduction possible. Simulation results agree with experiment results, except that the gripping force of the fabricated grippers is one order of magnitude smaller than expected, due to a line-width reduction in fabrication. Also, no improvement was achieved in the end-effector temperature with this preliminary design attempt and further optimization of the fabrication process and improvement of the optimized design is necessary. Despite the issues mentioned above, the results clearly demonstrate that topology optimization is a powerful approach for miniaturization of electrothermal actuators towards nano-scale dimensions and precision.

Acknowledgements

We would like to thank V. Eichhorn from the Division Microrobotics and Control Engineering, Oldenburg University, Germany, for actuation and nanomanipualtion experiments inside SEM.

This work is funded by the EU project NanoHand (IP 034272).

Appendix A. Supplementary data

Movies showing actuation and nanomanipulation experiments using topology optimized microgrippers can be found. Supplementary data associated with this article can be found, in the online version, at doi:10.1016/j.mee.2008.01.049.

References

[1] K. Mølhave, O. Hansen, J. Micromech. Microeng. 15 (2005) 1265–1270.
[2] P. Bøggild, D.H. Petersen, J. Kjelstrup-Hansen, K. Mølhave, K.N. Andersen, O. Sardan, Proc. Mechatron. 2006 (2006) 120–126.
[3] K. Carlson, K.N. Andersen, V. Eichhorn, D.H. Petersen, K. Mølhave, I.Y.Y. Bu, K.B.K. Teo, W.I. Milne, S. Fatikow, P. Bøggild, Nanotechnology 18 (2007) 345501–345508.
[4] K.B.K. Teo, S.-B. Lee, M. Chhowalla, V. Semet, V.T. Binh, O. Groening, M. Castignolles, A. Loiseau, G. Pirio, P. Legagneux, D. Pribat, D.G. Hasko, H. Ahmed, G.A.J. Amaratunga, W.I. Milne, Nanotechnology 14 (2003) 201–211.
[5] K. Mølhave, T. Wich, A. Kortschack, P. Bøggild, Nanotechnology 17 (2006) 2434–2441.
[6] M.P. Bendsøe, O. Sigmund, Topology Optimization, Theory Methods and Applications, second ed., Springer Verlag, Berlin, Heidelberg, 2003.
[7] O. Sigmund, Comput. Methods Appl. Mech. Eng. 190 (2001) 6577–6604.
[8] W. Fulkerson, J.P. Moore, R.K. Williams, R.S. Graves, D.L. McElroy, Phys. Rev. 167 (3) (1968) 765–782.

Proceedings of IMECE2009
2009 ASME International Mechanical Engineering Congress and Exposition
November 13-19, Lake Buena Vista, Florida, USA

IMECE2009-12932

MEASURING THE TEMPERATURE OF TOPOLOGY OPTIMIZED ELECTROTHERMAL MICROGRIPPERS USING RAMAN SPECTROSCOPY

O Sardan Sukas
Nanotech - Department of Micro and Nanotechnology, DTU
DK-2800, Kgs. Lyngby, Denmark

J Liu
EMPA – Materials Science & Technology
CH-3602, Thun, Switzerland

P Bøggild
Nanotech - Department of Micro and Nanotechnology, DTU
DK-2800, Kgs. Lyngby, Denmark

ABSTRACT

In this paper, we present the results of the temperature measurements performed on topology optimized polysilicon microgrippers using Raman spectroscopy. The results reveal that the temperature profile along the actuators is in correspondence with the finite element simulation results presented in [1] except an offset of ~250 °C due to chip heating. In order to predict this behavior, we included a section of the carrier chip into the finite element model. We also fabricated new devices with wider electrodes to reduce the overall Joule heating. Both finite element simulations and experimental results show that the devices with a wider electrodes design lead to a temperature drop of ~50 °C as compared to the devices with the previous electrode design.

INTRODUCTION

Topology optimized electrothermal microgrippers (Fig. 1) [1] are powerful tools for micro/nanomanipulation of carbon nanotubes (CNTs) [2] and nanowires (NWs) [3]. Electrothermal actuation is based on thermal expansion of a structure due to Joule heating, where heat is generated by passing a current through the actuator arms [4]. Apart from the displacement range and the actuator force, the most important performance criterion for electrothermal actuators is the end-effector temperature: too high temperatures can damage the manipulated object as well as the microgripper itself.

It is however, rather difficult to determine the temperature of a micro-actuator with a 1-2 μm feature size. For simple actuator designs, such as the conventional thin beam-thick beam actuator, the temperature can be calculated analytically. For complex designs, such as the topology optimized actuators, the temperature can only be determined through finite element simulations. For both of these methods the effect of the carrier chip and the interface should be taken into account. Raman spectroscopy is a powerful method, which enables temperature measurements in microelectromechanical (MEMS) devices with μm-resolution [5].

In this work, we used Raman spectroscopy to measure the temperature at different locations on topology optimized microgrippers. We also compared the experimental results with finite element simulations.

EXPERIMENTAL WORK

We used a Dilor XY modular laser Raman spectroscopy system to measure the temperature of topology optimized electrothermal actuators during actuation. The setup is composed of two main parts: The spectrometer and the fore-monochromator. The laser from a coherent Innova 90 Ar^+ laser, with a 514.5 nm wavelength, is focused on the sample after passing through a beam splitter and a 50X/100X Olympus objective. The sample can be positioned by switching to a camera, which is connected to a monitor.

The light scattered by the sample is filtered by an optical system of mirrors, slits and gratings in the fore-monochromator. Then, the filtered beam enters the spectrometer, where it is dispersed on a liquid-nitrogen-cooled CCD camera with a resolution of 1024 × 256 pixelsby passing through a grating of 1800 grooves/mm. Data acquired by the CCD is transferred to a computer, instantaneously processed by the NGS LabSpec software and displayed on the computer screen. All

Copyright © 2009 by ASME

measurements were performed on the Stokes side of the Raman spectrum.

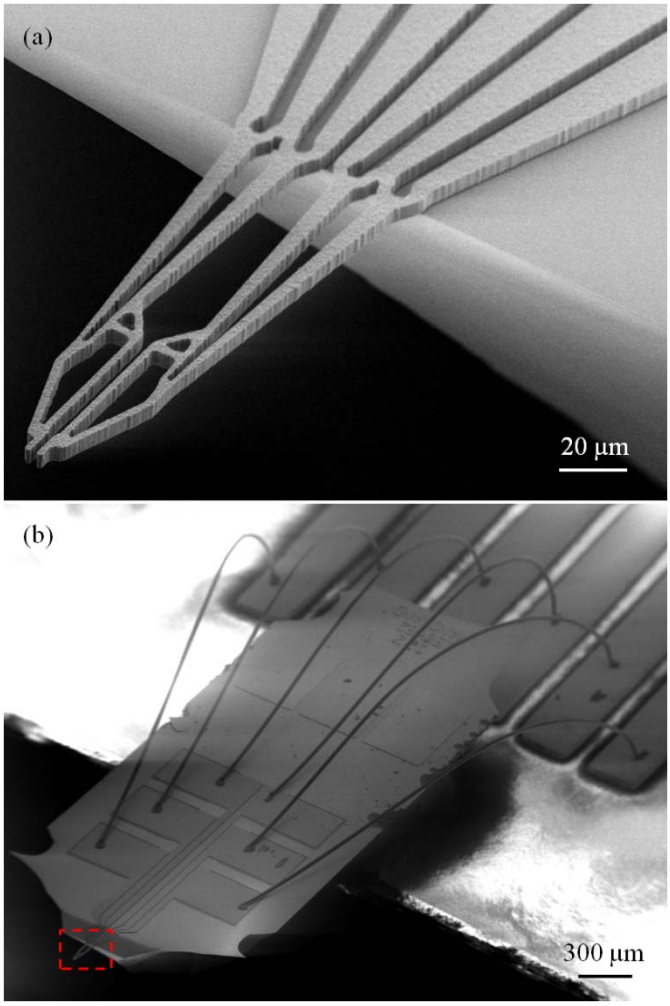

Fig. 1: (a) Topology optimized electrothermal microgrippers and (b) an overview of the carrier chip and the interface.

The sample stage is automated in X and Y directions and can be controlled via the user interface. This enables mapping of a certain area by performing measurements at a number of predefined points.

The device to be measured is placed on the sample stage and connected to a power supply through a PCB interface and can be actuated during the temperature measurements. The spot-size of roughly 1 µm allows measuring the temperature distribution of the microgrippers with a high spatial resolution.

The measurements were performed in ambient air. In addition to single measurements performed at specific points on the actuators, we also obtained a map of the temperature distribution by taking multiple measurements within a grid.

The temperature at the measurement point is then calculated according to [5]:

$$T = T_0 + \left(\frac{d\Omega}{dT}\right)^{-1} (\Omega - \Omega_0) \quad (1)$$

In equation (1), $T_0 = 25\,°C$, which is the initial temperature, $(d\Omega/dT) = -0.024\ cm^{-1}°C^{-1}$ for polysilicon, Ω is the average peak position of the two measurements collected and $\Omega_0 \approx 520.6\ cm^{-1}$ is the initial peak position at T_0.

The measurement points selected along the actuators with the initial, narrow electrode design are shown in Fig. 2.

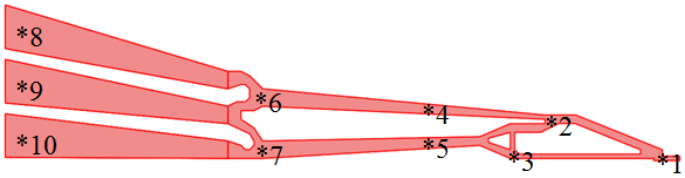

Fig. 2: Measurement points selected along the actuators with the narrow electrode design.

FINITE ELEMENT SIMULATIONS

Finite element simulations of the topology optimized actuators were performed using the MEMS Module of COMSOL Multiphysics. Coupled thermo-electro-mechanical analyzes were carried out using a 3D model. The model includes the actuator, first 100 µm-length of the electrodes, the insulating oxide layer underneath them and the front part of the carrier chip. An electric potential is applied at the end of the upper electrode (the electrode with point 8 in Fig. 2), where the ends of the remaining two electrodes were set as ground. Note that, this corresponds to the closing mode of the microgrippers. The heat conduction through the PCB interface was implemented as a heat flux at the bottom boundary of the carrier chip. Convection through the ambient air was also included as a thermal boundary condition.

RESULTS

Comparison of the experimental data with the finite element simulation results for the actuator with narrow electrodes (Fig. 2) can be seen in

Fig. 3.

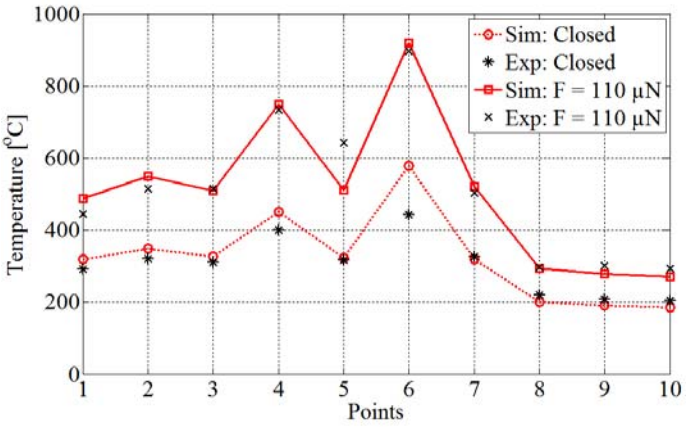

Fig. 3: Comparison of the experimental results with finite element simulations for the actuators with narrow electrodes.

Copyright © 2009 by ASME

At the closed position (operating voltage, V_o = 5.3 V), the temperature values measured at the end-effector (point 1), at the heater location (point 6) and on the inner lead (point 10) are 292 °C, 444 °C and 205 °C, respectively. Beyond the closed position, when the actuators are applying ~110 µN force (V_o = 7.5 V), the temperature values at points 1, 6 and 10 are measured as 444 °C, 897 °C and 298 °C, respectively.

The temperature map of the actuators is obtained at ~570 nm displacement (V_o = 4.1 V), i.e. when the gap is half closed, by performing measurements at different locations (Fig. 4).

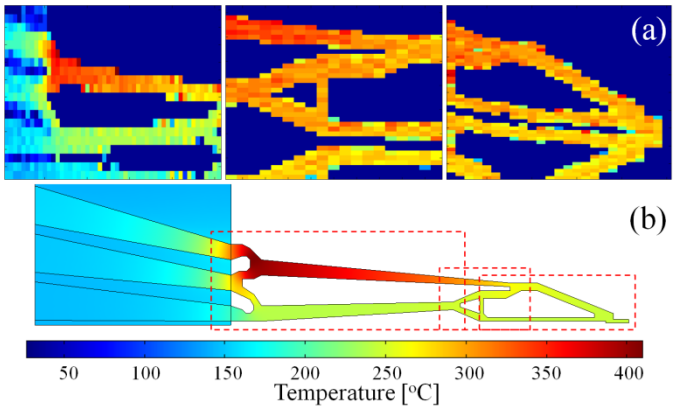

Fig. 4: Comparison of the mapping results with finite element simulations for the actuators with narrow electrodes at the half closed position.

In order to decrease chip heating, the leads connecting the actuators to the bonding pads are widened considerably compared to [1] as shown in Fig. 5. Comparison of the experimental data with the finite element simulation results for these new devices can be seen in Fig. 6.

At the closed position, the temperature values measured at points 1, 6 and 10 are 292 °C, 483 °C and 181 °C, respectively. When the actuators are applying ~116 µN force, these values are measured as 439 °C, 783 °C and 258 °C, respectively.

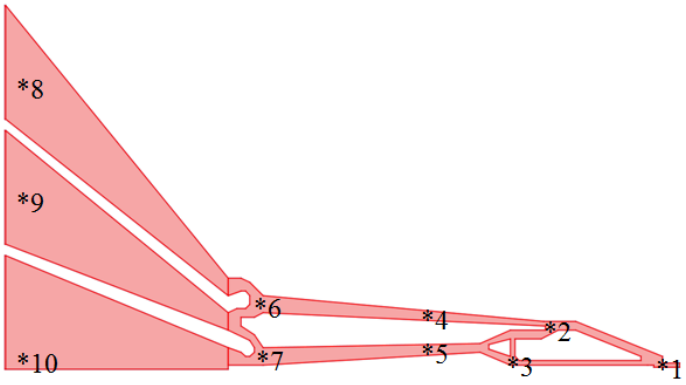

Fig. 5: Measurement points selected along the actuators with the wider electrode design.

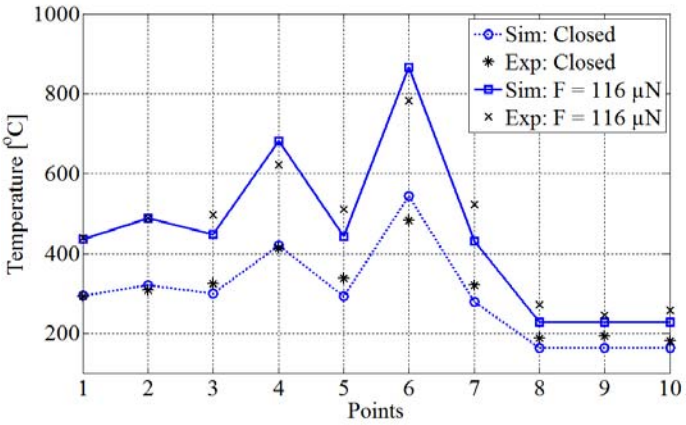

Fig. 6: Comparison of the experimental results with finite element simulations for the actuators with wider electrodes.

Comparison of the simulation results for the initial design with narrow leads and improved design with wider electrodes under the same conditions, where the displacement is equal to 1 µm, can be seen in Fig. 7.

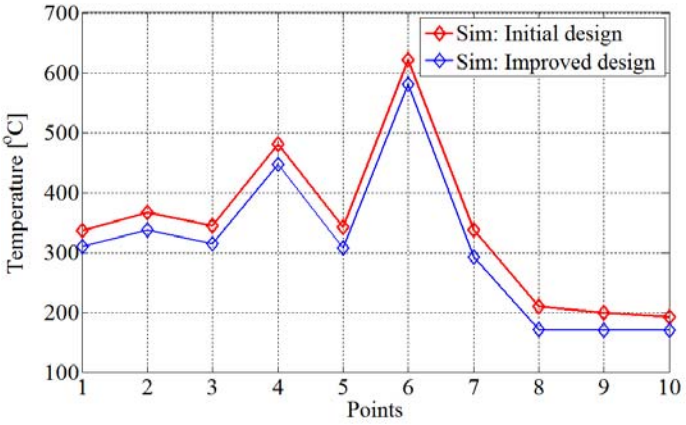

Fig. 7: Comparison of the finite element simulation results for the initial design with narrow leads and improved design with wider electrodes.

CONCLUSION

We performed temperature measurements on topology optimized polysilicon microgrippers using Raman spectroscopy. The finite element simulations are improved to include chip heating. New devices with wider electrodes were designed and fabricated in order to decrease this behavior. Widening the electrodes yields to a ~50 °C decrease in the overall temperature of the actuators.

The results of the point measurements agree rather well with the simulation results for both the initial and improved designs. Mapping results for the initial design are also in good correspondence with the results of the finite element analyzes.

ACKNOWLEDGMENTS

This project was supported by the EU grant NANOHAND (IP 034274).

Copyright © 2009 by ASME

REFERENCES

[1] O. Sardan, V. Eichhorn, D. Petersen, S. Fatikow, O. Sigmund, and P. Bøggild, "Rapid Prototyping of Nanotube-based Devices Using Topology-optimized Microgrippers," *Nanotechnology*, vol. 19, p. 495503, 2008.

[2] K. Teo, S. Lee, M. Chhowalla, V. Semet, V. Binh, O. Groening, M. Castignolles, A. Loiseau, G. Pirio, and P. Legagneux, "Plasma enhanced chemical vapour deposition carbon nanotubes/nanofibres-how uniform do they grow?," *Nanotechnology*, vol. 14, pp. 204-211, 2003.

[3] W. Seifert, M. Borgström, K. Deppert, K. Dick, J. Johansson, M. Larsson, T. Mårtensson, N. Sköld, C. Patrik T. Svensson, and B. Wacaser, "Growth of one-dimensional nanostructures in MOVPE," *Journal of Crystal Growth*, vol. 272, pp. 211-220, 2004.

[4] K. Mølhave and O. Hansen, "Electro-thermally Actuated Microgrippers with Integrated Force-feedback," *Journal of Micromechanics & Microengineering*, vol. 15, pp. 1265-1270, 2005.

[5] J. Serrano, L. Phinney, and S. Kearney, "Micro-Raman thermometry of thermal flexure actuators," *Journal of Micromechanics and Microengineering*, vol. 16, pp. 1128-1134, 2006.

Copyright © 2009 by ASME

Simulation of Topology Optimized Electrothermal Microgrippers

O. Sardan[*,1], D. H. Petersen[1], O. Sigmund[2] and P. Bøggild[1]
[1]DTU Nanotech, Denmark
[2]DTU Mechanical Engineering, Denmark
*Corresponding author: DTU Nanotech, Ørsteds Plads, DTU Building 345E, DK-2800, Kgs. Lyngby, Denmark, oezlem.sardan@nanotech.dtu.dk

Abstract: In this work, electrothermal microgrippers designed using topology optimization are modeled. The microgrippers are composed of two 5 μm-thick polysilicon actuators facing each other. The gap between the actuators are 2 μm in the initial state and the microgrippers are able to both fully close and further open this gap. The operation principle of the actuators is quite similar to that of a parallel-beam electrothermal actuator and relies on resistive heating by passing a current through the structure. COMSOL MEMS Module is used in order to model the temperature distribution, end-effector displacement and stiffness of both topology optimized and conventional parallel-beam actuators. End-effector displacement vs. bias voltage curves for both modes, i.e. open and close, of the microgrippers obtained through finite element analysis fit almost perfectly to the experimental data.

Keywords: Microgrippers, electrothermal actuators, topology optimization.

1. Introduction

Electrothermal microgrippers are promising tools enabling manipulation and assembly of nano-scale structures, which is rather challenging. A simple type of an electrothermal microgripper is composed of two parallel-beam actuators (Figure 1 (left)) [1, 2]. Parallel-beam opposing microgrippers are advantageous due to their compactness, design flexibility and operational simplicity.

The most important performance criteria for electrothermal microgrippers can be listed as the actuator force, the actuation range and the temperature of the end-effectors during actuation. Although parallel beam microgrippers have a relatively large actuation range, they are on the lower limit of supplying sufficient force to detach nano-structures which are firmly attached to a substrate surface [2], such as vertically grown carbon nanotubes (CNTs) [3]. Furthermore, the temperature of the end-effectors during actuation is quite high, enabling only manipulation of nanostructures with a high melting temperature.

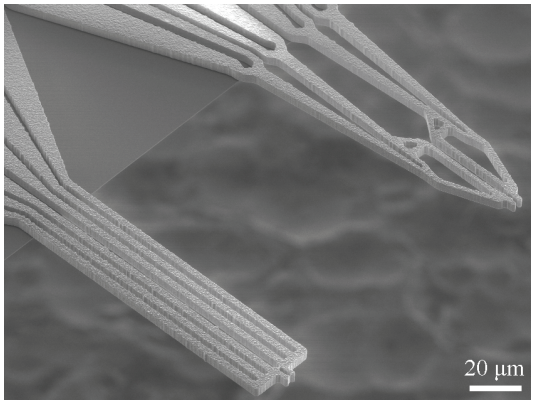

Figure 1. Electrothermal microgrippers: a parallel-beam (left) and a topology optimized (right) design.

We decided to use topology optimization in order to design electrothermal microgrippers with the highest possible actuator force at the desired actuation range and the lowest possible operation temperature. Topology optimization is a finite element based method, which relies on distribution of a certain amount of material within a well-defined design domain to perform a specific task [4].

In this paper, topology optimized electrothermal microgrippers and their operation principle are introduced initially. Then, the procedure for the finite element analysis performed using COMSOL MEMS Module is described in detail, mentioning about the 3D model and the simulation settings. Finally, the results of the finite element simulations are discussed, together with their comparison with the experimental data.

2. Topology Optimized Microgrippers

Electrothermal microgrippers were designed using topology optimization and they were fabricated from a 5 μm-thick highly boron-doped

polysilicon device layer with a 1 μm-thick buried silicon dioxide layer separating the device layer from the silicon handle wafer (Figure 1 (right)). Detailed design and fabrication procedures can be found elsewhere [5].

The operation principle of the topology optimized microgrippers is the same as that of a parallel beam microgripper, which relies on resistive heating of the structure by passing a current through it (Figure 2). The microgrippers can both open and close depending on the configuration of the voltages applied to the actuator beams.

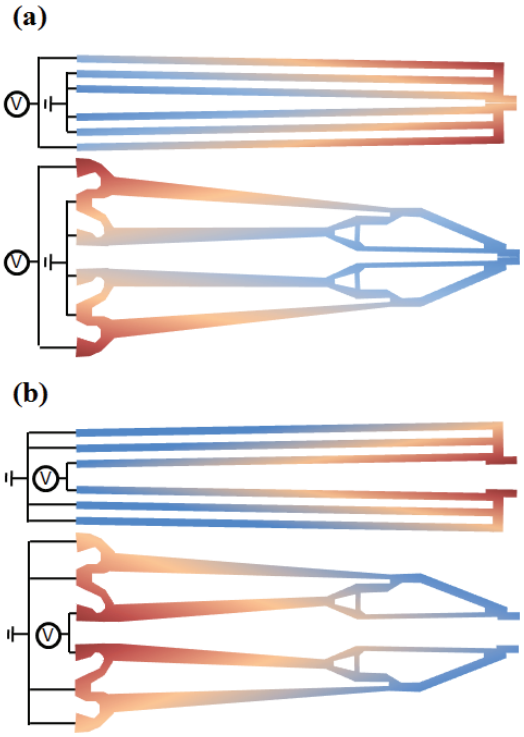

Figure 2. Operation principle of parallel-beam and topology optimized microgrippers showing the voltage configuration for (a) closing and (b) opening modes.

According to the results of the optimization algorithm, the topology optimized actuator is an order of magnitude stronger than that a three-beam actuator. However, mechanical properties of the actual devices are expected to be different as a result of the deviation from the original design during conversion of the gray-scale output of the topology optimization program to a binary image (see [5]). Such changes may also yield to a difference in the operation temperature of the actuator. Hence, performing finite element analysis of the topology optimized actuator prior to fabrication is of vital importance for predicting the performance of the fabricated devices.

3. Finite Element Simulations

Finite element simulations of the topology optimized actuator were performed using the MEMS Module of COMSOL 3.4. The model was composed of three application modes: Conductive Media DC (emdc), Heat Transfer by Conduction (ht) and Solid, Stress-Strain (smsld).

3.1 Geometry Settings

The workplane was selected as z=0 and a 2D CAD drawing of the topology optimized actuator was imported from a DXF file. The 3D model was then created by extruding the imported geometry along the z-axis. In addition to the actuator itself, the first 100 μm length of the leads connecting the device to the contact pads were also included in the model, together with the 1 μm-thick silicon dioxide layer underneath them (Figure 3).

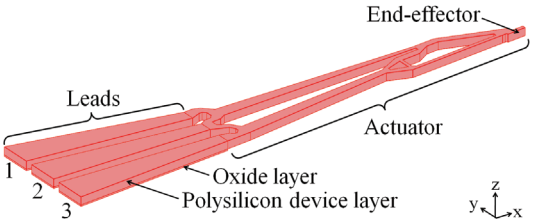

Figure 3. The 3D COMSOL model for the topology optimized actuator.

3.2 Subdomain Settings

Materials for the polysilicon and silicon dioxide layers were selected from the materials library of COMSOL MEMS Module as “poly-Si” and “SiO2”, respectively. However, coefficient of thermal expansion and electrical and thermal conductivities of polysilicon were changed and defined asappropriate functions of temperature [6] (Appendix 8.1 & 2).

In the Heat Transfer by Conduction application mode, a heat source was defined with the value “Q_dc”, which corresponds to the

resistive heating calculated during the electrical analysis. Also the initial temperature was set to 300 K for all subdomains in this application mode.

In the Solid, Stress-Strain application mode, and under the "Load" tab, the thermal expansion was included by defining the strain temperature as "T" and the strain reference temperatures as 300 K. Here, "T" is the temperature calculated during the thermal analysis.

3.3 Boundary Settings

Boundary settings for the electro-thermomechanical simulation of the closing mode of the microgrippers were as follows:

In the Conductive Media DC application mode, electric potential boundary conditions were applied to the ends of the polysilicon leads (Figure 3). For this mode, Lead 1 was set to an electric potential of "V0" and Leads 2 & 3 were defined as "Ground". All remaining boundaries were defined as "Electric Insulation".

In the Heat Transfer by Conduction application mode, temperature boundary conditions were applied to the bottom of the oxide layers underneath the leads (Figure 3) by setting all three to 300 K. Also, the effect of heat transfer through the air was included by defining a heat flux boundary condition to all boundaries, which are in contact with air. External temperature for the heat flux is defined as 300 K and a temperature dependent heat transfer coefficient was used [6] (Appendix 8.2). All remaining boundaries were defined as "Thermal Insulation".

In the Solid, Stress-Strain application mode, the bottom surfaces of the oxide layers underneath the leads were defined as "Fixed", where the remaining boundaries were defined as "Free".

Boundary settings for the opening mode of the microgrippers were the same as those for the closing mode, except the boundary conditions for Leads 1 & 3 are interchanged (Figure 2).

Finally, only a mechanical simulation of the microgrippers was performed in order to calculate the structural stiffness of the actuators. Mechanical boundary conditions for this simulation were the same as both opening and closing modes, except that a prescribed displacement of 1 μm along y-direction was applied to the end-effector boundary (Figure 3).

3.4 Mesh Settings

Since heater and end-effector locations are the most critical regions of the topology optimized actuator, a variable mesh density was used when meshing the structure and a smaller mesh size was used at these locations (Figure 4).

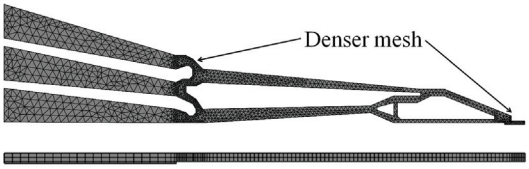

Figure 4. Meshed model: top (top) and side views (bottom).

In the Free Mesh Parameters menu, the edges at the heater and end-effector locations were meshed with a maximum element size of 1 μm. Then, top surfaces of the actuator and the leads were meshed with maximum element sizes of 2.5 μm and 5 μm, respectively. Finally, in the Swept Mesh Parameters menu, the meshes created on the top surfaces were swept along z-direction, using 2 and 1 element layers for polysilicon and oxide subdomains, respectively.

3.5 Solver Settings

The electrothermomechanical simulations of the microgrippers were performed using the parametric solver and the parameter "V0" was solved for values from 0.5 to 6 V with 0.5 V steps. The mechanical simulation of the microgrippers was performed using the stationary solver. The linear system solver is selected as "Direct (PARDISO)" for all cases.

4. Results and Discussion

Results for the temperature distribution within the topology optimized actuator at 1 μm displacement for both closing and opening modes are plotted in Figure 5, where the end-effector temperatures are 265 °C and 371 °C, respectively.

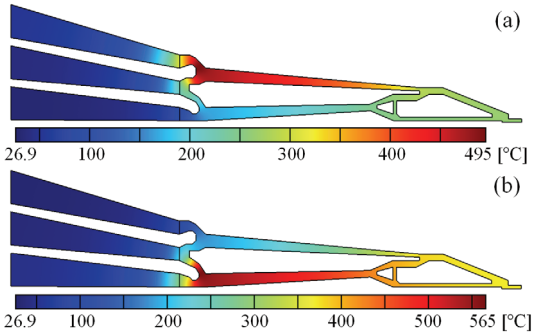

Figure 5. Simulation results for the temperature distribution within the topology optimized actuator at 1 µm displacement in (a) closing and (b) opening modes.

Actuation curves obtained experimentally are compared with the simulation results in Figure 6, where the experimental voltage was normalized to fit the simulation. This is done to account for interconnects serial resistance in the experimental setup.

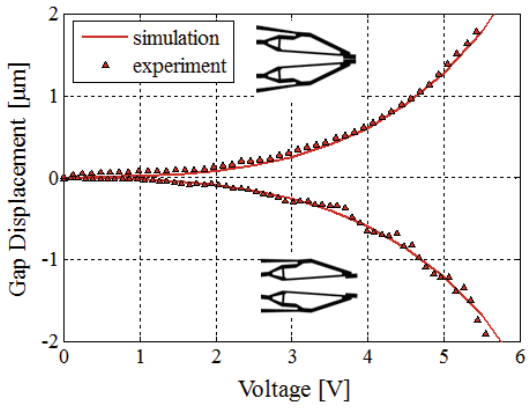

Figure 6. Comparison of the experiment results with finite element simulations for the gap displacement vs. bias curves for the topology optimized microgrippers.

Stiffness of the actuator was calculated as 235 N/m, by integrating the y-component of the force acting on the end-effector boundary, i.e., "lm4", at a displacement of 1 µm along the y-direction.

5. Conclusions

The simulation results seem credible as the displacement behavior of the topology optimized actuator fits quite well with the experimental data. Such an analysis is quite useful for predicting the maximum operation voltage as well as the end-effector temperature and the temperature distribution within the actuator. These parameters are rather important for selecting an appropriate gripper design for a specific type of sample to be manipulated.

The stiffness value calculated according to the mechanical simulation is much higher than that expected by the topology optimization algorithm [5]. The reason for this difference is the change in the mechanical properties of the device during various design steps (see Sect. 2).

In order to verify the correctness of the simulations, the same mechanical simulation was also performed for the 3-beam actuator. According to the results of this simulation, the stiffness of the 3-beam actuator is calculated as 2.2 N/m, which is the same as the theoretical value calculated using the formula given in [1].

6. References

1. K. Mølhave and O. Hansen, Electro-thermally actuated microgrippers with integrated force feedback, *J. Micromech. Microeng.*, **15**, 1265–70 (2005).
2. K.N. Andersen, D.H. Petersen, K. Carlson, K. Mølhave, O. Sardan, A. Horsewell, V. Eichhorn, S. Fatikow and P. Bøggild, Multimodal electrothermal silicon microgrippers for nanotube manipulation, *Paper accepted by IEEE Trans. Nanotechnol.* (2008).
3. K.B.K. Teo, S-B. Lee, M. Chhowalla, V. Semet, V.T. Binh, M. Castignolles, A. Loiseau, G. Pirio, P. Legagneux, D. Pribat, D.G. Hasko, H. Ahmed, G.A.J. Amaratunga and W.I. Milne, Plasma enhanced chemical vapour deposition carbon nanotubes/nanofibres—how uniform do they grow?, *Nanotechnology*, **14**, 204-11 (2003).
4. M.P. Bendsøe and O. Sigmund, Topology Optimization, Theory Methods and Applications, 2nd Ed., Springer Verlag, Berlin, Heidelberg (2003).
5. O. Sardan, D.H. Petersen, K. Mølhave, O. Sigmund and P. Bøggild, Topology optimized electrothermal polysilicon microgrippers, *Microelectron. Eng.*, **85 (5-6)**, 1096-9 (2008).
6. A.A. Geisberger, N. Sarkar, M. Ellis and G.D. Skidmore, Electrothermal Properties and Modeling of Polysilicon Microthermal Actuators, *J. Microelectromech. Syst.*, **12 (4)**, 513–22 (2003).

7. Acknowledgements

This project is supported by the EU grants NANOHAND (IP 034274) and NANORAC (STREP 013680).

Authors would like to Lars Gregersen and Thure Ralfs from COMSOL A/S for their assistance.

8. Appendix

8.1 Material Properties of Polysilicon

Table 1: Thermal conductivity and coefficient of thermal expansion values of polysilicon [6].

Temperature [K]	Thermal Conductivity [W/(m·K)]	CTE [K^{-1}]
300	65.00	2.5×10^{-6}
400	53.75	3.1×10^{-6}
500	46.54	3.5×10^{-6}
600	40.00	3.8×10^{-6}
700	35.00	4.1×10^{-6}
800	32.08	4.3×10^{-6}

8.2 Functions

Table 2: Function for the electrical resistivity of polysilicon [6].

$1/\rho = \alpha_{1+} \alpha_2 . T^{\alpha 3}$	
Coefficient	Value
α_1	2.6×10^{-3}
α_2	8.16×10^{-9}
α_3	1.946

Table 3: Heat transfer coefficient for air [6].

Temperature [K]	Heat Transfer Coefficient [$W/(m^2 \cdot K)$]
300	1101.7
400	1214.3
500	1381.0
600	1520.7
700	1660.3
800	1799.9

Proceedings of the ASME 2008 International Design Engineering Technical Conferences & Computers and Information in Engineering Conference
IDETC/CIE 2008
August 3-6, 2008, Brooklyn, New York, USA

DETC2008-49540

DRAFT: TOPOLOGY OPTIMIZED MICROGRIPPERS FOR NANOMANIPULATION OF CARBON NANOTUBES

Ozlem Sardan*
DTU Nanotech, Department of Micro & Nanotechnology, Technical University of Denmark, 2800, Lyngby, Denmark

Volkmar Eichhorn
Division of Microrobotics & Control Engineering, University of Oldenburg, 26111, Oldenburg, Germany

Dirch H. Petersen
DTU Nanotech, Department of Micro & Nanotechnology, Technical University of Denmark, 2800, Lyngby, Denmark

Sergej Fatikow
Division of Microrobotics & Control Engineering, University of Oldenburg, 26111, Oldenburg, Germany

Ole Sigmund
Department of Mechanical Engineering, Technical University of Denmark, 2800, Lyngby, Denmark

Peter Bøggild
DTU Nanotech, Department of Micro & Nanotechnology, Technical University of Denmark, 2800, Lyngby, Denmark

ABSTRACT
In this paper, we present the topology optimization procedure, fabrication and characterization results for electrothermally actuated polysilicon microgrippers for nanomanipulation purposes. In our previous work [1], we compared the performance of topology optimized actuator with the conventional three-beam electrothermal actuators [2] of the same size through finite-element simulations and experiments. Here, we further improve the topology optimized microgripper design and demonstrate the preliminary results of pick-and-place nanomanipulation experiments performed, where carbon nanotubes (CNTs) are transferred on four-point probes for electrical characterization.

1 INTRODUCTION
Electrothermal actuators have advantages such as flexible and compact design and simplicity of operation over various other actuator types. Although conventional designs composed of three-beam actuators [2] are suitable for basic nanomanipulation purposes, they are lacking to supply the gripping force necessary to detach nanostructures, which are fixed on a substrate, such as a vertically aligned array of chemical vapor deposition (CVD)–grown CNTs [3]. Furthermore, the high end-effector temperatures during operation limit the application field of such microgrippers to nanostructures with a high-melting point. Although a different microgripper design, which is composed of a rib-cage actuator [4], is a quite promising tool, providing solutions to the problems mentioned above, they are lacking in terms of flexibility and compactness.

2 TOPOLOGY OPTIMIZATION
Topology optimization is a finite-element-based optimization approach, which provides a rational method for finding the optimum structural layout in a well-defined design domain to perform a specific task [5]. Our method is based on an algorithm, which solves a set of mathematical programming problems, within a 200 μm × 40 μm design domain with a 15% volume constraint (Figure 1(a)), which corresponds to the volume occupied by a conventional three-beam actuator in the same domain. The force/end-effector displacement ratio is defined as 25 N/m, according to the detachment force estimate for a CNT of average radius and properties [4].

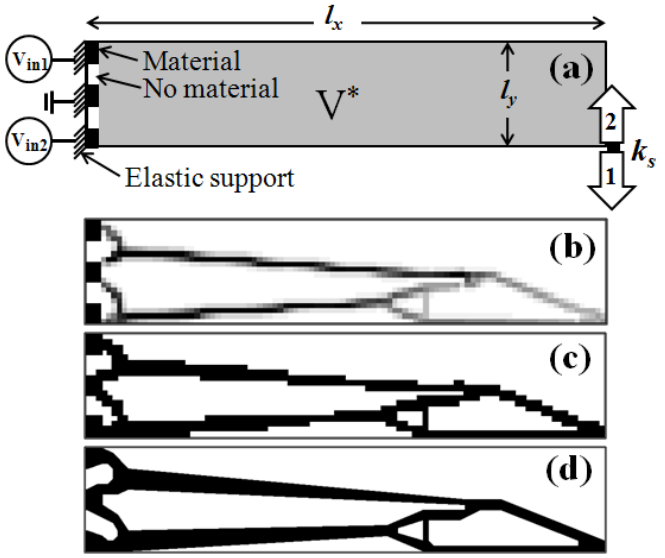

Figure 1. (a) Illustration of the design domain and boundary conditions for the two load cases of the optimization problem, (b) grey-scale output of topology optimization algorithm, (c) conversion of the result to a binary image and (d) final design with smoother features.

* M. Sc. and author of correspondence, Phone: (0045) 4525 6843, Fax: (0045) 4588 7762, Email: sar@mic.dtu.dk.

Copyright © 2007 by ASME

The result of the optimization algorithm is a grey-scale image (Figure 1(b)) with intensity of each pixel representing the material density. Since it is not possible to fabricate a microstructure with a variable material density, the result is converted into a binary (black-and-white) image (Figure 1(c)) and finally, the pixelated structure is removed by straightening the beams (Figure 1(d)).

3 MICROFABRICATION

The procedure seen in Figure 2 was used in the fabrication of the microgrippers with a polysilicon device layer thickness of 5 µm (Figure 3).

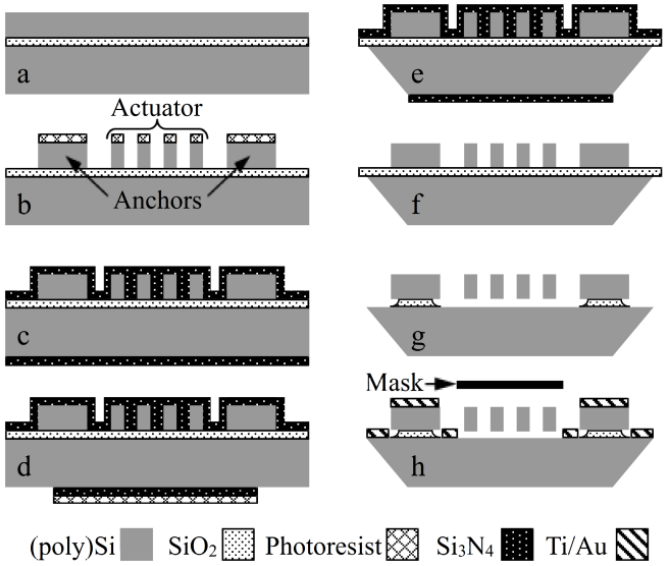

Figure 2. Fabrication sequence for the polysilicon microgrippers.

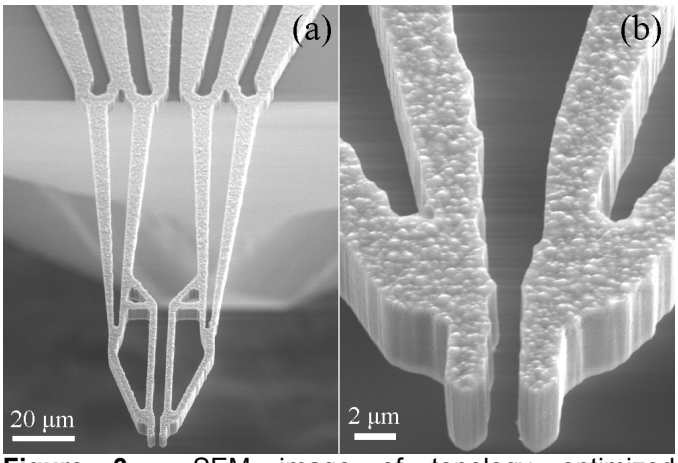

Figure 3. SEM image of topology optimized microgrippers after complete release: (a) 45° tilted front view with (b) a close-up view of the end-effectors.

4 EXPERIMENTAL WORK

4.1. Finite Element Simulations & Actuation:

Since a temperature constraint was not included in the optimization problem there is not a considerable improvement in temperature compared to the conventional design. Simulations foresee an end-effector temperature of 332°C (Figure 4(a)) and a stiffness of 170 N/m, i.e. ~2-fold improvement compared to our initial design [1]. Scaling down the lateral dimensions, i.e. beam-widths and the length, of the optimized actuator by a factor of 0.75 without changing the device thickness caused the stiffness to further increase to 200 N/m. Simulation results for gap displacement vs. voltage fit quite well to the experimental data for (Figure 4(b)), where temperature dependence of polysilicon material properties is taken into account during finite element analysis.

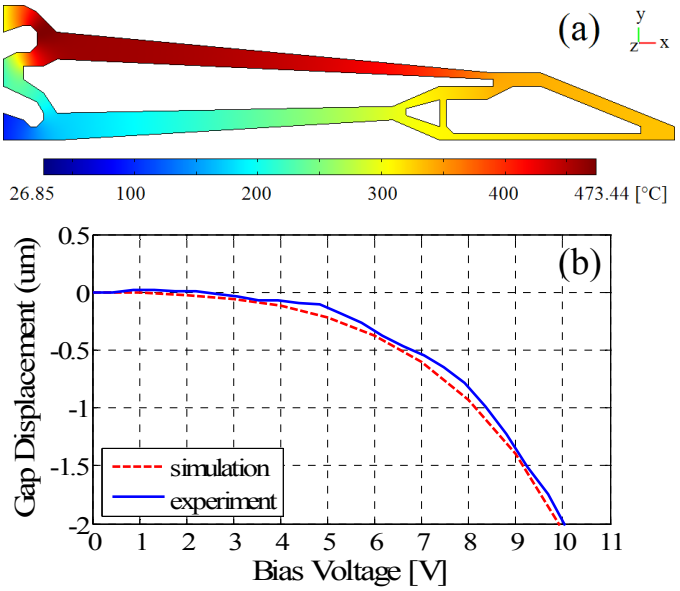

Figure 4. (a) Simulation of the temperature distribution in the as-designed (200 µm-long) actuator at ~1 µm displacement. (b) Comparison of simulation results with experimental data for gap displacement vs. bias voltage for 150 µm-long microgrippers.

4.2. Nanomanipulation of Carbon Nanotubes (CNTs):

The aim of the nanomanipulation experiments performed inside a scanning electron microscope (SEM) is to detach CNTs, which are firmly attached to the substrate surface, and transfer them on a four-point probe. Initially, conventional three-beam microgrippers were tried for detaching of CNTs. However, it was observed that they were not capable of supplying the sufficient force and they open due to a sideways movement of a CNT between the end-effectors, which is still attached to the substrate. Detaching experiments performed with topology optimized microgrippers were quite successful in that CNTs were picked in almost all trials and successfully transferred onto four-point probes in a repeatable manner (Figure 5).

Copyright © 2007 by ASME

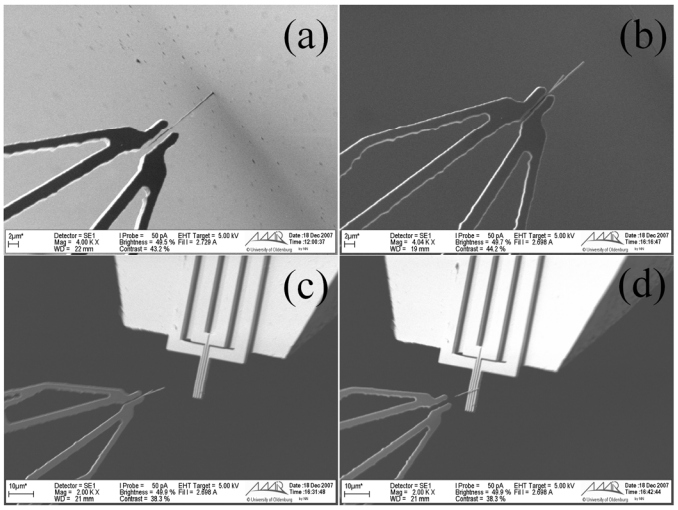

Figure 5. Sequence of SEM images demonstrating pick-and-place nanomanipulation of CNTs from a source substrate onto a four-point probe: (a) Microgrippers approaching to a CNT. (b) CNTs picked, within the microgripper jaws. (c) Microgrippers approaching to a four-point probe. (d) CNTs placed on the four-point probe cantilevers.

6 REFERENCES

[1] Sardan, O., Petersen, D. H., Mølhave, K., Sigmund, O. and Bøggild, P., 2008, *Journal of Microelectronic Engineering*, "Topology Optimized Electrothermal Polysilicon Microgrippers", In press, Corrected Proof, Available online 26 January 2008.

[2] Bøggild, P., Petersen, D. H., Kjelstrup-Hansen, J., Mølhave, K., Andersen, K. N. and Sardan O., 2006, "Microfabricated Tools for Pick-and-place of Nanoscale Components", *Proceedings of Mechatronics 2006, 4th IFAC Symposium on Mechatronic Systems*, pp. 120-126.

[3] Dai, H. J., 2002, "Carbon Nanotubes: Synthesis, Integration, and Properties", *Accounts of Chemical Research*, Vol. **35** (12), pp. 1035-1044.

[4] Carlson, K., Andersen, K. N., Eichhorn, V., Petersen, D. H., Mølhave, K., Bu, I. Y. Y., Teo, K. B. K., Milne, W. I., Fatikow, S. and Bøggild, P., 2007, "A Carbon Nanofibre Scanning Probe Assembled Using an Electrothermal Microgripper", *Nanotechnology*, Vol. **18**, pp. 345501.

[5] Sigmund, O., 2001, "Design of Multiphysics Actuators Using Topology Optimization - Part I: One-material Structures", *Computer Methods in Applied Mechanics and Engineering*, Vol. **190** (49-50), pp. 6577-6604.

Copyright © 2007 by ASME

Proceedings of the ASME 2008 International Design Engineering Technical Conferences & Computers and Information in Engineering Conference
IDETC/CIE 2008
August 3-6, 2007, Brooklyn, New York, USA

DETC2008-49543

DRAFT: FOCUSED ION BEAM (FIB) MODIFICATION OF TOPOLOGY OPTIMIZED POLYSILICON MICROGRIPPERS

Ozlem Sardan*
DTU Nanotech, Department of Micro & Nanotechnology, Technical University of Denmark, 2800, Lyngby, Denmark

Karin N. Andersen
DTU Nanotech, Department of Micro & Nanotechnology, Technical University of Denmark, 2800, Lyngby, Denmark

A. Nicole MacDonald
DTU CEN, Center for Electron Nanoscopy, Technical University of Denmark, 2800, Lyngby, Denmark

Ole Sigmund
Department of Mechanical Engineering, Technical University of Denmark, 2800, Lyngby, Denmark

Peter Bøggild
DTU Nanotech, Department of Micro & Nanotechnology, Technical University of Denmark, 2800, Lyngby, Denmark

Andy Horsewell
Department of Management Engineering, Technical University of Denmark, 2800, Lyngby, Denmark

ABSTRACT

In this paper, we present the preliminary results of the modification of topology optimized polysilicon microgrippers by focused ion beam (FIB) milling. The main aim of the experiments we performed is to functionalize a faulty microgripper by separating the merged end-effectors with a sub-micron gap and reshaping them to achieve a smaller contact area with the manipulated object. However, the method proposed is also rather important for recovery of the dimensional accuracy or missing features during fabrication. Furthermore, it will enable realization of the inverse microgripper concept, which is not possible with conventional UV lithography.

1 INTRODUCTION: NANOMANIPULATION & MICROGRIPPERS

Pick-and-place manipulation of nano-scale objects, such as carbon nanotubes (CNTs), will enable better characterization and understanding of their structural and electronic properties. Topology optimized polysilicon microgrippers, which are based on the electrothermal actuation principle, are promising tools for micro and nanomanipulation purposes due to the availability of high gripping forces together with design flexibility and simplicity of operation [1]. A pick-and-place nanomanipulation sequence, where a CNT is picked from a well-ordered vertical array using electrothermally actuated topology optimized microgrippers and transferred onto a transmission electron microscope (TEM) grid for inspection, is demonstrated in Figure 1.

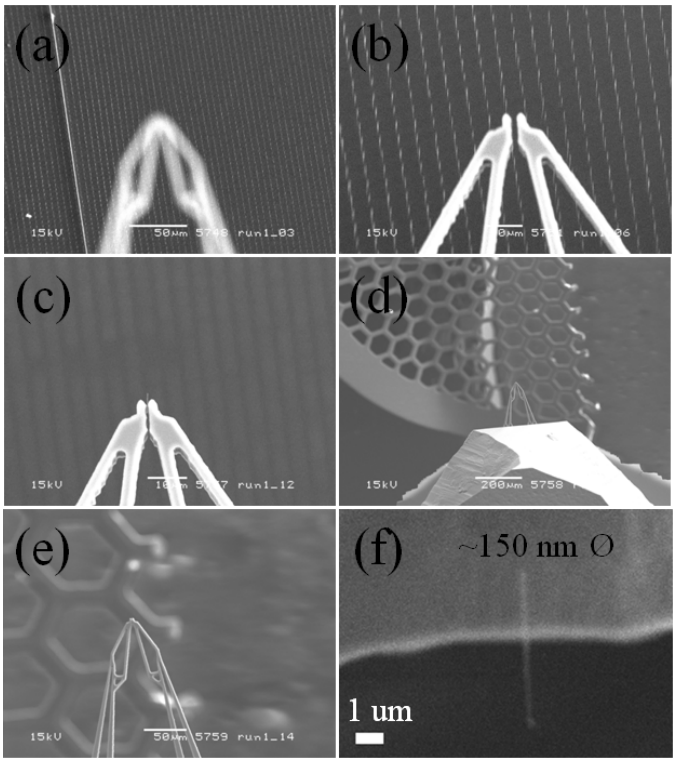

Figure 1. Pick-and-place sequence demonstrating manipulation of a CNT from an ordered 2D array using topology optimized electrothermal polysilicon microgrippers: (a-b) Overview of the CNT array and the microgrippers. (c) A gripped CNT between the end-effectors of the microgripper. (d) Overview of the microgripper chip (seen from below) and a half TEM grid placed next to the CNT substrate. (e) Approaching the

* M. Sc. and author of correspondence, Phone: (0045) 4525 6843, Fax: (0045) 4588 7762, Email: sar@mic.dtu.dk.

Copyright © 2007 by ASME

TEM grid with the gripped CNT. (f) The CNT placed on the TEM grid.

2 FOCUSED ION BEAM (FIB) MILLING

2.1 Applications for Microgrippers:

Designed features and dimensional accuracy should be conserved during the fabrication of topology optimized structures in order to achieve the desired performance. However, this is rather difficult to achieve with conventional UV lithography and fabricated structures may contain many defects such as merged end-effectors, increased and/or reduced dimensions (Figure 2).

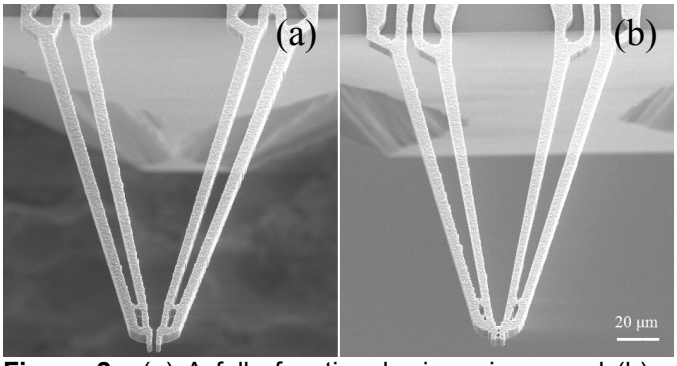

Figure 2. (a) A fully functional microgripper and (b) a non-functional microgripper with merged end-effectors and missing design features.

Devices with defects, such as merged end-effectors (Figure 3(a)), can be turned into functional devices (Figure 3(b)) by proper modification via focused ion beam (FIB) milling [2]. In addition to the separation of the end-effectors with a sub-micron gap (Figure 3(c)), which is not possible with conventional UV lithography, they can be reshaped to obtain a smaller contact area between the sample and the end-effector surface (Figure 3(d) & 4(a-b)) and to refine the shape (Figure 4(b-c)). This would be a solution to one of the main challenges of nanomanipulation: the difficulty in releasing the gripped sample, due to its stiction to the microgripper end-effectors as a result of the van der Waals forces or electrostatic interaction (Figure 5).

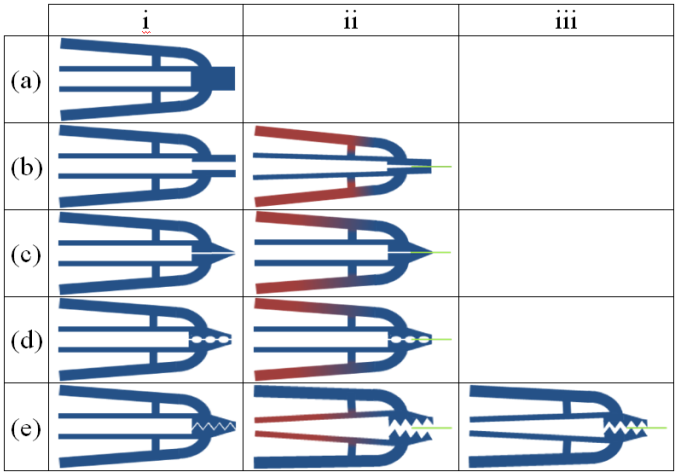

Figure 3. Microfabricated microgrippers: (a) Microgrippers with merged end-effectors. (b) Original microgripper design with 2 µm gap distance (i. Open at the neutral position, ii. closes to grip when actuated.) FIB modified microgrippers with sharp end-effectors and a sub-µm gap distance: (c) End-effectors with a large contact area (i. Open at the neutral position, ii. Actuate less to grip), (d) End-effectors with a small contact area (i. Open at the neutral position, ii. Actuate less to close). (e) Inverse microgrippers (i. Closed at the natural position, ii. Opens when actuated, iii. Grips when released).

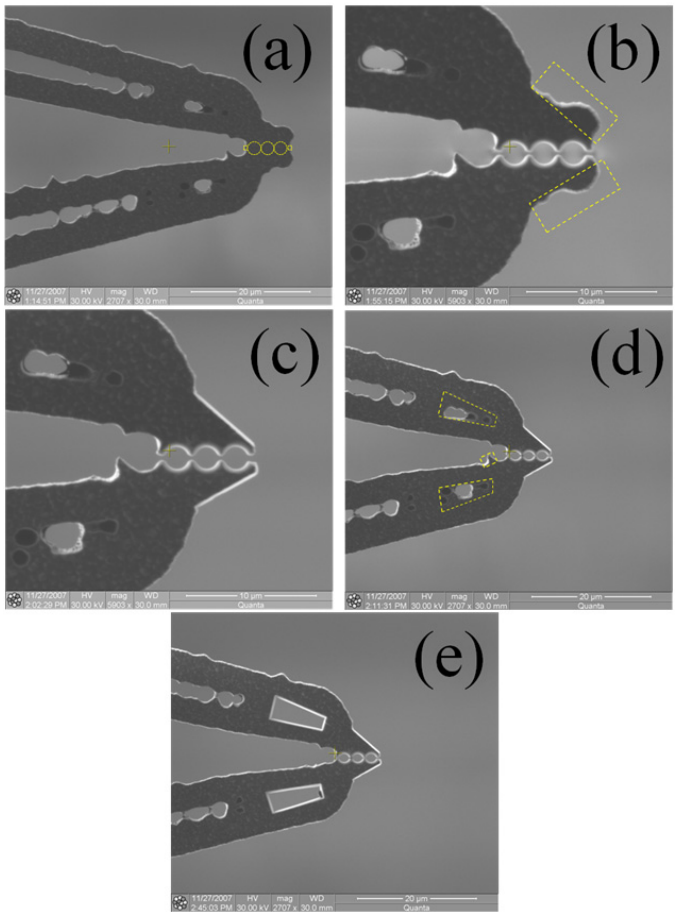

Figure 4. Sequence of images demonstrating modification of a topology optimized microgripper with fabricational defects via FIB micromachining: (a) Microgrippers before FIB modification, showing the region to be removed for separating the end-effectors. (b) Closer view after separation, showing the regions to be removed for further refinement. (c) Microgrippers with separated and functionalized end-effectors. (d) Overview before shape modification, showing the regions to be removed for recovery of features lost during fabrication. (e) Microgrippers after complete modification.

Copyright © 2007 by ASME

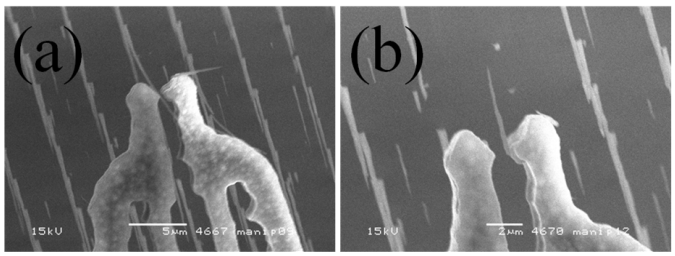

Figure 5. SEM images illustrating the non-uniform shape of the microgripper end-effectors and the stiction problem: (a) A CNT sticking to the right end-effector during picking of another CNT. (b) A picked CNT still remaining attached on the right end-effector after re-opening of the microgrippers.

2.2 Functionalization of End-Effectors:

Proper functionalization of the end-effectors will also enable realization of different microgripper concepts, such as inverse microgrippers (Figure 3(e)), i.e. closed in the neutral position, open when actuated. Using such devices, a gripped object can temporarily be fixed between the end-effectors for transfer to a measurement set-up or to serve as an exchangeable tool-tip.

2.3 Recovery of Design Features:

Finally, missing design features and dimensional variations during microfabrication have a great influence on the gripping and actuation performance of the topology optimized microgrippers. Finite element simulations indicate that even a small decrease in the line-width of an actuator yields to a drastic decrease in its stiffness (Figure 6). FIB milling can be used to remove excess material for recovering designed dimensions or missing features (Figure 4(d-e)).

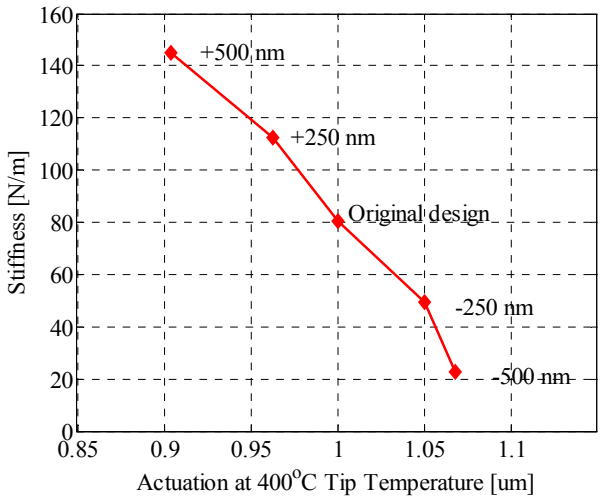

Figure 5. Dependence of actuation performance and stiffness of a topology optimized actuator to dimensional variations.

6 REFERENCES

[1] Sardan, O., Petersen, D. H., Mølhave, K., Sigmund, O. and Bøggild, P., 2008, *Journal of Microelectronic Engineering*, "Topology Optimized Electrothermal Polysilicon Microgrippers", In press, Corrected Proof, Available online 26 January 2008.

[2] Volkert, C. A. and Minor, A. M., 2007, "Focused Ion Beam Microscopy and Micromachining", *MRS Bulletin-Materials Research Society*, Vol. **32** (5), pp. 389-399.

Copyright © 2007 by ASME